NASA/TM-20220005643/Revision 1

Experimental Investigation of Distributed Sand-Grain Roughness Effects on Transition Onset and Turbulent Heating Augmentation at Mach 6

Brian R. Hollis
Langley Research Center, Hampton, Virginia

Kevin E. Hollingsworth
Jacobs Technology, Inc., Hampton, Virginia

February 2023

NASA STI Program Report Series

NASA/TM-20220005643/Revision 1

Experimental Investigation of Distributed Sand-Grain Roughness Effects on Transition Onset and Turbulent Heating Augmentation at Mach 6

Brian R. Hollis
Langley Research Center, Hampton, Virginia

Kevin E. Hollingsworth
Jacobs Technology, Inc., Hampton, Virginia

National Aeronautics and
Space Administration

Langley Research Center
Hampton, Virginia 23681-2199

February 2023

Available from:

NASA STI Program / Mail Stop 148
NASA Langley Research Center
Hampton, VA 23681-2199
Fax: 757-864-6500

Table of Contents

List of Tables

List of Figures

Abstract

An experimental investigation of distributed sand-grain surface roughness effects on boundary-layer transition and turbulent heating has been performed at hypersonic test conditions. Two representative entry vehicle geometries, a sphere-cone aeroshell and a spherical-cap aeroshell, were considered. Cast ceramic models of each geometry were fabricated with distributed sand-grain roughness patterns of different heights that simulated an ablated thermal protection system. Wind tunnel testing was performed at Mach 6 over a range of Reynolds numbers sufficient to produce laminar, transitional, and turbulent flow. Aeroheating and boundary-layer transition onset data were obtained using global phosphor thermography. The experimental heating data are presented herein, as are comparisons to laminar and turbulent smooth-wall heat transfer distributions from computational flow field simulations. The boundary-layer transition data were found to correlate with a functional representation developed in prior roughness studies, although the data scatter was greater owing to the height variability of distributed sand-grain roughness.

Nomenclature

Symbols

D	ASTM mesh particle diameter
H_0	tunnel total (reservoir) enthalpy
H_{AW}	adiabatic wall enthalpy
H_{k}	roughness height enthalpy
H_{W}	wall enthalpy
H_{300K}	wall enthalpy at 300 K
h	measured heat-transfer film coefficient
h_{FR}	Fay-Riddell theory heat-transfer film coefficient
h	measured roughness height
h_{hex}	hexcomb cell height
h_{nom}	nominal ASTM mesh particle roughness height
h_{mean}	measured mean roughness height
$h_{\mathrm{PV}xx}$	measured peak-to-valley roughness height for *xx*% exceedance height
h_{RMS}	measured root-mean-square roughness height
k	actual roughness height
$k_{\mathrm{PV}xx}$	actual peak-to-valley roughness height for *xx*% exceedance height
M_{e}	boundary-layer edge Mach number
M_∞	free stream Mach number
p	effective roughness height transfer parameter
q	heat transfer rate
r_{stag}	approximate radius of edge Mach stagnation cutoff region
R	model radius
R_N	model nose radius
R_C	model corner radius
$Re_{\mathrm{k+}}$	roughness height Reynolds number
Re_θ	boundary-layer momentum thickness Reynolds number
Re_∞	free stream unit Reynolds number
s	surface running length to edge Mach cutoff
s_0	surface running length from stagnation point
T_{e}	boundary-layer edge temperature
$T_{\mathrm{w,AVG}}$	average wall temperature
T_∞	free stream temperature
U_{e}	boundary-layer velocity
U_τ	smooth-wall friction velocity
U_∞	free stream velocity
x, y, z	Cartesian coordinates
X_{TR}	transition correlation disturbance parameter
Y_{TR}	transition correlation flow field parameter
z_{i}	local surface height measurement
β_N	model spherical nose included angle
β_{POHL}	modified Pohlhausen parameter
δ	boundary layer thickness
ϕ	streamline angular coordinate identifier
ϕ_{corr}	heating calibration corrector factor

λ_{POHL}	Pohlhausen parameter
ν_e	boundary-layer edge kinematic viscosity
μ_w	wall viscosity
ρ_e	boundary-layer edge density
ρ_∞	free stream density
θ	boundary-layer momentum thickness
σ_h	roughness height standard deviation

Subscripts and Superscripts

∞	wind tunnel free stream condition
0	wind tunnel stagnation or reservoir condition
e	boundary layer edge condition
k	roughness height condition
PV	peak-to-valley surface roughness distance
RMS	root mean square
TR	transition location
w	model wall condition

Acronyms

ASTM	American Society for Testing and Materials
CFD	Computational Fluid Dynamics
IHEAT	Imaging for Hypersonic Experimental Aerothermodynamic Testing
LAL	Langley Aerothermodynamic Laboratories
LAURA	Langley Aerothermodynamic Upwind Relaxation Algorithm
OML	Outer Mold Line
TPS	Thermal Protection System

Introduction

This report serves to document an experimental dataset of distributed sand-grain surface roughness effects on boundary-layer transition and heating augmentation. The data were obtained through hypersonic wind tunnel testing of two representative entry vehicle aeroshell geometries with roughness patterns that simulated those produced by the ablation of a monolithic thermal protection system (TPS). This report represents a reference document that can be used as the basis for future detailed analysis of the heat-transfer distributions and boundary-layer transition onset locations measured in the test program. This study is a direct follow-on to a previous study (Refs. [1–2]) of ablated TPS with hexcomb pattern roughness effects on the same aeroshell geometries in which the transition criterion applied to the current data was developed. Another related study (Refs. [3–4]) on the effects of distributed sand-grain surface roughness – on hemispherical nose tips, rather than aeroshell geometries – provided the basis for the distributed sand-grain roughness height analysis presented herein.

Background

"Roughness" is a generic term in aerospace literature that encompasses many types of surface features that deviate from that of a smooth outer mold line (OML) surface. Roughness can be divided into two general types, discrete and distributed. Discrete roughness (Figure 1) includes surface features such as: a) protruding compression pads or recessed cavities at mechanical attachment points; b) steps or gaps between heat shield tiles or blocks resulting from differential ablation of the TPS and the filler material between them; and c) physical damage to a TPS. Distributed roughness (Figure 2) includes features such as: a) regular patterns resulting from ablation of hexcomb-structure TPS; b) deflections of a flexible TPS over its support structure when subjected to aerodynamic loading; c) random “sand-grain” features resulting from ablation of a monolithic TPS; or d) the texture of overlapping fibers on a woven TPS.

Data on the effects of surface roughness are valuable because the roughness of an entry vehicle’s TPS can promote earlier boundary-layer transition and produce higher turbulent heating (and shear) levels than would be expected based on an idealized, smooth-surface analysis. However, due to the complexities of roughness effects, a vehicle’s TPS is typically designed using analytical, computational, and/or experimental techniques based on the assumption of a smooth surface. The effects of roughness on the aerothermodynamic environment are then included through approximate engineering correlations and methods.

The purpose of this test program was to obtain data on the effects of distributed sand-grain type roughness. Examples of ablating TPS that produce such patterns include the PICA material used on the Mars Science Laboratory and Mars 2020 missions’ entry vehicle heat shields and on the Stardust comet sample return mission. The data obtained in this test program are intended for use in the development and/or validation of engineering correlations for the effects of distributed sand-grain roughness on boundary-layer transition and turbulent heat transfer for such vehicles. These data can also serve as the basis for development and/or validation of higher-fidelity, numerical flow-field simulation models for roughness effects.

Experimental Tools and Methods

Wind Tunnel Models

Model Geometries

Roughness effects data were obtained on two representative entry vehicle geometries: a sphere-cone geometry (Figure 3) and a spherical-cap geometry (Figure 4). The sphere-cone geometry is representative of the Mars Viking – Mars Pathfinder – Mars Exploration Rover – Mars Phoenix – Mars Science Laboratory – Mars 2020 family of entry vehicles used in NASA’s robotic Mars exploration missions. The spherical-cap geometry is representative of the Mercury – Gemini – Apollo – Orion family of entry vehicles employed in NASA’s crewed space program. Geometry parameters for both model configurations are listed in Table 1. Multiple wind tunnel models of each configuration were fabricated with a range of distributed sand-grain roughness patterns, as detailed below.

Model Fabrication

Models with a wide range of distributed surface roughness heights were fabricated for this study. The fabrication process for a rough-surface model follows that for smooth models, as documented in Ref. [5], with additional steps to add roughness to the surface. The first step in fabrication of a smooth-surface model is the production of a rapid-prototype pattern of the geometry using a 3D wax printing machine. Investment casting is then used to make a mold from the pattern. A thin-shell silica ceramic model is then slip cast from the mold, dried and sintered. The shell is then backfilled with a hydraulically setting magnesia ceramic for strength and support and mounted on a stainless-steel support sting. Finally, the model is coated with a mixture of phosphors that luminesce under ultraviolet lighting and fiducial marks are placed at specified locations on the surface for image registration.

To fabricate a model with surface roughness, an adhesive coating is applied to the smooth wax pattern and then the pattern is placed into a container filled with precision-manufactured, spherical glass particles. The particles adhere to the wax pattern to form a distributed, sand-grain type roughness over the entire surface. The pattern may then be hand-worked if necessary to remove any obvious surface irregularities (i.e., clumps of glass spheres). A ceramic model with surface roughness can then be fabricated from the roughened pattern following the remaining steps detailed above for smooth-surface models.

The distributed sand-grain surface roughness was created using precision-manufactured, spherical glass particles ranging in size from 2.5 mil to 68.9 mil[1]. The spherical glass particle diameters are specified according to an ASTM standard (Ref. [6]) that defines the mesh sieve opening size through which the particle can pass, hence the 'ASTM-XXX' mesh nomenclature for the models. A nominal roughness height for each ASTM mesh size is defined based on the assumption that for a uniform array of roughness elements (the spherical particles) in contact with each other, the roughness height is equal to the vertical distance from the top of an element to the point of contact with the adjacent element – that is the roughness height is equal to the glass particle radius. This height measurement is referred to as the nominal "peak-to-valley" roughness. The characterization of the actual "as-built" roughness height, which differs from the specified nominal value, will be presented below in the "Roughness Height Characterization" section. A listing of the nominal ASTM roughness sizes used in this study is given in Table 2.

Photographs of sample cast ceramic sphere-cone and spherical-cap roughness models with inset closeup images of the roughness at the nose are provided in Figure 5 and Figure 6, respectively. Although the image contrast and resolution are generally not sufficient to display the smaller roughness heights, all the roughness element heights did produce measurable effects on boundary-layer transition and surface heating.

Roughness Height Characterization

Surface roughness scan data acquisition and processing

The surface roughness data presented previously in Table 2 represent ideal values based on the sizes of the particles used in the fabrication of each model. However, the characterization of the actual "as-built" roughness was more complex and was based on a statistical analysis of the surface height distributions. The differences between the ideal and as-built roughness geometries are illustrated in Figure 7. In the ideal geometry, the roughness is defined by perfectly formed hemispherical elements in a single, flat, layer. However, the process of binding the glass particles to the surface, forming the mold, and then casting and coating the ceramic model introduces random imperfections in the surface.

To determine the as-built roughness characterization parameters, laser scans were made of 4-in. x 4-in. square flat sample plates for each of the ASTM roughness sizes to obtain a data cloud of x-y-z points. Margins of 0.5 in. on the sides of the plates were specified to avoid any edge effects and so the actual scan area was a 3 in. by 3 in. square. These flat plates were used in place of the actual model geometries owing to the difficulty of performing a scan over a curved surface. The stated, ideal scan resolution of the system was ~ ±2.00 mil (~±0.05 mm), however, the actual achieved resolution was approximately ±4.00 mil (~±0.1 mm). The data cloud was then triangulated to form a continuous surface representation and the height (z) coordinate was shifted to put the average height of all points at zero.

Profile line-cuts were extracted from the global data sets at various stations to determine the height distribution of scan data points. The global surface scan data and representative profile line-cuts are shown

[1] The "mil" unit (0.001 inch) will be used frequently in the discussion of roughness heights rather than inches or SI units in deference to historical literature on surface roughness.

for each ASTM mesh size sample in Figure 8 – Figure 13. In the line plots, the dashed blue lines represent the nominal diameter and height of a roughness element, and the symbols represent the scan data point locations. As can be seen from these figures, several data points were obtained on each roughness element, for the larger roughness sizes, while for the smaller roughness sizes, the data point spacing was on the order of the roughness element diameter (e.g., 4.17 mil diameter for 140-Mesh and 2.48 mil diameter for the 240-Mesh). Therefore, while data and analyses for these smaller mesh sizes will be presented herein, these data are not considered to be quantitatively reliable.

Statistical Analysis of Roughness Data

The scan data were processed to determine several parameters, including the root-mean-square surface height distribution (h_{RMS}), local peak-to-valley roughness element heights (h_{PV}), and the actual effective peak-to-valley roughness height (k_{PV}).

The root mean square height distribution h_{RMS} is simply a function of the distribution of all height measurement points on the *entire* sample surface as per Eq. (1), where n is the number of points and z_i is the point height above a reference plane. This RMS value does not provide a direct characterization of the heights of the roughness elements, since sample points do not necessarily coincide with the maximum or minimum of an individual roughness element. Nevertheless, the RMS height is a relatively straightforward quantity to define and measure and is frequently reported in roughness studies. A functional relationship between RMS and peak-to-valley heights will be demonstrated subsequently.

$$\boldsymbol{h_{RMS}} = \sqrt{\frac{\boldsymbol{1}}{\boldsymbol{n}}\sum_{\boldsymbol{i}}(\boldsymbol{z_i})} \tag{1}$$

Previous studies of distributed roughness effects (e.g., Refs. [7–8]) have identified the peak-to-valley roughness height h_{PV} as a key parameter in the correlation of roughness data effects. This conclusion was confirmed in the more recent tests conducted in both wind tunnels (Refs. [3–4]) and ballistics ranges (Ref. [9]). The peak-to-valley roughness height represents the difference between the minimum and maximum surface heights of adjacent roughness elements, which for the idealized surface illustrated in Figure 7 would simply be the radius of the spherical roughness element.

To determine the h_{PV} of the actual roughness sample plates, peaks and valleys of adjacent roughness elements were determined manually from examination of the profile line-cut data. The selection of which points along the profiles of Figure 8 – Figure 13 actually represented the peaks and valleys of a roughness element, as opposed to minor variations over an element, was highly subjective and was additionally hindered by the resolution of the scans for the smallest ASTM mesh sample plates. Furthermore, while a fixed ASTM bead size was employed to create each roughness pattern, the application of roughness elements to the wax patterns, fabrication of molds, and final casting of the ceramic models introduced random deviations from the nominal peak-to-valley roughness height. A final complication is the difference between the peak-to-valley heights measured along an arbitrary profile line – which may not pass through the maximum and minimum of an element – as illustrated in Figure 14 – and the true peaks and valleys of individual elements.

These issues were dealt with using a statistical "exceedance" value to represent the random distribution of heights and a semiempirical correction factor to account for the differences between the peak-to-valley heights measured along an arbitrary profile and the actual peak-to-valley heights.

For each profile, the exceedance, which is defined as the percentage of data points in a set greater than a specified value, was computed from the database of peak-to-valley measurements. The exceedance height distributions obtained from scans of each sample plate are plotted in Figure 15. Also shown in this figure are Gaussian curve fits to these data of the form given by Eq. (2), where h_{mean} is the mean of the measured peak-to-valley heights and σ_h is the standard deviation.

$$\%\mathbf{exceedance\ fit} = \mathbf{100} \times \boldsymbol{exp}\left\{-\mathbf{0.5}\left[\frac{(\boldsymbol{h_{PV}} - \boldsymbol{h_{mean}}/\mathbf{2})}{\boldsymbol{\sigma_h}}\right]^{\mathbf{2}}\right\} \tag{2}$$

The exceedance height distributions are replotted in terms of the normalized roughness height (h_{PV}/h_{mean}) in Figure 16. As seen in these two figures, the exceedance distributions approximate the Gaussian distribution that would be expected from a large sample set with random deviations.

A relationship between the actual peak-to-valley height of a roughness element and that measured along a profile line (which does not necessarily pass through the center of the element) was developed by Dirling (Ref. 10) in an analysis for simple geometric elements including hemispheres, cones, and rectangles. Dirling's function for converting between a statistical mean of the measured height, h_{mean}, and the actual height, k, using a transfer function, p is given by Eq. (3). For the current analysis, where the roughness elements are represented as a tightly packed array of nominally hemispherical elements, the $\pi/4$ value of the transfer function is employed. Presumably, transfer functions could also be determined for more complex roughness shapes such as rods, fences, weaves, or honeycombs, but data would be required to validate such functions.

$$\boldsymbol{h_{mean}} = \boldsymbol{k} \times \boldsymbol{p}\text{: }\mathbf{where}\ \boldsymbol{p} = \begin{cases} \boldsymbol{\pi/4} & \textbf{hemispherical element} \\ \mathbf{0.5} & \textbf{conical element} \\ \mathbf{1} & \textbf{rectangular element} \end{cases} \tag{3}$$

For the purposes of this study, it was assumed that this relationship for the mean value also held for any arbitrary exceedance percentile value, allowing for estimation of the true peak-to-valley exceedance height values from the heights measured along the profile lines. Values of the 30^{th} and 50^{th} percentiles have typically been reported in roughness literature, and herein values for the 50^{th}, 30^{th}, 15^{th} and 5^{th} percentiles are given. These values were derived from the measured roughness height distributions of Figure 15 - Figure 16 and are listed in Table 3.

The relationship between the estimates for the actual, as-built, heights to the nominal heights for the 50^{th}, 30^{th}, 15^{th} and 5^{th} percentile exceedances is shown in Figure 17. For the larger ASTM Mesh sizes (10, 20 and 40-mesh), the ratios of k_{PV}/h_{nom} are approximately the same for each exceedance percentile, varying from ~0.5 for the 50^{th} percentile to ~1.0 for the 5^{th} percentile. However, the ratio of actual to nominal height begins to increase rapidly with decreasing mesh size for the smaller ASTM mesh sizes (80, 140, and 230-Mesh). For the smallest, ASTM 230-Mesh, the ratios of actual to nominal height varies from ~1.6 for the 50^{th} percentile to 2.7 for the 5^{th} percentile.

Given that the fabrication process results in a roughness height distribution with a Gaussian shape, the estimates for the as-built to nominal ratios for the larger ASTM mesh sizes seems to be reasonable. However, absent any other information, the estimated peak-to-valley heights for the smaller ASTM mesh sizes would appear to be much larger than the nominal values. As noted earlier though, the nominal roughness sizes for these models were on the order of the ideal image resolution of the scanning system used to obtain the data. Thus, while the results may indicate that the smaller mesh size model roughness heights were larger than intended, the fidelity of the scan data set was insufficient to definitively quantify the smaller mesh size heights. Instead, a rough estimate for the as-built heights for the smaller ASTM samples was made by fitting a curve through the higher ASTM sample ratios and extrapolating the results to the lower ASTM vales to provide a corrected estimate for the peak-to-valley heights. Table 4 provides a summary of these original and corrected values of the 50% exceedance heights, as well as the nominal and RMS values for each ASTM mesh size.

For purposes of comparison with prior studies in which only RMS values are cited, it is useful to provide a relationship between the RMS and peak-to-valley exceedance values. It has been shown (e.g., Refs. [7–8]) that an approximate linear relationship holds between RMS and peak-to-valley exceedance parameters that allows for conversion between the two types of measurements. A plot of the current RMS roughness vs. actual peak-to-valley roughness data from each sample plate is presented in Figure 18 along with a linear correlation for each exceedance value. Depending on the exceedance value, the ratio of k_{PV}/h_{RMS} was found to vary from approximately 2.8 to 4.8.

These results can be compared to those from Jackson in Ref. 8, where it was stated that the "significant" peak-to-valley roughness was equal to 3.6 times the RMS value. Unfortunately, the term "significant" was not explicitly defined, although in Ref. [7], Batt later concluded that the "significant" value was equal to the 30th percentile exceedance height. Reexamination of the limited roughness profile data available from Ref. [8] suggests that Batt's conclusion was tenuous, and that Jackson's "significant" values could just as easily be equated to the 50th percentile roughness height. However, it is possible that Batt had access to more of the original data set than has been published and drew conclusions based on those data. Regardless of the definition of "significant" for the Ref. [8] data set, the cited value of 3.6 for the ratio falls within the range of exceedance values for the current data set, which indicates that the approximate relationship between RMS and peak-to-valley exceedance values is valid.

Wind Tunnel Test Facility

Facility Description

Hypersonic wind tunnel testing of the roughness models was performed in the NASA Langley Aerothermodynamics Laboratory (LAL) 20-Inch Mach 6 Air Tunnel. This wind tunnel is described in brief below and more detailed information on the LAL facilities can be found in Refs. [11–12].

The 20-Inch Mach 6 Air Tunnel (Figure 19 – Figure 20) is a blow-down facility in which heated, dried, and filtered air is used as the test gas. The tunnel has a two-dimensional contoured nozzle that opens into a 20.5 in. × 20.0 in. test section. The tunnel is equipped with a bottom-mounted injection system with a -5-deg to +55-deg pitch range and ±5-deg yaw range that can transfer a model from a sheltered model box to the tunnel centerline in less than 0.5 sec. Run times of up to 15 minutes are possible in this facility, although for the current aeroheating study, run times of only a few seconds were required. The nominal reservoir conditions of this facility produce perfect-gas free stream flows with Mach numbers between 5.8 and 6.1 and unit Reynolds numbers of 0.5×10^6/ft to 8.3×10^6/ft. With its wide Reynolds number operating range capable of producing laminar, transitional, or turbulent flow on most geometries, this tunnel is primarily used for heat-transfer and boundary-layer transition studies.

Facility Operating Conditions

Data were obtained in Tests 7036 and 7057 in the 20-Inch Mach 6 Air Tunnel at six unit-Reynolds numbers from $Re_\infty = 2.1\times10^6$/ft to 8.1×10^6/ft with nominal free stream conditions as per Table 5. All sphere-cone data were obtained at α = 16 deg and all spherical-cap data were obtained at α = 28 deg. Full run matrices for the two tests are given in Table 6 and Table 7, respectively. Entries in these tables are sorted first by roughness height, then by free stream unit Reynolds number. These angles of attack and free stream conditions were selected for continuity with the hexcomb roughness dataset presented in Refs. [1–2].

Free stream velocity (U_∞), density (ρ_∞), temperature (T_∞), unit Reynolds number (Re_∞), and Mach number (M_∞) are provided in these tables. Additionally, an average model surface temperature (T_w), enthalpy difference (ΔH_{tot}), and reference heat transfer film-coefficient value (h_{FR}) are provided. The temperature is the average over the model surface when the thermographic phosphor image was obtained and is provided because boundary-layer transition is known to be sensitive to wall temperature. The enthalpy term is defined as the difference $H_0 - H_{300K}$ between the free stream total enthalpy and the wall enthalpy at cold wall (300 K) conditions. The film coefficient is the value from the Fay-Riddell theory (Ref. [13]) at cold wall conditions, where the radius is the nose radius of the model geometry.

Experimental Data

Data Acquisition and Reduction

Aeroheating data were obtained using the two-color, relative-intensity, global phosphor thermography method (Ref. [14]) and reduced using the IHEAT (Imaging for Hypersonic Experimental Aerothermodynamic Testing) code (Refs. [15–16]). In this method, a model is illuminated by ultraviolet light sources that induce temperature-dependent fluorescence of the phosphor coating. Fluorescent intensity images of a model are taken in the tunnel before and during a run using a three-color, charge-coupled device camera and the images are processed to determine heat-transfer distributions. The intensity data are then converted to temperatures using pretest calibrations of the data acquisition system.

Heat-transfer film coefficients are determined by assuming a step function in the film coefficient from the prerun temperature to the run temperature, which corresponds to a parabolic temperature-time history. The heating data are typically reported in terms of the ratio h/h_{FR} where the heat-transfer film coefficient, h, is defined in terms of enthalpy as:

$$\boldsymbol{h = q/\Delta H_{TOT} = q/(H_{AW} - H_w) = q/(H_0 - H_w)} \tag{4}$$

In the calculation of the heat-transfer film coefficient, it is assumed that for a blunt-body, the adiabatic wall enthalpy H_{AW} is equal to the free stream total enthalpy of the tunnel, H_0, and the wall enthalpy H_W is the determined from the surface temperature at each image pixel. This heat transfer coefficient definition provides a theoretically near-constant value over the course of a run since the decrease in time of the heat transfer rate in the numerator as the model surface becomes hotter is balanced by the decrease of the enthalpy-difference term in the denominator.

Data Mapping and Presentation

The two-dimensional (2-D) image data output from IHEAT (Figure 21) for each run were transformed to account for optical perspective effects and mapped to a three-dimensional (3-D) CAD surface of the wind tunnel model (Figure 22). To accomplish this mapping, perspective, translational, and rotational transformations were first performed on the 3-D CAD surface until its 2-D projection matched that of the 2-D image data. The image data were then assigned transformed (x, y, z) coordinates based on interpolation between the image and projected surface geometry. Finally, the transformation was inverted to obtain an orthographic, 3-D heating distribution map of the experimental data.

An additional data manipulation was performed to extract the streamline-based heating distributions from the mapped wind tunnel data set. These streamline-based data sets are used in boundary-layer transition analyses and for comparisons of Reynolds number and roughness effects. For each run, streamlines were defined based on the boundary-layer edge velocity vectors from the computed flow fields (to be discussed in the next section). Thirty-six streamline termini were established at locations spaced in 10-deg increments around the circumference of the geometry and the streamlines were then traced backward from each terminus toward the flow field stagnation point. Each streamline is identified by the angular location, ϕ, of its terminus. The resulting streamlines are shown in Figure 23 for the sphere-cone geometry and in Figure 24 for the spherical-cap geometry. The geometric (x, y, z) coordinates along each streamline were then interpolated onto the 3-D mapped image and h/h_{FR} heating data were extracted along each streamline in terms of s_0/R, which is the normalized streamline distance from the stagnation point. Additionally, the predicted flow field quantities (boundary-layer height, momentum-thickness Reynold number, etc.) were also extracted along these streamlines and combined with the wind tunnel data set to enable transition onset analyses.

One additional complication needs to be noted with respect to extraction of data along streamlines. The extraction algorithm tended to fail near the stagnation point where the velocity vectors approached zero; essentially, the physical location became indeterminate, resulting in unreliable path-lengths through the stagnation region. This problem was resolved by stopping the reverse tracing of the streamlines from the outer edge of the model toward that stagnation point at the location where the edge Mach number, M_e, dropped below 0.025. The “true” streamline length value, s_0 was determined from an estimate of the physical length from the M_e cutoff to the stagnation region as a function of the streamline terminus angular location ϕ and the approximate radius of the stagnation region, r_{stag}:

$$\boldsymbol{s_0 = s + \Delta s} \tag{5}$$

$$\Delta \boldsymbol{s} = \boldsymbol{cos(2\phi)} \times \boldsymbol{r_{stag}/3} + \boldsymbol{r_{stag}} \text{ , where } \boldsymbol{r_{stag}} \cong \mathbf{0.003\ m} \tag{6}$$

In the body of this report, plotted data will be shown in terms of s/R, as that is the quantity in which the data were extracted along streamlines. The estimated actual distance, s_0/R, can be determined using Eqs. (5) and (6).

The mapped data from all runs are collected in the Appendices and presented therein as large, high-resolution images. These images are ordered by model geometry, roughness height, and Reynolds numbers. Smaller images will be shown in the body of the report along with streamline-based heating distributions.

Phosphor Thermography Data Quality

An important factor that influences the quality of phosphor thermography data quality is the local surface inclination at a given point on the model with respect to both the camera and the UV lights. Phosphor thermography provides the best results when the surface to be imaged is normal to the camera, which reduces perspective distortion and image smearing, and when the surface is well illuminated, which induces the best temperature response of the phosphor coating. Because of the three-dimensional nature of a wind tunnel model, the entire surface of a model cannot be optimally imaged, or in some cases cannot even be viewed. For blunt bodies such as those in this test, the windward centerline region of the model – the 'bottom' of the model with respect to the view orientation - is the area where the data quality is most affected. This situation is illustrated for a simple hemispherical model in Figure 25. Because of this limitation, windward region data are only regarded as qualitative, not quantitative. Although image data from this region will be shown, quantitative plotted data and transition location data will not be provided for the streamlines originating from the ϕ = 160-deg through 200-deg termini.

Heat Transfer Data Uncertainty

The experimental uncertainty for convective heat transfer measurements on a *smooth, blunt body geometry* model in the 20-Inch Mach 6 Air Tunnel is quantified as a function of net uncertainties resulting from: the data acquisition method (±10%); flow quality and test-condition repeatability (±5%); and the accuracy of the 3D mapping process (±10%), which results in an overall root-sum-squared value of ±15%. Experience with this technique indicates that these values are usually conservative and agreement between laminar, smooth-wall measured and predicted heating levels is generally well within this range.

However, it is assumed that the distributed sand-grain roughness introduces additional uncertainties to the heat-transfer measurements. These roughness elements produce very detailed heating patterns due both to their three-dimensional shape and their influence on transition locations. In many cases, these patterns were smaller than the resolution of the camera system; thus, a measurement of heating over a roughness element is in effect, a spatial average, rather than a point measurement. Quantification of such errors on a macro-scale is not possible because of the localized and position/height dependency of each roughness element, but they are probably on the order of ±10–20%. Taken together with the smooth-wall uncertainty, the uncertainty in distributed sand-grain roughness heating is estimated to be in the ±18–25% range

Calibration Correction for Heat Transfer Data

A central premise in the analysis of wind tunnel heating data is that for a given Mach number, the normalized heat transfer film coefficient, h/h_{FR}, at any point on a geometry remains constant with varying Reynolds number at perfect gas conditions for attached flow over a blunt body. This behavior is demonstrated through CFD simulations for a 2-inch diameter hemisphere over the current range of test conditions. As shown in Figure 26, laminar simulations using the LAURA code (see section below on Computational Tools and Methods) predict a constant value of h/h_{FR} = 1.06 at the hemisphere stagnation point for all test condition Reynolds numbers. The fact that the ratio is not exactly 1 is due to the differences between a modern CFD prediction for the film coefficient at perfect-gas wind tunnel conditions and the semiempirical Fay-Riddell correlation for the film coefficient based on approximate boundary-layer solutions for reacting-gas flight conditions. That the two predictions are so close is a testament to the utility of the original Fay-Riddell method that was developed in the 1950s.

While the CFD predictions do indeed demonstrate a constant value of h/h_{FR} for the wind tunnel conditions, the same behavior was not observed during the test program; in fact, a dependency on free stream Reynolds number was noted in the experimental data. This dependency is illustrated by stagnation point heating data from pretest checkout and calibration runs on a phosphor-coated, 2 inch radius hemisphere shown in Figure 27 for Test 7036 and in Figure 28 for Test 7057. Instead of a constant value for h/h_{FR}, the measured values at lower Reynolds numbers were observed to be at or below the predicted value from the computations, while at higher Reynolds numbers the measured values were greater than the predictions. Second-order polynomial fits to the measured heating values that reflect these variations are also shown in the figures.

There are several potential sources of uncertainty which could be producing this dependency including: variations in the bulk materials used to cast the ceramic wind tunnel models; the consistency of the thermographic phosphor mixture used to coat the models; the fidelity of the phosphor intensity/temperature calibrations; degradation of the UV lighting or imaging camera; and/or the flow quality of the wind tunnel. Unfortunately, it was beyond the scope of this study to resolve whether any, or all, of these factors influenced the experimental data.

Because the differences in predicted and measured stagnation point film-coefficient ratios fell within the estimated uncertainty of ±18–25% range cited in the previous section, these results were considered "acceptable" from an experimental perspective. However, since the differences can be represented by a bias function that depends on Reynolds number, as opposed to a random dispersion, an additional data processing step was conducted to correct the heating data based on the hemisphere calibration run data. The original data were modified using the polynomial curve fits as per Eqs. (7) and (9) and all data and results presented herein reflect this calibration correction.

$$(\boldsymbol{h}/\boldsymbol{h_{FR}})_{\boldsymbol{exp,corr}} = (\boldsymbol{h}/\boldsymbol{h_{FR}})_{\boldsymbol{exp}} \times (\boldsymbol{h_{CFD}}/\boldsymbol{h_{FR}})_{\boldsymbol{hemi-stag}} \times \emptyset_{\boldsymbol{corr}} \tag{7}$$

where:

$$(\boldsymbol{h_{CFD}}/\boldsymbol{h_{FR}})_{hemi-stag} = 1.06 \tag{8}$$

$$\begin{gathered}
\emptyset_{\boldsymbol{corr}} = \mathbf{1}/(\boldsymbol{A} + \boldsymbol{Bx} + \boldsymbol{Cx}^{\mathbf{2}})\text{, and } \boldsymbol{x} = \boldsymbol{Re}_{\infty}/\mathbf{1,000,000} \\
\textbf{Test 7036}: \quad \boldsymbol{A} = \mathbf{0.8279} \quad \boldsymbol{B} = \mathbf{0.09120} \quad \mathrm{C} = -\mathbf{7.583} \times \mathbf{10^{-3}} \\
\textbf{Test 7057}: \quad \boldsymbol{A} = \mathbf{0.9971} \quad \boldsymbol{B} = \mathbf{0.03163} \quad \mathrm{C} = -\mathbf{2.034} \times \mathbf{10^{-3}}
\end{gathered} \tag{9}$$

Computational Tools and Methods

Flow field solutions were generated using the LAURA (Langley Aerothermodynamic Upwind Relaxation Algorithm) code. LAURA (Refs. [17–18]) is a three-dimensional, structured-grid, finite-volume solver that includes perfect-gas and nonequilibrium chemistry options, a variety of turbulence models, and ablation and radiative transport capabilities. LAURA solutions were used for comparisons of predicted heating levels with the measured data and to define the streamlines along which to extract the mapped experimental data, as described above.

Solutions were computed on multiblock grids of each geometry with a smooth (no roughness elements) outer mold line. Grid adaption was performed to align the grid outer boundary with the bow shock and to cluster cells near the surface to produce wall cell Reynolds numbers on the order of 1 to 10. Free stream conditions were set to the nominal wind tunnel conditions for each operating point as given in Table 5. For these wind tunnel conditions, the perfect-gas air option was used. Both laminar and turbulent solutions were generated. Turbulent cases were computed using the Cebeci-Smith algebraic model with fully turbulent flow over the entire geometry. Because the computations were performed on a smooth geometry, they are not quantitively applicable to the actual wind tunnel tests performed on rough-surface models with heating augmentation but are still provided for qualitative comparisons.

For the wall temperature boundary condition, a change in the normal practice for wind tunnel simulations of setting this value to a "cold-wall" ambient temperature (because of the small variation in heat-transfer coefficient with temperature) was employed. Literature on roughness effects indicates a dependence of transition onset location on the ratio of boundary-layer edge temperature to wall temperature T_e/T_w. To approximately account for this effect (which was expected to be small, but non-negligible, for these test conditions), the computations were performed using a uniform "hot-wall" wall temperature set to the average of the measured surface temperature on the model. These values varied between ~ 325 K to 410 K, depending on roughness height and Reynolds number.

The flow field solutions also provided boundary-layer parameters that can be used in the correlation of transition and heating augmentation data. Centerline profiles of selected boundary-layer parameters are presented to provide insight into the range of the test data and potential relevance to flight missions.

The ratio of the physical roughness height to that of the boundary-layer, k/δ, has a first-order influence on transition onset. Centerline distributions of k/δ are presented in Figure 29 for the sphere-cone geometry and in Figure 30 for the spherical-cap geometry for the range of roughness heights and free stream Reynolds number conditions. In these figures, k is the corrected 50% exceedance values from Table 4 and δ is the physical height of the boundary layer. Values of k/δ varied over two orders of magnitude depending on roughness height and Reynolds numbers. The smallest k/δ values are well within the boundary layer, while the highest exceed the boundary layer height.

The turbulent roughness height Reynolds number, Re_{k+} as per Eq. (10), can be used as a correlation parameter for turbulent roughness heating augmentation. Centerline distributions of Re_{k+} are presented in Figure 31 and Figure 32 for the sphere-cone geometry and spherical-cap geometries, respectively, for the range of roughness heights and free stream Reynolds number conditions. Values of Re_{k+} also vary over two orders of magnitude, indicative of laminar flow at the lowest levels and roughness-augmented turbulent flow at the highest levels.

$$Re_{k+} = \rho_w U_\tau k_{PV50}/\mu_w, \text{ where } U_\tau = \sqrt{\tau_w/\rho_w} \tag{10}$$

Experimental Data Analysis

Transition Onset Location Definition

From a flow physics standpoint, transition onset is defined as the point where smooth, laminar flow in the boundary layer begins to break down into small eddies. This location can, in theory, be determined through flow field imaging and/or diagnostic techniques (e.g., high-frequency pressure measurements, laser velocimetry) to determine when fluctuations in a quantity of interest, such as the mean velocity, exceeded a specified criterion. However, in this study, the only measurements are of the surface temperature and (through data reduction) the surface heating. For such measurements, the differences in temperature or heating levels between laminar flow and transitional flow can be too subtle at some conditions to permit precise definition of the onset location. This measurement is more difficult when the local roughness height is small, in which case, the change from laminar to transitional/turbulent flow is gradual, but easier when the local roughness height is large, and the transition length is very short.

In lieu of a precise measurement of the transition location, transition onset is defined herein through a common approach in which an “effective” or “apparent” onset point is determined through the “tangent-slope-intercept” method. As shown in Figure 33, using sample data for a hemisphere from Ref. 4, the effective transition onset location is identified as the point where a line drawn tangent to the slope of the heat-transfer distribution curve through the transition region intercepts the nominal, laminar level. While this method does not necessarily identify the precise location at which fluctuations in the boundary-layer flow begin, it is consistent with common practice for determining the roughness-induced transition location via surface-based measurement techniques. This method also permits a more consistent means of identifying a relevant transition parameter, since identification of the small rise in heating levels at the actual transition onset location would be highly susceptible to error through surface measurement techniques alone. If the data herein are compared to other datasets, then it will be necessary to ensure that the same definition of transition onset is applied to ensure consistency.

While this effective transition onset location is easy to define in principle, in practice, there can still be considerable uncertainty in determining the effects of roughness on transition location because of the difficulty in precisely defining the relevant roughness height. Consider again the distributed roughness hemisphere example, where now the heating data are shown in image form (Figure 34) rather than a plotted distribution. In the ideal case, where the surface roughness was invariant over the entire model surface, the transition onset location would be at a constant streamline length around the circumference of the model since the flow field is axisymmetric. However, as shown in Figure 34, there are clearly circumferential variations in the transition onset location. These variations occur because the local roughness height at any given location can vary from the nominal value for many reasons, including: the fidelity of the model fabrication process; the uniformity in application of the phosphor coating; and damage to the coating due to handling of the model or particle impacts during testing.

For an axisymmetric flow such as that over the example hemisphere, it was possible to reduce the uncertainty in the transition onset location by averaging multiple onset locations around the body to determine a mean value. This approach was followed in Ref. [4]. However, for the three-dimensional flow fields produced by the geometries considered herein, that was not possible. Thus, transition correlations drawn from this dataset can be expected to have greater scatter than those that were derived from Ref. [4].

Reynolds Number Effects on Heating and Transition

The effects of Reynolds number on the heating levels and boundary-layer transition onset locations are illustrated for each distributed sand-grain roughness pattern in Figure 35 – Figure 48 for the sphere-cone geometry and in Figure 49 –Figure 62 for the spherical-cap geometry. Two figures are provided for each case: in the first figure, global heating images are shown for each Reynolds number, ordered left-to-right, top-to-bottom in terms of increasing Reynolds number; in the second figure, line plots of h/h_{FR} vs. s/R are shown, ordered left-to-right, top-to-bottom in terms of streamline angular coordinate. For brevity and clarity, all the streamlines are not plotted in these figures. Instead, streamlines are shown at 30-deg increments from 0 deg to 150 deg. As noted earlier, the data for streamlines between 160 deg and 200-deg are considered qualitative, not quantitative, and were thus omitted. Data for streamlines from 210 deg to 360 deg are nominally symmetric with the data from 0 deg to 150 deg, although in practice, model surface irregularities can cause asymmetric behavior. Such local asymmetries can be observed in the images that accompany the line plots.

In these line-plots, the CFD predictions for smooth-wall, laminar and turbulent heating levels are also shown. Because the laminar heat-transfer film coefficient ratio, h/h_{FR}, remains nearly constant with Reynolds number, only the lowest Reynolds number laminar prediction is shown for each case. However, since this invariance does not hold for turbulent flow, turbulent predictions are shown for each Reynolds number. As noted previously, simulations for these cases were treated as fully turbulent flow over the entire geometry. These turbulent predictions are shown for qualitative comparisons only, since the actual transition occurred at different locations for each test condition / model geometry and since the turbulent heating levels were augmented above smooth-wall levels by the surface roughness.

Roughness Height Effects on Heating and Transition

The same data are shown in the next group of figures, but they are reordered to show the effects of the distributed sand-grain surface roughness height on transition and heating at each Reynolds number. The sphere-cone data are shown in Figure 63 – Figure 74 and the spherical-cap data are shown in Figure 75 – Figure 86. Two figures are provided for each case: in the first figure, global heating images are shown for each Reynolds number, ordered left-to-right, top-to-bottom in terms of increasing roughness height; in the second figure, line plots of h/h_{FR} vs. s/R are shown, ordered left-to-right, top-to-bottom in terms of streamline angular coordinate. As with the Reynold number effects figure set, both laminar and turbulent CFD heating predictions are shown in each line plot. It is assumed that facility noise effects on transition are minimal in these data because the surface OML roughness features (step or gaps) promote a "bypass transition" mode (Ref. [19]) that is separate from the small disturbance growth modes of conventional stability theory analyses.

General Reynolds Number and Roughness Height Trends

In these line plots for Reynolds number and roughness height effects, the laminar CFD predictions allow for baseline assessment of the computational accuracy through comparisons with the low Reynolds number, small roughness height cases for which transition did not occur. In general, good agreement between data and predictions was observed for all laminar cases. However, the turbulent predictions are shown only for illustrative purposes since the fully-turbulent, smooth-wall computations do not account for roughness effects on the transition location or heating augmentation above smooth-surface levels.

Reynolds-number and roughness-height effects on transition and heating follow expected trends. As Reynolds number is increased, the transition onset location moves upstream toward the stagnation point of the model. The transition onset location also moves upstream as roughness height is increased and the measured rough-wall turbulent heating levels grow increasingly higher than the predicted smooth-wall turbulent heating levels.

Roughness Heating Augmentation

In this report, analysis of the heating augmentation due to the roughness patterns is limited to the expected observation that heating levels increase with roughness height. This limitation is due to the complexities of the problem and the goal of quickly releasing this data set as a basis for further analysis. For any given roughness height / Reynolds number / body-point location, the heating augmentation with respect to smooth-wall laminar or turbulent predictions can be determined through reference to the data and figures presented herein. However, the development of engineering correlations or numerical models for simulation of these data depend on not just modeling the effects of roughness on heating, but also modeling the effects of roughness on transition onset; that is, it is not possible to accurately predict heating levels without being able to first predict the transition onset location. Implementation of a transition model into a CFD code and generation of transitional flow field solutions will be deferred to future in-depth analyses.

Transition Onset Data and Correlation

As per discussion above, transition locations (or lack thereof) were determined along each of 36 different streamlines for every run using the tangent-slope-intercept method. Discounting the windward streamline data from the ϕ = 160-deg through 200-deg rays with poor viewing angles and lighting, 2604 data points (2 model geometries × 6 free stream Reynolds numbers × 7 roughness heights × 31 rays) on the state of the boundary layer were obtained. Tabulations of these transition onset data for each streamline are given in Table 8 – Table 14 for the sphere-cone geometry and in Table 15 – Table 21 for the spherical-cap geometry. Tabular entries are only provided for the 1720 streamlines along which transition was noted. For reference, the boundary-layer momentum thickness, Re_θ, value at transition is also listed. This quantity, along with the roughness height, is a first-order factor in the correlation of roughness transition data.

A correlation for the effects of roughness on boundary-layer transition was developed originally in Ref. [3] based on a survey of transition data on hemispherical geometries with distributed sand-grain roughness as per Eq. (11) through Eq. (13).

$$Y_{TR} = \mathbf{165} \times (\boldsymbol{X_{TR}})^{-\mathbf{0.5}} \tag{11}$$

where

$$Y_{TR} = (\boldsymbol{Re_\theta})_{TR} \tag{12}$$

$$X_{TR} = \left[\left(\frac{\boldsymbol{kT_e}}{\boldsymbol{\theta T_w}} \right) \left(\frac{\boldsymbol{H_e}}{\boldsymbol{H_k}} \right)^{-1} (\boldsymbol{M_e})^{-0.5} \right]_{TR} \tag{13}$$

$$k = \begin{cases} \boldsymbol{k_{PV50}} & \text{sand-grain roughness} \\ \boldsymbol{h_{hex}} & \text{hexcomb pattern depth} \end{cases} \tag{14}$$

This original correlation was subsequently modified in Ref. [1] to account for the effects of varying pressure gradient in the non-axisymmetric flows over the current sphere-cone and spherical-cap geometries with patterned hexcomb roughness as per Eqs. (15) through (20). In this correlation, the pressure gradient effects are included through a modified Pohlhausen parameter, β_{POHL}, which is derived from the original Pohlhausen parameter, λ_{POHL}.

$$Y_{TR} = \mathbf{171.4} \times (\boldsymbol{X_{TR}})^{-\mathbf{0.6299}} \tag{15}$$

where

$$Y_{TR} = (\boldsymbol{Re_\theta})_{TR} \tag{16}$$

$$X_{TR} = \left[\left(\frac{\boldsymbol{kT_e}}{\boldsymbol{\theta T_w}}\right)^{\mathbf{0.45}}\left(\frac{\boldsymbol{H_e}}{\boldsymbol{H_k}}\right)^{\mathbf{-1.8}}(\boldsymbol{M_e})^{-\mathbf{0.6}}(\boldsymbol{\beta_{POHL}})^{-\mathbf{0.5}}\right]_{TR} \tag{17}$$

$$\boldsymbol{log}(\mathbf{1}/\boldsymbol{\beta_{POHL}}) = \overline{\boldsymbol{\lambda}}_{\boldsymbol{POHL}} \tag{18}$$

$$\overline{\boldsymbol{\lambda}}_{\boldsymbol{POHL}} = \boldsymbol{min}[\mathbf{10}, \boldsymbol{max}(-\mathbf{10}, \boldsymbol{\lambda_{POHL}})] \tag{19}$$

$$\boldsymbol{\lambda_{POHL}} = \frac{\boldsymbol{dU_e}}{\boldsymbol{ds}}\frac{\boldsymbol{\delta^2}}{\boldsymbol{\upsilon_e}} \tag{20}$$

In the Pohlhausen parameter, the pressure gradient is related to the velocity through the Bernoulli equation, which is approximately valid for the low Mach number boundary-layer conditions of a blunt body. The boundary-layer height, δ, and dynamic viscosity, ν_e, terms provide a consistent nondimensionalization of the velocity gradient over a wide range of conditions. However, to be used in the power-law form of this correlation, the pressure gradient term must have a positive value, and must also be limited to prevent computational overflow or underflow at the aeroshell shoulder or stagnation point. Thus, the original Pohlhausen parameter is modified by *min* and *max* limiters and redefined through the *log* function to ensure a positive value.

The utility of this correlation is demonstrated through the plots in Figure 87 for the sphere-cone and spherical-cap hexcomb roughness datasets of Refs. [1–2] and the hemisphere sand-grain roughness dataset of Refs. [3–4]. The majority of transition data points from these two different types of distributed roughness tested in multiple wind tunnels and ballistics ranges fell within a ±20% uncertainty bounds of the correlation.

The current test program permits evaluation of this correlation against distributed sand-grain roughness data from three-dimensional geometries that produce varying pressure gradients. Comparisons of these new data with the correlation are given in Figure 88. While this new distributed sand-grain roughness data set follows the same trend line as the correlation, it exhibits considerably more scatter than earlier data sets, with the majority of points bounded by a higher range of ±50%.

However, there is a key characteristic of the current data set that differs from prior data sets, which is the variability of roughness height over the surface of a wind tunnel model. As discussed earlier, the roughness elements in the current data set were found to exhibit an approximately Gaussian height distribution due to the method in which the roughness elements were created. The height values used in this analysis represent the 50% exceedance value, which means that half of the roughness elements have a larger height than the specified value and half have a smaller height. In contrast, the roughness heights for the prior hexcomb studies varied less because they were specified the hexcomb sizes were defined uniformly in the CAD design of the models and were fabricated as such. And for the hemispherical sand-grain roughness data sets, the transition data were based on analyses of multiple streamlines around the circumference of each model – all which experienced the same pressure gradient due to the axisymmetric nature of the flow– which had the effect on normalizing the data for the effects of varying roughness height.

Given these differences in the definition and reporting of the roughness heights between these studies, it is thus not surprising that the current data exhibit much more scatter than the earlier data. The current distributed sand-grain roughness data set is in fact, probably a more "flight-realistic" representation of roughness transition characteristics. The TPS of an actual flight vehicle is likely to exhibit more variability in roughness due to manufacturing defects, damage during handling and flight preparation, and random variations in material response. A real-world example of nonuniform transition response is illustrated in Figure 89 by a post-flight photograph (from Ref. [20]) of the Orion EFT-1 flight test mission heat shield. While the green-outlined areas that identify damage during recovery of the heatshield can be disregarded, the red-outlined areas represent isolated transition wedges caused by nonuniformities in the surface of the heatshield.

Since the new transition data follow the same trend as the earlier data, albeit with much more scatter, no modifications will be made to the transition of Eqs. (15) through (20). However, these wind tunnel data – and the flight data from EFT-1 – illustrate the need to consider large margins on the transition predictions to account for potential variations in roughness heights from an expected nominal value.

Summary

The effects of distributed sand-grain surface roughness patterns simulating that of a heat shield with an ablated TPS on hypersonic boundary-layer transition and turbulent heating have been investigated through wind tunnel testing of two representative entry vehicle geometries. Heating and transition onset data were obtained at Mach 6 over a range of roughness heights and free stream Reynolds numbers sufficient to produce laminar, transitional, and turbulent flow. Boundary-layer transition onset locations were tabulated, and heating distributions were provided in both line plot and image forms. Measured heating levels were found to increase with both Reynolds number and roughness height. The transition onset location trend was found to agree with a correlation developed from prior studies, although with greater scatter due to the variability of the sand-grain roughness heights over the surfaces of the wind tunnel models.

Acknowledgements

This work was supported by the NASA Entry Systems Modeling Project within the Game Changing Development Program of the Space Technology Mission Directorate.

References

1. Hollis, B. R., "Hexcomb-Pattern Roughness Effects on Blunt-Body Transition and Heating," *Journal of Spacecraft and Rockets*, Vol. 58, No. 6, November-December 2021, pp. 1612-1635.
2. Hollis, B. R., "Experimental Investigation of Hexcomb-Pattern Roughness Effects on Transition Onset and Turbulent Heating Augmentation at Mach 6," NASA/TM-2019-220424, November 2019.
3. Hollis, B. R., "Correlation of Recent and Historical Hemispherical Nose Tip Distributed Roughness Transition Data," *Journal of Spacecraft and Rockets*, Vol. 56, No. 5, May-June 2019, pp. 664-686.
4. Hollis, B. R., "Experimental Investigation of Roughness Effects on Transition Onset and Turbulent Heating Augmentation at Mach 6 and Mach 10," NASA/TM-2017-219613, May 2017.
5. Buck, G. M., "Rapid Model Fabrication and Testing for Aerospace Vehicles," AIAA Paper 2000-0826, 38th AIAA Aerospace Sciences Meeting and Exhibit, Reno, NV, January 10-13, 2000.
6. ASTM E11-01, Standard Specification for Wire Cloth and Sieves for Testing Purposes, ASTM International, West Conshohocken, PA, 2001.

7. Batt, R. G. and Legner, H. H., "A Review of Roughness-Induced Nosetip Transition," *AIAA Journal*, Vol. 21, No. 1, January 1983, pp. 7-22.

8. Jackson, M. D., "Passive Nosetip Technology (PANT) Program. Volume 15: Roughness Induced Transition on Blunt Axisymmetric Bodies – Data Report," Space and Missile Systems Organization TR-74-86-Vol-XV, April 1974.

9. Wilder, M. C. and Prabhu, D. K., "Rough-Wall Turbulent Heat Transfer Experiments in Hypersonic Free Flight", AIAA Paper 2019-3009, AIAA Aviation 2019 Forum, Dallas, TX, June 17-21, 2019.

10. Dirling, R. B., "On the Relationship Between Material Variability and Surface Roughness," AIAA Paper 1977-0402, 18th Structural Dynamics and Materials Conference, San Diego, CA, March 21-23, 1977.

11. Berger, K., Rufer, S., Hollingsworth, K. and Wright, S., "NASA Langley Aerothermodynamic Laboratory: Hypersonic Testing Capabilities," AIAA Paper 2015-1337, 53rd AIAA Aerospace Sciences Meeting, Kissimmee, FL, January 5-9, 2015.

12. Hollis, B. R., Berger, K. T., Berry, S. A., Brauckmann, G. J., et al, "Entry, Descent, and Landing Aerothermodynamics: NASA Langley Experimental Capabilities and Contributions," AIAA Paper 2014-1154, AIAA 52nd Aerospace Science Meeting, National Harbor, MD, January 13-17, 2014.

13. Fay, J. A., and Riddell, F. R., "Theory of Stagnation Point Heat Transfer in Dissociated Air," *Journal of Aeronautical Sciences*, Vol. 25, No. 2., February 1958, pp. 73-85.

14. Buck, G. M., "Surface Temperature/Heat Transfer Measurement Using a Quantitative Phosphor Thermography System," AIAA Paper 91-0064, 29th Aerospace Sciences Meeting, Reno, NV, January 7-10, 1991.

15. Merski, N. R., "Global Aeroheating Wind-Tunnel Measurements Using Improved Two-Color Phosphor Thermography Methods," *Journal of Spacecraft and Rockets*, Vol. 36, No. 2, March-April 1999, pp. 160-170.

16. Mason, M. L and Rufer, S. J., "Features of the Upgraded Imaging for Hypersonic Experimental Aeroheating Testing (IHEAT) Software," AIAA Paper 2016-4322, AIAA Aviation Forum, Washington, DC, June 13-17, 2016.

17. Gnoffo, P. A., "An Upwind-Biased, Point-Implicit Algorithm for Viscous, Compressible Perfect-Gas Flows," NASA TP-2953, February 1990.

18. Mazaheri, A., Gnoffo, P. A., Johnston, C. O., and Kleb, B., "LAURA User's Manual: 5.5-65135," NASA TM-2013-217800, February 2013.

19. Morkovin, M. V., "Critical Evaluation of Transition from Laminar to Turbulent Shear Layers with Emphasis on Hypersonically Travelling Blunt Bodies", Air Force Flight Dynamics Laboratory, AFFDL-TR-68-1949, March 1969.

20. Vander Kam, J. and Amar, A. "Orion Aerosciences and Thermal Protection System Overview," NASA Engineering and Safety Center, EDL Summer Series lecture, July 2021

Table 1. Model geometry parameters.

Model geometry	Model radius, R		Nose radius, R_N		Corner radius, R_C		Nose included angle, β	R_N/R	R_C/R
	in.	m	in.	m	in.	m	deg.		
Sphere-cone	3.000	0.0762	1.500	0.0371	0.1500	0.00381	20.00	0.5	0.050
Spherical-cap	3.000	0.0762	7.200	0.1829	0.3000	0.00762	23.04	2.4	0.100

Table 2. ASTM mesh parameters.

ASTM Mesh Designation	Spherical glass particle diameter, D (mil)	(mm)	Nominal element height, h_{nom} (mil)	(mm)
ASTM-10	68.90	1.7501	34.45	0.8750
ASTM-20	33.58	0.8529	16.79	0.4265
ASTM-40	16.73	0.1798	8.37	0.0899
ASTM-80	7.09	0.1062	3.54	0.0531
ASTM-140	4.17	0.0630	2.09	0.0315
ASTM-230	2.48	1.7501	1.24	0.8750

Table 3. Roughness data from sample plate scans.

Model ID	Nominal element eight h_{nom} (mil)	Measured RMS height h_{RMS} (mil)	50 % exceedance height k_{PV50} (mil)	30 % exceedance height k_{PV30} (mil)	15 % exceedance height k_{PV15} (mil)	5 % exceedance height k_{PV05} (mil)
10-Mesh	34.45	7.873	21.48	25.78	30.15	36.03
20-Mesh	16.79	2.380	8.49	10.19	14.18	16.93
40-Mesh	8.37	1.430	3.83	5.13	6.23	6.86
80-Mesh	3.54	1.181	3.40	4.38	5.09	6.47
140-Mesh	2.09	1.102	2.73	3.38	3.96	4.65
230-Mesh	1.24	0.683	1.94	2.30	2.71	3.32

Table 4. Model roughness information.

ASTM Mesh	Nominal height h (mil)	h (mm)	Measured RMS height h_{RMS} (mil)	h_{RMS} (mm)	Original 50% exceedance k_{PV50} (mil)	k_{PV50} (mm)	Corrected 50% exceedance k_{PV50} (mil)	k_{PV50} (mm)
10	34.45	0.8750	7.873	0.2000	21.48	0.5456	N/A	N/A
20	16.79	0.4265	2.380	0.0605	8.49	0.2156	N/A	N/A
40	8.37	0.2126	1.430	0.0363	3.83	0.0973	N/A	N/A
80	3.54	0.0899	1.181	0.0300	3.40#	0.0864#	2.63	0.0668
140	2.09	0.0531	1.102	0.0280	3.21#	0.0815#	2.15	0.0546
230	1.24	0.0315	0.683	0.0173	1.94#	0.0493#	1.29	0.0328
Smooth	N/A	N/A	0.500	0.0127	1.46#	0.0371#	0.98	0.0249

\# Values corrected due to lack of scan precision

Table 5. Nominal 20-Inch Mach 6 Air Tunnel Conditions.

Re_∞ (1/ft)	Re_∞ (1/m)	M_∞	T_∞ (K)	ρ_∞ (kg/m^3)	U_∞ (m/s)	ΔH (J/kg)	h_{FR} (kg/m^2-s) sphere-cone	h_{FR} (kg/m^2-s) spherical-cap
2.051E+06	6.725E+06	5.968	62.94	3.203E-02	948.4	2.121E+05	1.144E-01	2.536E-01
2.992E+06	9.816E+06	5.998	63.26	4.666E-02	955.1	2.187E+05	1.401E-01	3.072E-01
4.966E+06	1.629E+07	6.030	63.72	7.741E-02	962.9	2.266E+05	1.824E-01	3.992E-01
6.489E+06	2.129E+07	6.042	63.48	1.008E-01	962.1	2.256E+05	2.078E-01	4.555E-01
7.199E+06	2.362E+07	6.047	63.48	1.118E-01	962.7	2.261E+05	2.189E-01	4.800E-01
8.136E+06	2.669E+07	6.034	59.21	1.224E-01	924.9	1.860E+05	2.180E-01	4.781E-01

Table 6. 20-Inch Mach 6 Air Tunnel Test 7036 run matrix.

Run	Geometry	ASTM Mesh	α (deg)	Re_∞ (1/ft)	M_∞	T_∞ (K)	ρ_∞ (kg/m^3)	U_∞ (m/s)	ΔH (J/kg)	h_{FR} (kg/m^2-s)	$T_{w,avg}$ (K)
50	sphere-cone	smooth	16	2.02E+06	5.96	62.9	3.161E-02	948.0	2.116E+05	2.505E-01	331
51	sphere-cone	smooth	16	2.96E+06	6.00	63.4	4.629E-02	956.1	2.198E+05	3.062E-01	342
52	sphere-cone	smooth	16	4.96E+06	6.03	63.7	7.733E-02	962.4	2.262E+05	3.990E-01	359
53	sphere-cone	smooth	16	6.47E+06	6.04	63.6	1.007E-01	962.7	2.262E+05	4.554E-01	371
54	sphere-cone	smooth	16	7.23E+06	6.05	63.4	1.122E-01	961.5	2.248E+05	4.799E-01	378
55	sphere-cone	smooth	16	8.13E+06	6.03	59.2	1.224E-01	924.8	1.859E+05	4.778E-01	368
74	sphere-cone	230	16	2.02E+06	5.97	63.2	3.164E-02	949.8	2.136E+05	2.512E-01	333
75	sphere-cone	230	16	2.98E+06	6.00	63.4	4.660E-02	956.1	2.198E+05	3.073E-01	344
76	sphere-cone	230	16	4.99E+06	6.03	63.6	7.772E-02	961.2	2.249E+05	3.994E-01	368
77	sphere-cone	230	16	6.45E+06	6.04	63.7	1.005E-01	963.8	2.274E+05	4.556E-01	387
78	sphere-cone	230	16	7.19E+06	6.05	63.5	1.118E-01	963.0	2.265E+05	4.800E-01	395
79	sphere-cone	230	16	8.21E+06	6.03	59.0	1.232E-01	922.4	1.834E+05	4.779E-01	380
80	sphere-cone	140	16	2.01E+06	5.97	63.4	3.159E-02	951.8	2.157E+05	2.516E-01	332
81	sphere-cone	140	16	2.97E+06	6.00	63.3	4.636E-02	955.1	2.187E+05	3.061E-01	342
82	sphere-cone	140	16	4.99E+06	6.03	63.6	7.771E-02	961.6	2.253E+05	3.995E-01	364
83	sphere-cone	140	16	6.48E+06	6.04	63.6	1.007E-01	962.7	2.262E+05	4.555E-01	387
84	sphere-cone	140	16	7.16E+06	6.05	63.7	1.115E-01	964.5	2.282E+05	4.803E-01	394
85	sphere-cone	140	16	8.15E+06	6.03	59.2	1.227E-01	924.8	1.859E+05	4.784E-01	381
87	sphere-cone	80	16	2.01E+06	5.97	63.4	3.151E-02	951.8	2.157E+05	2.513E-01	331
88	sphere-cone	80	16	2.97E+06	6.00	63.7	4.648E-02	958.4	2.223E+05	3.078E-01	343
89	sphere-cone	80	16	4.98E+06	6.03	63.7	7.770E-02	962.5	2.262E+05	3.999E-01	374
90	sphere-cone	80	16	6.51E+06	6.04	63.5	1.012E-01	962.0	2.255E+05	4.561E-01	394
91	sphere-cone	80	16	7.15E+06	6.05	63.8	1.113E-01	964.9	2.286E+05	4.802E-01	400
92	sphere-cone	80	16	8.14E+06	6.03	59.3	1.225E-01	925.1	1.862E+05	4.782E-01	386
93	sphere-cone	40	16	2.01E+06	5.97	63.2	3.148E-02	950.4	2.143E+05	2.507E-01	332
94	sphere-cone	40	16	2.97E+06	6.00	63.7	4.649E-02	958.5	2.224E+05	3.079E-01	350
95	sphere-cone	40	16	4.95E+06	6.03	63.9	7.733E-02	964.4	2.282E+05	3.999E-01	389
96	sphere-cone	40	16	6.48E+06	6.04	63.5	1.008E-01	962.1	2.256E+05	4.553E-01	406
97	sphere-cone	40	16	7.23E+06	6.05	63.4	1.122E-01	961.8	2.252E+05	4.801E-01	412
98	sphere-cone	40	16	8.20E+06	6.03	59.1	1.231E-01	923.3	1.844E+05	4.784E-01	394
99	sphere-cone	20	16	2.01E+06	5.97	63.4	3.157E-02	951.4	2.153E+05	2.514E-01	350
100	sphere-cone	20	16	2.98E+06	6.00	63.5	4.653E-02	956.5	2.203E+05	3.072E-01	375
101	sphere-cone	20	16	4.92E+06	6.03	63.8	7.679E-02	963.4	2.272E+05	3.981E-01	405
102	sphere-cone	20	16	6.47E+06	6.04	63.5	1.005E-01	961.9	2.254E+05	4.546E-01	415
103	sphere-cone	20	16	7.24E+06	6.05	63.3	1.123E-01	960.7	2.241E+05	4.798E-01	414
104	sphere-cone	20	16	8.17E+06	6.03	59.0	1.227E-01	922.5	1.835E+05	4.770E-01	404
107	sphere-cone	10	16	2.01E+06	5.97	63.3	3.153E-02	951.1	2.150E+05	2.512E-01	374
106	sphere-cone	10	16	2.97E+06	6.00	63.7	4.646E-02	958.6	2.225E+05	3.078E-01	393
105	sphere-cone	10	16	4.98E+06	6.03	63.9	7.776E-02	964.2	2.280E+05	4.010E-01	409
108	sphere-cone	10	16	6.45E+06	6.04	63.7	1.004E-01	964.1	2.277E+05	4.555E-01	393
109	sphere-cone	10	16	7.21E+06	6.05	63.4	1.119E-01	961.6	2.250E+05	4.795E-01	375
110	sphere-cone	10	16	8.20E+06	6.03	59.0	1.232E-01	922.9	1.840E+05	4.782E-01	407

Table 7. 20-Inch Mach 6 Air Tunnel Test 7057 run matrix.

Run	Geometry	ASTM Mesh	α (deg)	Re_∞ (1/ft)	M_∞	T_∞ (K)	ρ_∞ (kg/m^3)	U_∞ (m/s)	ΔH (J/kg)	h_{FR} (kg/m^2-s)	$T_{w,avg}$ (K)
7	spherical-cap	smooth	28	2.04E+06	5.97	62.6	3.178E-02	946.0	2.094E+05	9.900E-02	332
8	spherical-cap	smooth	28	3.01E+06	6.00	63.0	4.676E-02	953.4	2.168E+05	1.212E-01	342
9	spherical-cap	smooth	28	5.03E+06	6.03	63.4	7.821E-02	960.8	2.243E+05	1.583E-01	357
10	spherical-cap	smooth	28	6.52E+06	6.04	63.3	1.011E-01	960.6	2.239E+05	1.799E-01	366
11	spherical-cap	smooth	28	7.28E+06	6.05	63.0	1.126E-01	959.1	2.223E+05	2.188E-01	364
12	spherical-cap	smooth	28	8.02E+06	6.04	59.5	1.208E-01	928.0	1.892E+05	2.176E-01	356
13	spherical-cap	230	28	2.02E+06	5.97	62.8	3.152E-02	947.8	2.113E+05	1.141E-01	329
14	spherical-cap	230	28	2.99E+06	6.00	63.1	4.665E-02	954.6	2.181E+05	1.400E-01	338
15	spherical-cap	230	28	4.94E+06	6.03	63.9	7.702E-02	964.5	2.283E+05	1.822E-01	357
16	spherical-cap	230	28	6.47E+06	6.04	63.5	1.006E-01	962.6	2.261E+05	2.077E-01	374
17	spherical-cap	230	28	7.20E+06	6.05	63.4	1.118E-01	961.9	2.253E+05	2.187E-01	386
18	spherical-cap	230	28	8.20E+06	6.03	59.0	1.230E-01	923.0	1.839E+05	2.181E-01	375
19	spherical-cap	140	28	2.04E+06	5.97	62.7	3.180E-02	946.8	2.102E+05	1.145E-01	329
20	spherical-cap	140	28	3.01E+06	6.00	62.9	4.687E-02	952.8	2.161E+05	1.401E-01	340
21	spherical-cap	140	28	4.95E+06	6.03	63.8	7.711E-02	963.6	2.273E+05	1.821E-01	384
22	spherical-cap	140	28	6.56E+06	6.04	63.1	1.016E-01	959.6	2.228E+05	2.080E-01	400
23	spherical-cap	140	28	7.15E+06	6.05	63.6	1.111E-01	964.1	2.276E+05	2.187E-01	405
24	spherical-cap	140	28	8.16E+06	6.03	59.0	1.225E-01	923.3	1.842E+05	2.178E-01	390
25	spherical-cap	80	28	2.04E+06	5.97	62.7	3.188E-02	947.3	2.107E+05	1.147E-01	330
26	spherical-cap	80	28	3.00E+06	6.00	63.1	4.676E-02	954.5	2.180E+05	1.402E-01	359
28	spherical-cap	80	28	4.97E+06	6.03	63.6	7.742E-02	961.8	2.254E+05	1.821E-01	398
29	spherical-cap	80	28	6.48E+06	6.04	63.4	1.006E-01	961.7	2.251E+05	2.075E-01	409
30	spherical-cap	80	28	7.19E+06	6.05	63.5	1.116E-01	963.1	2.266E+05	2.189E-01	422
31	spherical-cap	80	28	8.06E+06	6.04	59.3	1.214E-01	926.2	1.874E+05	2.176E-01	398
32	spherical-cap	40	28	2.05E+06	5.97	62.7	3.198E-02	947.3	2.108E+05	1.149E-01	338
33	spherical-cap	40	28	2.99E+06	6.00	63.2	4.665E-02	955.3	2.188E+05	1.402E-01	366
34	spherical-cap	40	28	4.97E+06	6.03	63.8	7.745E-02	963.7	2.274E+05	1.825E-01	402
35	spherical-cap	40	28	6.45E+06	6.04	63.6	1.003E-01	963.2	2.268E+05	2.076E-01	415
36	spherical-cap	40	28	7.19E+06	6.05	63.5	1.116E-01	962.9	2.264E+05	2.189E-01	418
37	spherical-cap	40	28	8.08E+06	6.04	59.4	1.217E-01	926.8	1.880E+05	2.180E-01	400
55	spherical-cap	20	28	2.04E+06	5.97	62.7	3.178E-02	947.3	2.107E+05	1.145E-01	342
56	spherical-cap	20	28	3.07E+06	6.00	62.4	4.755E-02	948.7	2.117E+05	1.403E-01	361
57	spherical-cap	20	28	4.98E+06	6.03	63.8	7.766E-02	963.4	2.271E+05	1.827E-01	393
58	spherical-cap	20	28	6.45E+06	6.04	63.6	1.003E-01	963.9	2.275E+05	2.077E-01	407
59	spherical-cap	20	28	7.22E+06	6.05	63.4	1.120E-01	962.6	2.261E+05	2.192E-01	414
60	spherical-cap	20	28	8.10E+06	6.04	59.2	1.219E-01	925.5	1.865E+05	2.178E-01	394
42	spherical-cap	10	28	2.01E+06	5.97	62.9	3.141E-02	948.1	2.117E+05	1.140E-01	359
43	spherical-cap	10	28	3.00E+06	6.00	63.1	4.672E-02	954.6	2.181E+05	1.401E-01	382
44	spherical-cap	10	28	4.94E+06	6.03	63.9	7.710E-02	964.6	2.285E+05	1.823E-01	408
45	spherical-cap	10	28	6.46E+06	6.04	63.6	1.004E-01	963.4	2.270E+05	2.077E-01	416
46	spherical-cap	10	28	7.19E+06	6.05	63.5	1.116E-01	962.8	2.262E+05	2.188E-01	411
47	spherical-cap	10	28	8.16E+06	6.03	59.1	1.226E-01	923.9	1.849E+05	2.180E-01	396

Table 8. Test 7036 sphere-cone 10-mesh transition locations.

Model	Run	Ray	s_0/R	Re_θ
10-Mesh	105	0	0.135	16.1
10-Mesh	105	10	0.165	18.8
10-Mesh	105	20	0.213	24.7
10-Mesh	105	30	0.216	28.2
10-Mesh	105	40	0.218	30.7
10-Mesh	105	50	0.202	29.8
10-Mesh	105	60	0.058	11.9
10-Mesh	105	70	0.124	20.9
10-Mesh	105	80	0.126	20.9
10-Mesh	105	90	0.154	23.7
10-Mesh	105	100	0.095	15.6
10-Mesh	105	110	0.173	24.7
10-Mesh	105	120	0.166	23.2
10-Mesh	105	130	0.172	23.7
10-Mesh	105	140	0.125	17.8
10-Mesh	105	150	0.154	19.8
10-Mesh	105	220	0.159	21.2
10-Mesh	105	230	0.147	21.1
10-Mesh	105	240	0.233	30.4
10-Mesh	105	250	0.224	30.4
10-Mesh	105	260	0.169	24.7
10-Mesh	105	270	0.190	28.0
10-Mesh	105	280	0.172	26.8
10-Mesh	105	290	0.159	25.4
10-Mesh	105	300	0.192	29.9
10-Mesh	105	310	0.172	25.5
10-Mesh	105	320	0.167	23.9
10-Mesh	105	330	0.141	18.7
10-Mesh	105	340	0.192	22.7
10-Mesh	105	350	0.149	17.4
10-Mesh	106	0	0.156	20.7
10-Mesh	106	10	0.187	24.2
10-Mesh	106	20	0.252	34.9
10-Mesh	106	30	0.224	34.4
10-Mesh	106	40	0.289	48.5
10-Mesh	106	50	0.220	38.5
10-Mesh	106	60	0.116	23.4
10-Mesh	106	70	0.130	25.1
10-Mesh	106	80	0.147	28.2
10-Mesh	106	90	0.180	33.0
10-Mesh	106	100	0.107	21.1
10-Mesh	106	110	0.218	35.9
10-Mesh	106	120	0.181	29.2
10-Mesh	106	130	0.189	29.2
10-Mesh	106	140	0.237	33.9
10-Mesh	106	150	0.157	23.6
10-Mesh	106	220	0.183	28.2
10-Mesh	106	230	0.159	25.7
10-Mesh	106	240	0.246	38.3
10-Mesh	106	250	0.258	41.2
10-Mesh	106	260	0.268	43.9
10-Mesh	106	270	0.213	38.0
10-Mesh	106	280	0.234	41.4
10-Mesh	106	290	0.232	41.8
10-Mesh	106	300	0.212	39.7
10-Mesh	106	310	0.197	34.7
10-Mesh	106	320	0.230	39.1
10-Mesh	106	330	0.158	24.3
10-Mesh	106	340	0.222	30.5
10-Mesh	106	350	0.178	23.4
10-Mesh	107	0	0.161	26.6
10-Mesh	107	10	0.194	30.9
10-Mesh	107	20	0.273	48.1
10-Mesh	107	30	0.268	52.2
10-Mesh	107	40	0.321	68.2
10-Mesh	107	50	0.249	54.5
10-Mesh	107	60	0.142	34.6
10-Mesh	107	70	0.154	37.9
10-Mesh	107	80	0.170	40.1
10-Mesh	107	90	0.192	42.6
10-Mesh	107	100	0.123	29.7
10-Mesh	107	110	0.229	46.9
10-Mesh	107	120	0.193	39.9
10-Mesh	107	130	0.286	53.2
10-Mesh	107	140	0.252	45.9
10-Mesh	107	150	0.175	33.0
10-Mesh	107	220	0.196	37.4
10-Mesh	107	230	0.172	35.6
10-Mesh	107	240	0.253	49.2
10-Mesh	107	250	0.277	54.6
10-Mesh	107	260	0.339	66.8
10-Mesh	107	270	0.242	52.5
10-Mesh	107	280	0.303	66.2
10-Mesh	107	290	0.344	75.4
10-Mesh	107	300	0.384	85.0
10-Mesh	107	310	0.288	63.4
10-Mesh	107	320	0.240	50.7
10-Mesh	107	330	0.182	34.3
10-Mesh	107	340	0.238	40.4
10-Mesh	107	350	0.183	29.7
10-Mesh	108	0	0.127	26.7
10-Mesh	108	10	0.149	30.2
10-Mesh	108	20	0.195	40.2
10-Mesh	108	30	0.192	43.4
10-Mesh	108	40	0.209	51.3
10-Mesh	108	50	0.189	49.7
10-Mesh	108	60	0.051	20.0
10-Mesh	108	70	0.115	33.5
10-Mesh	108	80	0.119	35.2
10-Mesh	108	90	0.140	38.9
10-Mesh	108	100	0.092	27.5
10-Mesh	108	110	0.158	40.7
10-Mesh	108	120	0.162	39.5
10-Mesh	108	130	0.146	35.4
10-Mesh	108	140	0.108	26.8
10-Mesh	108	150	0.133	29.7
10-Mesh	108	220	0.153	36.0
10-Mesh	108	230	0.144	35.3
10-Mesh	108	240	0.213	50.4
10-Mesh	108	250	0.211	52.3
10-Mesh	108	260	0.157	42.6
10-Mesh	108	270	0.129	37.4
10-Mesh	108	280	0.155	43.7
10-Mesh	108	290	0.151	42.9
10-Mesh	108	300	0.186	52.4
10-Mesh	108	310	0.167	44.2
10-Mesh	108	320	0.157	39.2
10-Mesh	108	330	0.104	25.4
10-Mesh	108	340	0.179	37.4
10-Mesh	108	350	0.143	29.5
10-Mesh	109	0	0.113	25.4
10-Mesh	109	10	0.130	28.5
10-Mesh	109	20	0.180	39.7
10-Mesh	109	30	0.167	40.6
10-Mesh	109	40	0.200	53.5
10-Mesh	109	50	0.183	50.9
10-Mesh	109	60	0.045	18.6
10-Mesh	109	70	0.106	35.8
10-Mesh	109	80	0.106	35.0
10-Mesh	109	90	0.132	40.5
10-Mesh	109	100	0.083	27.9
10-Mesh	109	110	0.142	40.0
10-Mesh	109	120	0.155	41.6
10-Mesh	109	130	0.129	35.0
10-Mesh	109	140	0.081	23.4
10-Mesh	109	150	0.122	31.2
10-Mesh	109	220	0.123	33.2
10-Mesh	109	230	0.140	37.4
10-Mesh	109	240	0.193	49.7
10-Mesh	109	250	0.188	50.8
10-Mesh	109	260	0.142	42.1
10-Mesh	109	270	0.112	36.2
10-Mesh	109	280	0.144	44.7
10-Mesh	109	290	0.144	43.5
10-Mesh	109	300	0.172	51.2
10-Mesh	109	310	0.143	41.1
10-Mesh	109	320	0.146	39.4
10-Mesh	109	330	0.091	23.9
10-Mesh	109	340	0.137	31.2
10-Mesh	109	350	0.144	30.8
10-Mesh	110	0	0.104	22.1
10-Mesh	110	10	0.111	23.5
10-Mesh	110	20	0.172	36.4
10-Mesh	110	30	0.152	34.4
10-Mesh	110	40	0.179	45.3
10-Mesh	110	60	0.039	16.3
10-Mesh	110	70	0.092	30.3
10-Mesh	110	80	0.100	32.9
10-Mesh	110	90	0.102	32.2
10-Mesh	110	100	0.075	24.6
10-Mesh	110	110	0.140	38.4
10-Mesh	110	120	0.121	33.9
10-Mesh	110	130	0.119	33.1
10-Mesh	110	140	0.035	15.9
10-Mesh	110	150	0.109	27.0
10-Mesh	110	220	0.091	26.1
10-Mesh	110	230	0.132	34.4
10-Mesh	110	240	0.183	46.1
10-Mesh	110	250	0.161	43.5
10-Mesh	110	260	0.125	36.9
10-Mesh	110	270	0.099	31.8
10-Mesh	110	280	0.132	40.8
10-Mesh	110	290	0.131	40.3
10-Mesh	110	300	0.175	51.4
10-Mesh	110	310	0.141	39.2
10-Mesh	110	320	0.135	34.1
10-Mesh	110	330	0.084	20.7
10-Mesh	110	340	0.131	27.8
10-Mesh	110	350	0.136	27.8

Table 9. Test 7036 sphere-cone 20-mesh transition locations

Model	Run	Ray	s_0/R	Re_θ	Model	Run	Ray	s_0/R	Re_θ	Model	Run	Ray	s_0/R	Re_θ
20-Mesh	99	0	0.324	38.0	20-Mesh	101	20	0.318	57.0	20-Mesh	103	40	0.181	45.5
20-Mesh	99	10	0.323	38.5	20-Mesh	101	30	0.243	45.9	20-Mesh	103	50	0.242	64.1
20-Mesh	99	20	0.547	84.7	20-Mesh	101	40	0.280	58.8	20-Mesh	103	60	0.117	36.3
20-Mesh	99	30	0.637	94.4	20-Mesh	101	50	0.276	62.2	20-Mesh	103	70	0.119	36.9
20-Mesh	99	40	0.460	68.9	20-Mesh	101	60	0.166	40.7	20-Mesh	103	80	0.134	39.3
20-Mesh	99	50	0.346	51.3	20-Mesh	101	70	0.174	41.2	20-Mesh	103	90	0.175	47.7
20-Mesh	99	60	0.279	42.9	20-Mesh	101	80	0.149	36.5	20-Mesh	103	100	0.188	49.0
20-Mesh	99	70	0.275	41.7	20-Mesh	101	90	0.198	44.7	20-Mesh	103	110	0.161	42.1
20-Mesh	99	80	0.181	28.6	20-Mesh	101	100	0.222	47.3	20-Mesh	103	120	0.166	42.0
20-Mesh	99	90	0.214	32.5	20-Mesh	101	110	0.177	38.3	20-Mesh	103	130	0.145	38.0
20-Mesh	99	100	0.240	34.5	20-Mesh	101	120	0.174	36.9	20-Mesh	103	140	0.154	37.5
20-Mesh	99	110	0.395	49.8	20-Mesh	101	130	0.170	35.8	20-Mesh	103	150	0.194	42.3
20-Mesh	99	120	0.380	46.7	20-Mesh	101	140	0.173	34.9	20-Mesh	103	220	0.126	32.3
20-Mesh	99	130	0.403	46.7	20-Mesh	101	150	0.212	38.2	20-Mesh	103	230	0.102	28.7
20-Mesh	99	140	0.550	57.1	20-Mesh	101	220	0.179	35.6	20-Mesh	103	240	0.132	35.7
20-Mesh	99	150	0.268	31.5	20-Mesh	101	230	0.124	27.7	20-Mesh	103	250	0.125	35.1
20-Mesh	99	220	0.473	50.8	20-Mesh	101	240	0.146	32.6	20-Mesh	103	260	0.130	36.7
20-Mesh	99	230	0.167	22.9	20-Mesh	101	250	0.136	31.3	20-Mesh	103	270	0.143	41.3
20-Mesh	99	240	0.307	39.0	20-Mesh	101	260	0.147	33.9	20-Mesh	103	280	0.150	43.5
20-Mesh	99	250	0.234	32.3	20-Mesh	101	270	0.151	35.9	20-Mesh	103	290	0.229	64.3
20-Mesh	99	260	0.713	79.3	20-Mesh	101	280	0.184	43.1	20-Mesh	103	300	0.134	40.5
20-Mesh	99	270	0.723	83.9	20-Mesh	101	290	0.259	59.0	20-Mesh	103	310	0.210	58.7
20-Mesh	99	280	0.915	99.2	20-Mesh	101	300	0.177	41.9	20-Mesh	103	320	0.221	57.2
20-Mesh	99	290	0.925	106.1	20-Mesh	101	310	0.244	54.9	20-Mesh	103	330	0.329	81.3
20-Mesh	99	300	0.673	89.9	20-Mesh	101	320	0.374	80.9	20-Mesh	103	340	0.214	44.0
20-Mesh	99	310	0.677	93.1	20-Mesh	101	330	0.388	81.1	20-Mesh	103	350	0.278	57.0
20-Mesh	99	320	0.557	82.8	20-Mesh	101	340	0.278	50.2	20-Mesh	104	0	0.266	55.1
20-Mesh	99	330	0.460	67.8	20-Mesh	101	350	0.295	52.1	20-Mesh	104	10	0.257	53.9
20-Mesh	99	340	0.469	69.1	20-Mesh	102	0	0.287	53.6	20-Mesh	104	20	0.173	37.3
20-Mesh	99	350	0.564	94.9	20-Mesh	102	10	0.286	54.3	20-Mesh	104	30	0.144	32.8
20-Mesh	100	0	0.315	43.9	20-Mesh	102	20	0.245	46.9	20-Mesh	104	40	0.165	40.9
20-Mesh	100	10	0.311	44.4	20-Mesh	102	30	0.188	40.4	20-Mesh	104	50	0.238	64.7
20-Mesh	100	20	0.380	59.9	20-Mesh	102	40	0.212	50.5	20-Mesh	104	60	0.106	33.8
20-Mesh	100	30	0.540	95.5	20-Mesh	102	50	0.253	64.5	20-Mesh	104	70	0.094	31.4
20-Mesh	100	40	0.435	76.0	20-Mesh	102	60	0.129	36.1	20-Mesh	104	80	0.126	39.2
20-Mesh	100	50	0.320	56.5	20-Mesh	102	70	0.126	36.0	20-Mesh	104	90	0.169	48.2
20-Mesh	100	60	0.255	47.3	20-Mesh	102	80	0.139	38.8	20-Mesh	104	100	0.182	49.9
20-Mesh	100	70	0.245	44.5	20-Mesh	102	90	0.190	48.1	20-Mesh	104	110	0.153	42.5
20-Mesh	100	80	0.161	30.9	20-Mesh	102	100	0.197	49.1	20-Mesh	104	120	0.168	43.3
20-Mesh	100	90	0.203	36.5	20-Mesh	102	110	0.166	40.4	20-Mesh	104	130	0.138	36.3
20-Mesh	100	100	0.230	39.3	20-Mesh	102	120	0.170	40.5	20-Mesh	104	140	0.149	37.8
20-Mesh	100	110	0.383	57.4	20-Mesh	102	130	0.156	36.5	20-Mesh	104	150	0.192	44.4
20-Mesh	100	120	0.354	52.1	20-Mesh	102	140	0.161	35.9	20-Mesh	104	220	0.111	29.6
20-Mesh	100	130	0.341	48.1	20-Mesh	102	150	0.198	40.8	20-Mesh	104	230	0.094	27.4
20-Mesh	100	140	0.217	32.1	20-Mesh	102	220	0.134	30.5	20-Mesh	104	240	0.129	35.9
20-Mesh	100	150	0.226	31.5	20-Mesh	102	230	0.114	28.2	20-Mesh	104	250	0.115	33.9
20-Mesh	100	220	0.460	58.9	20-Mesh	102	240	0.137	33.8	20-Mesh	104	260	0.127	37.0
20-Mesh	100	230	0.157	25.8	20-Mesh	102	250	0.132	35.0	20-Mesh	104	270	0.144	42.8
20-Mesh	100	240	0.153	26.4	20-Mesh	102	260	0.141	37.8	20-Mesh	104	280	0.144	43.2
20-Mesh	100	250	0.178	30.8	20-Mesh	102	270	0.146	39.8	20-Mesh	104	290	0.217	60.7
20-Mesh	100	260	0.680	91.6	20-Mesh	102	280	0.158	42.8	20-Mesh	104	300	0.121	38.0
20-Mesh	100	270	0.378	61.4	20-Mesh	102	290	0.242	62.5	20-Mesh	104	310	0.200	54.1
20-Mesh	100	280	0.412	67.3	20-Mesh	102	300	0.165	45.0	20-Mesh	104	320	0.210	53.5
20-Mesh	100	290	0.687	104.2	20-Mesh	102	310	0.221	56.3	20-Mesh	104	330	0.307	77.0
20-Mesh	100	300	0.592	97.2	20-Mesh	102	320	0.227	54.1	20-Mesh	104	340	0.216	46.5
20-Mesh	100	310	0.643	106.3	20-Mesh	102	330	0.379	89.5	20-Mesh	104	350	0.242	50.2
20-Mesh	100	320	0.506	89.8	20-Mesh	102	340	0.216	41.2					
20-Mesh	100	330	0.420	73.1	20-Mesh	102	350	0.282	53.4					
20-Mesh	100	340	0.431	72.4	20-Mesh	103	0	0.275	55.1					
20-Mesh	100	350	0.452	72.5	20-Mesh	103	10	0.261	52.4					
20-Mesh	101	0	0.303	52.0	20-Mesh	103	20	0.193	40.5					
20-Mesh	101	10	0.296	50.2	20-Mesh	103	30	0.172	39.9					

Table 10. Test 7036 sphere-cone 40-mesh transition locations.

Model	Run	Ray	s_0/R	Re_θ	Model	Run	Ray	s_0/R	Re_θ	Model	Run	Ray	s_0/R	Re_θ
40-Mesh	93	0	1.165	154.2	40-Mesh	96	100	0.363	81.1	40-Mesh	98	120	0.295	70.2
40-Mesh	93	240	0.673	71.6	40-Mesh	96	110	0.317	70.3	40-Mesh	98	130	0.328	72.7
40-Mesh	93	350	1.079	149.6	40-Mesh	96	120	0.336	70.6	40-Mesh	98	140	0.277	62.0
40-Mesh	94	0	1.098	181.8	40-Mesh	96	130	0.348	71.0	40-Mesh	98	150	0.322	66.2
40-Mesh	94	20	0.577	108.6	40-Mesh	96	140	0.314	62.7	40-Mesh	98	220	0.381	79.4
40-Mesh	94	30	0.668	118.3	40-Mesh	96	150	0.354	65.2	40-Mesh	98	230	0.411	87.7
40-Mesh	94	40	0.607	106.8	40-Mesh	96	220	0.465	84.4	40-Mesh	98	240	0.441	95.9
40-Mesh	94	50	1.086	149.0	40-Mesh	96	230	0.492	90.8	40-Mesh	98	250	0.409	92.4
40-Mesh	94	60	0.996	138.0	40-Mesh	96	240	0.502	96.5	40-Mesh	98	260	0.380	91.7
40-Mesh	94	70	0.886	124.4	40-Mesh	96	250	0.535	105.5	40-Mesh	98	270	0.394	100.1
40-Mesh	94	90	0.942	114.1	40-Mesh	96	260	0.401	88.2	40-Mesh	98	280	0.421	108.4
40-Mesh	94	100	0.772	100.5	40-Mesh	96	270	0.421	95.6	40-Mesh	98	290	0.369	98.6
40-Mesh	94	240	0.667	84.5	40-Mesh	96	280	0.452	103.7	40-Mesh	98	300	0.303	85.7
40-Mesh	94	250	0.649	86.0	40-Mesh	96	290	0.405	98.4	40-Mesh	98	310	0.364	101.9
40-Mesh	94	260	0.777	100.8	40-Mesh	96	300	0.351	89.8	40-Mesh	98	320	0.302	81.8
40-Mesh	94	290	1.020	131.2	40-Mesh	96	310	0.449	112.6	40-Mesh	98	330	0.431	115.8
40-Mesh	94	300	0.936	134.4	40-Mesh	96	320	0.399	101.4	40-Mesh	98	340	0.430	111.1
40-Mesh	94	310	0.904	137.2	40-Mesh	96	330	0.447	112.4	40-Mesh	98	350	0.511	141.4
40-Mesh	94	320	0.986	151.0	40-Mesh	96	340	0.477	122.2					
40-Mesh	94	330	1.115	162.9	40-Mesh	96	350	0.555	160.9					
40-Mesh	94	340	0.884	153.4	40-Mesh	97	0	0.491	121.5					
40-Mesh	94	350	1.034	175.3	40-Mesh	97	10	0.462	112.5					
40-Mesh	95	0	0.518	114.2	40-Mesh	97	20	0.328	73.7					
40-Mesh	95	10	0.650	168.6	40-Mesh	97	30	0.320	78.6					
40-Mesh	95	20	0.460	102.4	40-Mesh	97	40	0.254	65.6					
40-Mesh	95	30	0.364	76.1	40-Mesh	97	50	0.310	82.0					
40-Mesh	95	40	0.281	60.3	40-Mesh	97	60	0.259	72.5					
40-Mesh	95	50	0.354	79.7	40-Mesh	97	70	0.247	68.5					
40-Mesh	95	60	0.335	76.5	40-Mesh	97	80	0.234	63.3					
40-Mesh	95	70	0.400	87.0	40-Mesh	97	90	0.337	83.6					
40-Mesh	95	80	0.455	93.9	40-Mesh	97	100	0.329	79.0					
40-Mesh	95	90	0.588	110.8	40-Mesh	97	110	0.299	70.1					
40-Mesh	95	100	0.553	100.1	40-Mesh	97	120	0.330	73.9					
40-Mesh	95	110	0.574	99.1	40-Mesh	97	130	0.334	71.3					
40-Mesh	95	120	0.440	78.7	40-Mesh	97	140	0.295	61.6					
40-Mesh	95	130	0.506	84.5	40-Mesh	97	150	0.332	66.0					
40-Mesh	95	140	0.486	78.4	40-Mesh	97	220	0.427	82.5					
40-Mesh	95	150	0.422	67.5	40-Mesh	97	230	0.453	90.3					
40-Mesh	95	220	0.504	81.4	40-Mesh	97	240	0.488	100.2					
40-Mesh	95	230	0.553	90.1	40-Mesh	97	250	0.481	103.6					
40-Mesh	95	240	0.596	97.1	40-Mesh	97	260	0.392	91.9					
40-Mesh	95	250	0.600	101.5	40-Mesh	97	270	0.405	97.0					
40-Mesh	95	260	0.485	90.5	40-Mesh	97	280	0.444	108.7					
40-Mesh	95	270	0.472	93.9	40-Mesh	97	290	0.379	99.1					
40-Mesh	95	280	0.561	111.4	40-Mesh	97	300	0.337	91.5					
40-Mesh	95	290	0.617	121.4	40-Mesh	97	310	0.410	109.4					
40-Mesh	95	300	0.580	123.4	40-Mesh	97	320	0.316	84.2					
40-Mesh	95	310	0.591	127.2	40-Mesh	97	330	0.422	110.5					
40-Mesh	95	320	0.592	129.9	40-Mesh	97	340	0.467	124.6					
40-Mesh	95	330	0.718	157.6	40-Mesh	97	350	0.532	155.9					
40-Mesh	95	340	0.518	121.3	40-Mesh	98	0	0.485	122.9					
40-Mesh	95	350	0.624	163.4	40-Mesh	98	10	0.452	112.7					
40-Mesh	96	0	0.503	120.0	40-Mesh	98	20	0.327	75.9					
40-Mesh	96	10	0.472	110.6	40-Mesh	98	30	0.305	75.6					
40-Mesh	96	20	0.335	72.4	40-Mesh	98	40	0.232	61.8					
40-Mesh	96	30	0.331	77.7	40-Mesh	98	50	0.292	82.4					
40-Mesh	96	40	0.265	64.6	40-Mesh	98	60	0.219	63.1					
40-Mesh	96	50	0.315	79.0	40-Mesh	98	70	0.228	65.7					
40-Mesh	96	60	0.276	73.3	40-Mesh	98	80	0.213	61.2					
40-Mesh	96	70	0.253	65.9	40-Mesh	98	90	0.290	78.8					
40-Mesh	96	80	0.245	62.3	40-Mesh	98	100	0.255	67.5					
40-Mesh	96	90	0.364	83.9	40-Mesh	98	110	0.278	69.3					

Table 11. Test 7036 sphere-cone 80-mesh transition locations.

Model	Run	Ray	s_0/R	Re_θ	Model	Run	Ray	s_0/R	Re_θ
80-Mesh	88	0	0.868	168.1	80-Mesh	91	140	0.583	105.9
80-Mesh	88	10	0.665	137.9	80-Mesh	91	150	0.446	85.7
80-Mesh	89	0	0.522	116.8	80-Mesh	91	220	0.550	101.5
80-Mesh	89	10	0.512	116.1	80-Mesh	91	230	0.369	78.1
80-Mesh	89	20	0.746	174.2	80-Mesh	91	240	0.592	115.2
80-Mesh	89	30	0.524	118.4	80-Mesh	91	250	0.584	120.2
80-Mesh	89	40	0.596	132.2	80-Mesh	91	260	0.579	124.2
80-Mesh	89	50	0.873	170.5	80-Mesh	91	270	0.555	126.0
80-Mesh	89	60	0.762	152.6	80-Mesh	91	280	0.648	145.7
80-Mesh	89	70	0.811	148.5	80-Mesh	91	290	0.569	139.1
80-Mesh	89	80	0.899	150.6	80-Mesh	91	300	0.512	132.3
80-Mesh	89	90	0.956	144.7	80-Mesh	91	310	0.480	126.9
80-Mesh	89	230	0.642	99.2	80-Mesh	91	320	0.427	114.7
80-Mesh	89	260	0.740	122.6	80-Mesh	91	330	0.444	117.1
80-Mesh	89	300	0.869	164.8	80-Mesh	91	340	0.446	114.0
80-Mesh	89	310	0.768	157.1	80-Mesh	91	350	0.499	127.4
80-Mesh	89	320	0.565	126.8	80-Mesh	92	0	0.362	84.3
80-Mesh	89	330	0.551	125.9	80-Mesh	92	10	0.421	105.0
80-Mesh	89	340	0.450	100.5	80-Mesh	92	20	0.413	107.5
80-Mesh	89	350	0.514	117.6	80-Mesh	92	30	0.434	119.1
80-Mesh	90	0	0.430	93.0	80-Mesh	92	40	0.502	139.0
80-Mesh	90	10	0.494	118.4	80-Mesh	92	50	0.480	131.4
80-Mesh	90	20	0.428	101.2	80-Mesh	92	60	0.396	108.6
80-Mesh	90	30	0.460	115.5	80-Mesh	92	70	0.525	132.1
80-Mesh	90	40	0.523	133.1	80-Mesh	92	80	0.525	129.6
80-Mesh	90	50	0.545	133.9	80-Mesh	92	90	0.500	121.8
80-Mesh	90	60	0.486	120.7	80-Mesh	92	100	0.509	117.6
80-Mesh	90	70	0.535	124.7	80-Mesh	92	110	0.515	113.1
80-Mesh	90	80	0.533	119.9	80-Mesh	92	120	0.550	112.9
80-Mesh	90	90	0.561	120.0	80-Mesh	92	130	0.474	98.1
80-Mesh	90	100	0.557	114.7	80-Mesh	92	140	0.520	101.1
80-Mesh	90	110	0.580	113.0	80-Mesh	92	150	0.410	81.6
80-Mesh	90	120	0.609	112.0	80-Mesh	92	220	0.512	100.6
80-Mesh	90	130	0.513	95.8	80-Mesh	92	230	0.332	74.2
80-Mesh	90	150	0.472	83.7	80-Mesh	92	240	0.572	116.5
80-Mesh	90	230	0.518	96.1	80-Mesh	92	250	0.574	121.7
80-Mesh	90	240	0.640	114.8	80-Mesh	92	260	0.565	127.4
80-Mesh	90	250	0.602	116.0	80-Mesh	92	270	0.539	128.9
80-Mesh	90	260	0.587	119.3	80-Mesh	92	280	0.613	144.7
80-Mesh	90	270	0.670	136.0	80-Mesh	92	290	0.556	138.1
80-Mesh	90	280	0.705	145.1	80-Mesh	92	300	0.437	118.9
80-Mesh	90	290	0.600	136.5	80-Mesh	92	310	0.465	128.3
80-Mesh	90	300	0.588	141.2	80-Mesh	92	320	0.419	118.1
80-Mesh	90	310	0.515	128.4	80-Mesh	92	330	0.423	116.5
80-Mesh	90	320	0.438	111.6	80-Mesh	92	340	0.415	107.1
80-Mesh	90	330	0.482	121.5	80-Mesh	92	350	0.499	134.3
80-Mesh	90	340	0.441	105.8					
80-Mesh	90	350	0.505	123.9					
80-Mesh	91	0	0.381	84.0					
80-Mesh	91	10	0.440	105.2					
80-Mesh	91	20	0.419	102.7					
80-Mesh	91	30	0.452	119.7					
80-Mesh	91	40	0.512	137.9					
80-Mesh	91	50	0.509	133.0					
80-Mesh	91	60	0.415	110.1					
80-Mesh	91	70	0.526	130.4					
80-Mesh	91	80	0.533	127.1					
80-Mesh	91	90	0.522	120.7					
80-Mesh	91	100	0.547	119.0					
80-Mesh	91	110	0.552	115.7					
80-Mesh	91	120	0.572	113.5					
80-Mesh	91	130	0.490	96.4					

Table 12. Test 7036 sphere-cone 140-mesh transition locations.

Model	Run	Ray	s_0/R	Re_θ
140-Mesh	82	0	0.592	157.7
140-Mesh	82	10	0.969	217.5
140-Mesh	82	20	1.095	217.2
140-Mesh	82	30	1.063	205.3
140-Mesh	82	40	1.113	201.2
140-Mesh	82	310	1.062	189.8
140-Mesh	82	320	1.210	202.0
140-Mesh	82	330	0.602	137.0
140-Mesh	82	340	0.521	123.2
140-Mesh	82	350	0.841	203.1
140-Mesh	83	0	0.546	149.7
140-Mesh	83	10	0.522	139.2
140-Mesh	83	20	0.605	163.9
140-Mesh	83	30	0.610	157.2
140-Mesh	83	40	0.699	172.7
140-Mesh	83	50	0.628	151.3
140-Mesh	83	60	0.681	157.9
140-Mesh	83	70	0.548	128.6
140-Mesh	83	80	0.655	140.0
140-Mesh	83	90	0.703	141.1
140-Mesh	83	100	0.680	133.1
140-Mesh	83	240	0.696	121.2
140-Mesh	83	250	0.695	127.4
140-Mesh	83	260	0.721	137.8
140-Mesh	83	270	0.531	116.4
140-Mesh	83	280	0.752	153.0
140-Mesh	83	290	0.747	161.1
140-Mesh	83	300	0.649	152.2
140-Mesh	83	310	0.599	145.4
140-Mesh	83	320	0.674	168.0
140-Mesh	83	330	0.473	121.5
140-Mesh	83	340	0.501	132.7
140-Mesh	83	350	0.522	139.0
140-Mesh	84	0	0.498	126.8
140-Mesh	84	10	0.496	129.4
140-Mesh	84	20	0.589	168.2
140-Mesh	84	30	0.542	147.7
140-Mesh	84	40	0.525	143.2
140-Mesh	84	50	0.545	141.5
140-Mesh	84	60	0.583	148.3
140-Mesh	84	70	0.502	126.5
140-Mesh	84	80	0.649	146.7
140-Mesh	84	90	0.607	134.7
140-Mesh	84	100	0.385	91.4
140-Mesh	84	110	0.690	133.7
140-Mesh	84	240	0.632	121.4
140-Mesh	84	250	0.663	130.9
140-Mesh	84	260	0.670	138.2
140-Mesh	84	270	0.519	121.0
140-Mesh	84	280	0.702	153.9
140-Mesh	84	290	0.641	152.7
140-Mesh	84	300	0.574	145.5
140-Mesh	84	310	0.579	148.6
140-Mesh	84	320	0.647	172.1
140-Mesh	84	330	0.446	119.4
140-Mesh	84	340	0.484	133.6
140-Mesh	84	350	0.510	138.7
140-Mesh	85	0	0.473	120.0
140-Mesh	85	10	0.482	126.7
140-Mesh	85	20	0.573	167.8
140-Mesh	85	30	0.528	147.7
140-Mesh	85	40	0.480	134.5

Model	Run	Ray	s_0/R	Re_θ
140-Mesh	85	50	0.503	138.9
140-Mesh	85	60	0.548	145.2
140-Mesh	85	70	0.434	115.1
140-Mesh	85	80	0.619	147.2
140-Mesh	85	90	0.578	136.9
140-Mesh	85	100	0.379	93.5
140-Mesh	85	110	0.599	125.8
140-Mesh	85	120	0.699	131.3
140-Mesh	85	240	0.614	123.0
140-Mesh	85	250	0.651	132.5
140-Mesh	85	260	0.662	141.7
140-Mesh	85	270	0.510	124.5
140-Mesh	85	280	0.685	157.1
140-Mesh	85	290	0.620	151.6
140-Mesh	85	300	0.570	149.9
140-Mesh	85	310	0.531	146.1
140-Mesh	85	320	0.631	172.1
140-Mesh	85	330	1.411	134.5
140-Mesh	85	340	0.480	135.5
140-Mesh	85	350	0.504	138.5

Table 13. Test 7036 sphere-cone 230-mesh transition locations.

Model	Run	Ray	s_0/R	Re_θ
230-Mesh	74	310	1.226	124.7
230-Mesh	75	60	0.556	94.1
230-Mesh	75	80	0.774	110.1
230-Mesh	75	300	1.072	141.5
230-Mesh	75	310	1.199	150.4
230-Mesh	75	320	1.213	159.5
230-Mesh	76	10	0.940	214.1
230-Mesh	76	20	1.003	208.8
230-Mesh	76	30	0.766	167.4
230-Mesh	76	40	0.568	127.8
230-Mesh	76	50	0.965	180.1
230-Mesh	76	60	0.481	107.2
230-Mesh	76	70	0.691	134.7
230-Mesh	76	80	0.652	125.9
230-Mesh	76	140	0.564	89.7
230-Mesh	76	280	1.026	155.9
230-Mesh	76	290	1.022	166.7
230-Mesh	76	300	1.006	177.0
230-Mesh	76	310	1.087	189.6
230-Mesh	76	320	1.136	201.1
230-Mesh	76	330	1.044	202.4
230-Mesh	76	340	1.023	210.5
230-Mesh	76	350	1.032	222.3
230-Mesh	77	0	0.879	241.3
230-Mesh	77	10	0.799	221.2
230-Mesh	77	20	0.782	201.3
230-Mesh	77	30	0.638	162.6
230-Mesh	77	40	0.545	140.0
230-Mesh	77	50	0.526	130.6
230-Mesh	77	60	0.477	119.5
230-Mesh	77	70	0.646	145.8
230-Mesh	77	80	0.541	122.1
230-Mesh	77	90	0.498	111.1
230-Mesh	77	100	0.556	116.3
230-Mesh	77	110	0.613	117.7
230-Mesh	77	140	0.550	96.9
230-Mesh	77	270	0.744	146.3
230-Mesh	77	280	0.936	170.3
230-Mesh	77	290	0.657	146.7
230-Mesh	77	300	0.634	150.9
230-Mesh	77	310	0.717	167.8
230-Mesh	77	320	0.864	200.6
230-Mesh	77	330	0.904	211.4
230-Mesh	77	340	0.627	168.0
230-Mesh	77	350	0.758	213.7
230-Mesh	78	0	0.823	246.7
230-Mesh	78	10	0.753	224.2
230-Mesh	78	20	0.680	190.5
230-Mesh	78	30	0.631	168.8
230-Mesh	78	40	0.515	138.8
230-Mesh	78	50	0.464	123.5
230-Mesh	78	60	0.470	123.8
230-Mesh	78	70	0.571	139.8
230-Mesh	78	80	0.520	124.4
230-Mesh	78	90	0.468	110.9
230-Mesh	78	100	0.520	115.8
230-Mesh	78	110	0.519	111.2
230-Mesh	78	120	0.604	117.3
230-Mesh	78	140	0.529	99.0
230-Mesh	78	260	0.851	155.4
230-Mesh	78	270	0.728	152.7
230-Mesh	78	280	0.919	177.7
230-Mesh	78	290	0.577	140.3
230-Mesh	78	300	0.603	151.4
230-Mesh	78	310	0.646	163.8
230-Mesh	78	320	0.709	184.2
230-Mesh	78	330	0.790	205.1
230-Mesh	78	340	0.604	174.3
230-Mesh	78	350	0.713	218.6
230-Mesh	79	0	0.774	247.9
230-Mesh	79	10	0.733	229.7
230-Mesh	79	20	0.627	185.5
230-Mesh	79	30	0.539	152.1
230-Mesh	79	40	0.465	130.7
230-Mesh	79	50	0.409	114.6
230-Mesh	79	60	0.468	127.6
230-Mesh	79	70	0.498	128.4
230-Mesh	79	80	0.449	115.2
230-Mesh	79	90	0.440	112.0
230-Mesh	79	100	0.497	116.4
230-Mesh	79	110	0.475	107.4
230-Mesh	79	120	0.586	118.5
230-Mesh	79	140	0.526	102.5
230-Mesh	79	260	0.809	157.6
230-Mesh	79	270	0.714	157.0
230-Mesh	79	280	0.843	177.4
230-Mesh	79	290	0.569	141.9
230-Mesh	79	300	0.585	154.4
230-Mesh	79	310	0.586	156.7
230-Mesh	79	320	0.666	180.4
230-Mesh	79	330	0.727	197.6
230-Mesh	79	340	0.585	173.6
230-Mesh	79	350	0.650	210.9

Table 14. Test 7036 sphere-cone smooth-OML transition locations.

Model	Run	Ray	s_0/R	Re_θ
Smooth	53	0	0.883	246.0
Smooth	53	10	0.971	246.6
Smooth	53	20	0.853	216.9
Smooth	53	30	1.070	234.8
Smooth	53	40	0.733	182.1
Smooth	53	50	0.792	183.2
Smooth	53	60	0.773	174.1
Smooth	53	70	0.778	167.6
Smooth	53	80	0.961	174.8
Smooth	53	280	0.987	175.0
Smooth	53	290	0.876	179.3
Smooth	53	300	0.767	174.0
Smooth	53	310	0.846	190.8
Smooth	53	320	0.896	208.7
Smooth	53	330	0.988	226.8
Smooth	53	340	0.830	213.7
Smooth	53	350	0.977	247.1
Smooth	54	0	0.831	251.8
Smooth	54	10	0.849	244.1
Smooth	54	20	0.819	222.3
Smooth	54	30	0.824	213.9
Smooth	54	40	0.689	184.4
Smooth	54	50	0.717	178.7
Smooth	54	60	0.695	170.4
Smooth	54	70	0.724	168.0
Smooth	54	80	0.792	169.4
Smooth	54	90	0.855	169.2
Smooth	54	270	0.914	173.0
Smooth	54	280	0.788	168.1
Smooth	54	290	0.719	167.8
Smooth	54	300	0.684	167.8
Smooth	54	310	0.675	172.5
Smooth	54	320	0.758	197.3
Smooth	54	330	0.823	213.5
Smooth	54	340	0.638	183.5
Smooth	54	350	0.870	247.4
Smooth	55	0	0.824	258.0
Smooth	55	10	0.842	250.3
Smooth	55	20	0.809	228.0
Smooth	55	30	0.777	209.9
Smooth	55	40	0.645	177.4
Smooth	55	50	0.650	173.2
Smooth	55	60	0.588	156.1
Smooth	55	70	0.714	169.3
Smooth	55	80	0.740	166.5
Smooth	55	90	0.807	170.9
Smooth	55	270	0.837	172.5
Smooth	55	280	0.728	165.0
Smooth	55	290	0.696	165.4
Smooth	55	300	0.671	172.4
Smooth	55	310	0.619	167.2
Smooth	55	320	0.690	188.0
Smooth	55	330	0.788	211.6
Smooth	55	340	0.828	232.0
Smooth	55	350	0.822	247.4

Table 15. Test 7057 spherical-cap 10-mesh transition locations.

Model	Run	Ray	s_0/R	Re_θ
10-Mesh	42	0	0.160	27.0
10-Mesh	42	10	0.100	18.6
10-Mesh	42	20	0.110	18.0
10-Mesh	42	30	0.103	17.6
10-Mesh	42	40	0.093	16.2
10-Mesh	42	50	0.137	21.7
10-Mesh	42	60	0.106	17.1
10-Mesh	42	70	0.114	17.1
10-Mesh	42	80	0.089	14.2
10-Mesh	42	90	0.162	21.8
10-Mesh	42	100	0.119	16.5
10-Mesh	42	110	0.165	21.3
10-Mesh	42	120	0.212	25.9
10-Mesh	42	130	0.336	37.5
10-Mesh	42	140	0.297	32.8
10-Mesh	42	150	0.350	37.4
10-Mesh	42	220	0.177	21.8
10-Mesh	42	230	0.143	18.2
10-Mesh	42	240	0.158	20.7
10-Mesh	42	250	0.173	22.0
10-Mesh	42	260	0.161	21.7
10-Mesh	42	270	0.215	28.0
10-Mesh	42	280	0.214	28.7
10-Mesh	42	290	0.131	19.5
10-Mesh	42	300	0.156	23.8
10-Mesh	42	310	0.189	28.0
10-Mesh	42	320	0.166	25.6
10-Mesh	42	330	0.151	23.4
10-Mesh	42	340	0.142	22.9
10-Mesh	42	350	0.124	22.1
10-Mesh	43	0	0.056	14.4
10-Mesh	43	10	0.076	17.4
10-Mesh	43	20	0.052	13.5
10-Mesh	43	30	0.093	18.6
10-Mesh	43	40	0.089	17.0
10-Mesh	43	50	0.123	22.8
10-Mesh	43	60	0.080	16.1
10-Mesh	43	70	0.079	15.5
10-Mesh	43	80	0.082	15.5
10-Mesh	43	90	0.125	20.8
10-Mesh	43	100	0.101	16.9
10-Mesh	43	110	0.155	24.4
10-Mesh	43	120	0.202	29.8
10-Mesh	43	130	0.200	28.4
10-Mesh	43	140	0.218	30.1
10-Mesh	43	150	0.299	39.5
10-Mesh	43	220	0.128	20.9
10-Mesh	43	230	0.128	20.8
10-Mesh	43	240	0.087	15.9
10-Mesh	43	250	0.090	16.1
10-Mesh	43	260	0.110	19.5
10-Mesh	43	270	0.097	17.2
10-Mesh	43	280	0.098	17.8
10-Mesh	43	290	0.100	18.9
10-Mesh	43	300	0.134	24.1
10-Mesh	43	310	0.154	27.5
10-Mesh	43	320	0.123	23.0
10-Mesh	43	330	0.117	21.9
10-Mesh	43	340	0.138	27.2
10-Mesh	43	350	0.105	22.3
10-Mesh	44	0	0.026	13.4
10-Mesh	44	10	0.023	10.9
10-Mesh	44	20	0.042	14.0
10-Mesh	44	30	0.036	13.3
10-Mesh	44	40	0.064	19.2
10-Mesh	44	50	0.074	21.4
10-Mesh	44	60	0.090	22.7
10-Mesh	44	70	0.055	15.1
10-Mesh	44	80	0.049	14.0
10-Mesh	44	90	0.077	17.8
10-Mesh	44	100	0.069	16.5
10-Mesh	44	110	0.079	18.6
10-Mesh	44	120	0.069	16.2
10-Mesh	44	130	0.147	27.6
10-Mesh	44	140	0.149	27.9
10-Mesh	44	150	0.133	26.2
10-Mesh	44	220	0.104	21.0
10-Mesh	44	230	0.087	19.2
10-Mesh	44	240	0.057	14.8
10-Mesh	44	250	0.063	16.0
10-Mesh	44	260	0.069	16.7
10-Mesh	44	270	0.071	16.9
10-Mesh	44	280	0.042	13.2
10-Mesh	44	290	0.059	15.6
10-Mesh	44	300	0.097	23.2
10-Mesh	44	310	0.074	20.4
10-Mesh	44	320	0.052	16.5
10-Mesh	44	330	0.046	15.0
10-Mesh	44	340	0.067	19.0
10-Mesh	44	350	0.050	15.6
10-Mesh	45	0	0.027	15.2
10-Mesh	45	10	0.015	12.0
10-Mesh	45	20	0.035	14.5
10-Mesh	45	30	0.027	12.4
10-Mesh	45	40	0.055	19.4
10-Mesh	45	50	0.067	22.2
10-Mesh	45	60	0.093	26.9
10-Mesh	45	70	0.043	15.8
10-Mesh	45	80	0.039	15.1
10-Mesh	45	90	0.055	17.7
10-Mesh	45	100	0.061	18.5
10-Mesh	45	110	0.060	18.1
10-Mesh	45	120	0.058	17.7
10-Mesh	45	130	0.097	23.1
10-Mesh	45	140	0.119	26.5
10-Mesh	45	150	0.100	23.7
10-Mesh	45	220	0.087	21.7
10-Mesh	45	230	0.079	20.8
10-Mesh	45	240	0.041	13.7
10-Mesh	45	250	0.038	13.8
10-Mesh	45	260	0.049	14.9
10-Mesh	45	270	0.043	14.7
10-Mesh	45	280	0.034	14.3
10-Mesh	45	290	0.055	17.6
10-Mesh	45	300	0.061	20.1
10-Mesh	45	310	0.043	17.6
10-Mesh	45	320	0.042	16.2
10-Mesh	45	330	0.027	12.4
10-Mesh	45	340	0.031	13.8
10-Mesh	45	350	0.021	10.7
10-Mesh	46	0	0.023	15.6
10-Mesh	46	10	0.013	9.6
10-Mesh	46	20	0.027	13.5
10-Mesh	46	30	0.018	10.9
10-Mesh	46	40	0.047	18.6
10-Mesh	46	50	0.060	21.1
10-Mesh	46	60	0.075	24.3
10-Mesh	46	70	0.025	11.9
10-Mesh	46	80	0.027	12.5
10-Mesh	46	90	0.042	15.4
10-Mesh	46	100	0.052	16.9
10-Mesh	46	110	0.048	15.3
10-Mesh	46	120	0.044	14.7
10-Mesh	46	130	0.087	23.2
10-Mesh	46	140	0.100	24.6
10-Mesh	46	150	0.091	23.1
10-Mesh	46	220	0.087	23.1
10-Mesh	46	230	0.070	19.1
10-Mesh	46	240	0.032	13.2
10-Mesh	46	250	0.033	13.7
10-Mesh	46	260	0.039	14.7
10-Mesh	46	270	0.032	13.7
10-Mesh	46	280	0.030	13.1
10-Mesh	46	290	0.055	17.4
10-Mesh	46	300	0.056	18.8
10-Mesh	46	310	0.041	17.6
10-Mesh	46	320	0.034	16.0
10-Mesh	46	330	0.025	12.3
10-Mesh	46	340	0.026	13.3
10-Mesh	46	350	0.017	11.2
10-Mesh	47	0	0.017	14.3
10-Mesh	47	10	0.011	9.4
10-Mesh	47	20	0.024	13.0
10-Mesh	47	30	0.021	12.1
10-Mesh	47	40	0.029	15.7
10-Mesh	47	50	0.054	20.6
10-Mesh	47	60	0.070	24.0
10-Mesh	47	70	0.015	10.8
10-Mesh	47	80	0.019	10.8
10-Mesh	47	90	0.033	14.5
10-Mesh	47	100	0.040	15.2
10-Mesh	47	110	0.041	15.0
10-Mesh	47	120	0.038	14.8
10-Mesh	47	130	0.081	22.7
10-Mesh	47	140	0.086	23.5
10-Mesh	47	150	0.079	21.9
10-Mesh	47	220	0.080	22.1
10-Mesh	47	230	0.058	18.7
10-Mesh	47	240	0.029	12.6
10-Mesh	47	250	0.030	13.1
10-Mesh	47	260	0.029	12.7
10-Mesh	47	270	0.025	11.5
10-Mesh	47	280	0.031	13.7
10-Mesh	47	290	0.048	17.3
10-Mesh	47	300	0.048	18.1
10-Mesh	47	310	0.033	15.2
10-Mesh	47	320	0.032	16.1
10-Mesh	47	330	0.018	11.3
10-Mesh	47	340	0.013	10.3
10-Mesh	47	350	0.014	10.9

Table 16. Test 7057 spherical-cap 20-mesh transition locations.

Model	Run	Ray	s_0/R	Re_θ
20-Mesh	55	0	0.439	60.7
20-Mesh	55	10	0.731	91.5
20-Mesh	55	20	1.193	132.5
20-Mesh	55	30	0.519	67.9
20-Mesh	55	40	0.271	39.0
20-Mesh	55	50	0.463	60.4
20-Mesh	55	60	0.329	45.2
20-Mesh	55	70	0.310	41.3
20-Mesh	55	80	0.496	60.4
20-Mesh	55	90	0.637	73.2
20-Mesh	55	110	0.456	52.7
20-Mesh	55	130	0.498	53.3
20-Mesh	55	220	0.528	53.5
20-Mesh	55	230	0.502	53.3
20-Mesh	55	240	0.705	71.6
20-Mesh	55	250	0.672	71.6
20-Mesh	55	260	0.687	75.5
20-Mesh	55	270	0.909	95.6
20-Mesh	55	280	1.121	112.8
20-Mesh	55	290	0.664	78.3
20-Mesh	55	300	0.631	76.4
20-Mesh	55	310	0.433	57.3
20-Mesh	55	320	0.353	48.7
20-Mesh	55	330	0.364	50.2
20-Mesh	55	340	0.395	54.5
20-Mesh	55	350	0.763	93.0
20-Mesh	56	0	0.355	60.0
20-Mesh	56	10	0.276	48.5
20-Mesh	56	20	0.286	49.9
20-Mesh	56	30	0.351	58.1
20-Mesh	56	40	0.222	37.7
20-Mesh	56	50	0.367	57.7
20-Mesh	56	60	0.229	37.9
20-Mesh	56	70	0.178	30.2
20-Mesh	56	80	0.218	35.6
20-Mesh	56	90	0.589	80.8
20-Mesh	56	100	0.630	83.8
20-Mesh	56	110	0.412	57.2
20-Mesh	56	120	0.350	48.5
20-Mesh	56	130	0.326	45.1
20-Mesh	56	140	0.526	63.3
20-Mesh	56	220	0.487	60.2
20-Mesh	56	230	0.480	61.1
20-Mesh	56	240	0.621	77.3
20-Mesh	56	250	0.635	81.5
20-Mesh	56	260	0.621	81.9
20-Mesh	56	270	0.656	87.7
20-Mesh	56	280	0.276	42.2
20-Mesh	56	290	0.324	50.5
20-Mesh	56	300	0.364	56.6
20-Mesh	56	310	0.416	64.2
20-Mesh	56	320	0.339	54.6
20-Mesh	56	330	0.320	53.1
20-Mesh	56	340	0.318	54.5
20-Mesh	56	350	0.286	50.4
20-Mesh	57	0	0.236	54.9
20-Mesh	57	10	0.188	46.1
20-Mesh	57	20	0.279	62.3
20-Mesh	57	30	0.292	62.2
20-Mesh	57	40	0.171	38.8
20-Mesh	57	50	0.107	26.6
20-Mesh	57	60	0.080	21.0
20-Mesh	57	70	0.093	22.8
20-Mesh	57	80	0.182	36.9
20-Mesh	57	90	0.194	38.4
20-Mesh	57	100	0.239	45.0
20-Mesh	57	110	0.262	47.6
20-Mesh	57	120	0.309	53.5
20-Mesh	57	130	0.295	49.9
20-Mesh	57	140	0.283	48.6
20-Mesh	57	150	0.450	68.6
20-Mesh	57	220	0.190	34.5
20-Mesh	57	230	0.195	35.2
20-Mesh	57	240	0.182	35.2
20-Mesh	57	250	0.178	34.3
20-Mesh	57	260	0.173	33.5
20-Mesh	57	270	0.181	35.8
20-Mesh	57	280	0.250	48.9
20-Mesh	57	290	0.320	62.4
20-Mesh	57	300	0.239	50.6
20-Mesh	57	310	0.413	81.9
20-Mesh	57	320	0.305	64.1
20-Mesh	57	330	0.235	52.2
20-Mesh	57	340	0.171	39.6
20-Mesh	57	350	0.256	56.7
20-Mesh	58	0	0.214	56.7
20-Mesh	58	10	0.187	51.6
20-Mesh	58	20	0.263	65.4
20-Mesh	58	30	0.263	63.8
20-Mesh	58	40	0.085	25.1
20-Mesh	58	50	0.079	24.7
20-Mesh	58	60	0.079	23.9
20-Mesh	58	70	0.084	23.6
20-Mesh	58	80	0.161	37.9
20-Mesh	58	90	0.182	40.9
20-Mesh	58	100	0.229	49.0
20-Mesh	58	110	0.240	49.3
20-Mesh	58	120	0.277	55.8
20-Mesh	58	130	0.286	55.4
20-Mesh	58	140	0.273	52.4
20-Mesh	58	150	0.273	52.1
20-Mesh	58	220	0.162	34.5
20-Mesh	58	230	0.188	39.2
20-Mesh	58	240	0.170	36.6
20-Mesh	58	250	0.172	37.8
20-Mesh	58	260	0.165	37.1
20-Mesh	58	270	0.169	38.8
20-Mesh	58	280	0.181	42.6
20-Mesh	58	290	0.198	47.9
20-Mesh	58	300	0.198	48.8
20-Mesh	58	310	0.201	50.2
20-Mesh	58	320	0.258	62.7
20-Mesh	58	330	0.194	50.2
20-Mesh	58	340	0.149	41.4
20-Mesh	58	350	0.240	61.7
20-Mesh	59	0	0.205	57.4
20-Mesh	59	10	0.184	53.6
20-Mesh	59	20	0.261	68.3
20-Mesh	59	30	0.252	64.9
20-Mesh	59	40	0.080	25.1
20-Mesh	59	50	0.062	20.6
20-Mesh	59	60	0.077	24.8
20-Mesh	59	70	0.049	16.8
20-Mesh	59	80	0.131	33.6
20-Mesh	59	90	0.172	41.2
20-Mesh	59	100	0.215	48.5
20-Mesh	59	110	0.235	51.6
20-Mesh	59	120	0.264	54.8
20-Mesh	59	130	0.273	56.1
20-Mesh	59	140	0.266	53.8
20-Mesh	59	150	0.263	53.3
20-Mesh	59	220	0.149	34.5
20-Mesh	59	230	0.176	40.0
20-Mesh	59	240	0.161	37.1
20-Mesh	59	250	0.160	37.8
20-Mesh	59	260	0.159	38.7
20-Mesh	59	270	0.169	40.8
20-Mesh	59	280	0.176	43.7
20-Mesh	59	290	0.189	47.9
20-Mesh	59	300	0.182	48.4
20-Mesh	59	310	0.188	49.7
20-Mesh	59	320	0.246	63.8
20-Mesh	59	330	0.187	51.1
20-Mesh	59	340	0.140	41.1
20-Mesh	59	350	0.228	63.6
20-Mesh	60	0	0.203	58.8
20-Mesh	60	10	0.173	52.1
20-Mesh	60	20	0.257	72.1
20-Mesh	60	30	0.246	65.4
20-Mesh	60	40	0.071	23.7
20-Mesh	60	50	0.053	19.7
20-Mesh	60	60	0.067	23.5
20-Mesh	60	70	0.044	16.7
20-Mesh	60	80	0.121	33.0
20-Mesh	60	90	0.156	39.0
20-Mesh	60	100	0.206	48.9
20-Mesh	60	110	0.224	50.9
20-Mesh	60	120	0.246	53.4
20-Mesh	60	130	0.266	56.4
20-Mesh	60	140	0.256	54.5
20-Mesh	60	150	0.254	52.3
20-Mesh	60	220	0.139	33.0
20-Mesh	60	230	0.165	38.1
20-Mesh	60	240	0.151	37.0
20-Mesh	60	250	0.154	38.5
20-Mesh	60	260	0.153	38.3
20-Mesh	60	270	0.159	40.9
20-Mesh	60	280	0.169	44.0
20-Mesh	60	290	0.187	48.8
20-Mesh	60	300	0.176	47.9
20-Mesh	60	310	0.181	50.6
20-Mesh	60	320	0.237	62.9
20-Mesh	60	330	1.782	181.0
20-Mesh	60	340	0.134	40.4
20-Mesh	60	350	0.222	63.6

Table 17. Test 7057 spherical-cap 40-mesh transition locations.

Model	Run	Ray	s_0/R	Re_θ
40-Mesh	32	0	0.999	116.4
40-Mesh	32	10	0.754	93.4
40-Mesh	32	20	1.055	121.6
40-Mesh	32	30	1.141	126.3
40-Mesh	32	40	1.264	134.5
40-Mesh	32	50	1.016	114.1
40-Mesh	32	60	1.059	115.4
40-Mesh	32	260	1.018	98.2
40-Mesh	32	270	0.883	94.0
40-Mesh	32	280	0.672	77.5
40-Mesh	32	290	0.806	91.6
40-Mesh	32	300	0.995	109.7
40-Mesh	32	310	1.132	123.8
40-Mesh	32	320	0.905	105.1
40-Mesh	32	330	0.842	100.2
40-Mesh	32	340	0.741	92.1
40-Mesh	32	350	1.079	123.6
40-Mesh	33	0	0.569	88.1
40-Mesh	33	10	0.571	88.7
40-Mesh	33	20	0.451	73.4
40-Mesh	33	30	0.319	52.7
40-Mesh	33	40	0.498	76.7
40-Mesh	33	50	0.630	91.8
40-Mesh	33	60	0.591	85.8
40-Mesh	33	70	0.655	91.4
40-Mesh	33	80	0.769	101.9
40-Mesh	33	90	0.811	103.8
40-Mesh	33	100	0.925	110.5
40-Mesh	33	110	0.737	91.3
40-Mesh	33	250	0.671	84.3
40-Mesh	33	260	0.510	69.0
40-Mesh	33	270	0.562	76.9
40-Mesh	33	280	0.405	59.0
40-Mesh	33	290	0.592	83.6
40-Mesh	33	300	0.580	83.4
40-Mesh	33	310	0.671	96.2
40-Mesh	33	320	0.548	83.0
40-Mesh	33	330	0.432	68.7
40-Mesh	33	340	0.409	66.6
40-Mesh	33	350	0.357	60.4
40-Mesh	34	0	0.184	45.0
40-Mesh	34	10	0.115	31.5
40-Mesh	34	20	0.185	41.8
40-Mesh	34	30	0.134	32.2
40-Mesh	34	40	0.237	51.6
40-Mesh	34	50	0.154	35.5
40-Mesh	34	60	0.279	56.6
40-Mesh	34	70	0.212	43.5
40-Mesh	34	80	0.202	40.5
40-Mesh	34	90	0.205	39.8
40-Mesh	34	100	0.279	51.3
40-Mesh	34	110	0.314	54.8
40-Mesh	34	120	0.307	53.0
40-Mesh	34	130	0.364	59.7
40-Mesh	34	140	0.298	49.4
40-Mesh	34	150	0.265	45.1
40-Mesh	34	220	0.245	41.5
40-Mesh	34	230	0.274	47.2
40-Mesh	34	240	0.281	49.3
40-Mesh	34	250	0.352	61.3
40-Mesh	34	260	0.347	62.0
40-Mesh	34	270	0.283	52.6
40-Mesh	34	280	0.267	51.9
40-Mesh	34	290	0.257	50.8
40-Mesh	34	300	0.228	46.9
40-Mesh	34	310	0.215	46.4
40-Mesh	34	320	0.189	43.0
40-Mesh	34	330	0.154	36.6
40-Mesh	34	340	0.153	36.6
40-Mesh	34	350	0.162	38.9
40-Mesh	35	0	0.139	40.6
40-Mesh	35	10	0.108	34.2
40-Mesh	35	20	0.179	45.8
40-Mesh	35	30	0.120	33.1
40-Mesh	35	40	0.143	39.0
40-Mesh	35	50	0.136	36.6
40-Mesh	35	60	0.145	37.0
40-Mesh	35	70	0.150	36.7
40-Mesh	35	80	0.168	39.5
40-Mesh	35	90	0.181	40.4
40-Mesh	35	100	0.210	45.4
40-Mesh	35	110	0.208	44.2
40-Mesh	35	120	0.281	55.6
40-Mesh	35	130	0.268	51.2
40-Mesh	35	140	0.256	49.9
40-Mesh	35	150	0.219	42.7
40-Mesh	35	220	0.235	46.3
40-Mesh	35	230	0.232	46.6
40-Mesh	35	240	0.272	53.2
40-Mesh	35	250	0.279	56.4
40-Mesh	35	260	0.258	53.8
40-Mesh	35	270	0.225	48.1
40-Mesh	35	280	0.222	49.7
40-Mesh	35	290	0.209	47.9
40-Mesh	35	300	0.214	50.4
40-Mesh	35	310	0.184	46.2
40-Mesh	35	320	0.167	43.5
40-Mesh	35	330	0.140	37.9
40-Mesh	35	340	0.141	38.0
40-Mesh	35	350	0.152	41.6
40-Mesh	36	0	0.128	39.5
40-Mesh	36	10	0.098	33.7
40-Mesh	36	20	0.166	45.9
40-Mesh	36	30	0.121	34.6
40-Mesh	36	40	0.119	33.9
40-Mesh	36	50	0.137	38.3
40-Mesh	36	60	0.128	35.8
40-Mesh	36	70	0.138	36.0
40-Mesh	36	80	0.145	36.7
40-Mesh	36	90	0.152	36.2
40-Mesh	36	100	0.160	38.0
40-Mesh	36	110	0.187	42.2
40-Mesh	36	120	0.272	56.3
40-Mesh	36	130	0.226	48.0
40-Mesh	36	140	0.214	44.7
40-Mesh	36	150	0.200	41.4
40-Mesh	36	220	0.220	45.1
40-Mesh	36	230	0.220	45.4
40-Mesh	36	240	0.240	50.2
40-Mesh	36	250	0.239	51.4
40-Mesh	36	260	0.235	52.4
40-Mesh	36	270	0.210	48.5
40-Mesh	36	280	0.205	47.8
40-Mesh	36	290	0.194	47.1
40-Mesh	36	300	0.200	49.3
40-Mesh	36	310	0.181	48.1
40-Mesh	36	320	0.156	43.5
40-Mesh	36	330	0.033	14.1
40-Mesh	36	340	0.126	36.4
40-Mesh	36	350	0.135	38.7
40-Mesh	37	0	0.113	35.9
40-Mesh	37	10	0.092	30.8
40-Mesh	37	20	0.161	48.1
40-Mesh	37	30	0.117	37.2
40-Mesh	37	40	0.109	32.3
40-Mesh	37	50	0.122	34.4
40-Mesh	37	60	0.125	34.1
40-Mesh	37	70	0.138	35.6
40-Mesh	37	80	0.131	34.0
40-Mesh	37	90	0.147	36.6
40-Mesh	37	100	0.157	38.8
40-Mesh	37	110	0.171	39.2
40-Mesh	37	120	0.227	49.7
40-Mesh	37	130	0.212	46.3
40-Mesh	37	140	0.205	45.1
40-Mesh	37	150	0.172	37.3
40-Mesh	37	220	0.201	42.7
40-Mesh	37	230	0.190	41.8
40-Mesh	37	240	0.207	46.1
40-Mesh	37	250	0.208	46.9
40-Mesh	37	260	0.197	45.0
40-Mesh	37	270	0.190	45.2
40-Mesh	37	280	0.191	45.8
40-Mesh	37	290	0.179	45.1
40-Mesh	37	300	0.193	49.5
40-Mesh	37	310	0.171	45.1
40-Mesh	37	320	0.140	39.2
40-Mesh	37	330	0.125	37.2
40-Mesh	37	340	0.117	36.8
40-Mesh	37	350	0.122	38.8

Table 18. Test 7057 spherical-cap 80-mesh transition locations.

Model	Run	Ray	s_0/R	Re_θ	Model	Run	Ray	s_0/R	Re_θ	Model	Run	Ray	s_0/R	Re_θ
80-Mesh	26	0	0.388	64.7	80-Mesh	29	70	0.244	56.6	80-Mesh	31	90	0.219	51.8
80-Mesh	26	10	0.607	92.4	80-Mesh	29	80	0.202	46.2	80-Mesh	31	100	0.231	54.1
80-Mesh	26	20	0.682	101.6	80-Mesh	29	90	0.306	64.8	80-Mesh	31	110	0.230	52.8
80-Mesh	26	30	0.786	112.6	80-Mesh	29	100	0.318	65.4	80-Mesh	31	120	0.206	47.2
80-Mesh	26	40	0.763	109.7	80-Mesh	29	110	0.312	61.9	80-Mesh	31	130	0.220	47.7
80-Mesh	26	50	0.478	74.0	80-Mesh	29	120	0.231	48.0	80-Mesh	31	140	0.198	42.8
80-Mesh	26	60	0.758	105.3	80-Mesh	29	130	0.266	51.6	80-Mesh	31	150	0.226	46.9
80-Mesh	26	70	0.833	112.1	80-Mesh	29	140	0.280	53.8	80-Mesh	31	220	0.305	62.9
80-Mesh	26	80	0.671	91.7	80-Mesh	29	150	0.295	55.6	80-Mesh	31	230	0.244	51.7
80-Mesh	26	90	0.792	102.9	80-Mesh	29	220	0.326	60.9	80-Mesh	31	240	0.236	51.7
80-Mesh	26	100	0.766	97.1	80-Mesh	29	230	0.277	54.9	80-Mesh	31	250	0.231	52.5
80-Mesh	26	110	0.669	84.7	80-Mesh	29	240	0.239	48.2	80-Mesh	31	260	0.198	46.1
80-Mesh	26	120	0.642	78.9	80-Mesh	29	250	0.248	51.3	80-Mesh	31	270	0.189	46.5
80-Mesh	26	240	0.655	81.0	80-Mesh	29	260	0.241	50.9	80-Mesh	31	280	0.234	56.1
80-Mesh	26	250	0.625	80.7	80-Mesh	29	270	0.219	48.1	80-Mesh	31	290	0.241	59.3
80-Mesh	26	260	0.392	55.8	80-Mesh	29	280	0.263	58.2	80-Mesh	31	300	0.204	52.9
80-Mesh	26	270	0.735	96.4	80-Mesh	29	290	0.272	61.3	80-Mesh	31	310	0.177	50.0
80-Mesh	26	280	0.684	93.6	80-Mesh	29	300	0.238	56.4	80-Mesh	31	320	0.181	51.4
80-Mesh	26	290	0.921	120.5	80-Mesh	29	310	0.243	58.8	80-Mesh	31	330	0.168	47.8
80-Mesh	26	300	0.754	104.5	80-Mesh	29	320	0.207	53.2	80-Mesh	31	340	0.241	65.0
80-Mesh	26	310	0.832	115.9	80-Mesh	29	330	0.247	61.6	80-Mesh	31	350	0.215	60.0
80-Mesh	26	320	0.634	94.9	80-Mesh	29	340	0.267	65.4					
80-Mesh	26	330	0.753	109.5	80-Mesh	29	350	0.233	58.6					
80-Mesh	26	340	0.721	106.1	80-Mesh	30	0	0.165	48.7					
80-Mesh	26	350	0.728	107.5	80-Mesh	30	10	0.131	41.2					
80-Mesh	28	0	0.226	51.8	80-Mesh	30	20	0.123	35.6					
80-Mesh	28	10	0.174	41.8	80-Mesh	30	30	0.127	36.8					
80-Mesh	28	20	0.170	40.7	80-Mesh	30	40	0.113	32.8					
80-Mesh	28	30	0.341	71.3	80-Mesh	30	50	0.139	39.4					
80-Mesh	28	40	0.366	73.3	80-Mesh	30	60	0.149	40.6					
80-Mesh	28	50	0.378	74.2	80-Mesh	30	70	0.164	42.0					
80-Mesh	28	60	0.396	76.5	80-Mesh	30	80	0.194	47.5					
80-Mesh	28	70	0.364	70.1	80-Mesh	30	90	0.233	53.7					
80-Mesh	28	80	0.348	65.6	80-Mesh	30	100	0.280	61.0					
80-Mesh	28	90	0.361	66.0	80-Mesh	30	110	0.254	55.1					
80-Mesh	28	100	0.380	67.1	80-Mesh	30	120	0.223	48.1					
80-Mesh	28	110	0.423	72.3	80-Mesh	30	130	0.240	49.4					
80-Mesh	28	120	0.405	67.6	80-Mesh	30	140	0.239	48.7					
80-Mesh	28	130	0.401	66.0	80-Mesh	30	150	0.237	48.9					
80-Mesh	28	140	0.404	64.4	80-Mesh	30	220	0.314	61.4					
80-Mesh	28	150	0.372	59.4	80-Mesh	30	230	0.256	53.1					
80-Mesh	28	220	0.351	57.3	80-Mesh	30	240	0.240	50.4					
80-Mesh	28	230	0.336	56.1	80-Mesh	30	250	0.233	51.0					
80-Mesh	28	240	0.257	46.2	80-Mesh	30	260	0.209	47.9					
80-Mesh	28	250	0.254	47.0	80-Mesh	30	270	0.203	46.4					
80-Mesh	28	260	0.270	49.2	80-Mesh	30	280	0.249	57.0					
80-Mesh	28	270	0.264	50.0	80-Mesh	30	290	0.247	58.7					
80-Mesh	28	280	0.308	58.4	80-Mesh	30	300	0.210	52.5					
80-Mesh	28	290	0.313	59.9	80-Mesh	30	310	0.190	49.1					
80-Mesh	28	300	0.370	71.8	80-Mesh	30	320	0.196	52.1					
80-Mesh	28	310	0.448	86.3	80-Mesh	30	330	0.171	46.6					
80-Mesh	28	320	0.386	76.8	80-Mesh	30	340	0.256	66.2					
80-Mesh	28	330	0.312	65.2	80-Mesh	30	350	0.220	59.1					
80-Mesh	28	340	0.289	63.3	80-Mesh	31	0	0.129	42.3					
80-Mesh	28	350	0.371	77.9	80-Mesh	31	10	0.109	36.6					
80-Mesh	29	0	0.196	53.2	80-Mesh	31	20	0.114	35.3					
80-Mesh	29	10	0.142	42.0	80-Mesh	31	30	0.096	31.6					
80-Mesh	29	20	0.150	41.0	80-Mesh	31	40	0.098	31.9					
80-Mesh	29	30	0.168	44.0	80-Mesh	31	50	0.121	36.4					
80-Mesh	29	40	0.176	46.3	80-Mesh	31	60	0.118	34.6					
80-Mesh	29	50	0.234	57.6	80-Mesh	31	70	0.148	40.2					
80-Mesh	29	60	0.327	74.1	80-Mesh	31	80	0.188	47.5					

Table 19. Test 7057 spherical-cap 140-mesh transition locations.

Model	Run	Ray	s_0/R	Re_θ	Model	Run	Ray	s_0/R	Re_θ
140-Mesh	20	20	0.897	129.6	140-Mesh	23	40	0.255	65.4
140-Mesh	20	30	1.123	150.3	140-Mesh	23	50	0.367	87.7
140-Mesh	20	40	1.199	156.4	140-Mesh	23	60	0.451	103.1
140-Mesh	20	80	1.054	131.9	140-Mesh	23	70	0.445	99.3
140-Mesh	21	0	0.556	109.4	140-Mesh	23	80	0.461	99.6
140-Mesh	21	10	0.489	99.6	140-Mesh	23	90	0.434	93.1
140-Mesh	21	20	0.473	97.5	140-Mesh	23	100	0.441	91.4
140-Mesh	21	30	0.525	102.4	140-Mesh	23	110	0.471	94.5
140-Mesh	21	40	0.511	100.0	140-Mesh	23	120	0.383	77.0
140-Mesh	21	50	0.497	95.8	140-Mesh	23	130	0.282	58.7
140-Mesh	21	60	0.605	111.0	140-Mesh	23	140	0.252	52.4
140-Mesh	21	70	0.728	126.9	140-Mesh	23	150	0.279	55.8
140-Mesh	21	80	0.793	132.5	140-Mesh	23	220	0.379	73.1
140-Mesh	21	90	0.686	115.2	140-Mesh	23	230	0.412	79.8
140-Mesh	21	100	0.728	117.9	140-Mesh	23	240	0.412	83.3
140-Mesh	21	110	0.830	125.3	140-Mesh	23	250	0.395	82.1
140-Mesh	21	120	0.726	109.6	140-Mesh	23	260	0.319	69.6
140-Mesh	21	140	0.283	49.1	140-Mesh	23	270	0.376	81.8
140-Mesh	21	240	0.649	101.3	140-Mesh	23	280	0.457	99.2
140-Mesh	21	250	0.730	114.7	140-Mesh	23	290	0.484	106.4
140-Mesh	21	260	0.832	129.1	140-Mesh	23	300	0.426	97.4
140-Mesh	21	270	0.860	136.4	140-Mesh	23	310	0.475	109.5
140-Mesh	21	280	0.854	140.3	140-Mesh	23	320	0.447	105.4
140-Mesh	21	290	0.898	149.0	140-Mesh	23	340	0.383	95.0
140-Mesh	21	300	0.805	139.1	140-Mesh	23	350	0.398	98.7
140-Mesh	21	310	0.775	138.1	140-Mesh	24	0	0.284	77.3
140-Mesh	21	320	0.704	129.8	140-Mesh	24	10	0.294	80.8
140-Mesh	21	340	0.571	111.7	140-Mesh	24	20	0.244	68.9
140-Mesh	21	350	0.542	108.3	140-Mesh	24	30	0.234	63.9
140-Mesh	22	0	0.320	78.8	140-Mesh	24	40	0.242	64.5
140-Mesh	22	10	0.306	76.4	140-Mesh	24	50	0.350	86.6
140-Mesh	22	20	0.274	68.4	140-Mesh	24	60	0.434	102.5
140-Mesh	22	30	0.273	67.1	140-Mesh	24	70	0.427	98.8
140-Mesh	22	40	0.352	82.9	140-Mesh	24	80	0.445	99.3
140-Mesh	22	50	0.447	99.8	140-Mesh	24	90	0.406	89.7
140-Mesh	22	60	0.458	98.5	140-Mesh	24	100	0.425	90.8
140-Mesh	22	70	0.470	98.6	140-Mesh	24	110	0.441	92.0
140-Mesh	22	80	0.485	98.9	140-Mesh	24	120	0.349	73.8
140-Mesh	22	90	0.499	98.7	140-Mesh	24	130	0.276	59.5
140-Mesh	22	100	0.475	93.1	140-Mesh	24	140	0.246	51.9
140-Mesh	22	110	0.520	98.4	140-Mesh	24	150	0.269	56.2
140-Mesh	22	120	0.493	91.8	140-Mesh	24	220	0.371	73.5
140-Mesh	22	130	0.286	55.7	140-Mesh	24	230	0.400	81.1
140-Mesh	22	140	0.277	53.7	140-Mesh	24	240	0.402	82.7
140-Mesh	22	150	0.285	54.0	140-Mesh	24	250	0.379	80.2
140-Mesh	22	220	0.381	68.9	140-Mesh	24	260	0.310	68.8
140-Mesh	22	230	0.434	79.6	140-Mesh	24	270	0.369	83.0
140-Mesh	22	240	0.474	88.6	140-Mesh	24	280	0.446	99.2
140-Mesh	22	250	0.504	95.4	140-Mesh	24	290	0.465	105.6
140-Mesh	22	260	0.463	90.3	140-Mesh	24	300	0.422	99.0
140-Mesh	22	270	0.399	81.2	140-Mesh	24	310	0.472	112.1
140-Mesh	22	280	0.570	113.3	140-Mesh	24	320	0.437	106.1
140-Mesh	22	290	0.538	109.9	140-Mesh	24	340	0.367	93.6
140-Mesh	22	300	0.516	107.9	140-Mesh	24	350	0.351	92.4
140-Mesh	22	310	0.503	108.1					
140-Mesh	22	320	0.488	108.6					
140-Mesh	22	340	0.466	105.9					
140-Mesh	22	350	0.419	97.1					
140-Mesh	23	0	0.304	80.2					
140-Mesh	23	10	0.302	79.1					
140-Mesh	23	20	0.261	70.3					
140-Mesh	23	30	0.254	66.3					

Table 20. Test 7057 spherical-cap 230-mesh transition locations.

Model	Run	Ray	s_0/R	Re_θ	Model	Run	Ray	s_0/R	Re_θ
230-Mesh	14	320	1.166	153.8	230-Mesh	18	110	0.733	142.1
230-Mesh	15	0	1.055	185.5	230-Mesh	18	120	0.736	136.0
230-Mesh	15	10	0.980	176.4	230-Mesh	18	250	0.786	149.4
230-Mesh	15	20	1.383	225.9	230-Mesh	18	260	0.708	142.9
230-Mesh	15	50	1.120	188.6	230-Mesh	18	270	0.717	148.2
230-Mesh	15	320	0.822	149.7	230-Mesh	18	280	0.748	156.6
230-Mesh	15	340	0.958	172.3	230-Mesh	18	290	0.755	160.6
230-Mesh	16	0	0.932	188.6	230-Mesh	18	300	0.781	167.6
230-Mesh	16	10	0.912	186.5	230-Mesh	18	310	0.726	161.2
230-Mesh	16	20	0.920	187.5	230-Mesh	18	320	0.706	160.2
230-Mesh	16	30	0.867	176.4	230-Mesh	18	330	0.935	202.5
230-Mesh	16	40	0.886	177.1	230-Mesh	18	340	0.613	147.3
230-Mesh	16	50	0.879	174.3	230-Mesh	18	350	0.847	189.7
230-Mesh	16	60	1.072	198.7					
230-Mesh	16	70	1.018	188.6					
230-Mesh	16	80	0.987	179.5					
230-Mesh	16	90	1.102	183.6					
230-Mesh	16	100	0.874	154.2					
230-Mesh	16	260	0.735	136.1					
230-Mesh	16	270	0.931	167.7					
230-Mesh	16	290	1.133	202.6					
230-Mesh	16	300	1.138	206.6					
230-Mesh	16	310	1.044	198.9					
230-Mesh	16	320	0.757	156.9					
230-Mesh	16	330	0.989	196.4					
230-Mesh	16	340	0.836	174.2					
230-Mesh	16	350	0.913	186.5					
230-Mesh	17	0	0.777	172.3					
230-Mesh	17	10	0.746	166.4					
230-Mesh	17	20	0.650	148.6					
230-Mesh	17	30	0.675	152.2					
230-Mesh	17	40	0.754	165.6					
230-Mesh	17	50	0.800	171.8					
230-Mesh	17	60	0.817	170.6					
230-Mesh	17	70	0.750	156.5					
230-Mesh	17	80	0.716	148.0					
230-Mesh	17	90	0.934	175.4					
230-Mesh	17	100	0.849	157.9					
230-Mesh	17	110	0.747	140.1					
230-Mesh	17	120	0.746	135.3					
230-Mesh	17	250	0.802	146.9					
230-Mesh	17	260	0.719	140.4					
230-Mesh	17	270	0.721	145.3					
230-Mesh	17	280	0.781	159.1					
230-Mesh	17	290	0.802	165.0					
230-Mesh	17	300	0.798	167.8					
230-Mesh	17	310	0.733	159.8					
230-Mesh	17	320	0.718	159.4					
230-Mesh	17	330	0.960	200.9					
230-Mesh	17	340	0.644	147.6					
230-Mesh	17	350	0.860	185.5					
230-Mesh	18	0	0.768	174.1					
230-Mesh	18	10	0.729	168.9					
230-Mesh	18	20	0.621	148.6					
230-Mesh	18	30	0.652	151.5					
230-Mesh	18	40	0.749	167.6					
230-Mesh	18	50	0.787	171.8					
230-Mesh	18	60	0.799	170.7					
230-Mesh	18	70	0.740	158.9					
230-Mesh	18	80	0.709	150.2					
230-Mesh	18	90	0.932	180.0					
230-Mesh	18	100	0.844	162.0					

Table 21. Test 7057 spherical-cap smooth-OML transition locations.

Model	Run	Ray	s_0/R	Re_θ
Smooth	10	310	1.393	245.5
Smooth	10	320	1.371	245.4
Smooth	10	330	1.390	247.7
Smooth	10	340	1.336	249.4
Smooth	11	0	1.311	262.9
Smooth	11	10	1.344	266.2
Smooth	11	20	0.902	197.0
Smooth	11	30	1.040	217.9
Smooth	11	40	1.170	235.2
Smooth	11	50	1.152	231.5
Smooth	11	60	1.158	225.5
Smooth	11	70	1.106	214.0
Smooth	11	300	1.124	221.1
Smooth	11	310	1.080	220.2
Smooth	11	320	1.025	213.4
Smooth	11	330	1.044	218.7
Smooth	11	340	1.115	231.9
Smooth	11	350	1.261	253.5
Smooth	12	0	1.296	266.1
Smooth	12	10	1.330	270.6
Smooth	12	20	0.818	187.9
Smooth	12	30	1.154	239.9
Smooth	12	40	1.318	260.9
Smooth	12	50	1.373	265.6
Smooth	12	300	1.177	234.7
Smooth	12	310	1.246	251.4
Smooth	12	320	1.052	223.2
Smooth	12	330	1.099	232.4
Smooth	12	340	1.103	236.5
Smooth	12	350	1.250	258.1

Cavities and protrusions	Tile/panel steps and gaps	Physical Damage

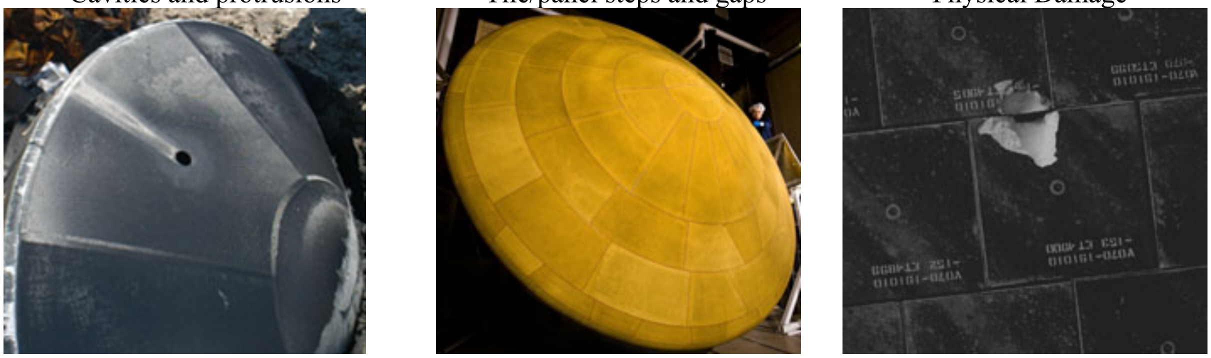

a) Heat shield attachment point cavity on Genesis entry vehicle	b) TPS block panels on MSL entry vehicle	c) Damaged TPS tile on Shuttle Orbiter

Figure 1. Discrete surface roughness types.

Pattern	Flexible TPS	Sand-grain	Woven

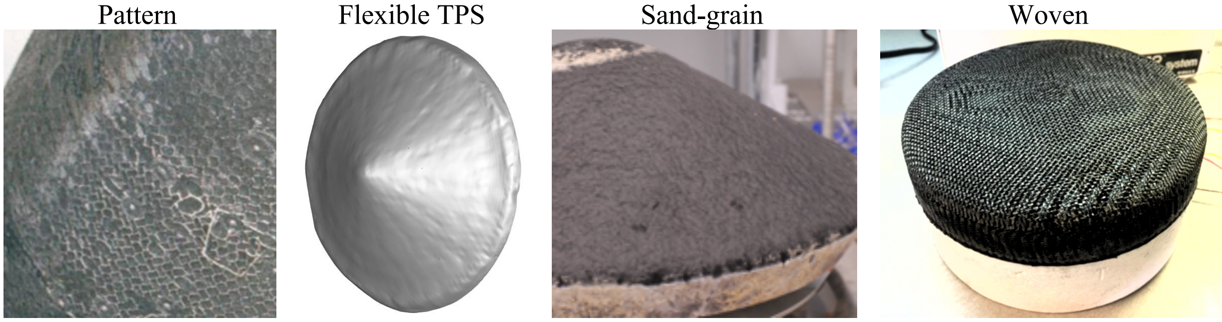

a) Hexcomb cavities on Apollo ablated TPS	b) Flexible TPS deflection under aerodynamic load	c) Ablation of monolithic TPS on Stardust capsule	c) Arc jet test sample of woven TPS

Figure 2. Distributed surface roughness types.

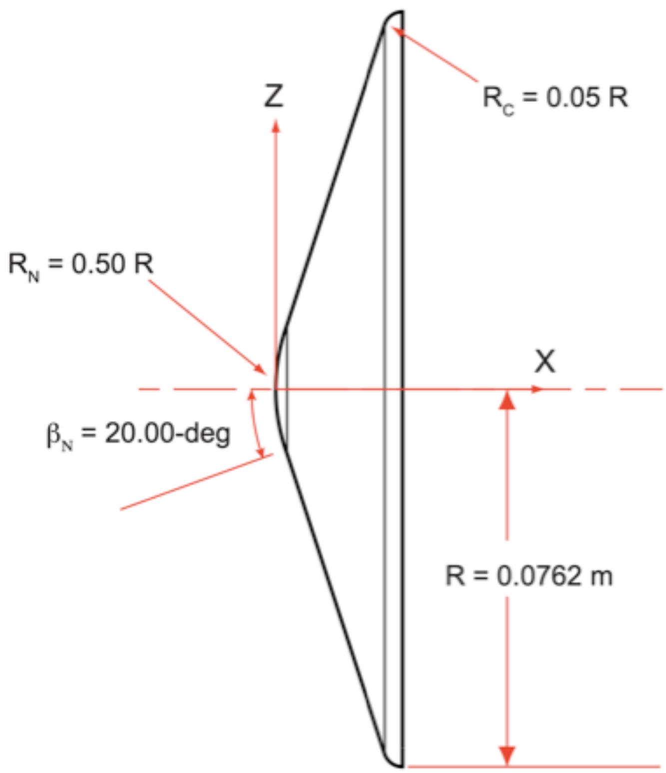

Figure 3. Sphere-cone geometry.

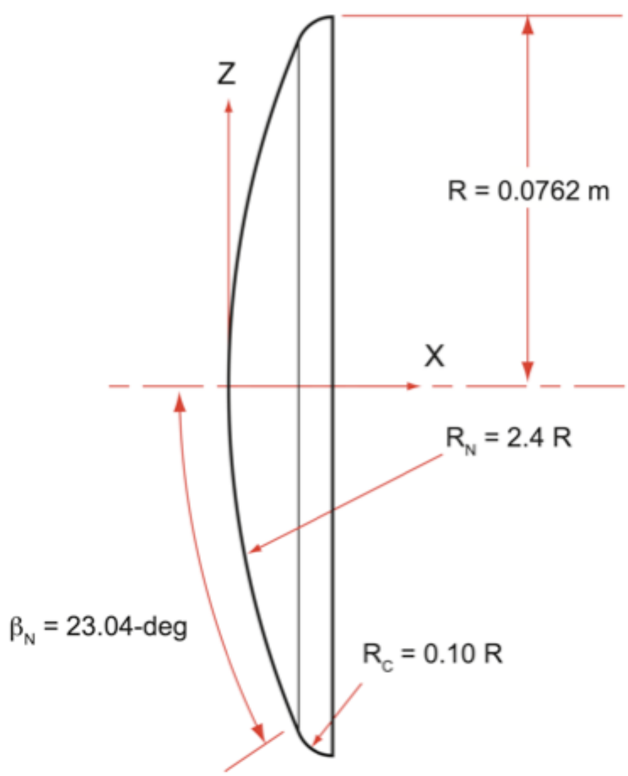

Figure 4. Spherical-cap geometry.

Sphere-cone smooth model

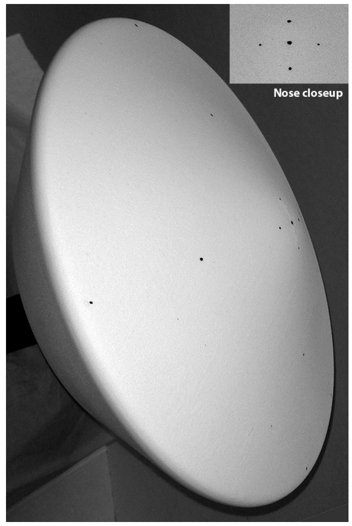

Sphere-cone 230-mesh model

Sphere-cone 140-mesh model

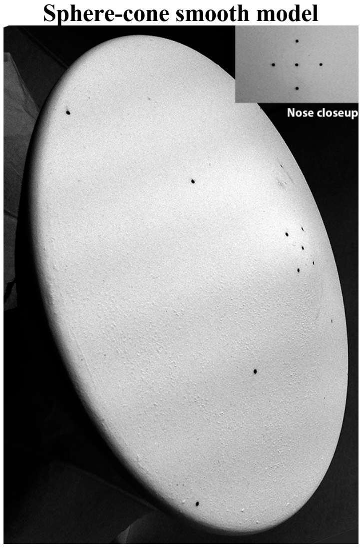

Sphere-cone 80-mesh model

Sphere-cone 40-mesh model

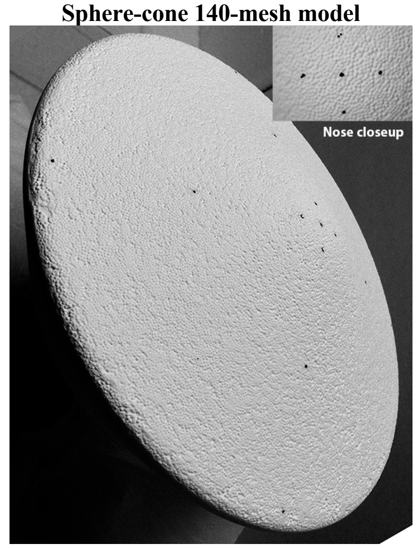

Sphere-cone 20-mesh model

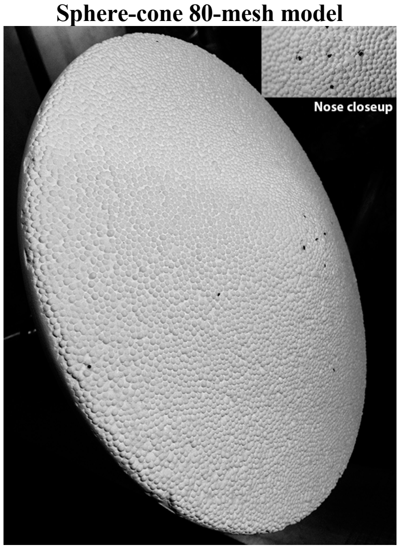

Sphere-cone 10-mesh model

Figure 5. Sphere-cone model photographs

Spherical-cap smooth model

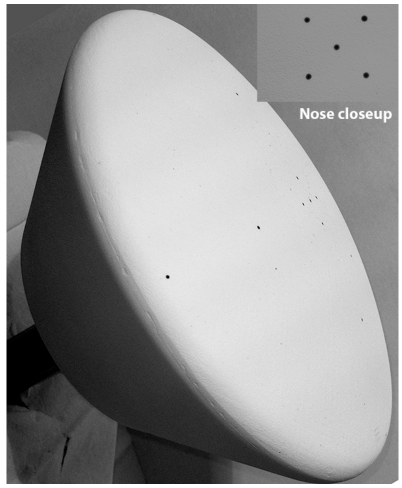

Spherical-cap 230-mesh model

Spherical-cap 140-mesh model

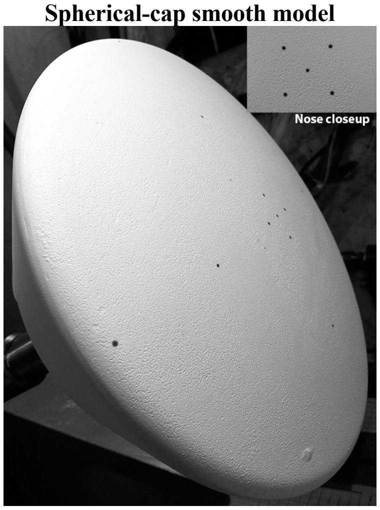

Spherical-cap 80-mesh model

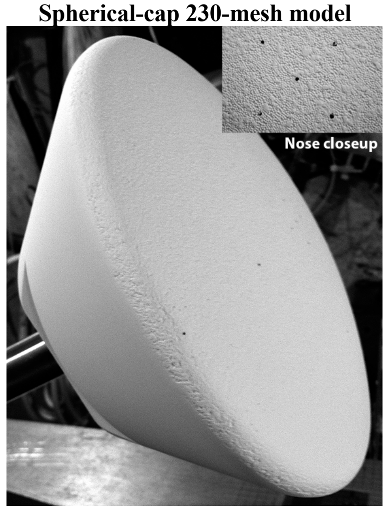

Spherical-cap 40-mesh model

Spherical-cap 20-mesh model

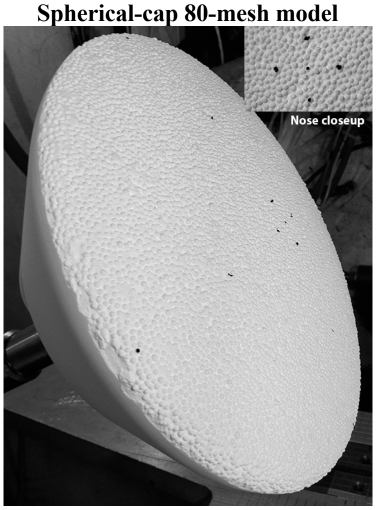

Spherical-cap 10-mesh model

Figure 6. Spherical-cap model photographs

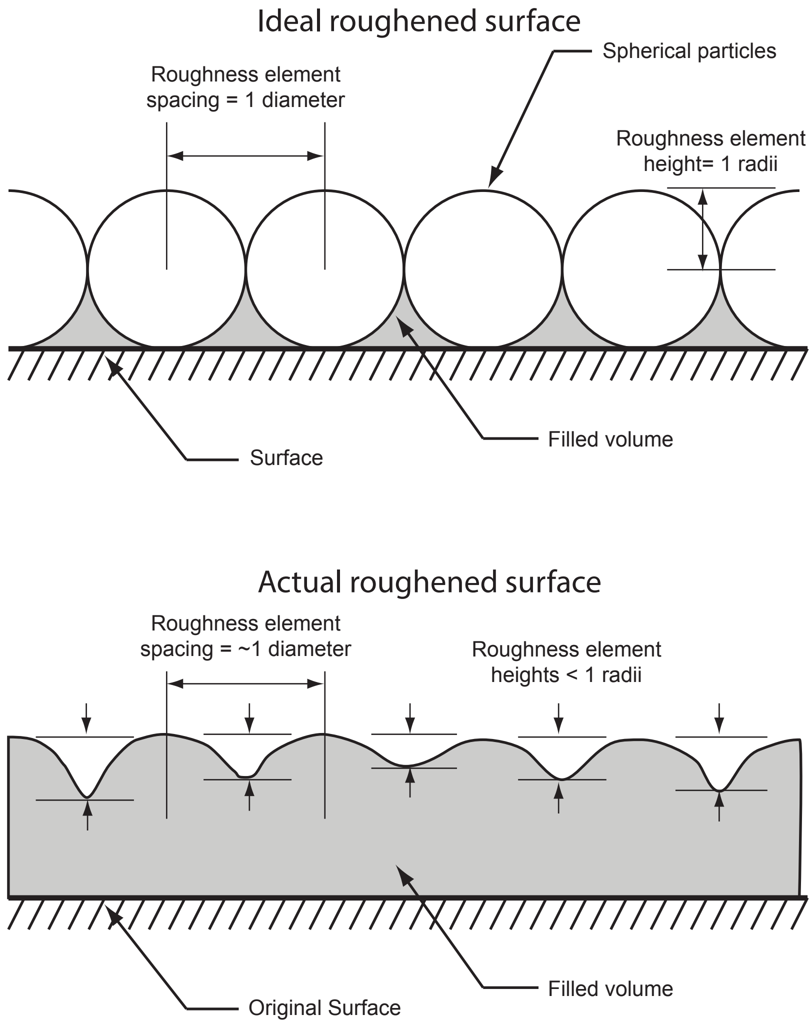

Figure 7. Illustration of ideal and actual surface roughness.

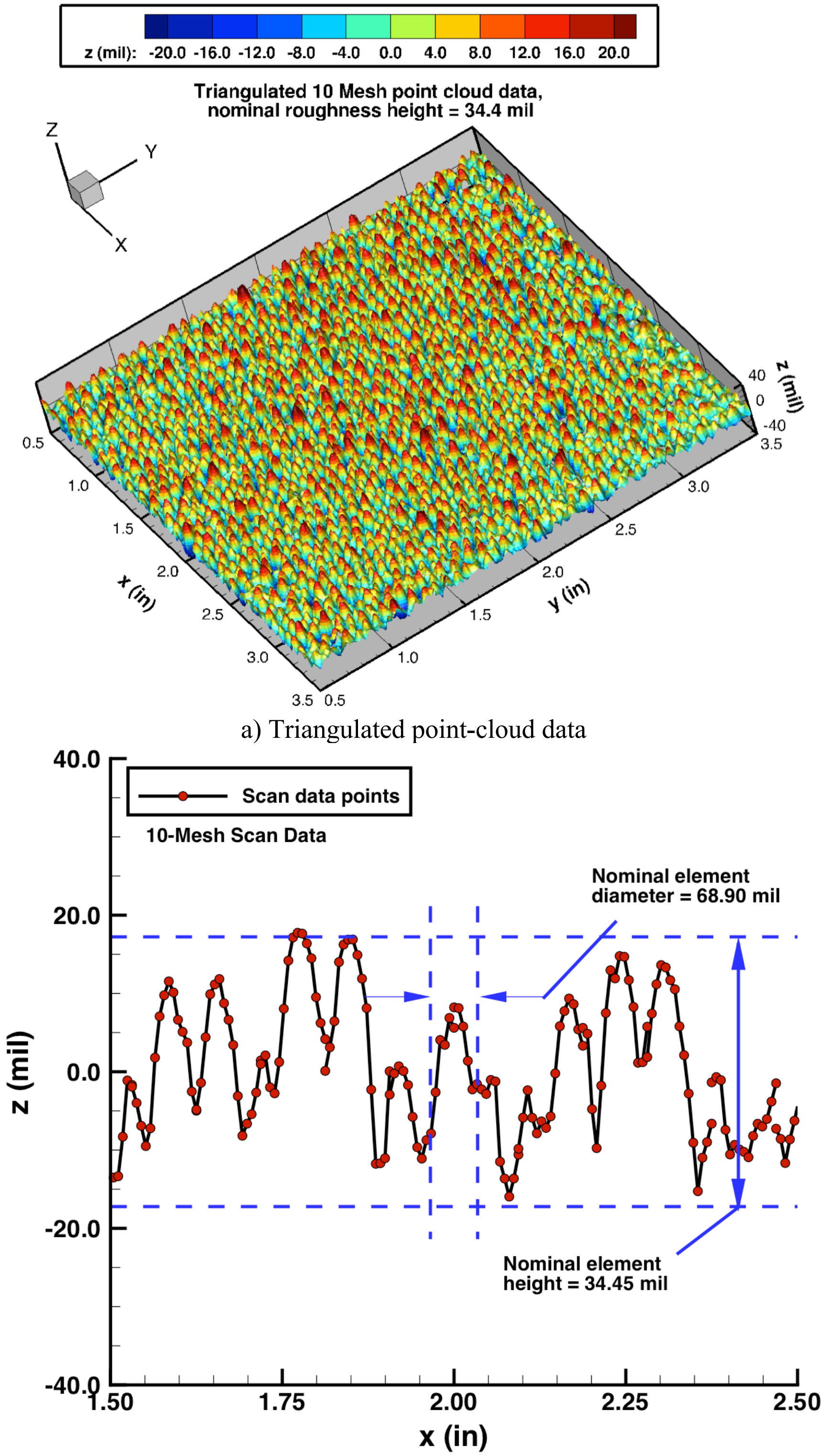

a) Triangulated point-cloud data

b) Profile line-cut

Figure 8. 10-Mesh sample plate scan data.

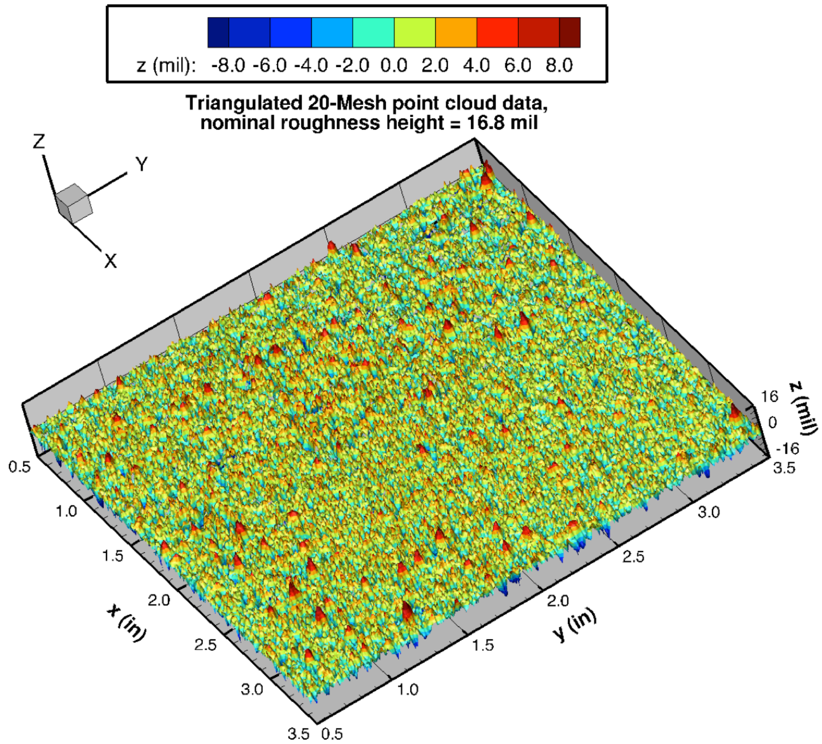

a) Triangulated point-cloud data

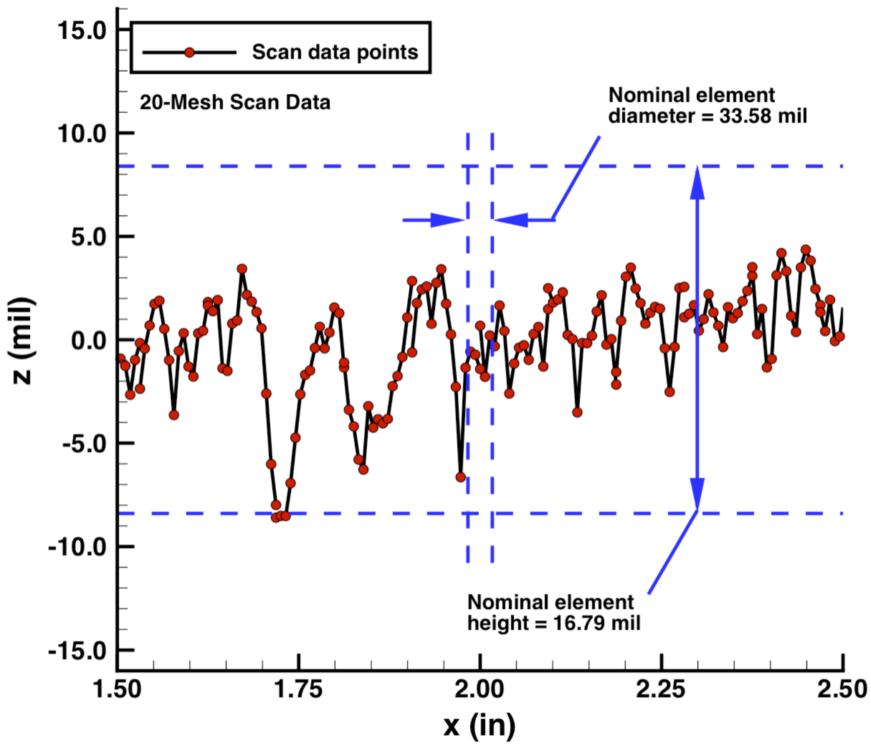

b) Profile line-cut

Figure 9. 20-Mesh sample plate scan data.

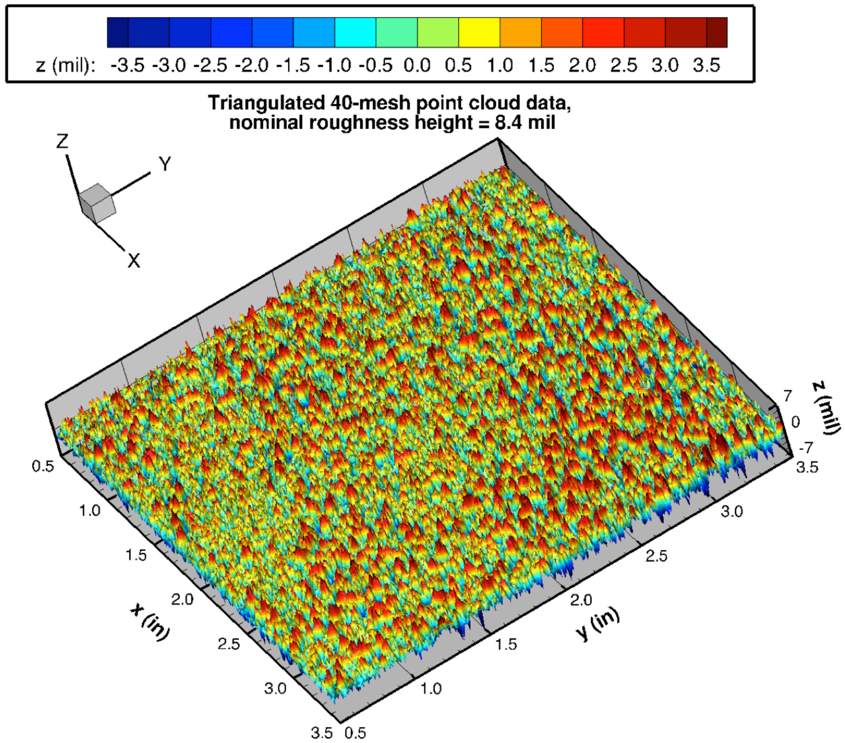

a) Triangulated point-cloud data

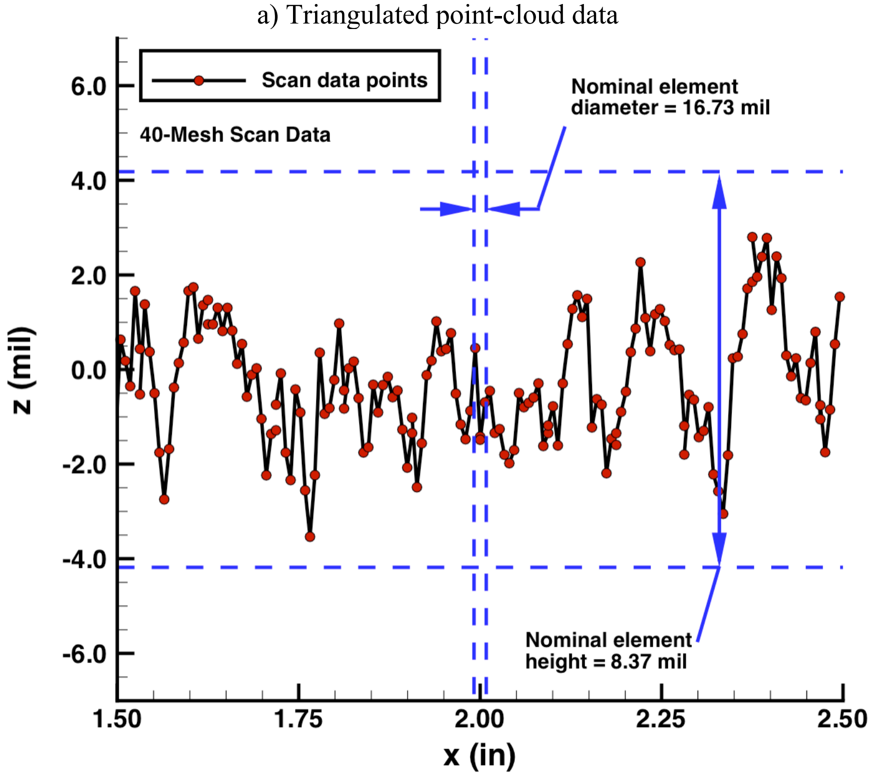

b) Profile line-cut

Figure 10. 40-Mesh sample plate scan data.

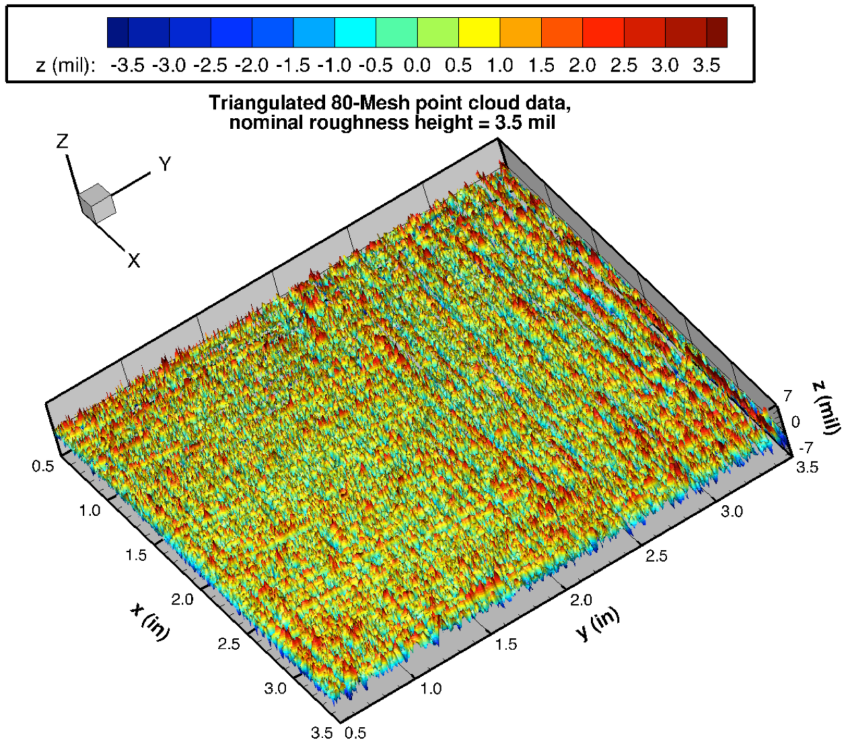

a) Triangulated point-cloud data

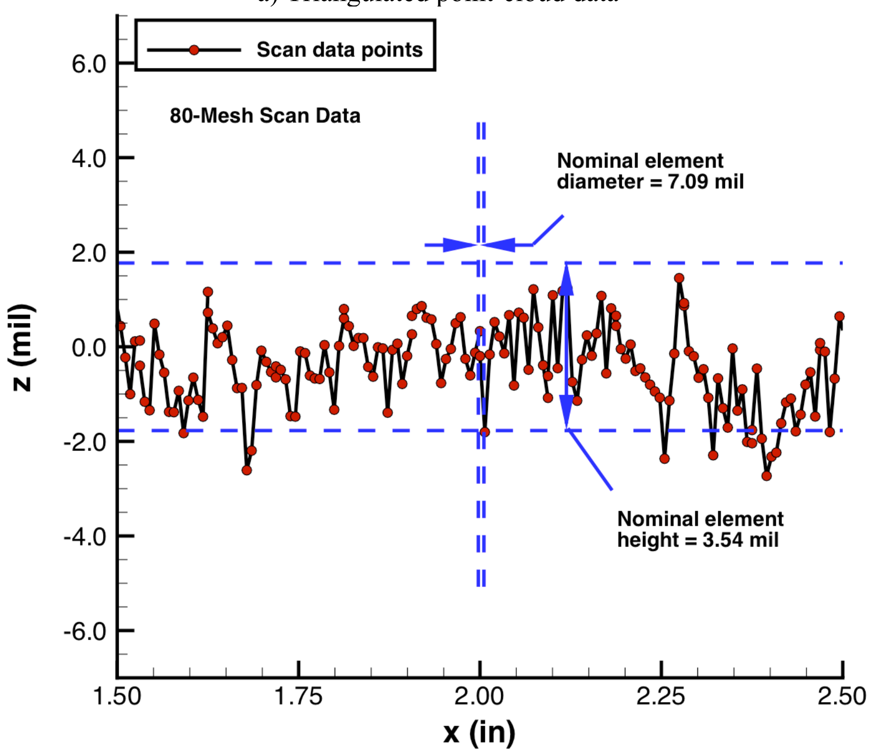

b) Profile line-cut

Figure 11. 80-Mesh sample plate scan data.

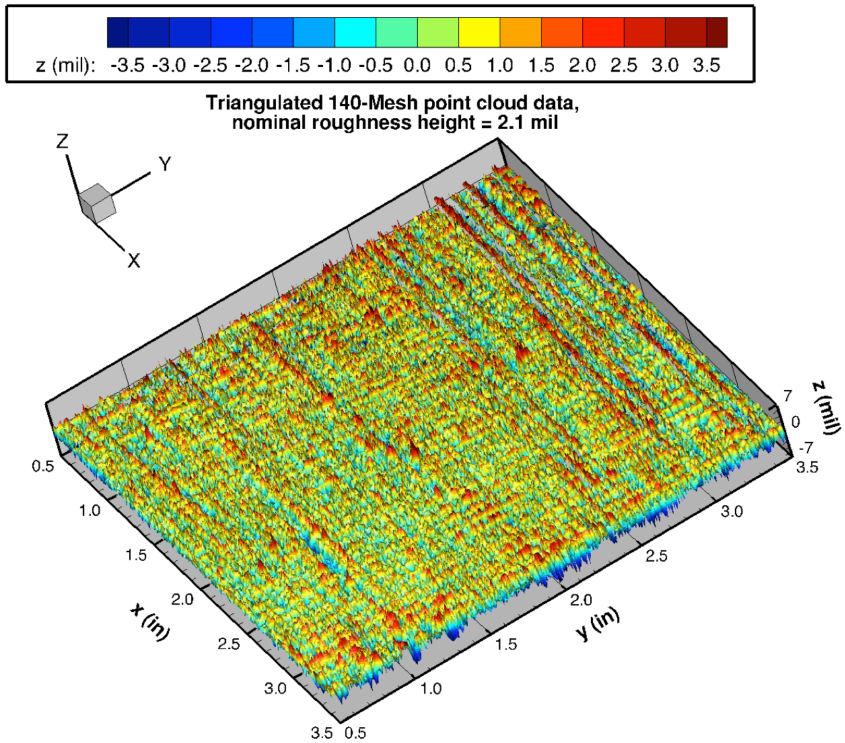

a) Triangulated point-cloud data

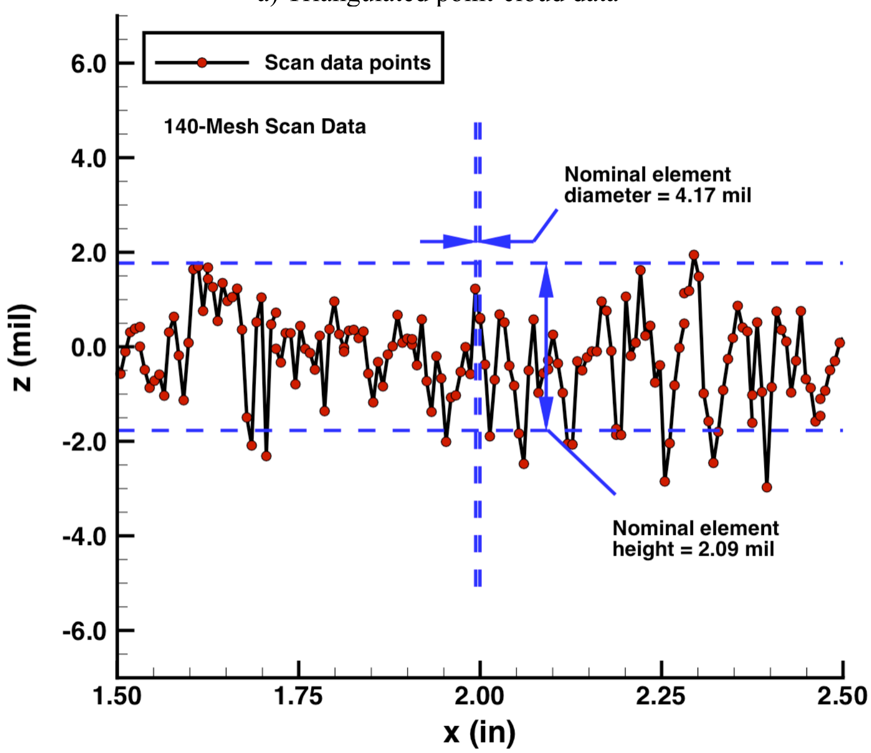

b) Profile line-cut

Figure 12. 140-Mesh sample plate scan data.

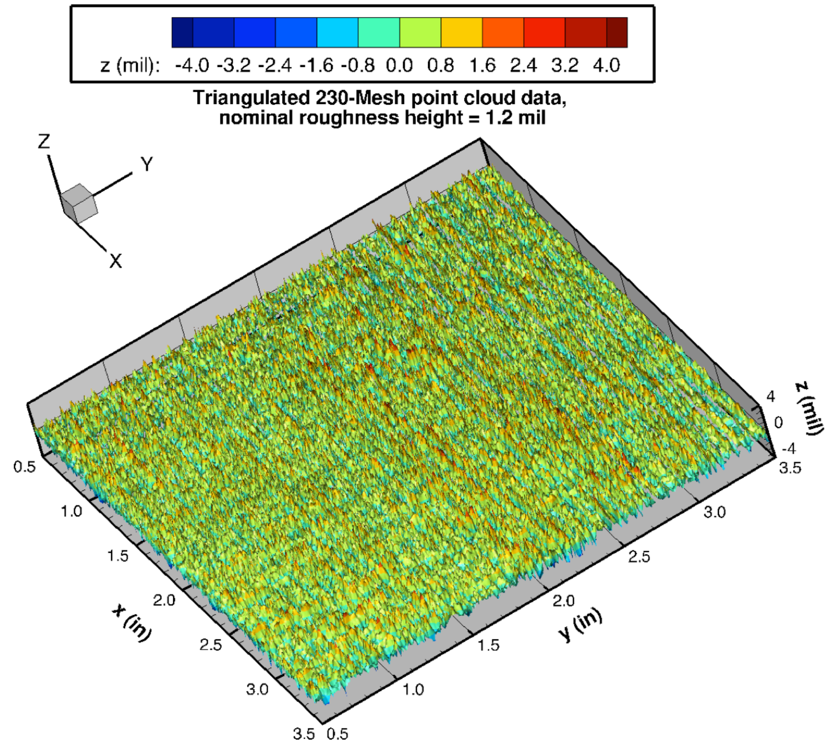

a) Triangulated point-cloud data

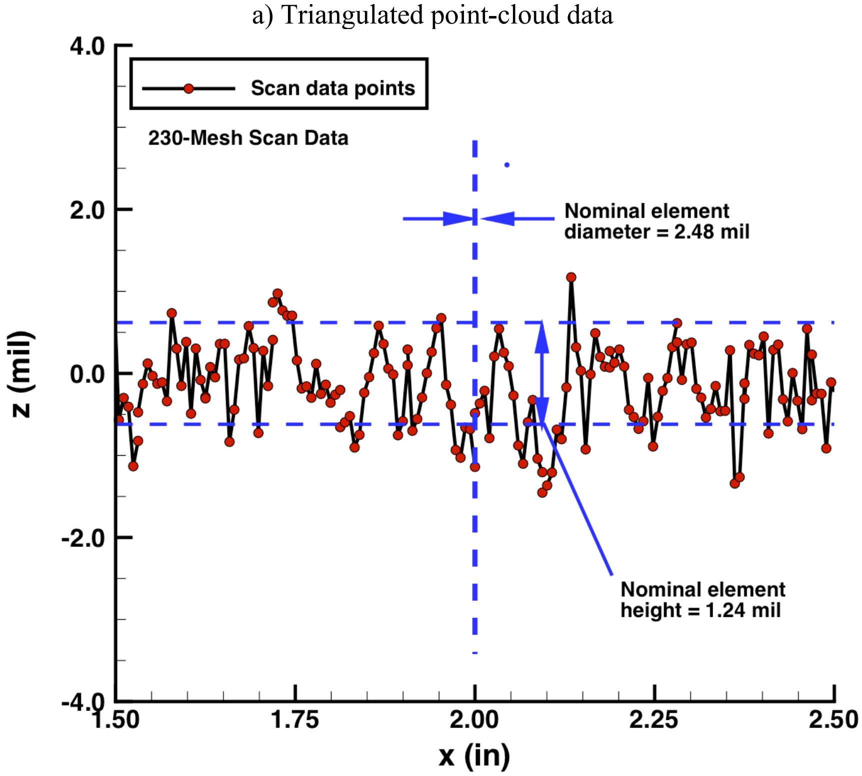

b) Profile line-cut

Figure 13. 230-Mesh sample plate scan data.

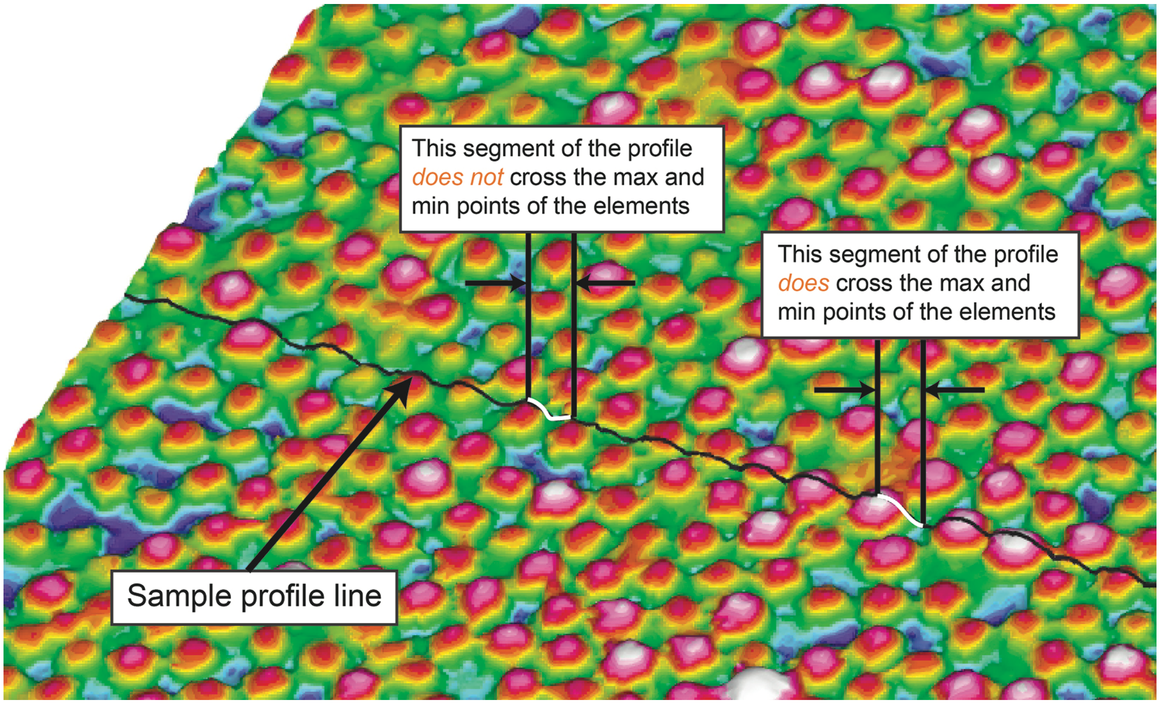

Figure 14. Profile alignment with roughness elements.

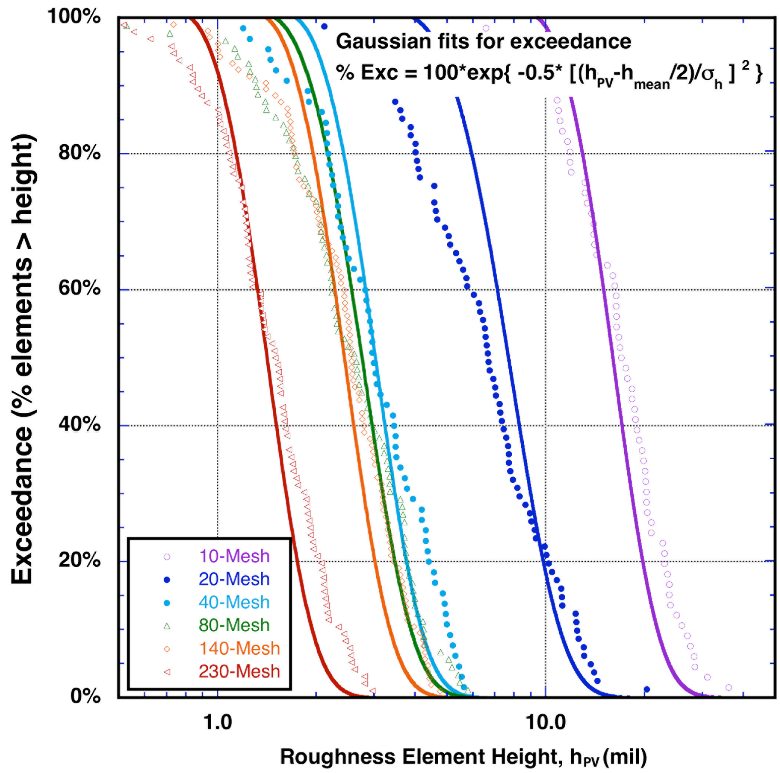

Figure 15. Roughness height probability of exceedance distributions.

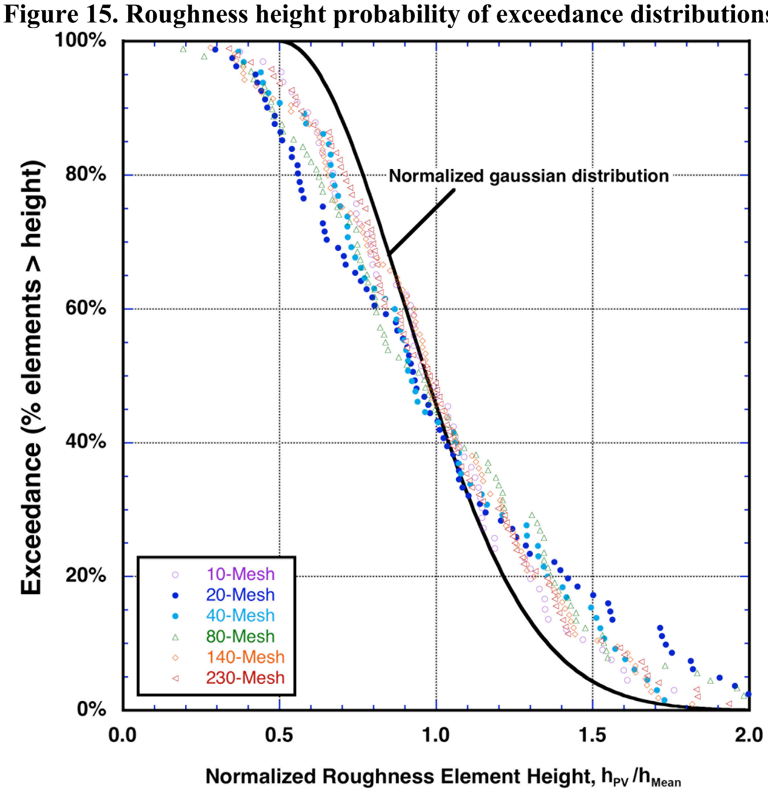

Figure 16. Normalized exceedance distributions.

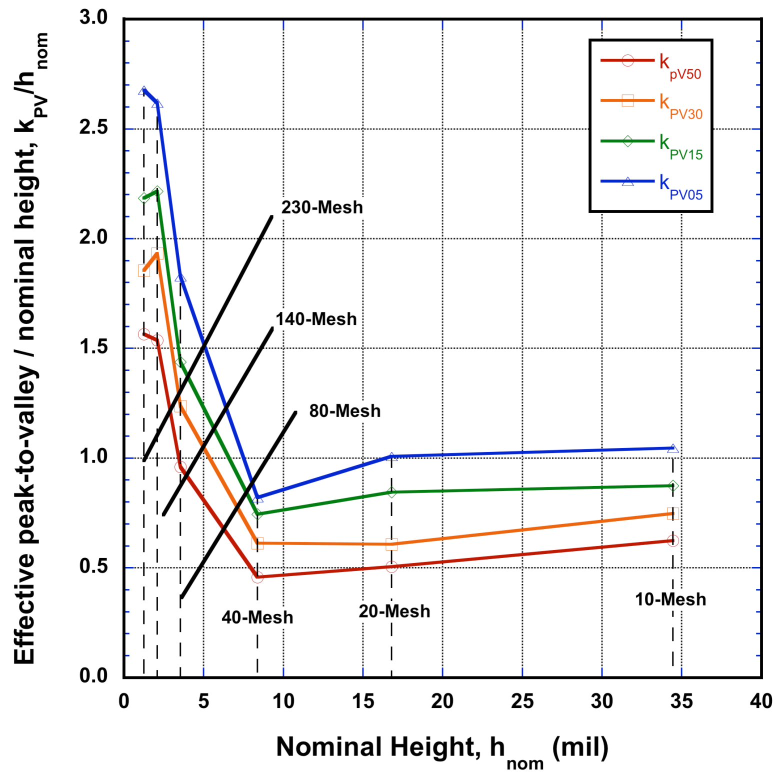

Figure 17. Comparison of effective and nominal roughness heights.

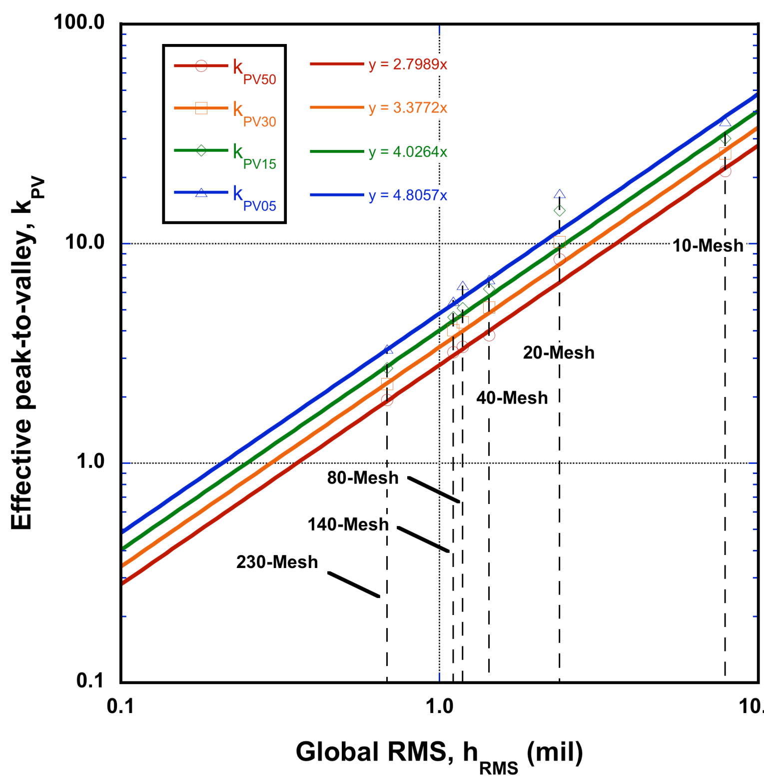

Figure 18. Relationship between effective roughness heights and measured RMS heights.

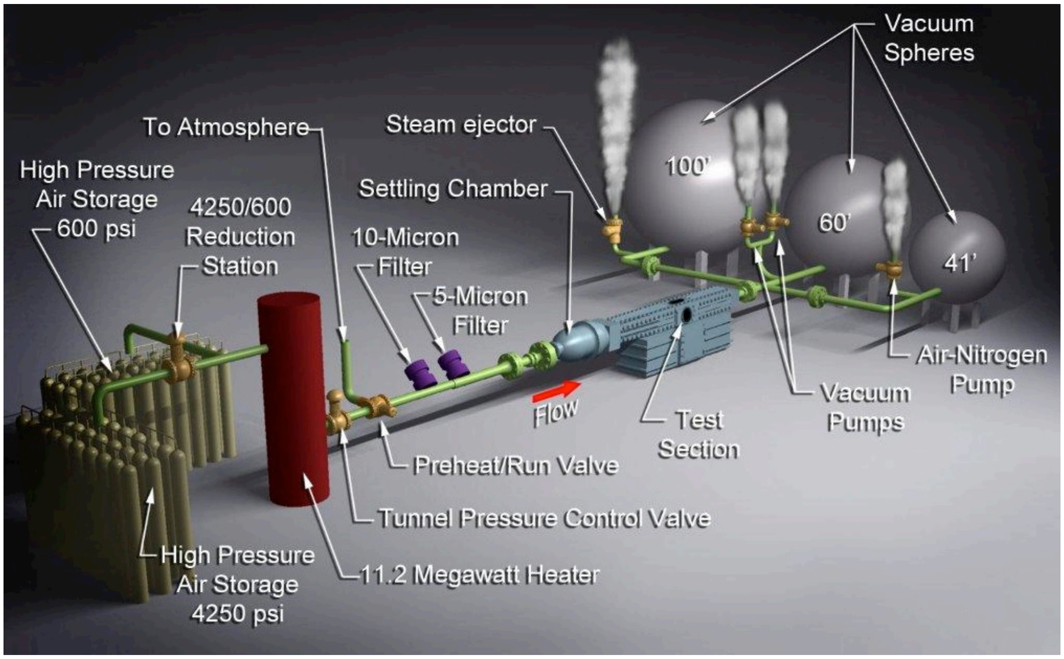

Figure 19. Schematic of Langley Research Center 20-Inch Mach 6 Air Tunnel.

Figure 20. Langley Research Center 20-Inch Mach 6 Air Tunnel test section.

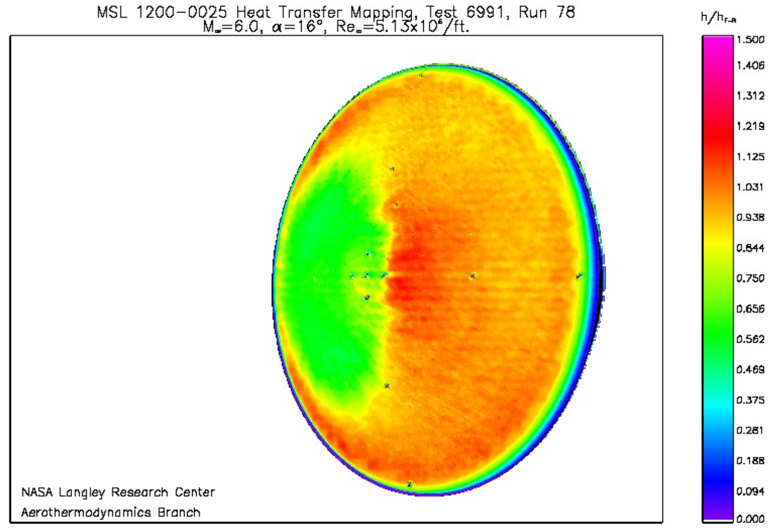

Figure 21. Sample phosphor thermography 2-D image data.

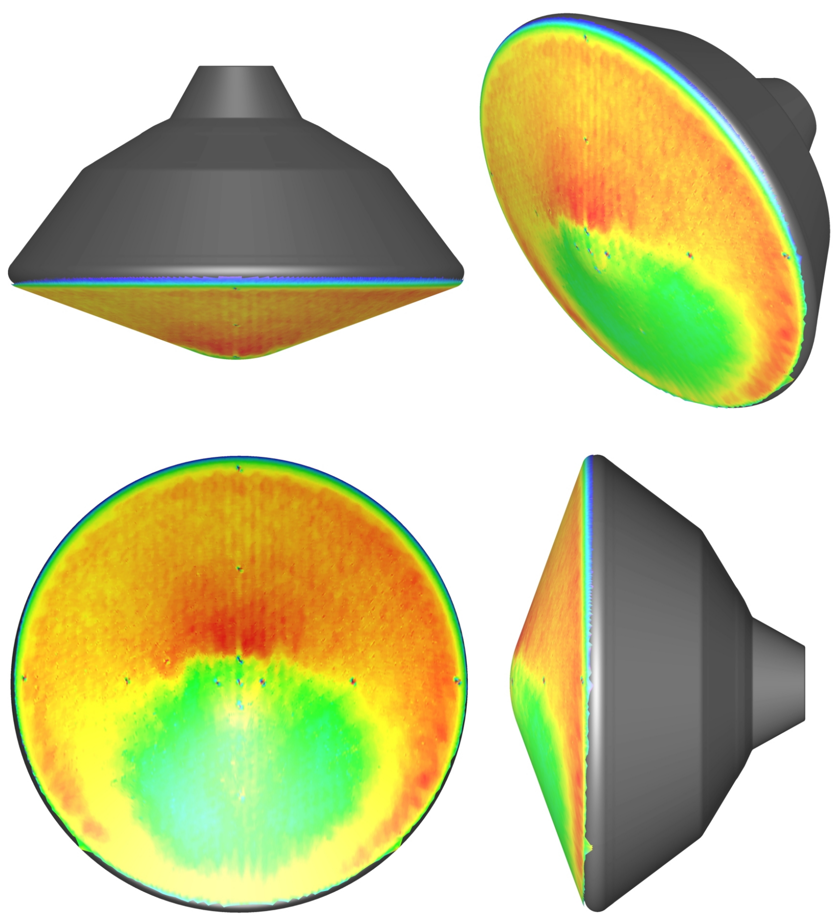

Figure 22. Sample 3-D mapping of phosphor thermography data.

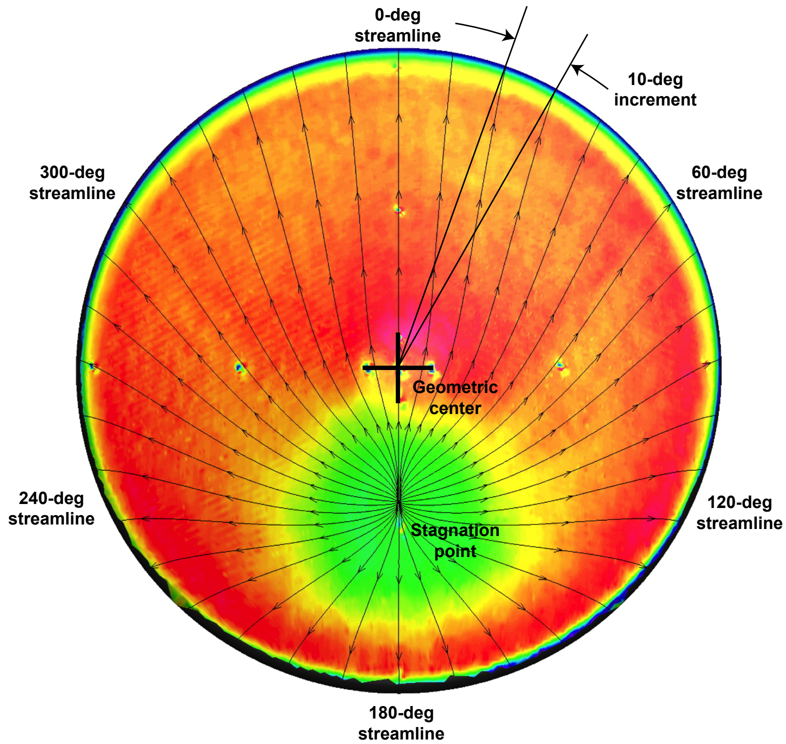

Figure 23. Streamlines for data extraction on sphere-cone geometry.

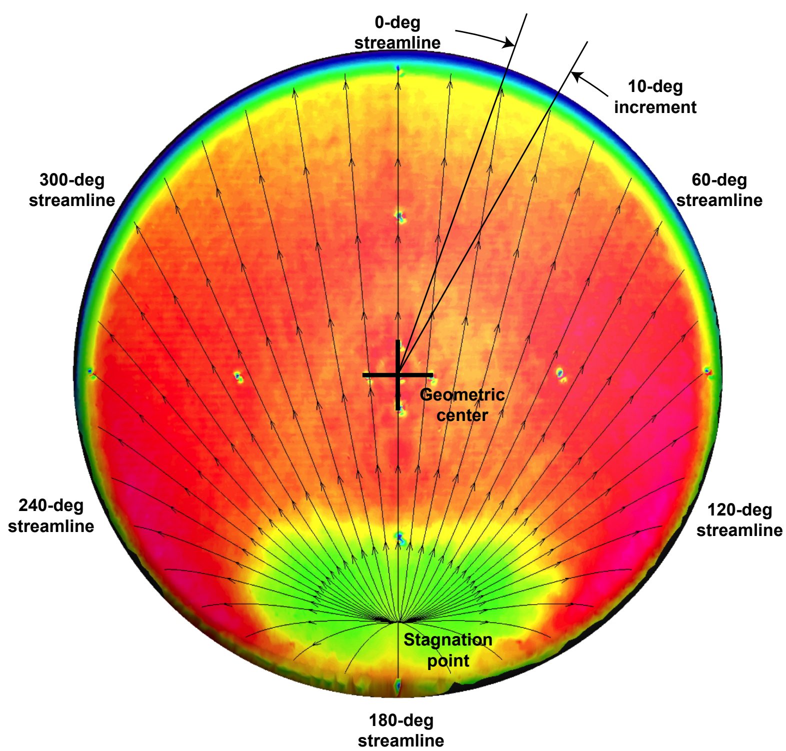

Figure 24. Streamlines for data extraction on spherical-cap geometry.

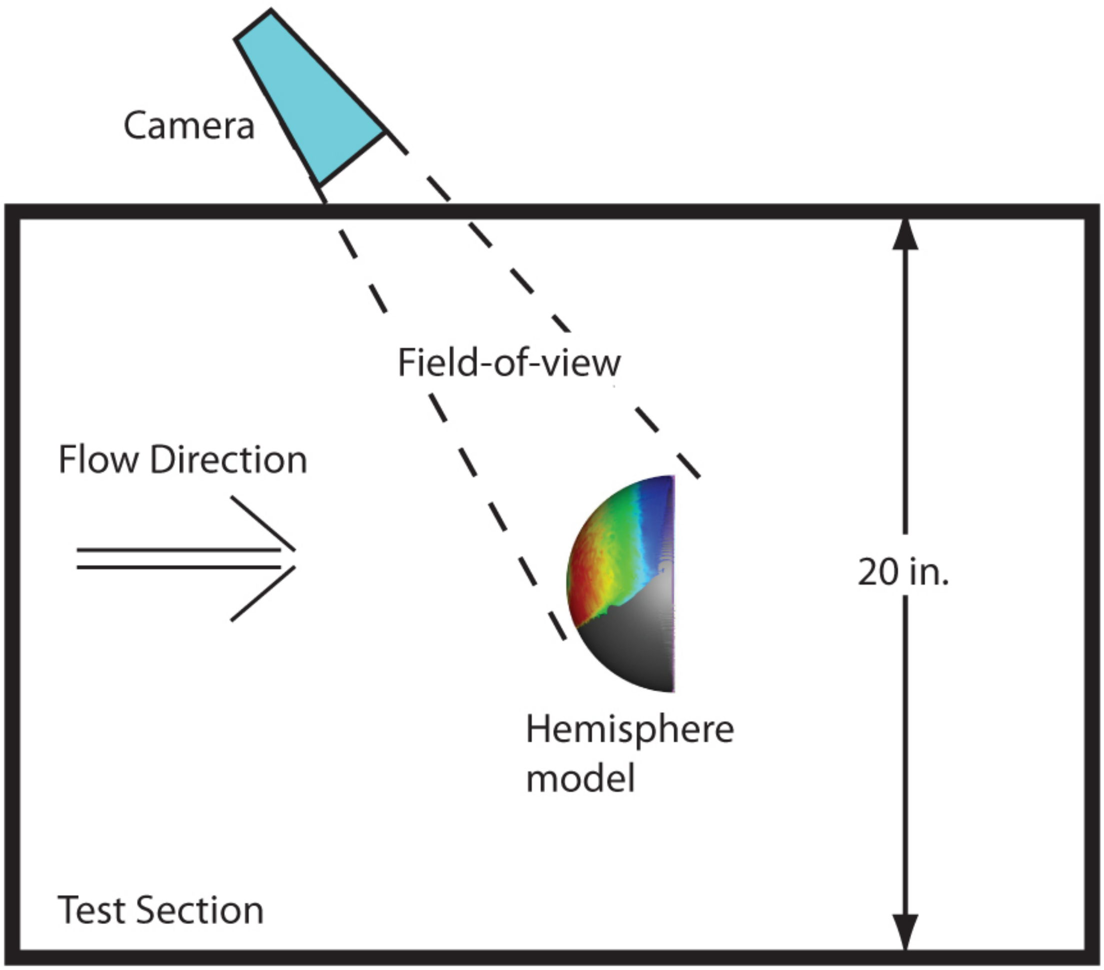

Figure 25. Illustration of camera field-of-view for hemisphere model in 20-Inch Mach 6 Air Tunnel.

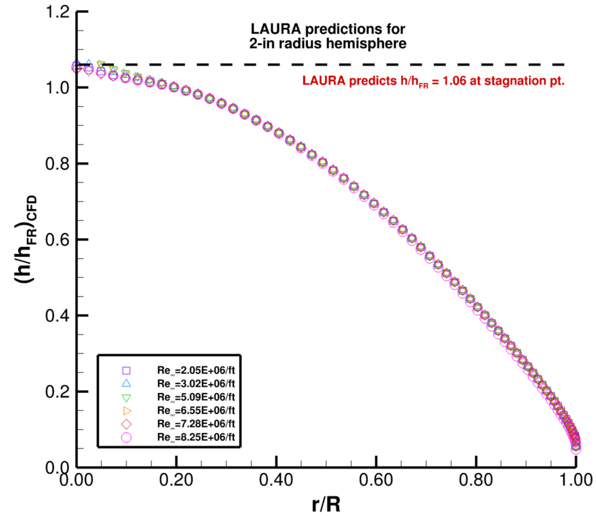

Figure 26. CFD predictions for hemisphere heating at wind tunnel conditions.

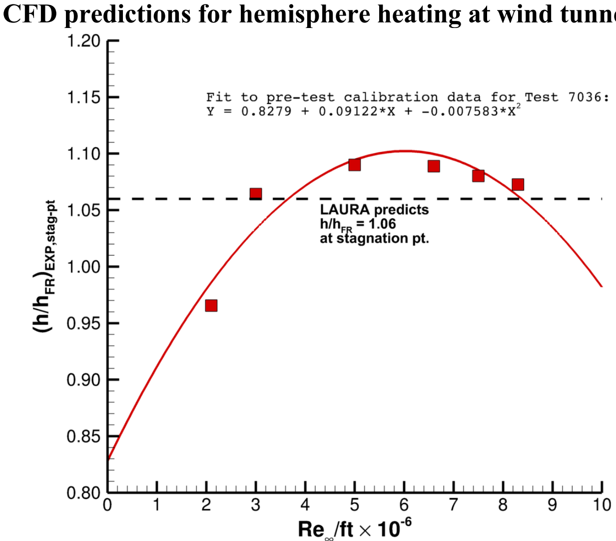

Figure 27. Measured stagnation point heating for pretest calibrations for Test 7036.

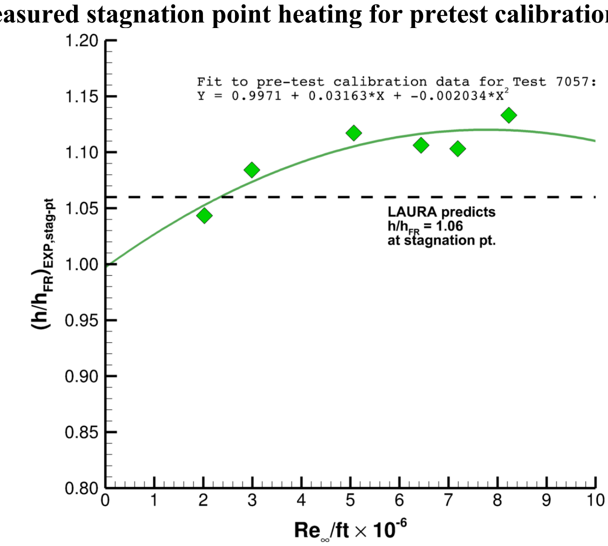

Figure 28. Measured stagnation point heating for pretest calibrations for Test 7057.

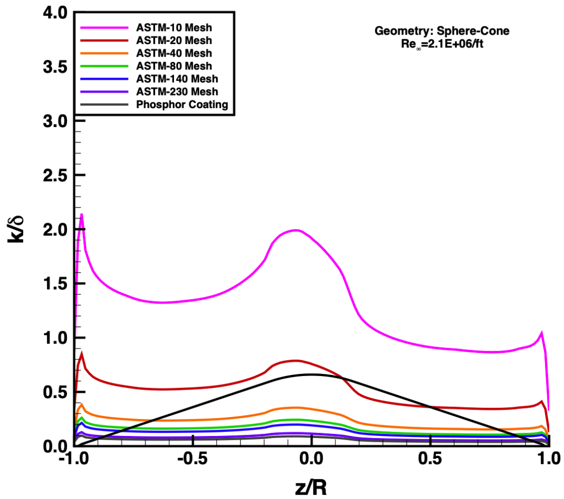

a) $Re_\infty = 2.1\times10^6$/ft

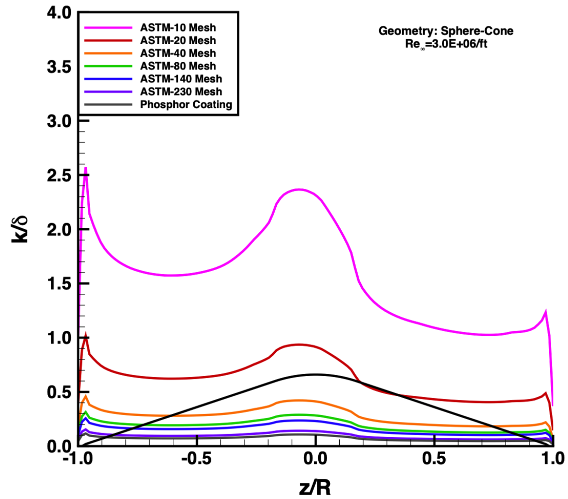

b) $Re_\infty = 3.0\times10^6$/ft

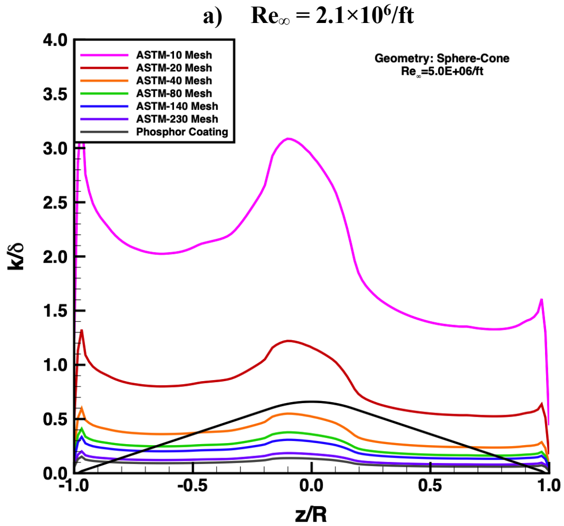

c) $Re_\infty = 5.0\times10^6$/ft

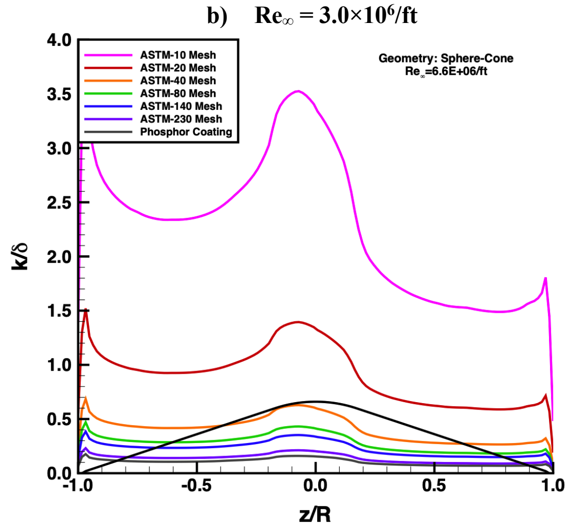

d) $Re_\infty = 6.6\times10^6$/ft

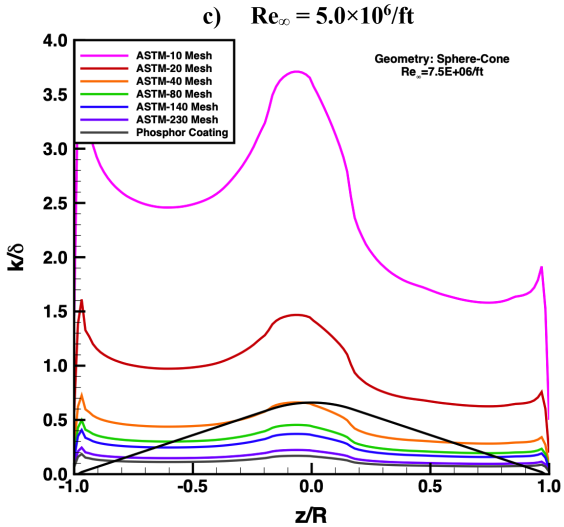

e) $Re_\infty = 7.5\times10^6$/ft

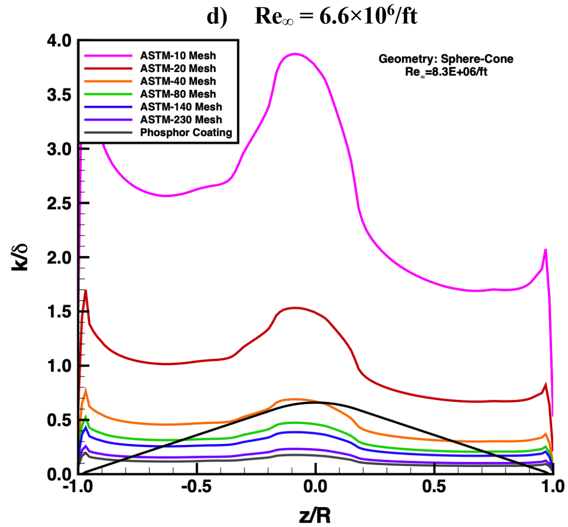

f) $Re_\infty = 8.3\times10^6$/ft

Figure 29. Centerline profiles of roughness effects on k/δ, sphere-cone geometry.

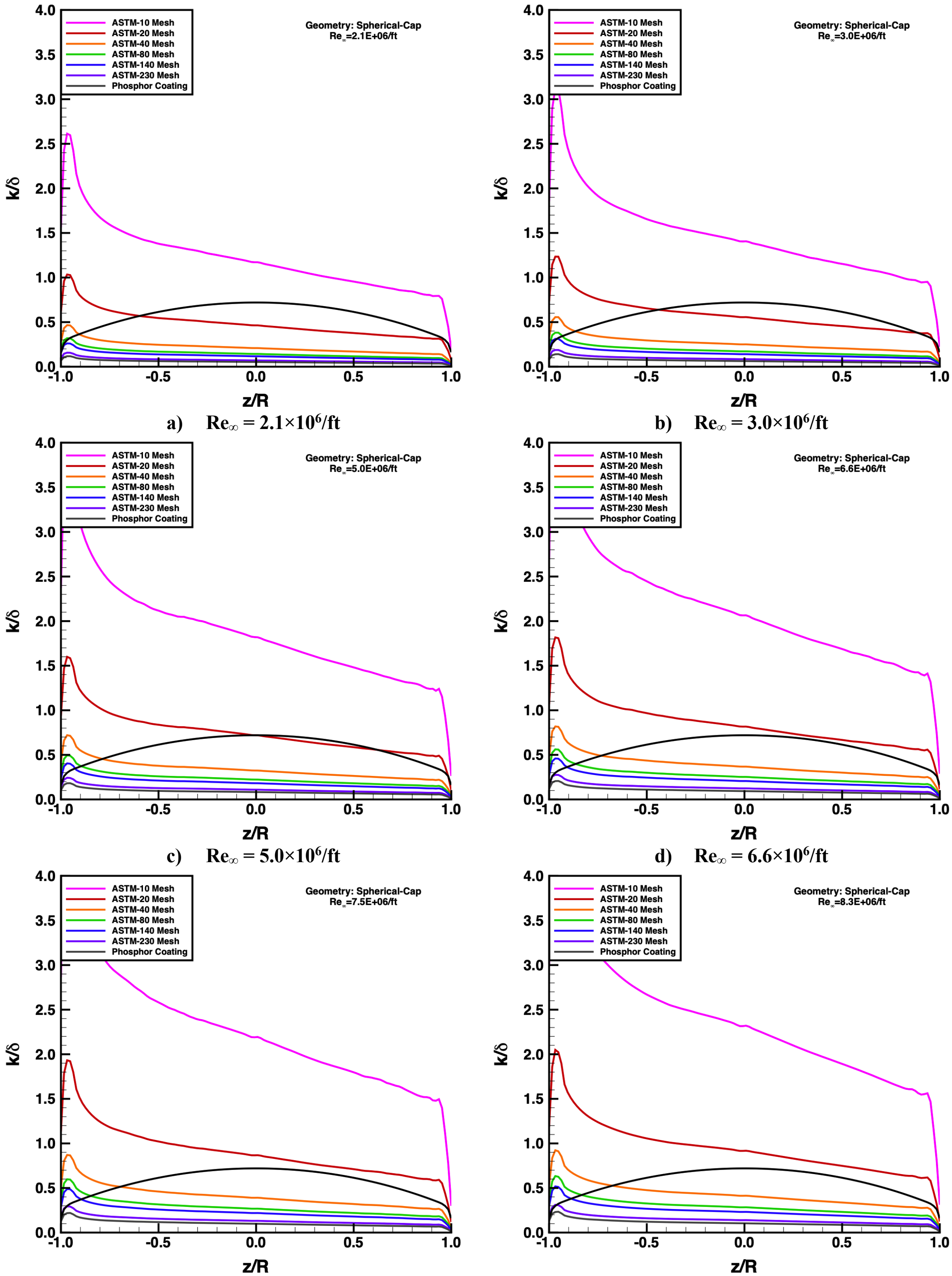

a) $Re_\infty = 2.1\times10^6$/ft

b) $Re_\infty = 3.0\times10^6$/ft

c) $Re_\infty = 5.0\times10^6$/ft

d) $Re_\infty = 6.6\times10^6$/ft

e) $Re_\infty = 7.5\times10^6$/ft

f) $Re_\infty = 8.3\times10^6$/ft

Figure 30. Centerline profiles of roughness effects on k/δ, spherical-cap geometry.

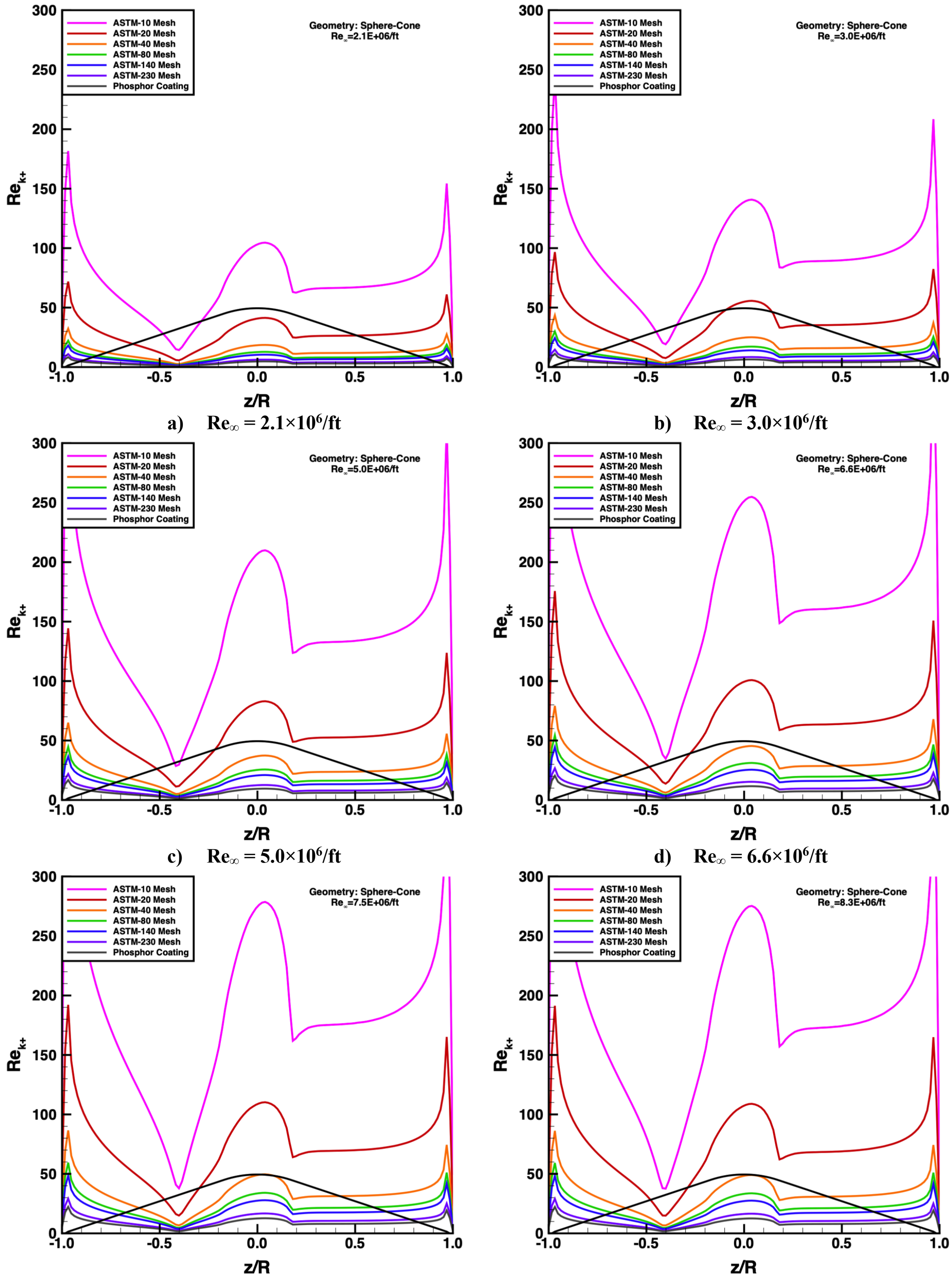

a) $Re_\infty = 2.1\times10^6$/ft

b) $Re_\infty = 3.0\times10^6$/ft

c) $Re_\infty = 5.0\times10^6$/ft

d) $Re_\infty = 6.6\times10^6$/ft

e) $Re_\infty = 7.5\times10^6$/ft

f) $Re_\infty = 8.3\times10^6$/ft

Figure 31. Centerline profiles of roughness effects on Re_{k+}, sphere-cone geometry.

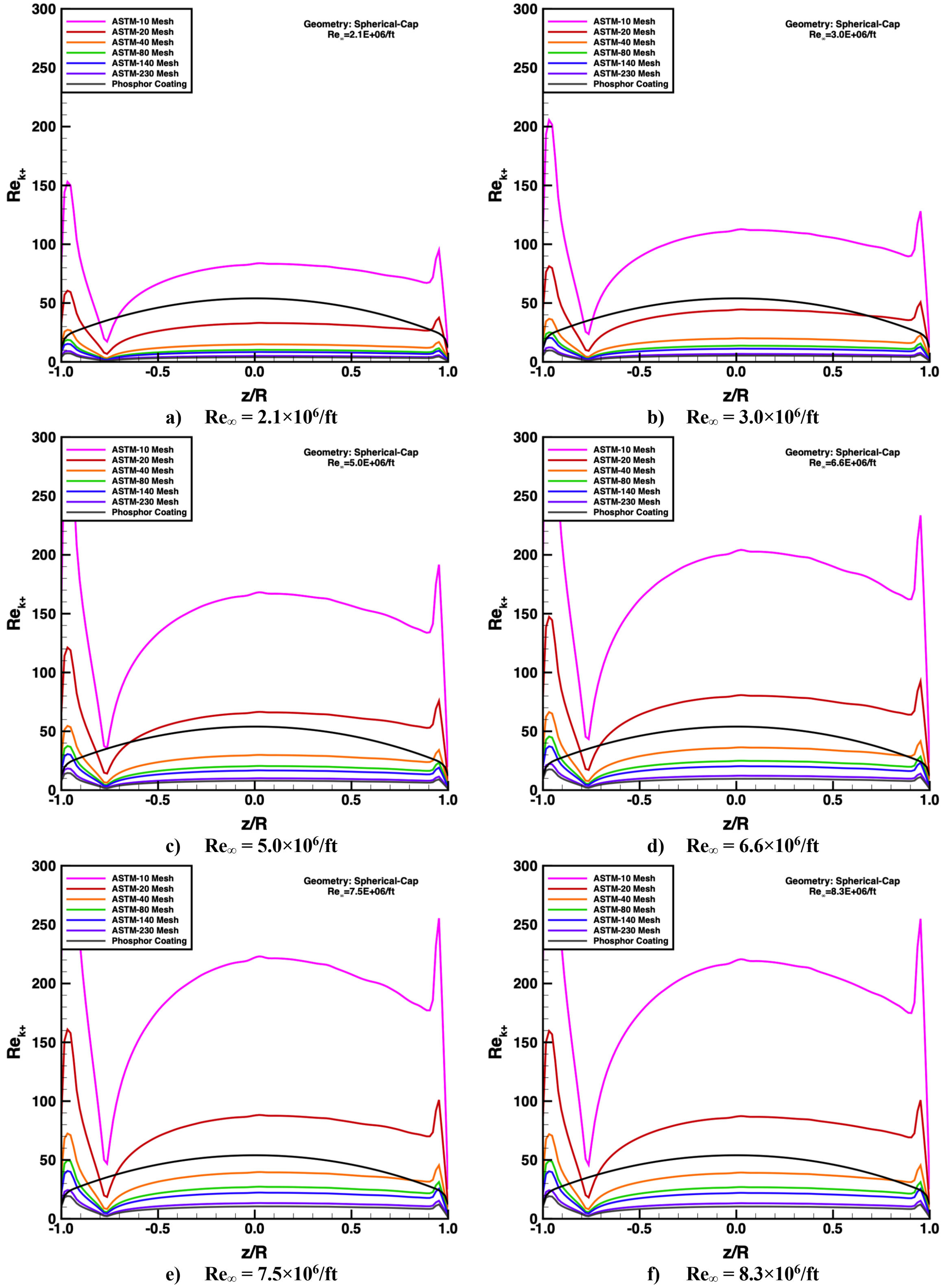

a) $Re_\infty = 2.1\times10^6$/ft b) $Re_\infty = 3.0\times10^6$/ft

c) $Re_\infty = 5.0\times10^6$/ft d) $Re_\infty = 6.6\times10^6$/ft

e) $Re_\infty = 7.5\times10^6$/ft f) $Re_\infty = 8.3\times10^6$/ft

Figure 32. Centerline profiles of roughness effects on Re_{k+}, spherical-cap geometry.

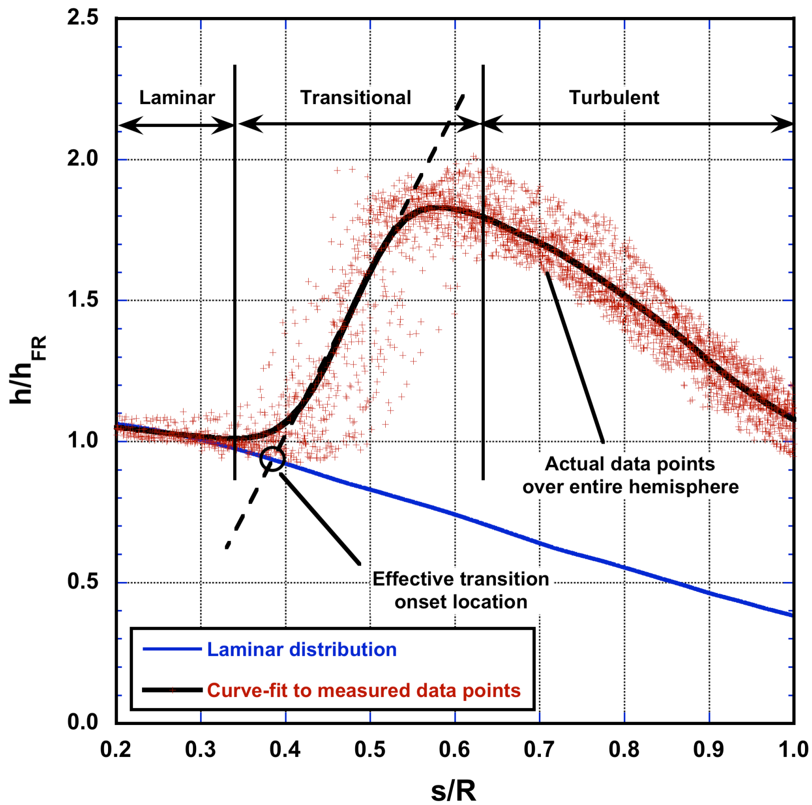

Figure 33. Tangent-slope-intercept method for determination of effect transition onset location.

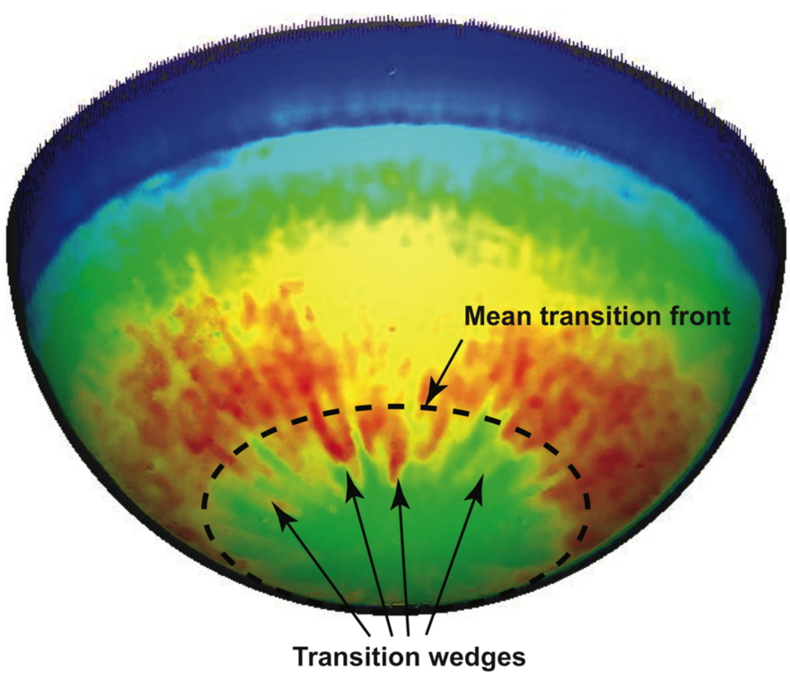

Figure 34. Comparison of irregular transition wedges vs. mean transition front.

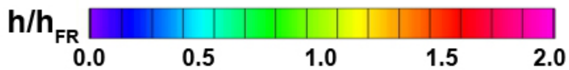

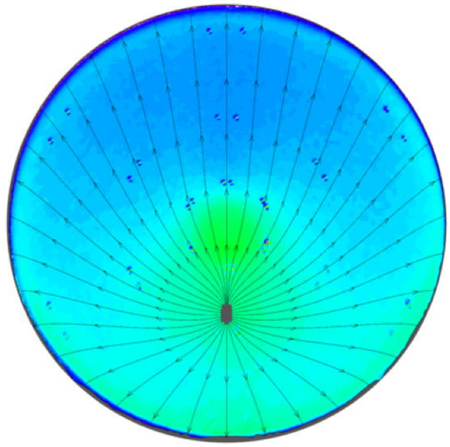

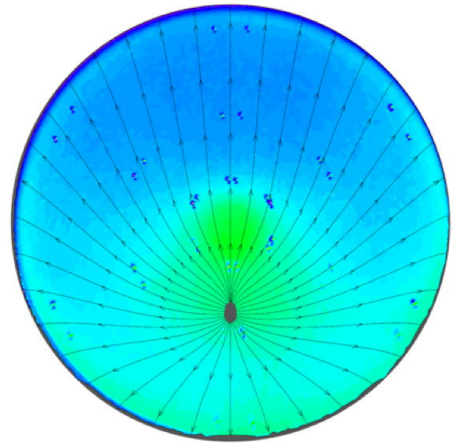

a) Test 7036, Run 50, $Re_\infty = 2.1\times10^6$/ft

b) Test 7036, Run 51, $Re_\infty = 3.0\times10^6$/ft

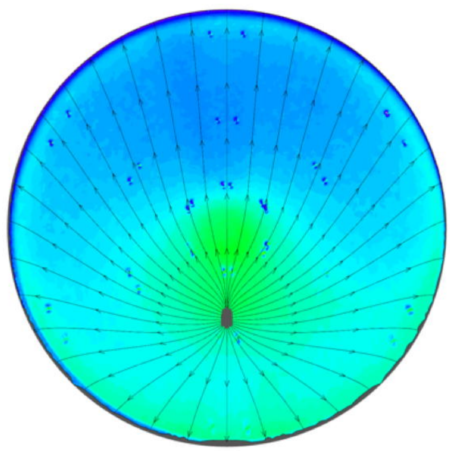

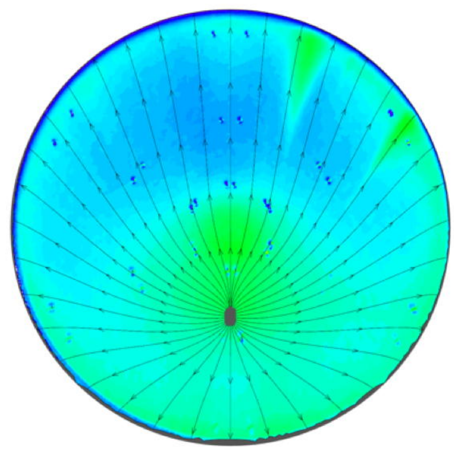

c) Test 7036, Run 52, $Re_\infty = 5.0\times10^6$/ft

d) Test 7036, Run 53 $Re_\infty = 6.5\times10^6$/ft

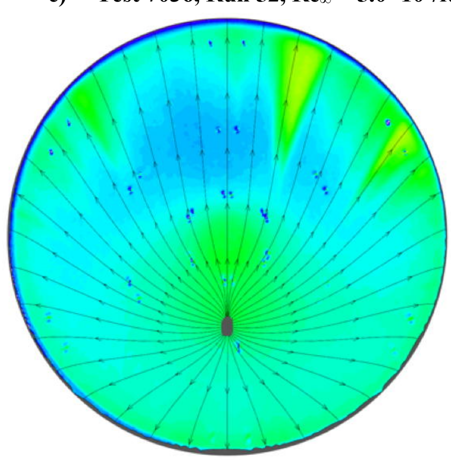

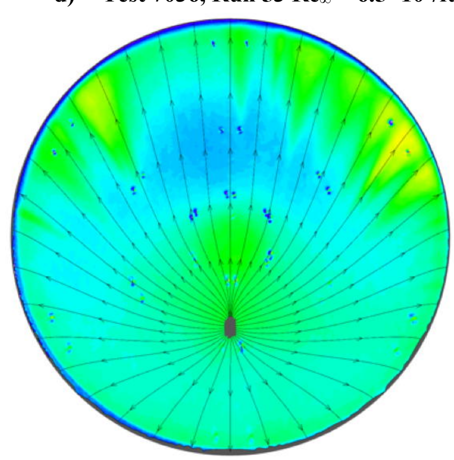

e) Test 7036, Run 54, $Re_\infty = 7.2\times10^6$/ft

f) Test 7036, Run 55, $Re_\infty = 8.1\times10^6$/ft

Figure 35. Reynolds Number effects, sphere-cone geometry, smooth model images.

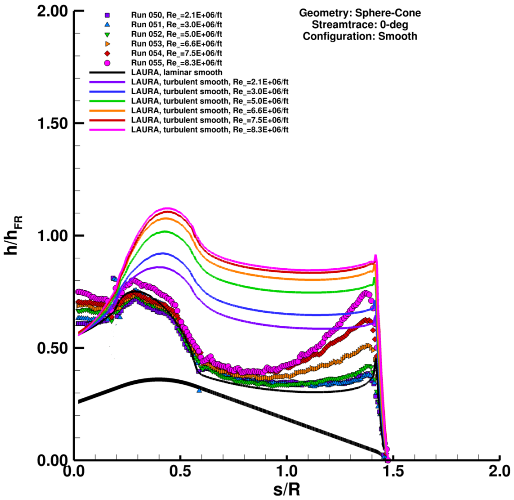

a) 0-deg streamline

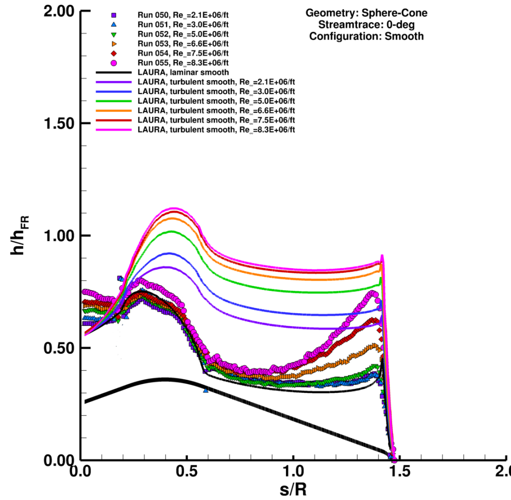

b) 30-deg streamline

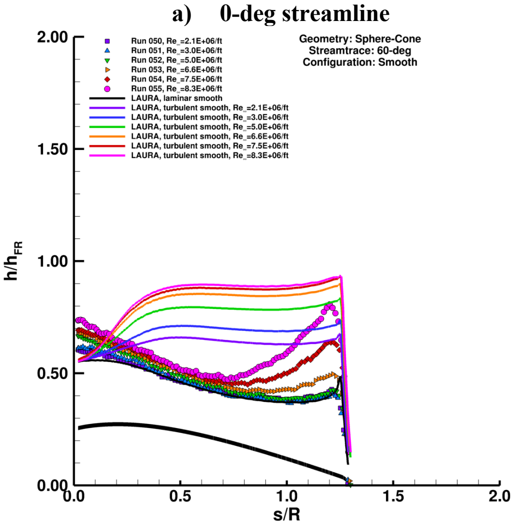

c) 60-deg streamline

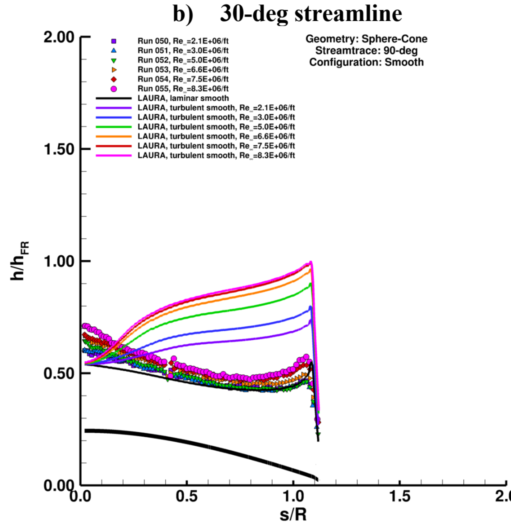

d) 90-deg streamline

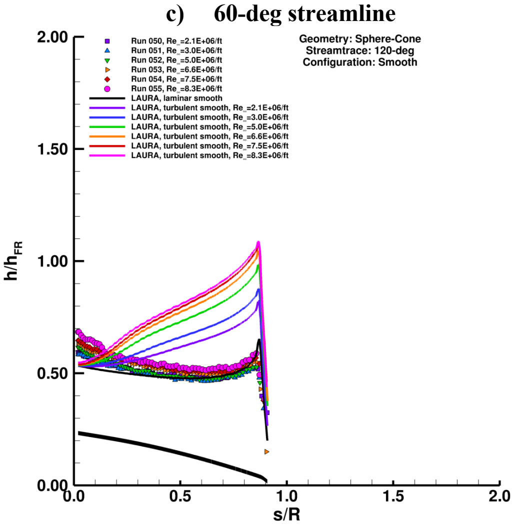

e) 120-deg streamline

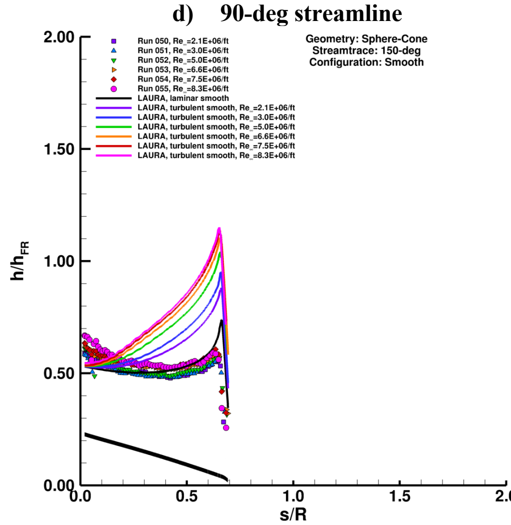

f) 150-deg streamline

Figure 36. Reynolds number effects, sphere-cone geometry, smooth model plots.

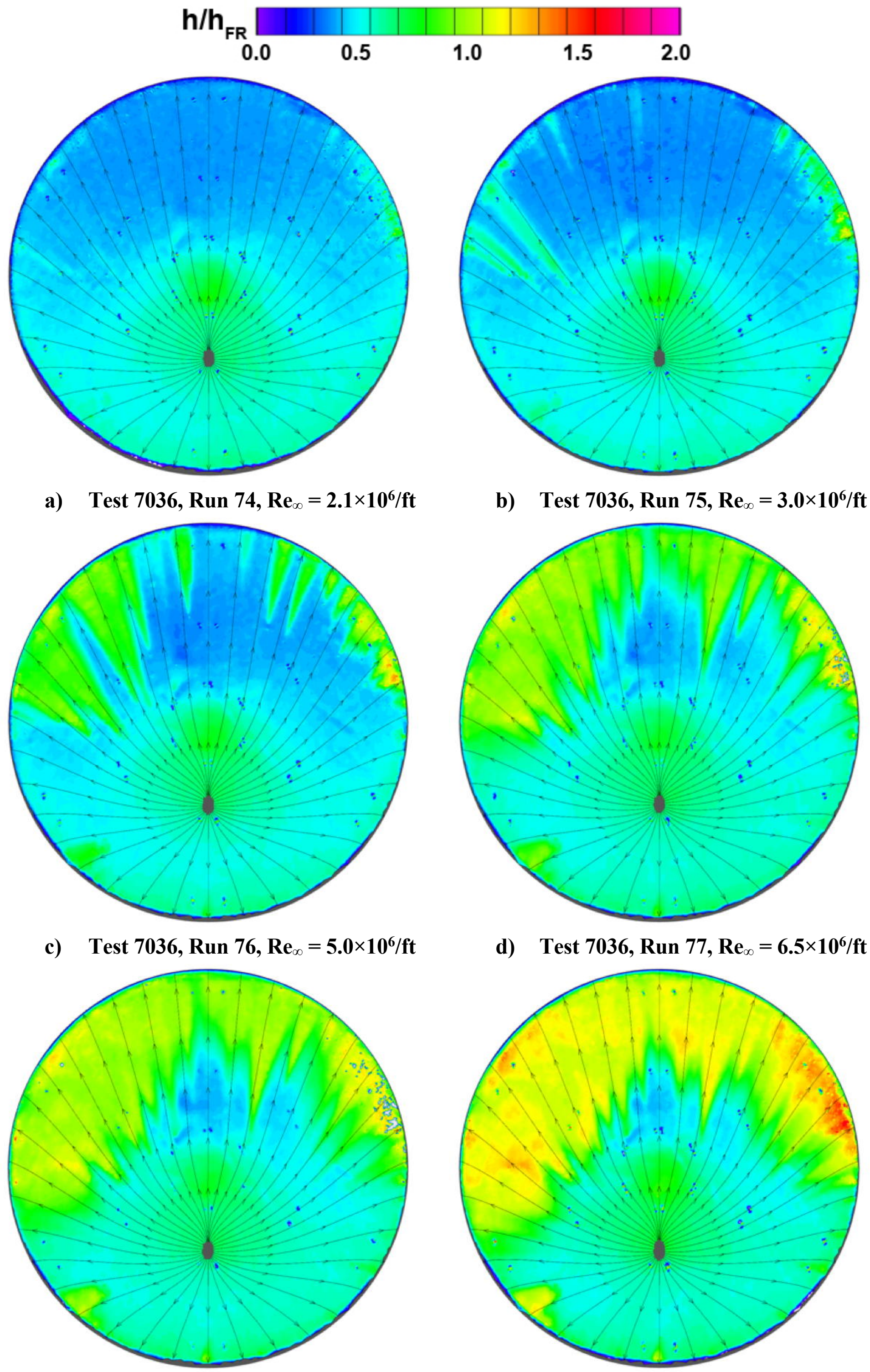

a) Test 7036, Run 74, Re$_\infty$ = 2.1×10^6/ft

b) Test 7036, Run 75, Re$_\infty$ = 3.0×10^6/ft

c) Test 7036, Run 76, Re$_\infty$ = 5.0×10^6/ft

d) Test 7036, Run 77, Re$_\infty$ = 6.5×10^6/ft

e) Test 7036, Run 78, Re$_\infty$ = 7.2×10^6/ft

f) Test 7036, Run 79, Re$_\infty$ = 8.1×10^6/ft

Figure 37. Reynolds Number effects, sphere-cone geometry, 230-mesh model images.

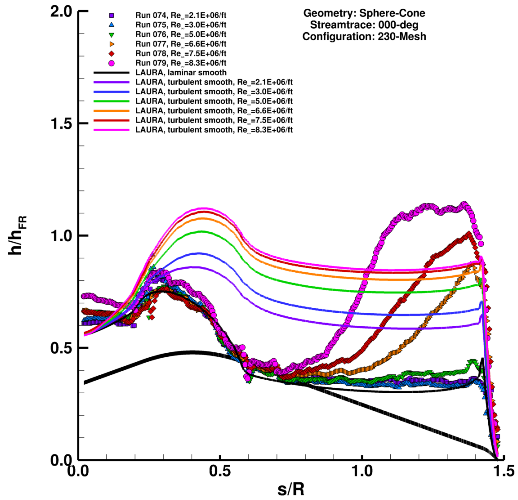

a) 0-deg streamline

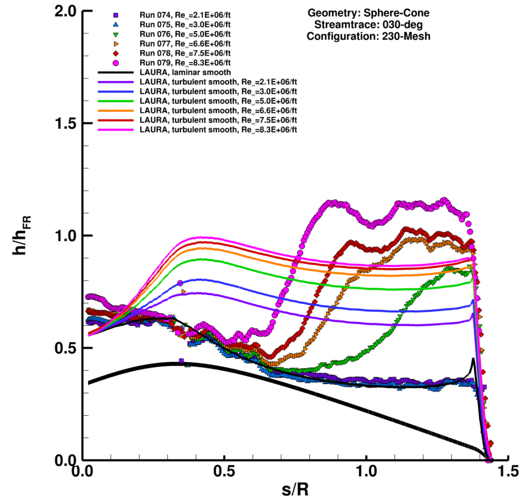

b) 30-deg streamline

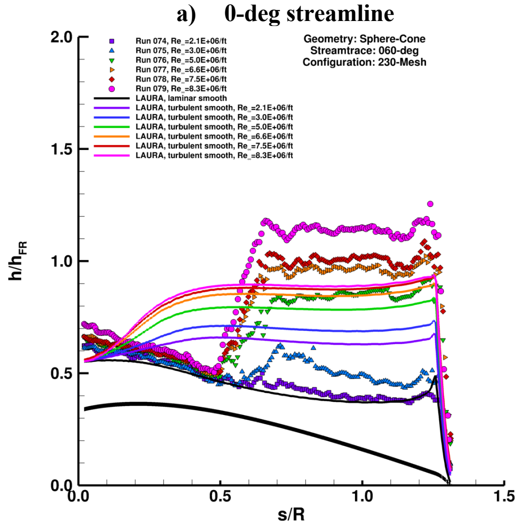

c) 60-deg streamline

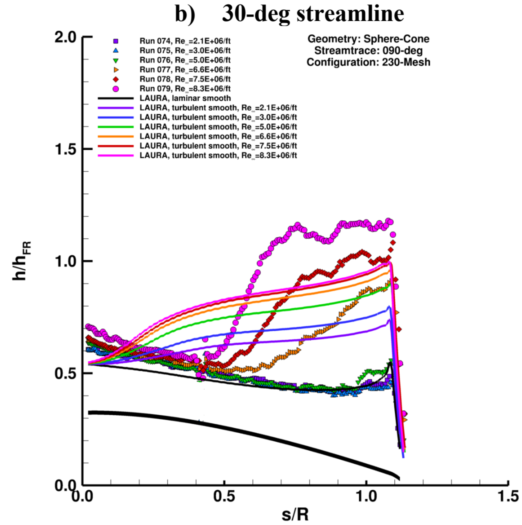

d) 90-deg streamline

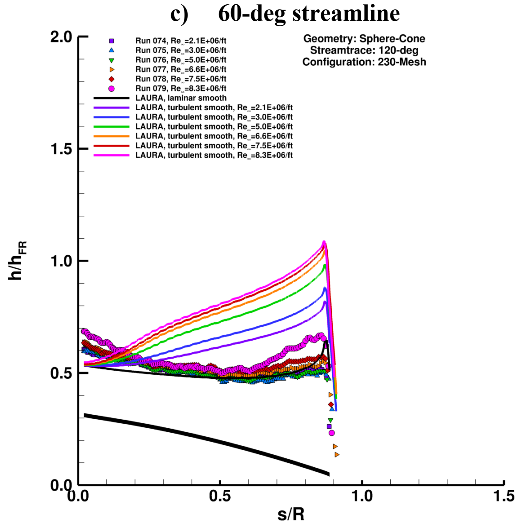

e) 120-deg streamline

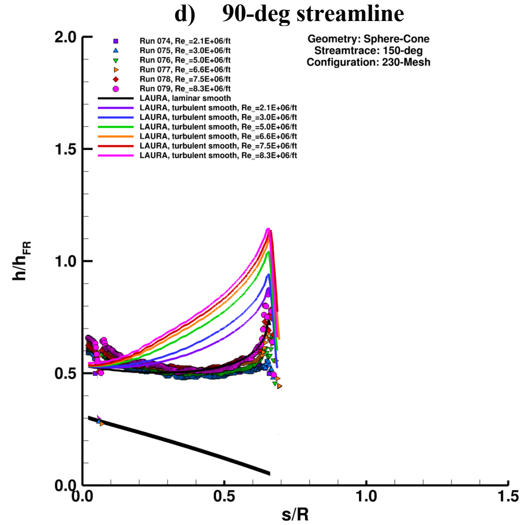

f) 150-deg streamline

Figure 38. Reynolds Number effects, sphere-cone geometry, 230-mesh model plots.

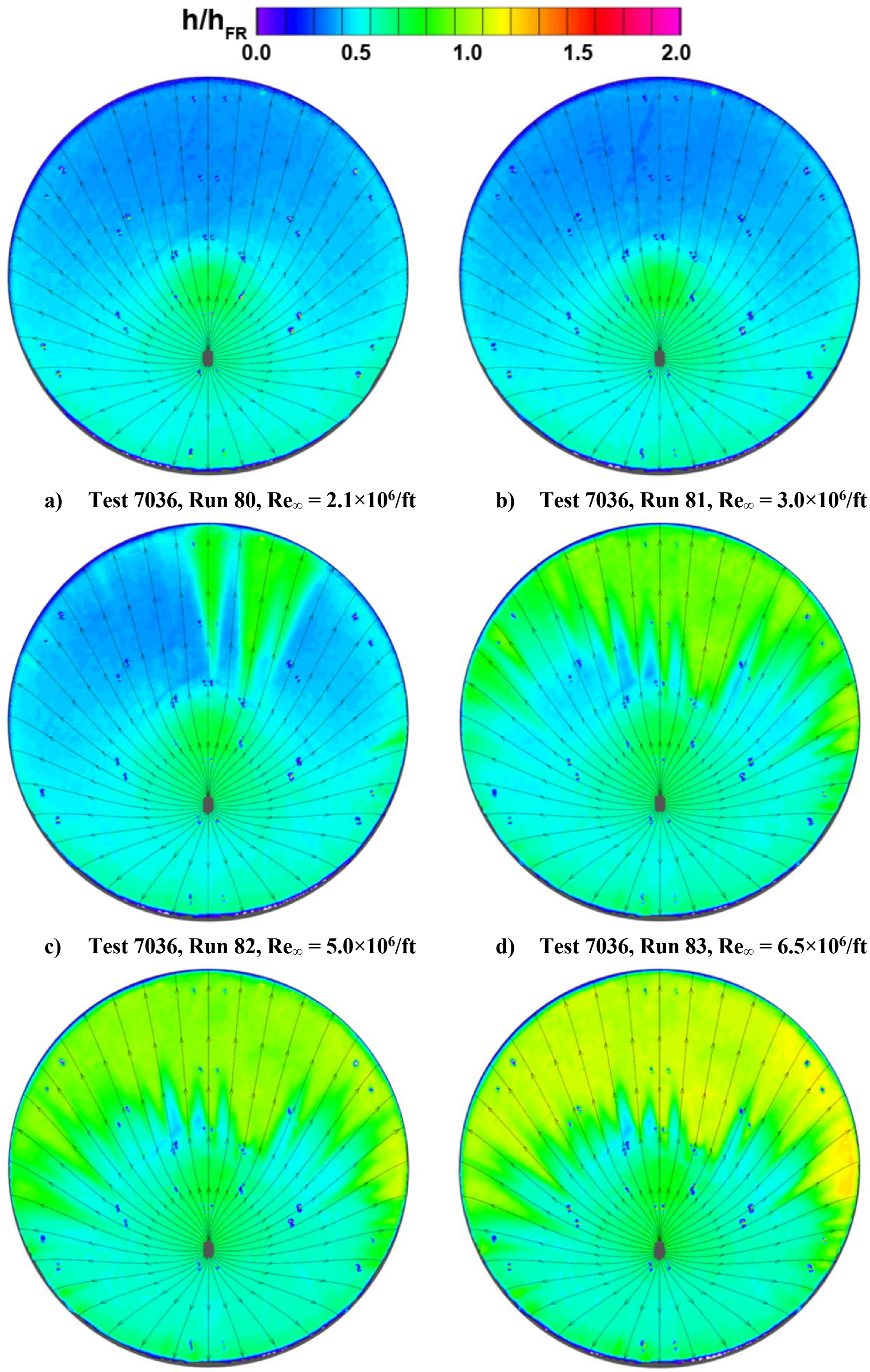

a) Test 7036, Run 80, $Re_\infty = 2.1\times10^6$/ft b) Test 7036, Run 81, $Re_\infty = 3.0\times10^6$/ft

c) Test 7036, Run 82, $Re_\infty = 5.0\times10^6$/ft d) Test 7036, Run 83, $Re_\infty = 6.5\times10^6$/ft

e) Test 7036, Run 84, $Re_\infty = 7.2\times10^6$/ft f) Test 7036, Run 85, $Re_\infty = 8.1\times10^6$/ft

Figure 39. Reynolds Number effects, sphere-cone geometry, 140-mesh model images.

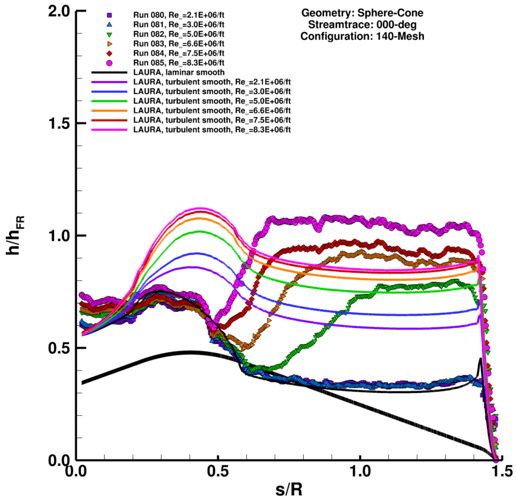

a) 0-deg streamline

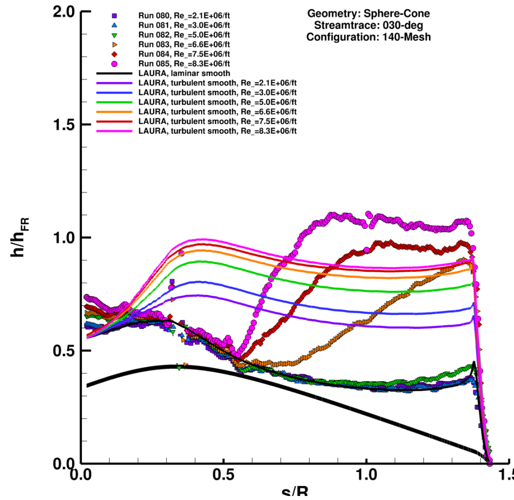

b) 30-deg streamline

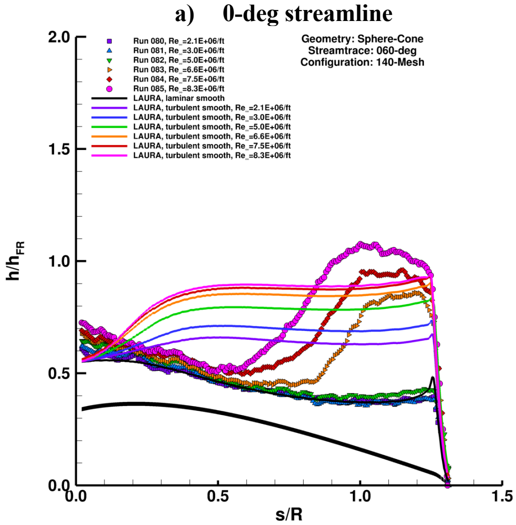

c) 60-deg streamline

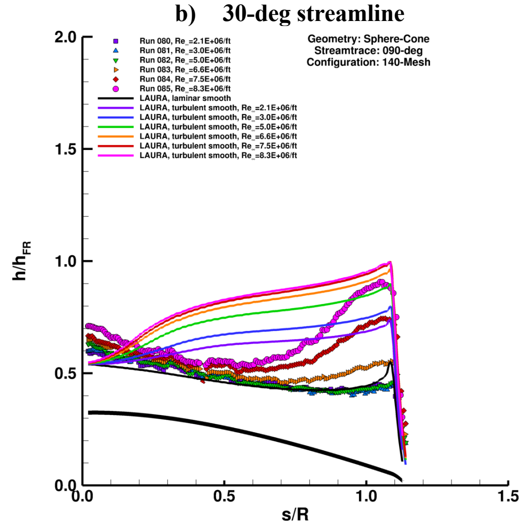

d) 90-deg streamline

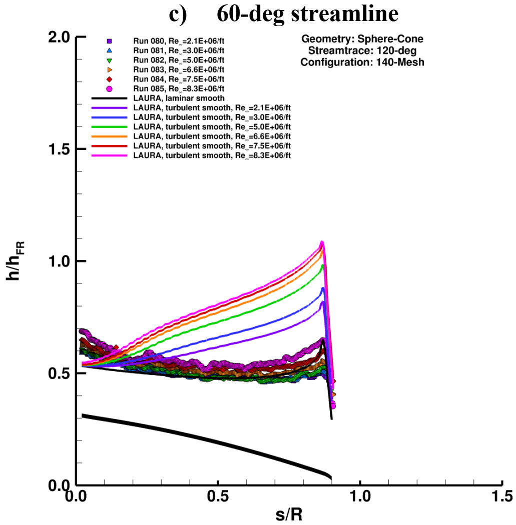

e) 120-deg streamline

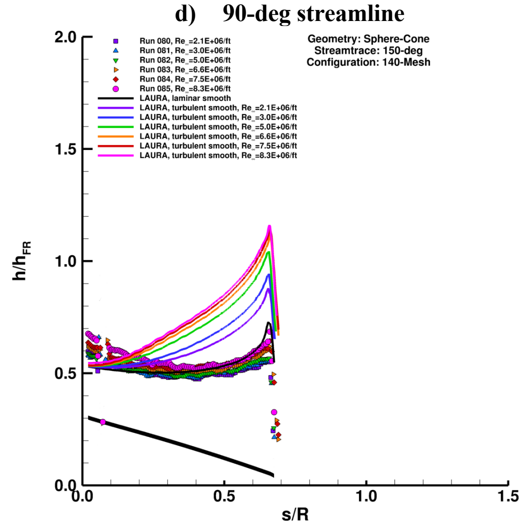

f) 150-deg streamline

Figure 40. Reynolds Number effects, sphere-cone geometry, 140-mesh model plots.

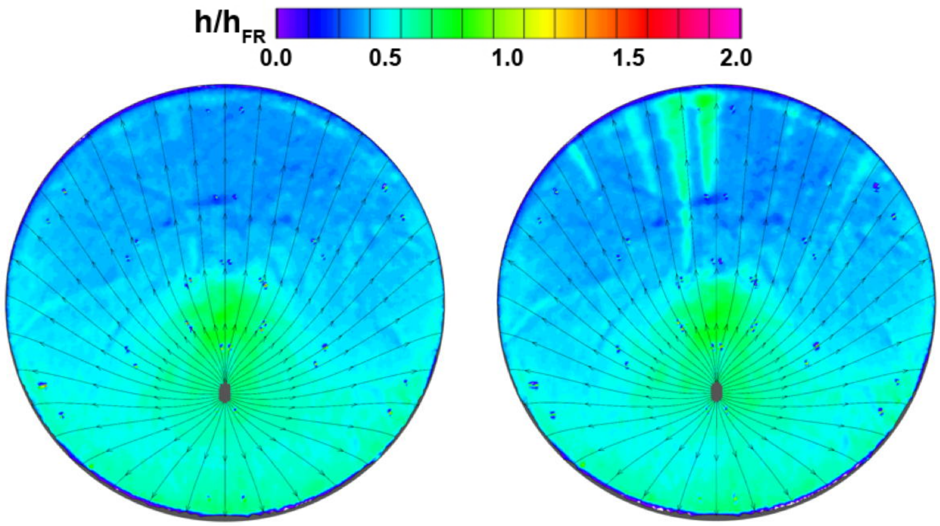

a) Test 7036, Run 87, $Re_\infty = 2.1\times10^6$/ft **b) Test 7036, Run 88, $Re_\infty = 3.0\times10^6$/ft**

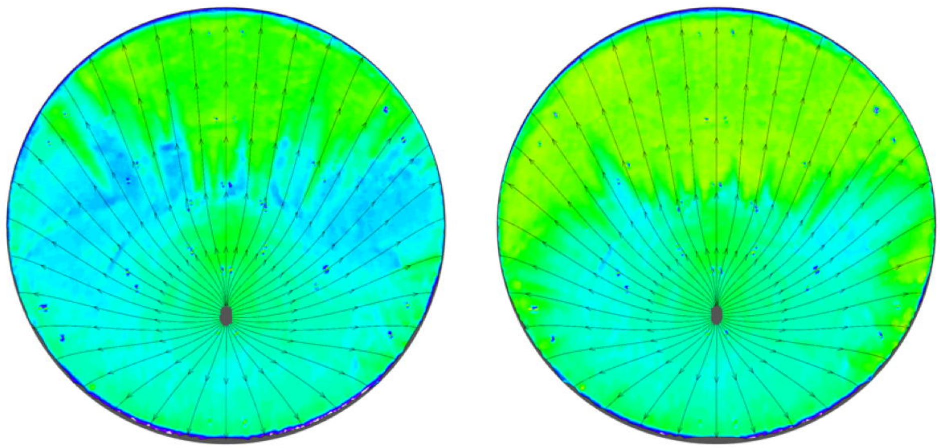

c) Test 7036, Run 89, $Re_\infty = 5.0\times10^6$/ft **d) Test 7036, Run 90, $Re_\infty = 6.5\times10^6$/ft**

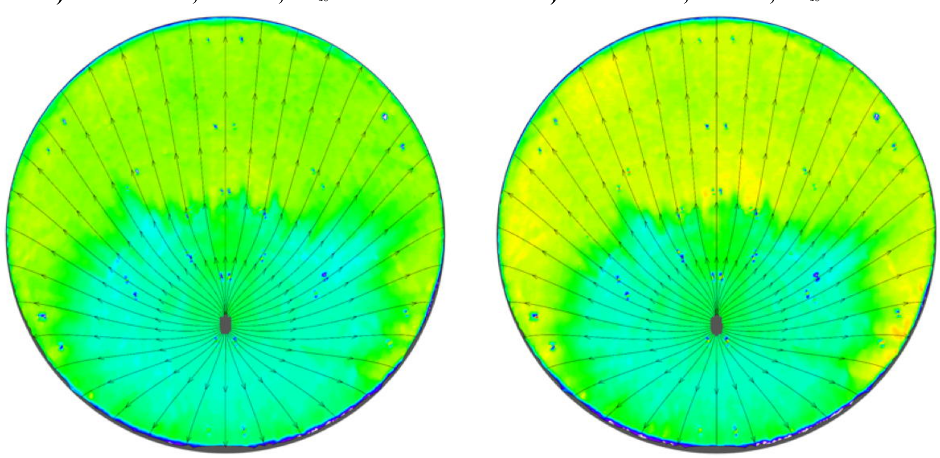

e) Test 7036, Run 91, $Re_\infty = 7.2\times10^6$/ft **f) Test 7036, Run 92, $Re_\infty = 8.1\times10^6$/ft**

Figure 41. Reynolds Number effects, sphere-cone geometry, 80-mesh model images.

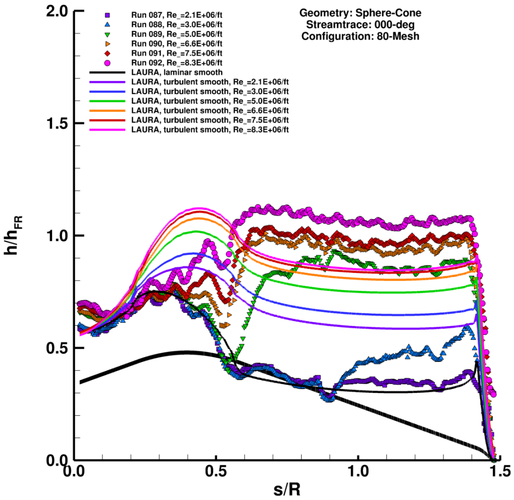

a) 0-deg streamline

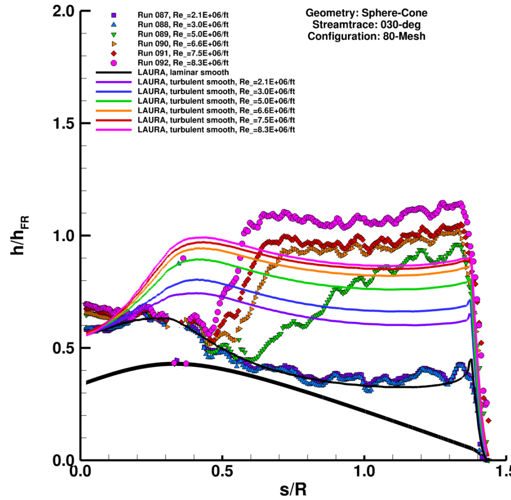

b) 30-deg streamline

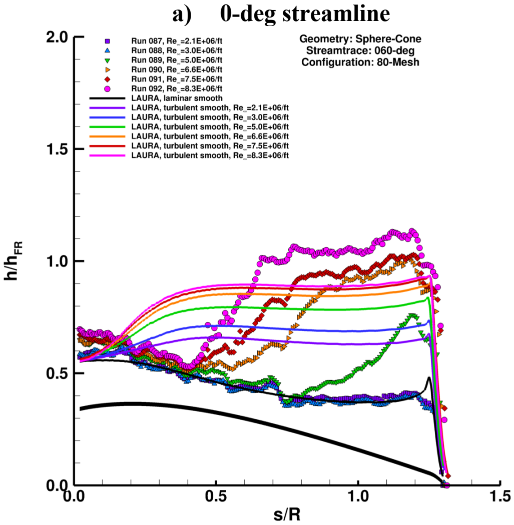

c) 60-deg streamline

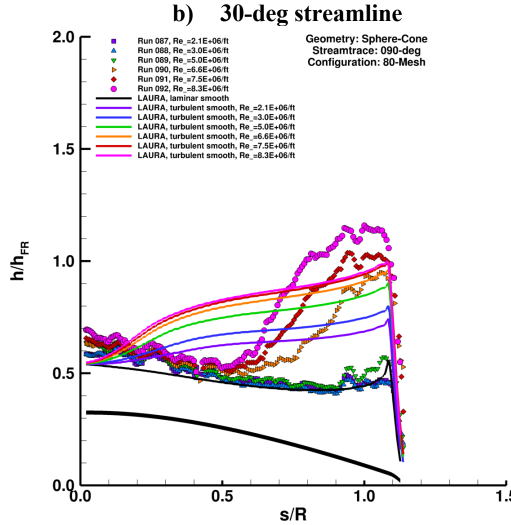

d) 90-deg streamline

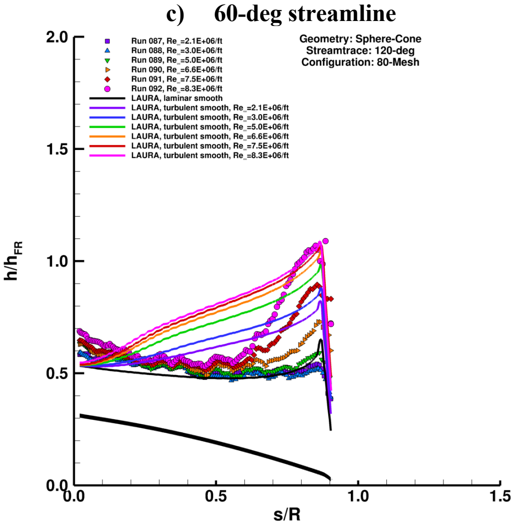

e) 120-deg streamline

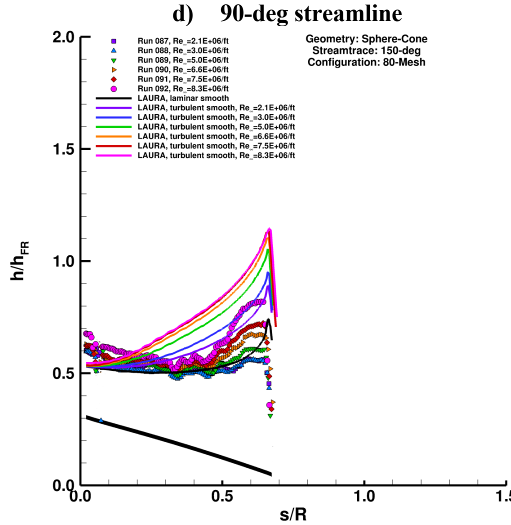

f) 150-deg streamline

Figure 42. Reynolds Number effects, sphere-cone geometry, 80-mesh model plots.

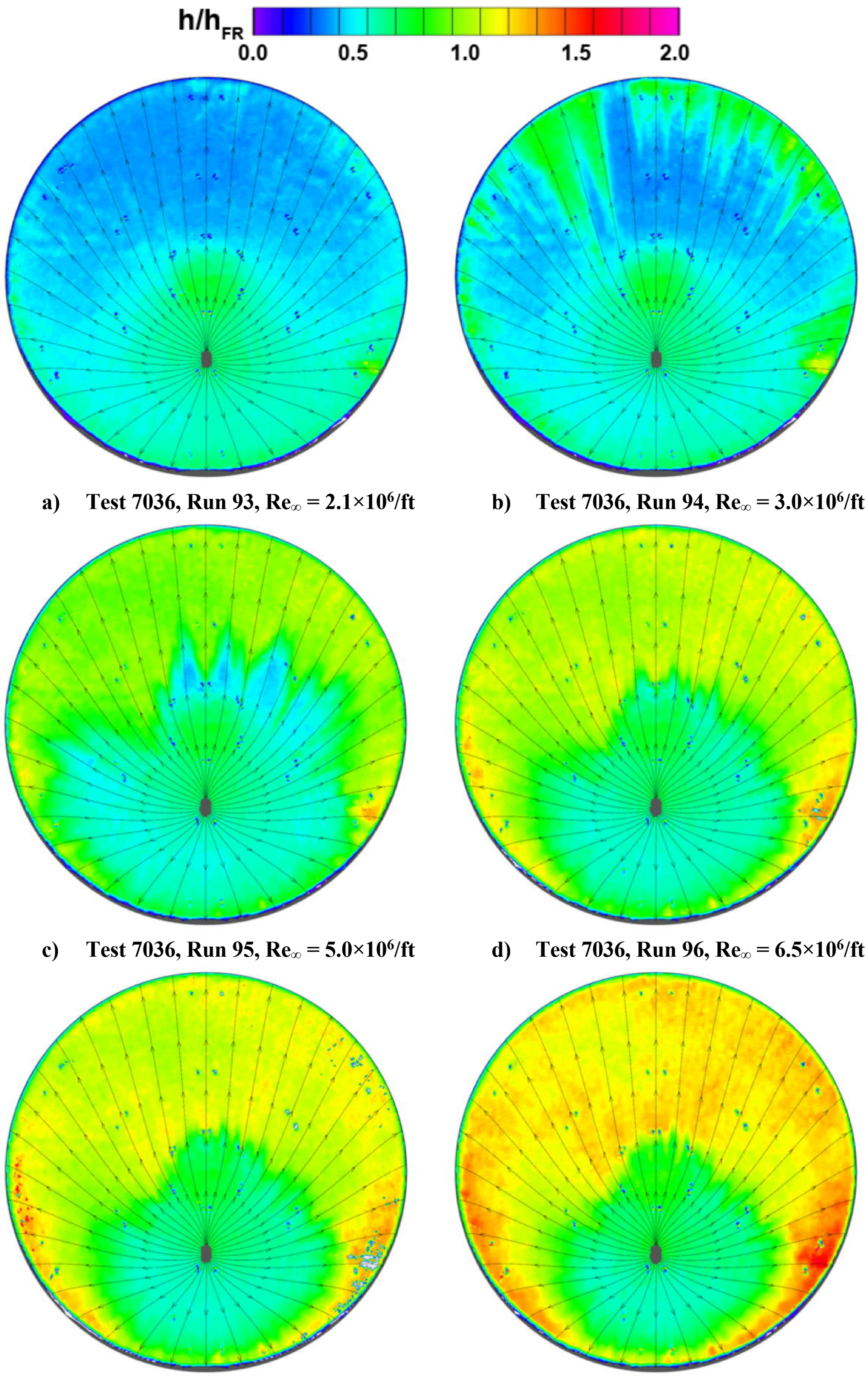

a) Test 7036, Run 93, $Re_\infty = 2.1\times10^6$/ft
b) Test 7036, Run 94, $Re_\infty = 3.0\times10^6$/ft
c) Test 7036, Run 95, $Re_\infty = 5.0\times10^6$/ft
d) Test 7036, Run 96, $Re_\infty = 6.5\times10^6$/ft
e) Test 7036, Run 97, $Re_\infty = 7.2\times10^6$/ft
f) Test 7036, Run 98, $Re_\infty = 8.1\times10^6$/ft

Figure 43. Reynolds Number effects, sphere-cone geometry, 40-mesh model images.

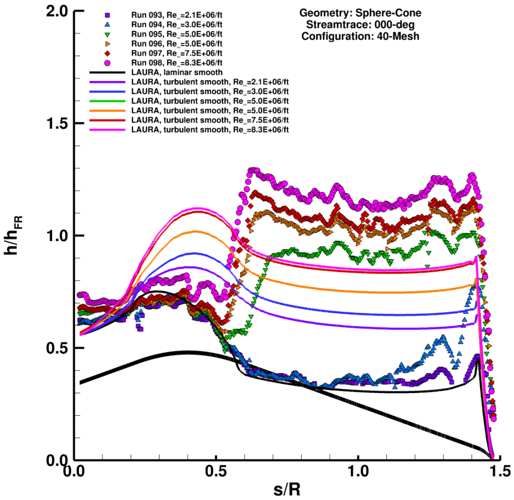

a) 0-deg streamline

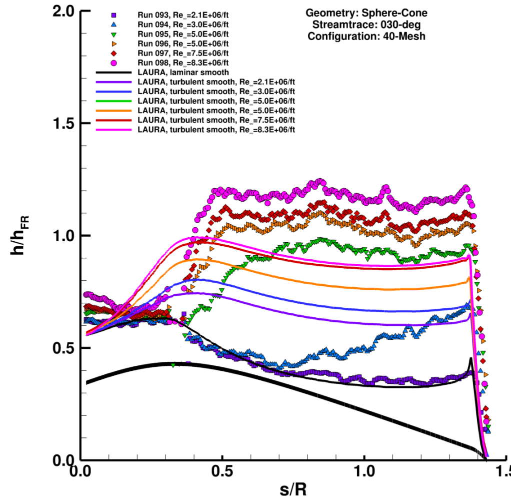

b) 30-deg streamline

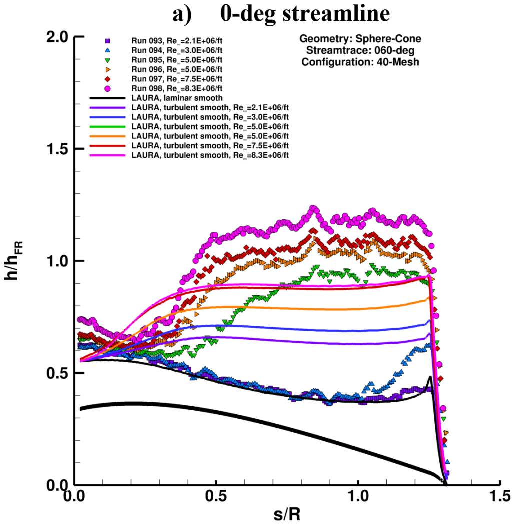

c) 60-deg streamline

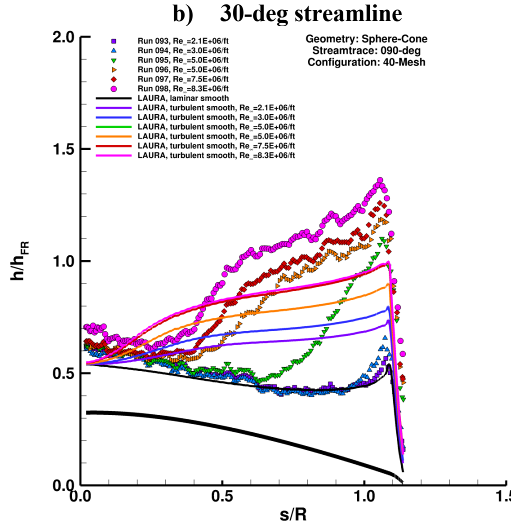

d) 90-deg streamline

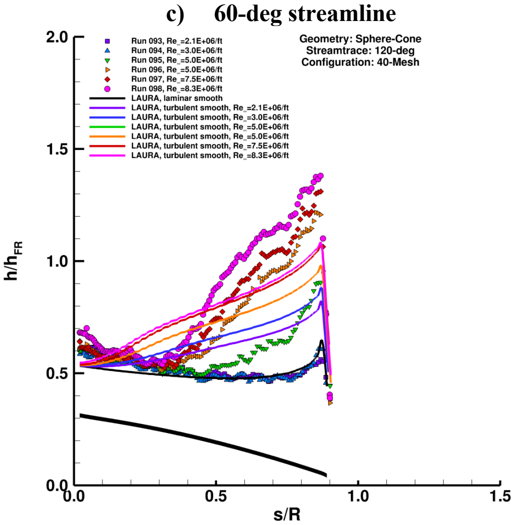

e) 120-deg streamline

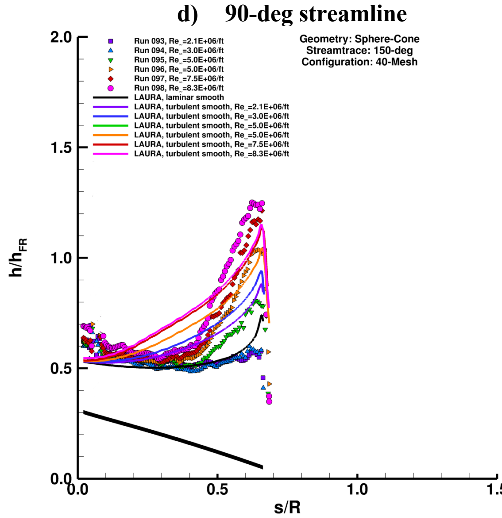

f) 150-deg streamline

Figure 44. Reynolds Number effects, sphere-cone geometry, 40-mesh model plots.

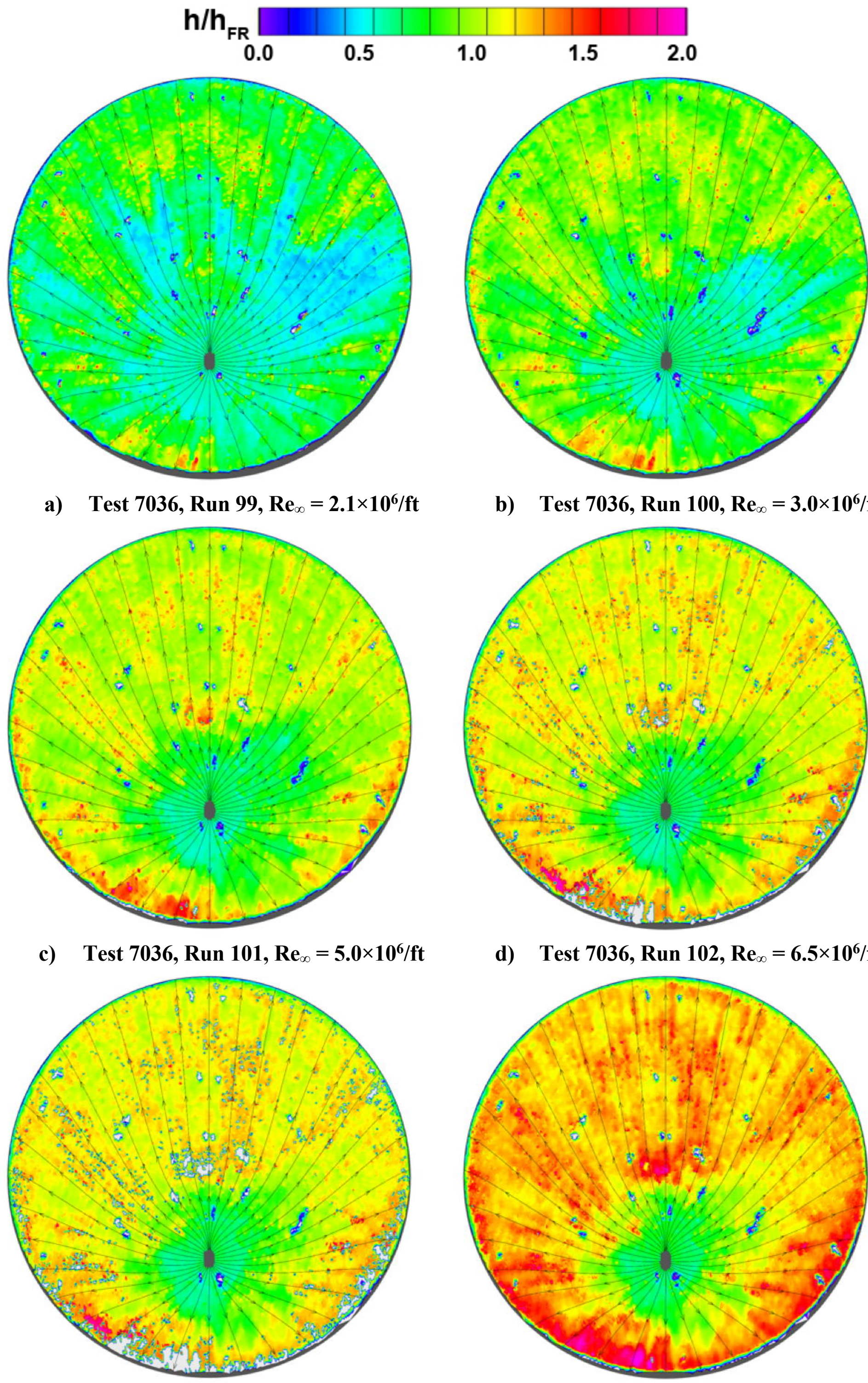

a) Test 7036, Run 99, $Re_\infty = 2.1\times10^6$/ft **b) Test 7036, Run 100, $Re_\infty = 3.0\times10^6$/ft**

c) Test 7036, Run 101, $Re_\infty = 5.0\times10^6$/ft **d) Test 7036, Run 102, $Re_\infty = 6.5\times10^6$/ft**

e) Test 7036, Run 103, $Re_\infty = 7.2\times10^6$/ft **f) Test 7036, Run 104, $Re_\infty = 8.1\times10^6$/ft**

Figure 45. Reynolds Number effects, sphere-cone geometry, 20-mesh model images.

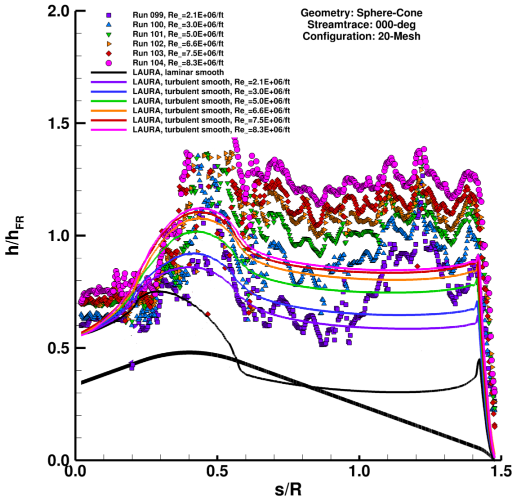

a) 0-deg streamline

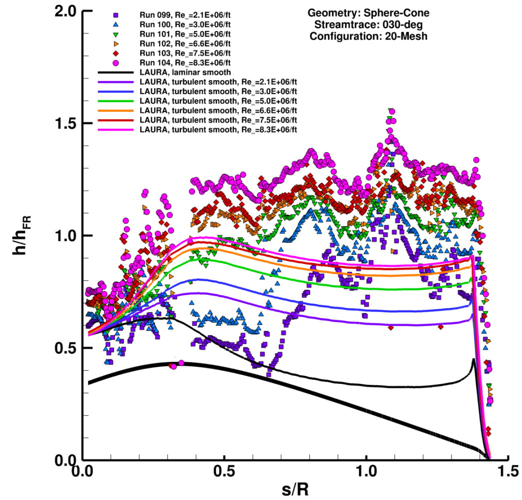

b) 30-deg streamline

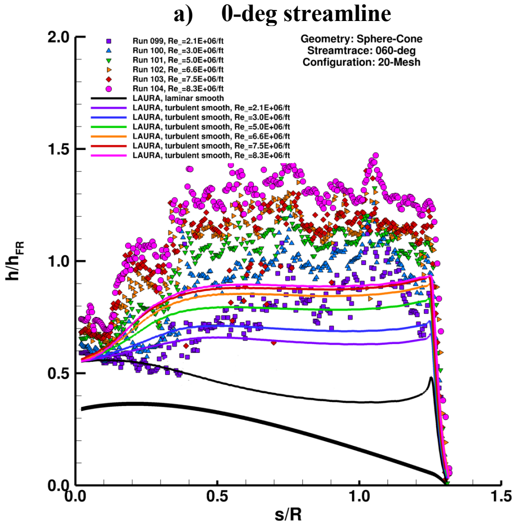

c) 60-deg streamline

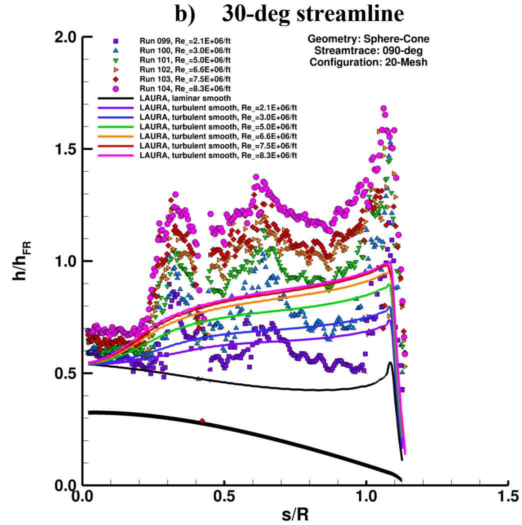

d) 90-deg streamline

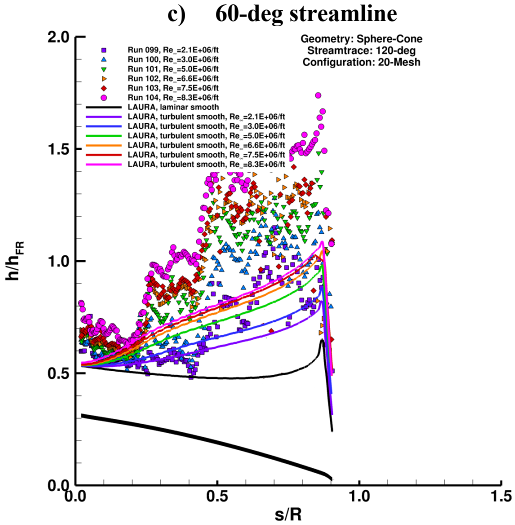

e) 120-deg streamline

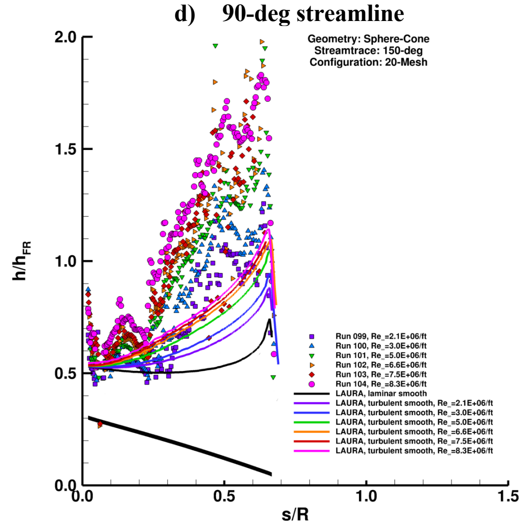

f) 150-deg streamline

Figure 46. Reynolds Number effects, sphere-cone geometry, 20-mesh model plots.

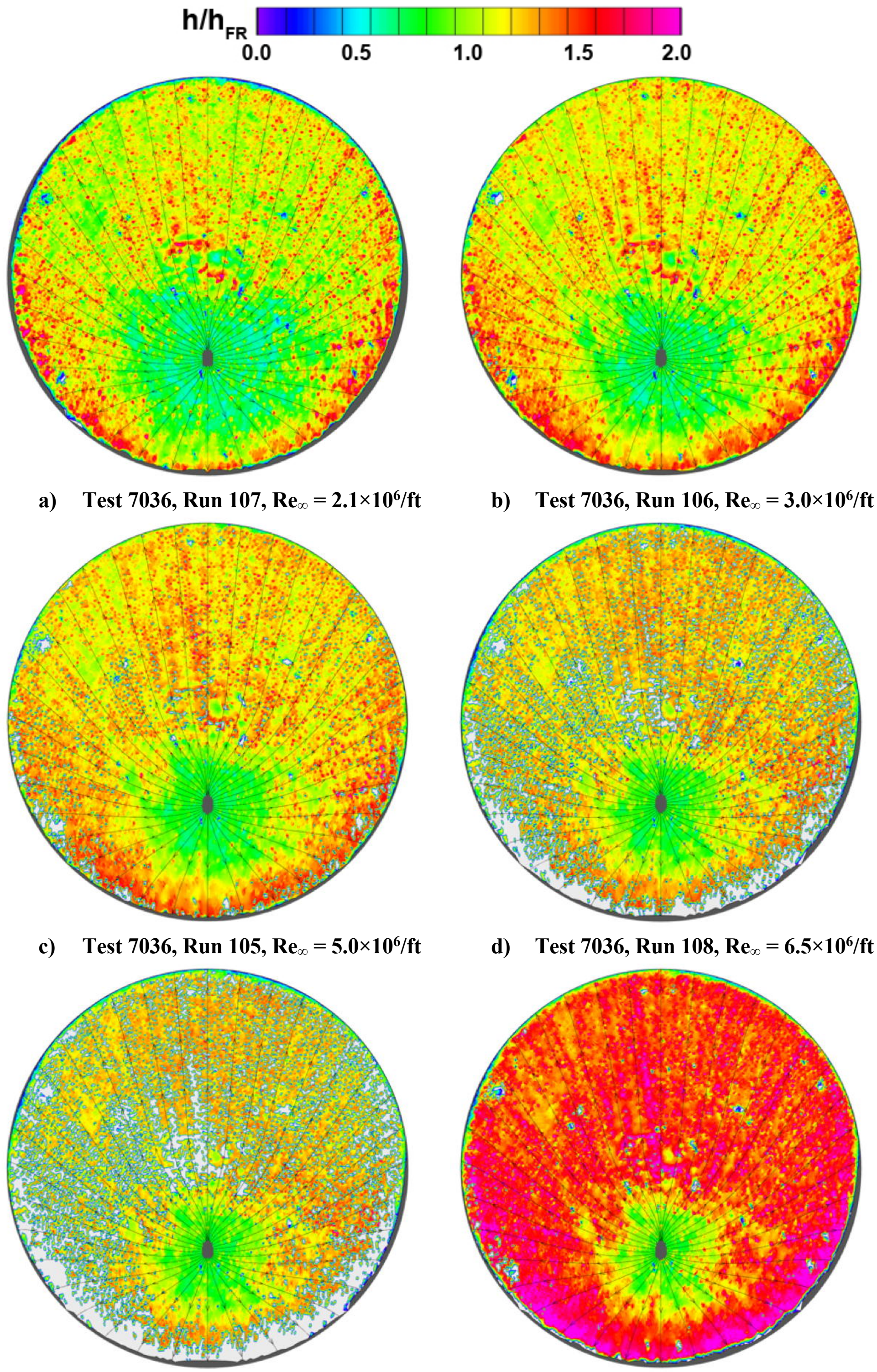

a) Test 7036, Run 107, $Re_\infty = 2.1\times10^6$/ft b) Test 7036, Run 106, $Re_\infty = 3.0\times10^6$/ft

c) Test 7036, Run 105, $Re_\infty = 5.0\times10^6$/ft d) Test 7036, Run 108, $Re_\infty = 6.5\times10^6$/ft

e) Test 7036, Run 109, $Re_\infty = 7.2\times10^6$/ft f) Test 7036, Run 110, $Re_\infty = 8.1\times10^6$/ft

Figure 47. Reynolds Number effects, sphere-cone geometry, 10-mesh model images.

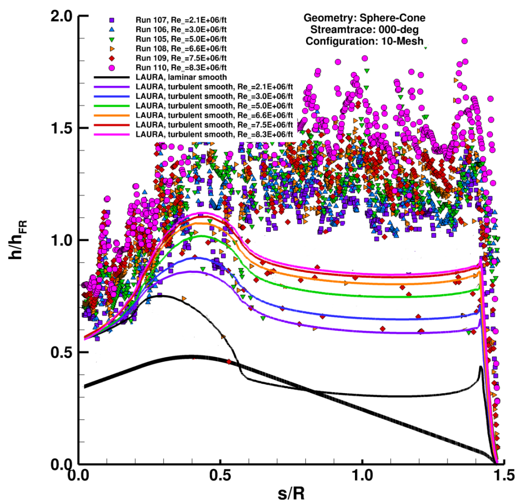

a) 0-deg streamline

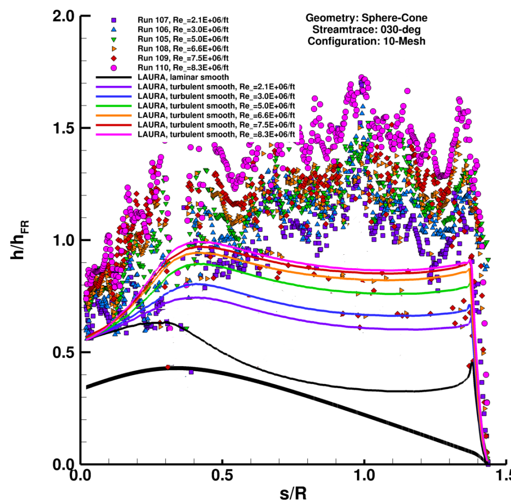

b) 30-deg streamline

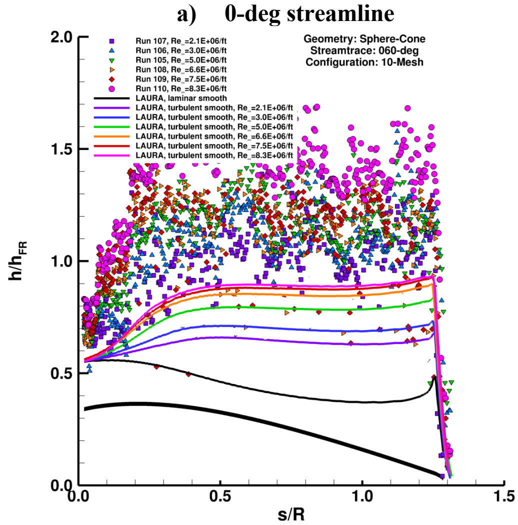

c) 60-deg streamline

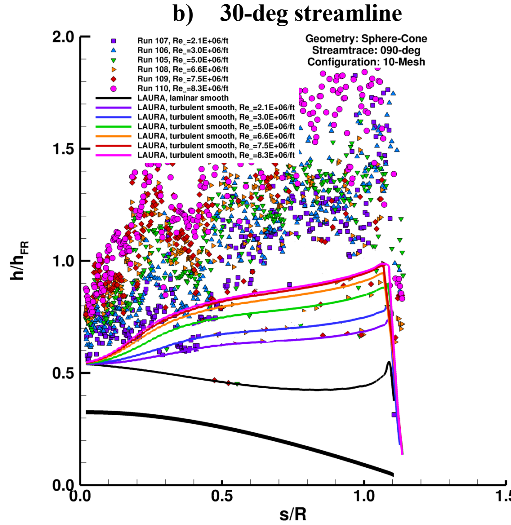

d) 90-deg streamline

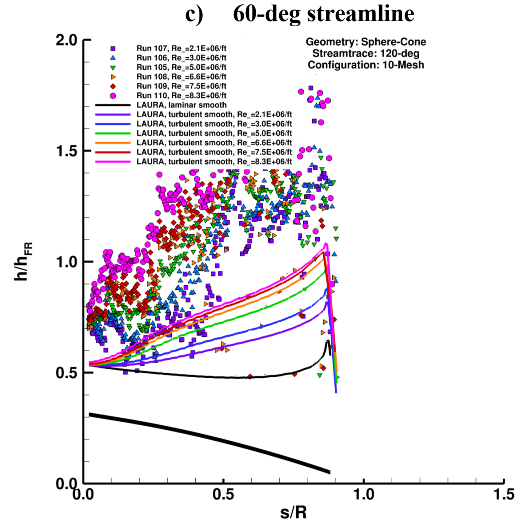

e) 120-deg streamline

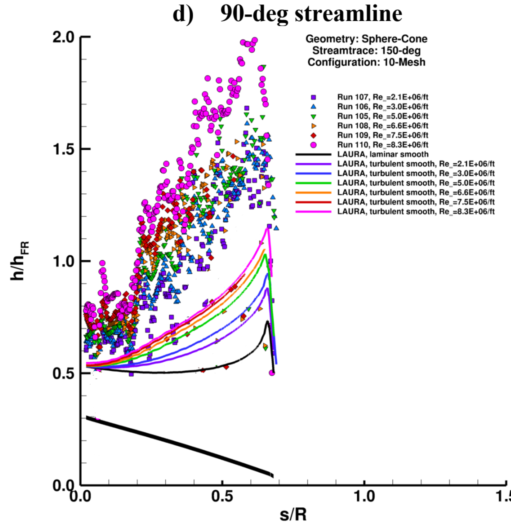

f) 150-deg streamline

Figure 48. Reynolds Number effects, sphere-cone geometry, 10-mesh model plots.

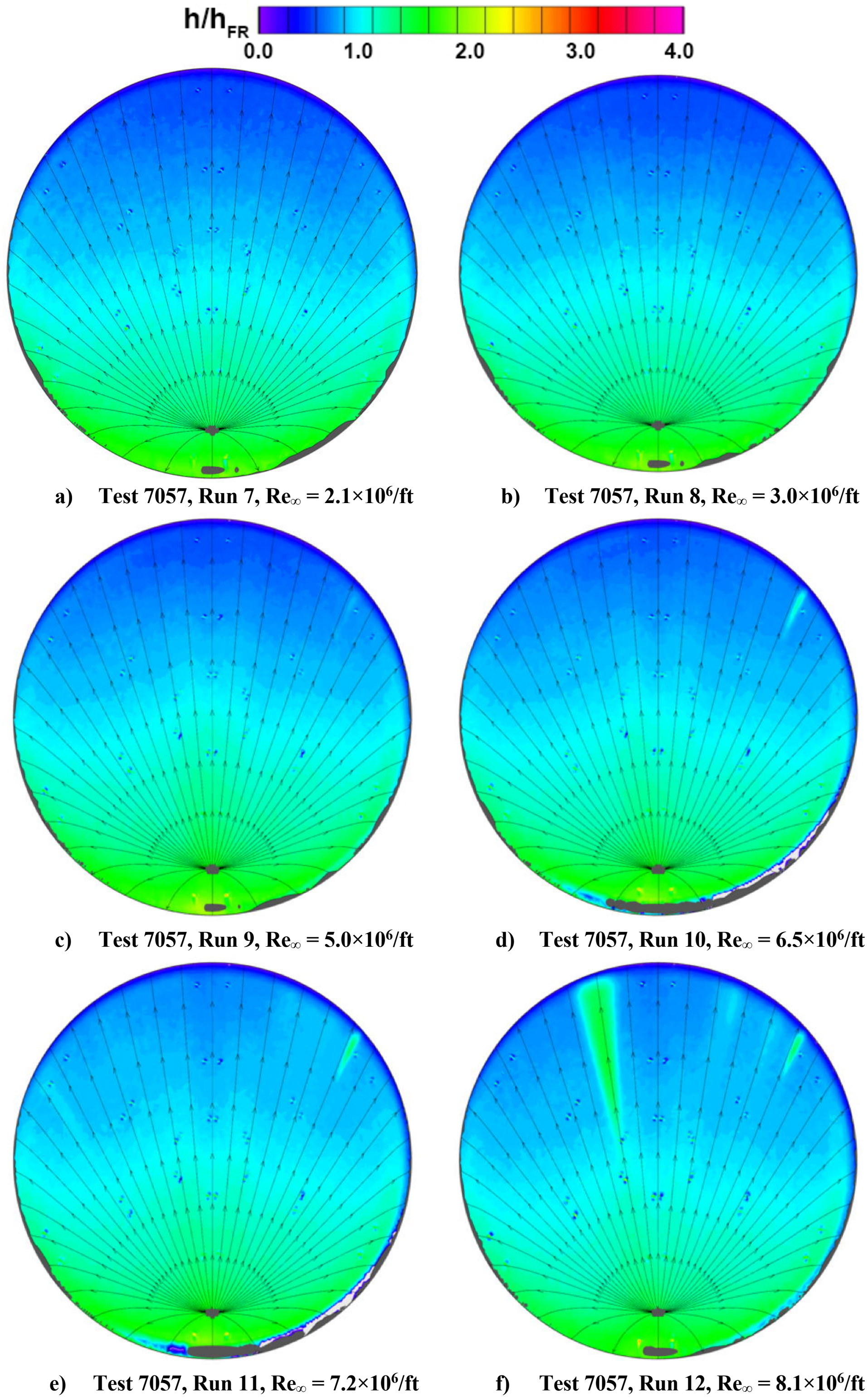

a) Test 7057, Run 7, $Re_\infty = 2.1\times10^6$/ft

b) Test 7057, Run 8, $Re_\infty = 3.0\times10^6$/ft

c) Test 7057, Run 9, $Re_\infty = 5.0\times10^6$/ft

d) Test 7057, Run 10, $Re_\infty = 6.5\times10^6$/ft

e) Test 7057, Run 11, $Re_\infty = 7.2\times10^6$/ft

f) Test 7057, Run 12, $Re_\infty = 8.1\times10^6$/ft

Figure 49. Reynolds Number effects, spherical-cap geometry, smooth model images.

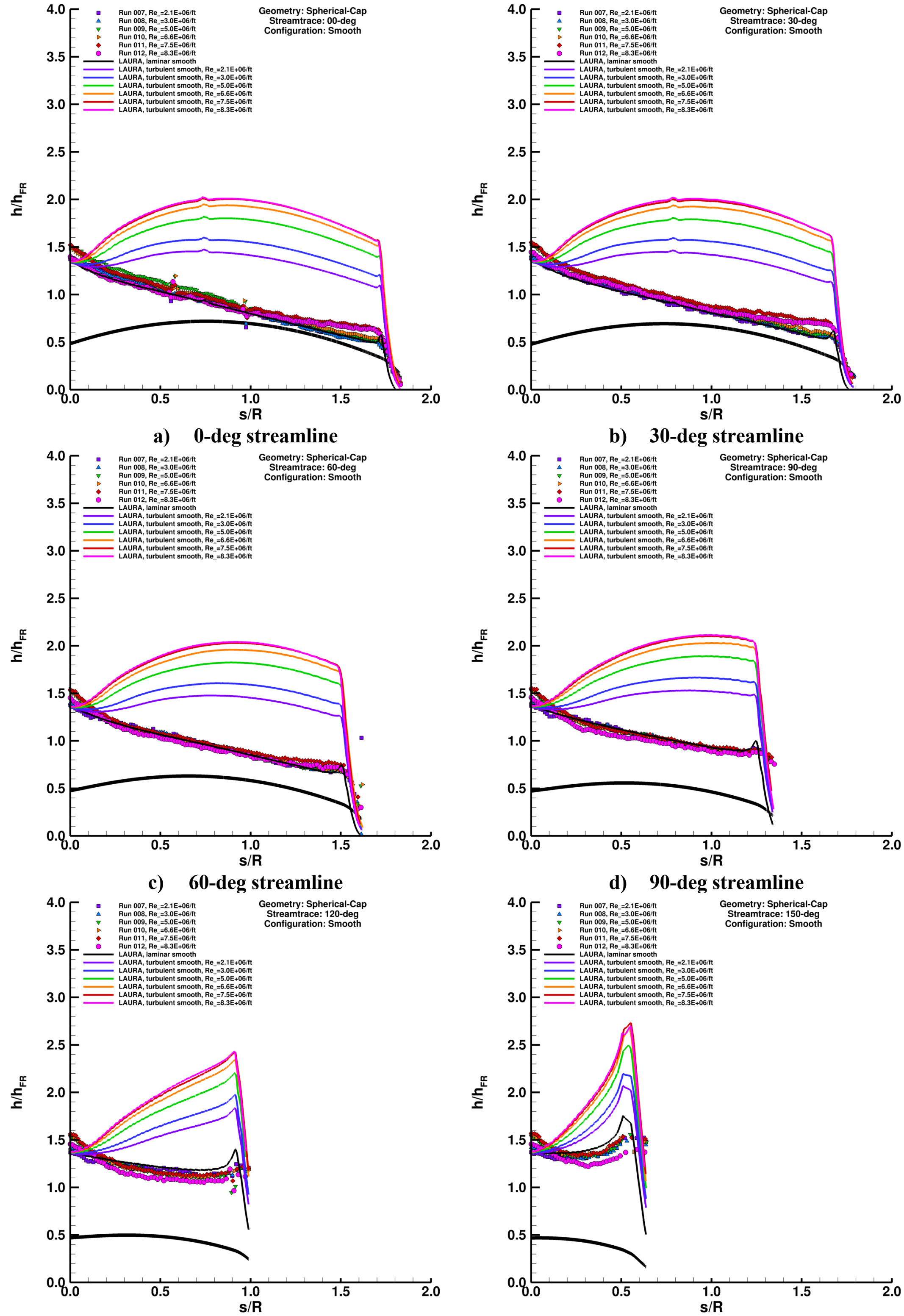

a) 0-deg streamline

b) 30-deg streamline

c) 60-deg streamline

d) 90-deg streamline

e) 120-deg streamline

f) 150-deg streamline

Figure 50. Reynolds number effects, spherical-cap geometry, smooth model plots.

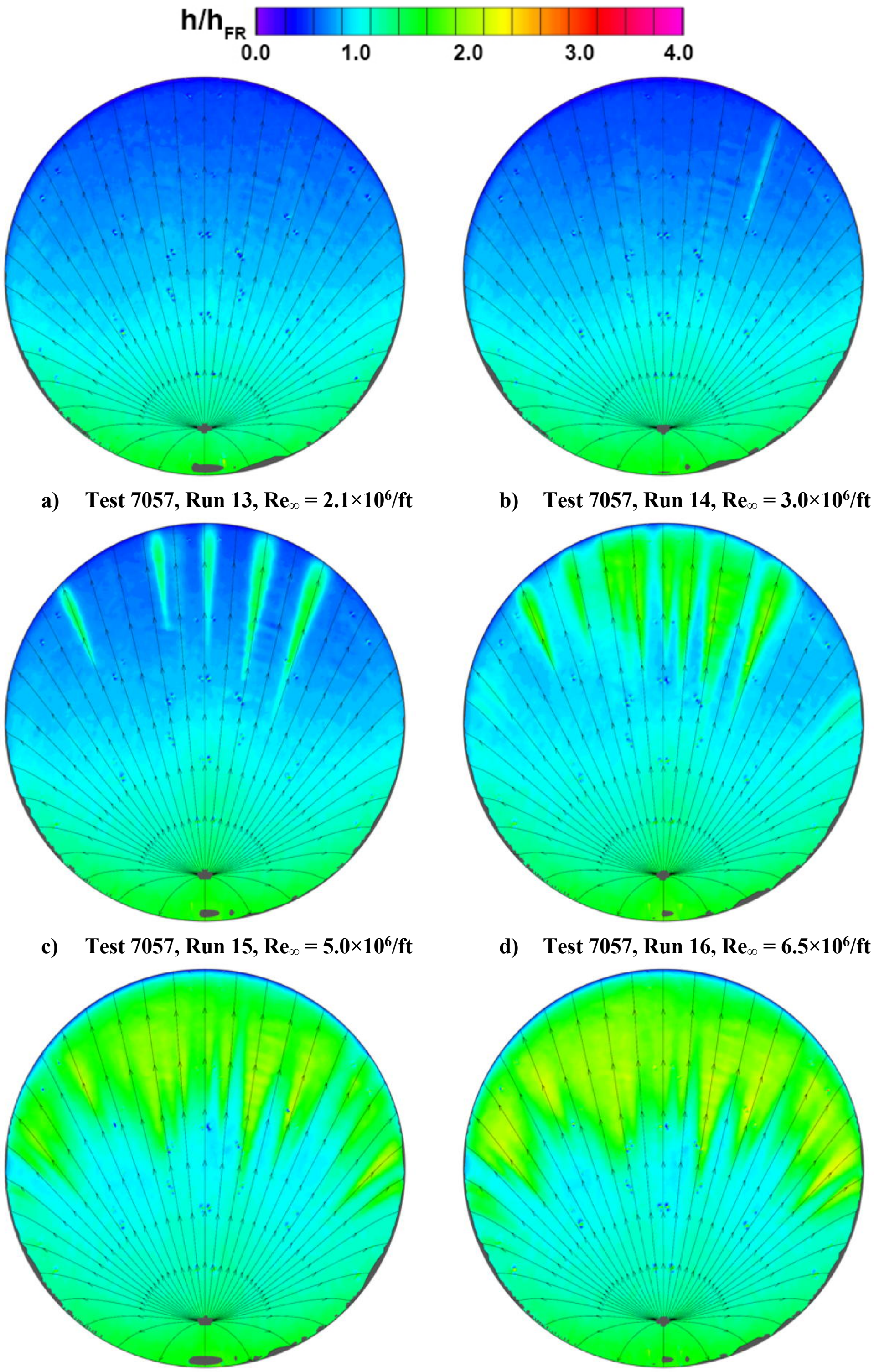

a) Test 7057, Run 13, $Re_\infty = 2.1\times10^6$/ft

b) Test 7057, Run 14, $Re_\infty = 3.0\times10^6$/ft

c) Test 7057, Run 15, $Re_\infty = 5.0\times10^6$/ft

d) Test 7057, Run 16, $Re_\infty = 6.5\times10^6$/ft

e) Test 7057, Run 17, $Re_\infty = 7.2\times10^6$/ft

f) Test 7057, Run 18, $Re_\infty = 8.1\times10^6$/ft

Figure 51. Reynolds Number effects, spherical-cap geometry, 230-mesh model images.

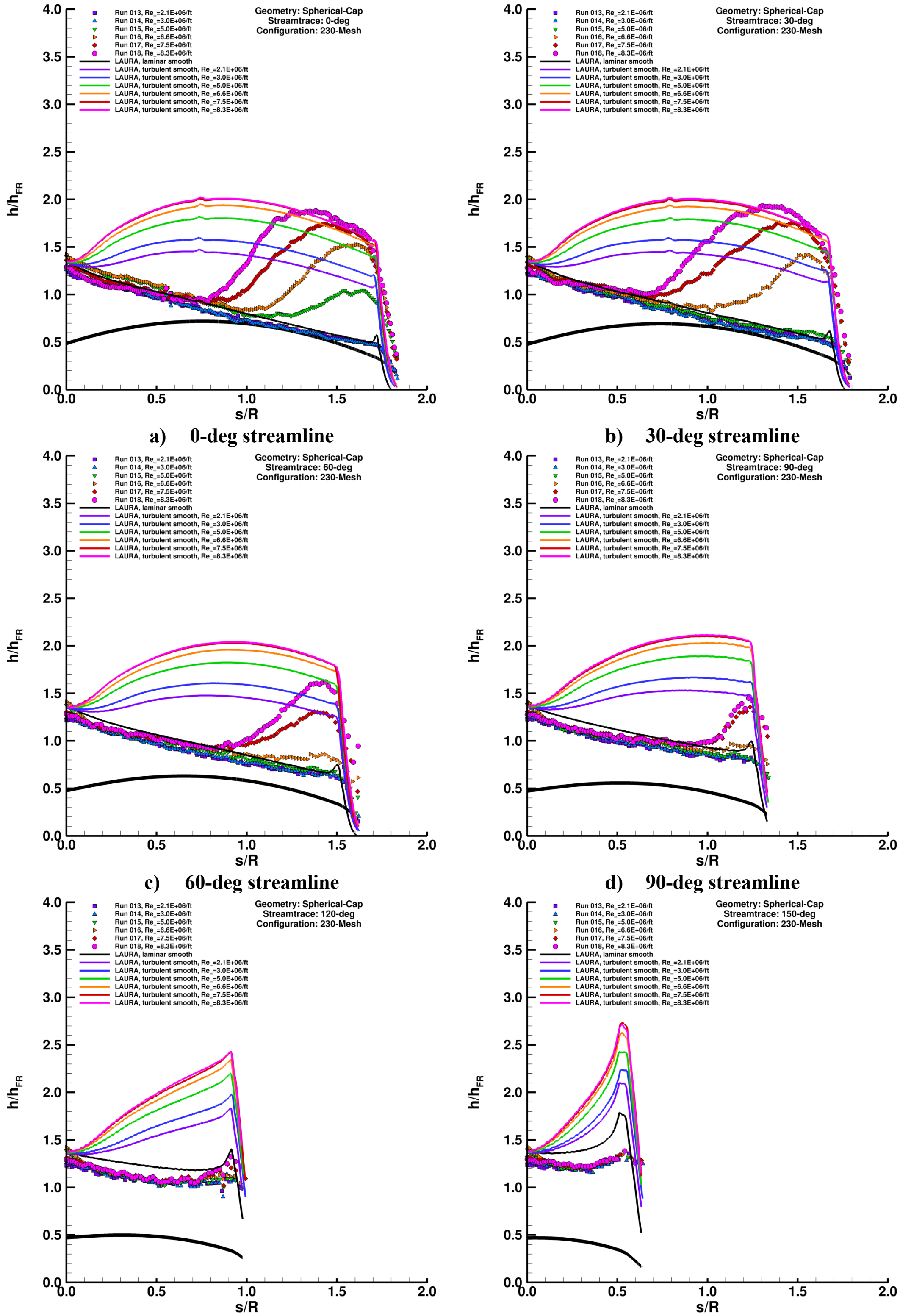

a) 0-deg streamline

b) 30-deg streamline

c) 60-deg streamline

d) 90-deg streamline

e) 120-deg streamline

f) 150-deg streamline

Figure 52. Reynolds Number effects, spherical-cap geometry, 230-mesh model plots.

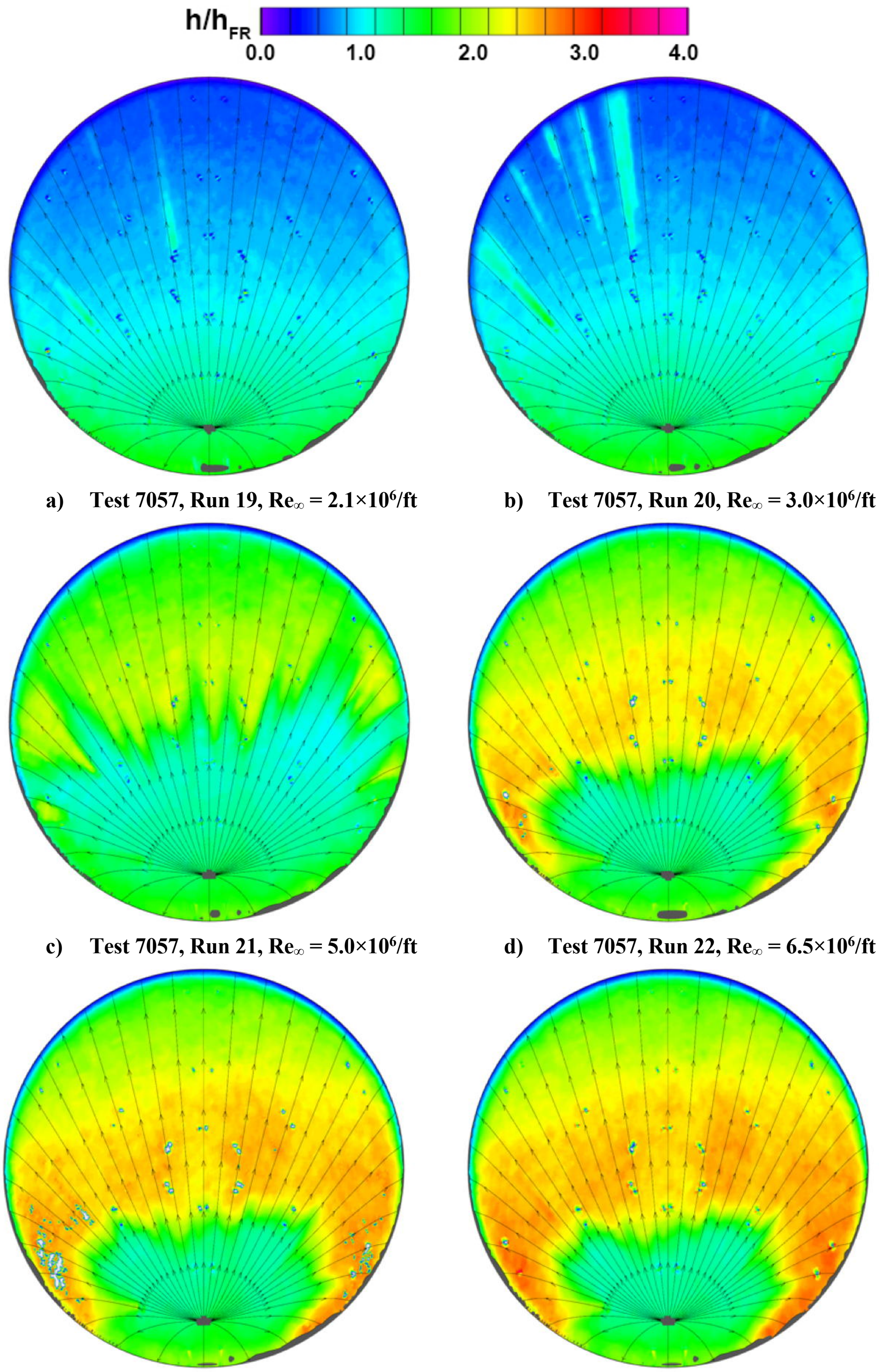

a) Test 7057, Run 19, Re∞ = 2.1×10⁶/ft **b) Test 7057, Run 20, Re∞ = 3.0×10⁶/ft**

c) Test 7057, Run 21, Re∞ = 5.0×10⁶/ft **d) Test 7057, Run 22, Re∞ = 6.5×10⁶/ft**

e) Test 7057, Run 23, Re∞ = 7.2×10⁶/ft **f) Test 7057, Run 24, Re∞ = 8.1×10⁶/ft**

Figure 53. Reynolds Number effects, spherical-cap geometry, 140-mesh model images.

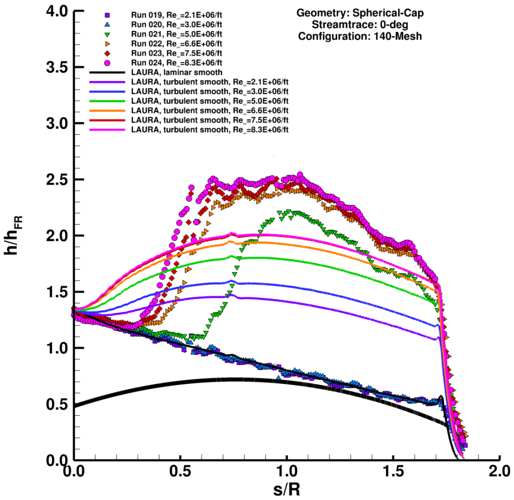

a) 0-deg streamline

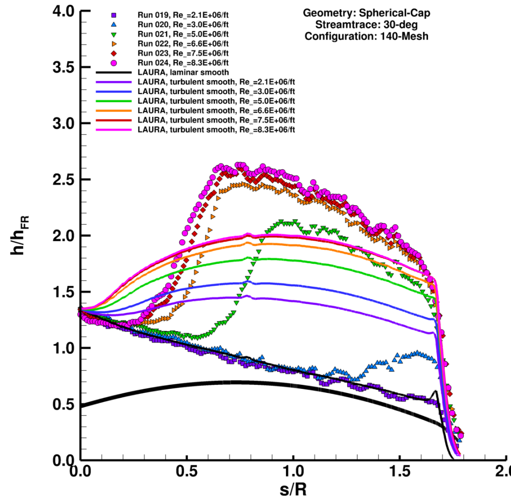

b) 30-deg streamline

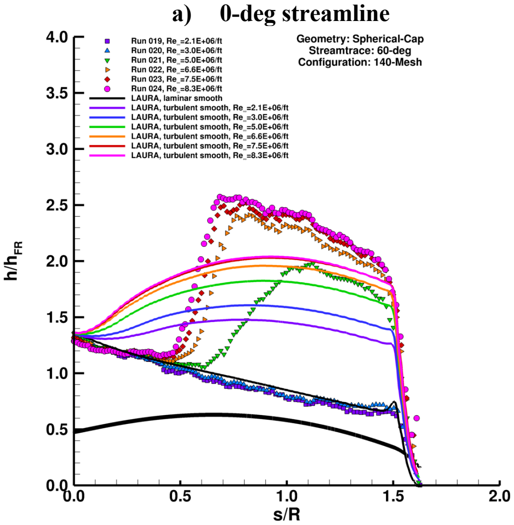

c) 60-deg streamline

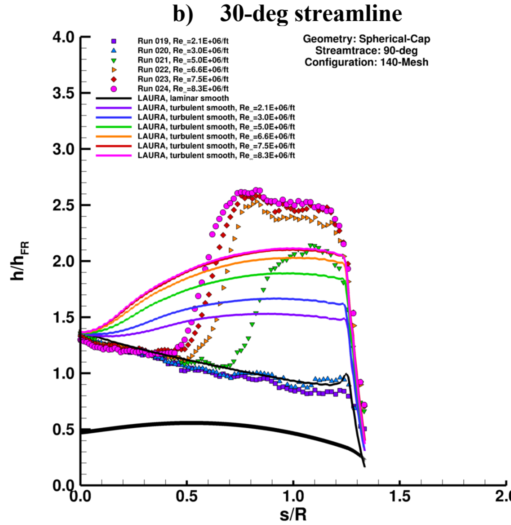

d) 90-deg streamline

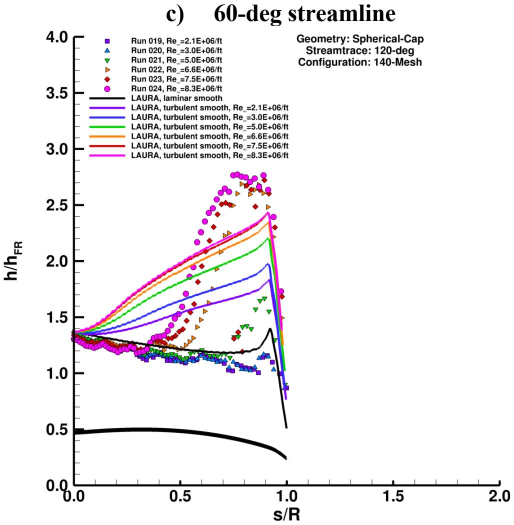

e) 120-deg streamline

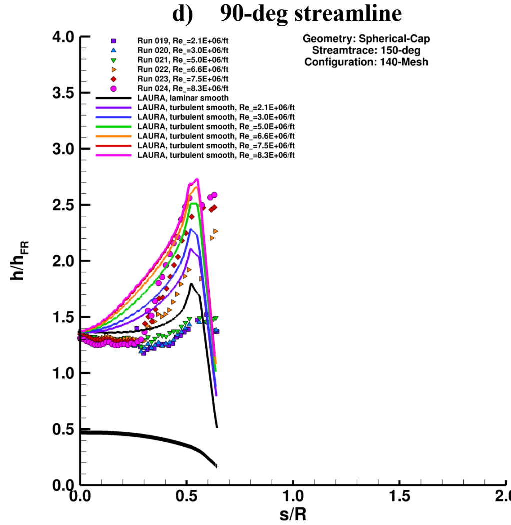

f) 150-deg streamline

Figure 54. Reynolds Number effects, spherical-cap geometry, 140-mesh model plots.

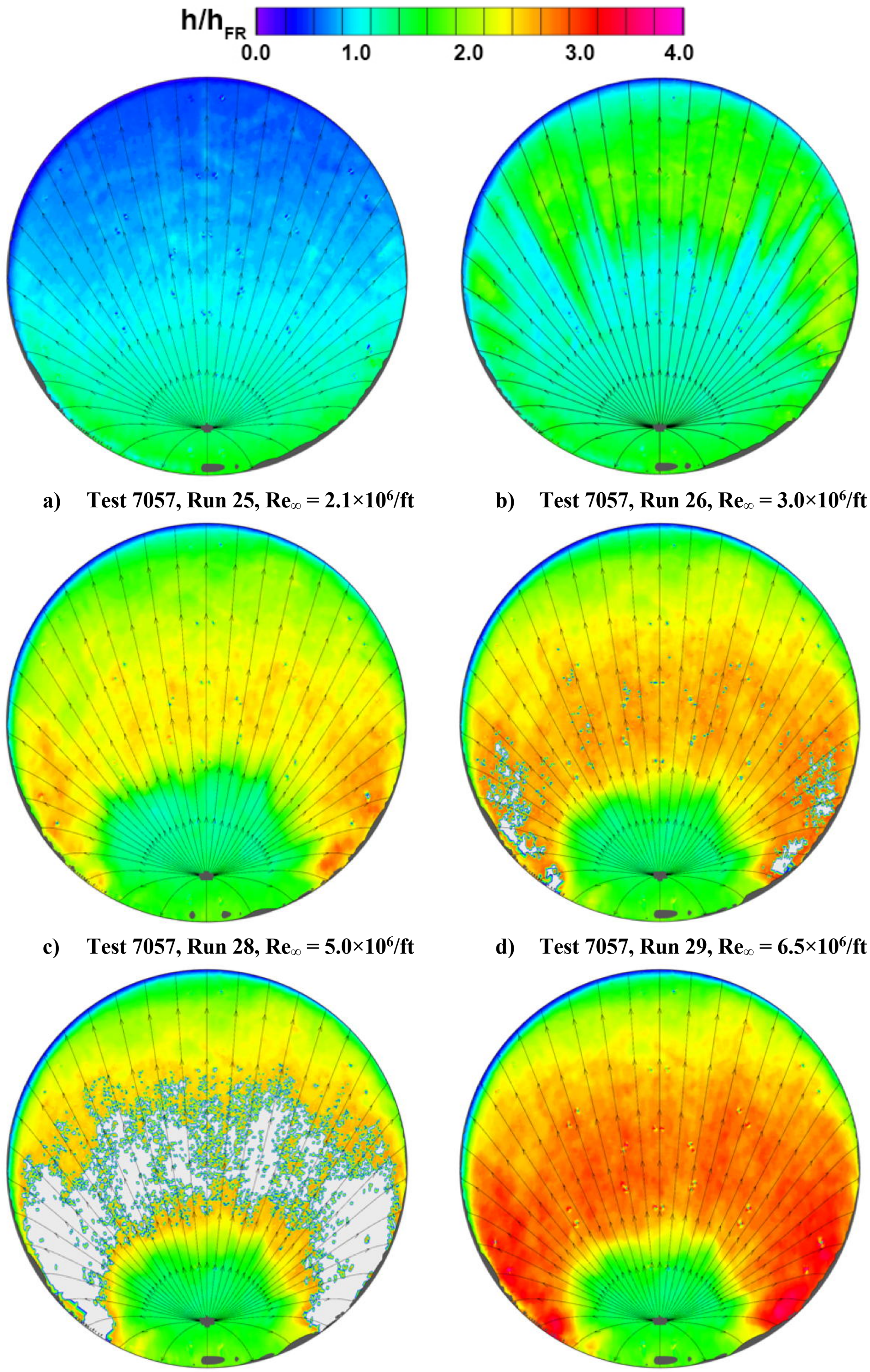

a) Test 7057, Run 25, Re∞ = 2.1×10⁶/ft b) Test 7057, Run 26, Re∞ = 3.0×10⁶/ft

c) Test 7057, Run 28, Re∞ = 5.0×10⁶/ft d) Test 7057, Run 29, Re∞ = 6.5×10⁶/ft

e) Test 7057, Run 30, Re∞ = 7.2×10⁶/ft f) Test 7057, Run 31, Re∞ = 8.1×10⁶/ft

Figure 55. Reynolds Number effects, spherical-cap geometry, 80-mesh model images.

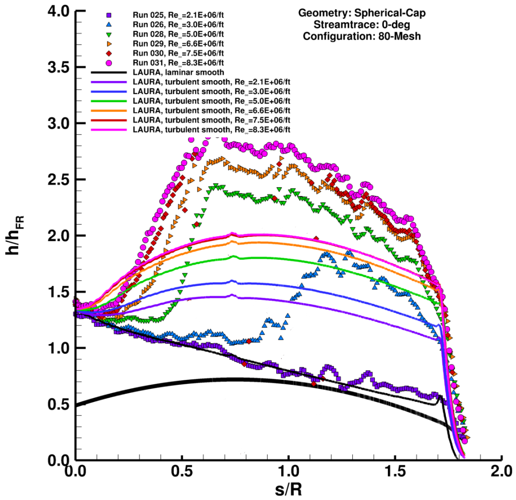

a) 0-deg streamline

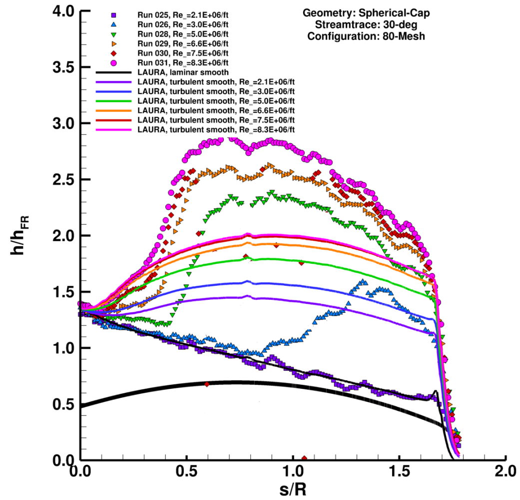

b) 30-deg streamline

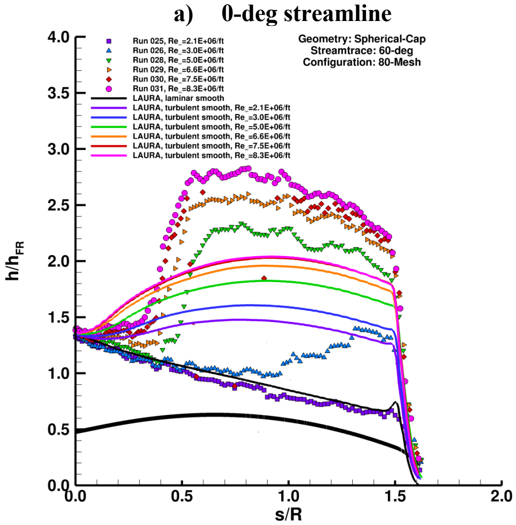

c) 60-deg streamline

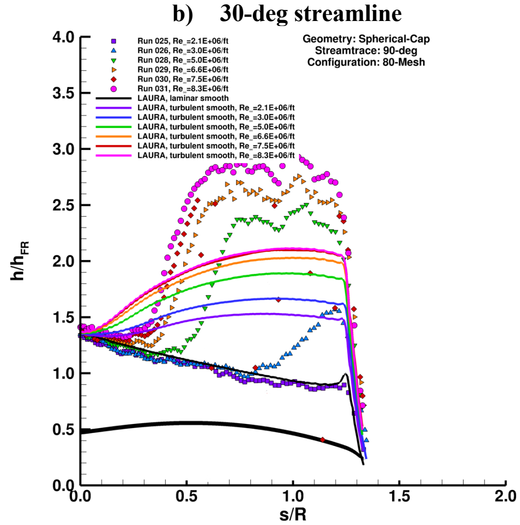

d) 90-deg streamline

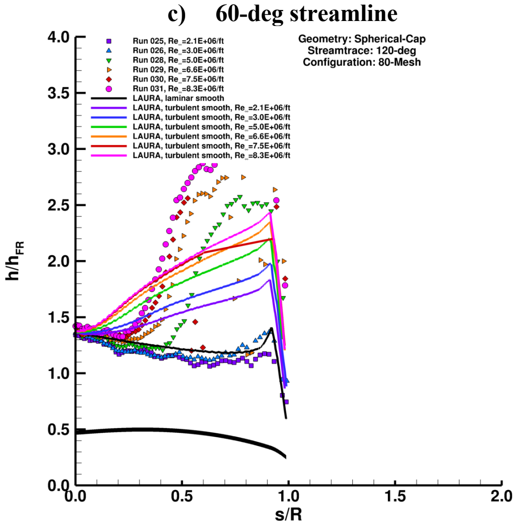

e) 120-deg streamline

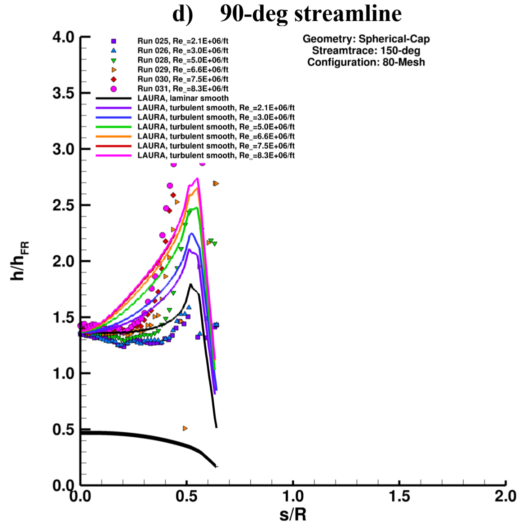

f) 150-deg streamline

Figure 56. Reynolds Number effects, spherical-cap geometry, 80-mesh model plots.

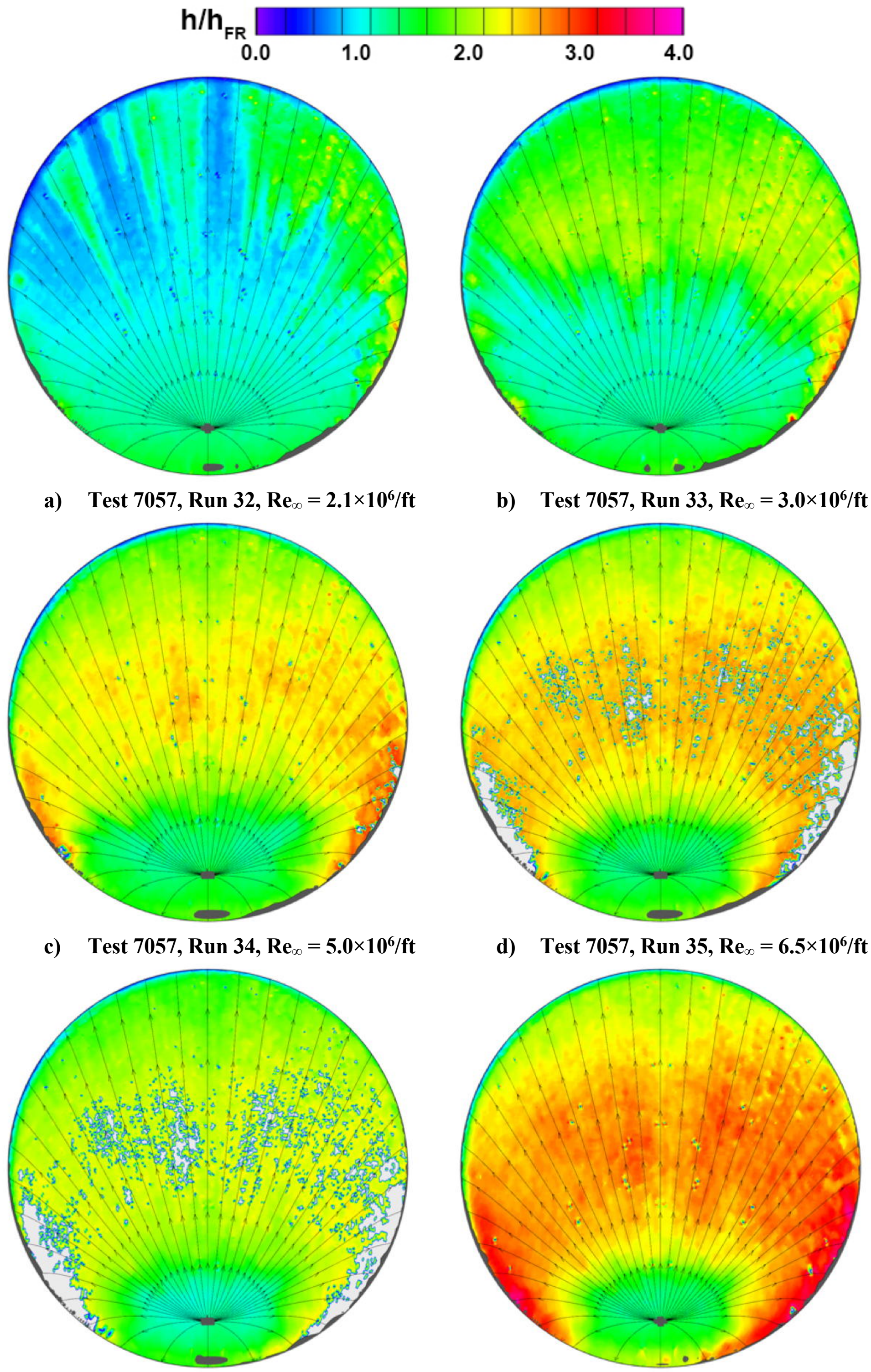

a) Test 7057, Run 32, $Re_\infty = 2.1 \times 10^6$/ft
b) Test 7057, Run 33, $Re_\infty = 3.0 \times 10^6$/ft
c) Test 7057, Run 34, $Re_\infty = 5.0 \times 10^6$/ft
d) Test 7057, Run 35, $Re_\infty = 6.5 \times 10^6$/ft
e) Test 7057, Run 36, $Re_\infty = 7.2 \times 10^6$/ft
f) Test 7057, Run 37, $Re_\infty = 8.1 \times 10^6$/ft

Figure 57. Reynolds Number effects, spherical-cap geometry, 40-mesh model images.

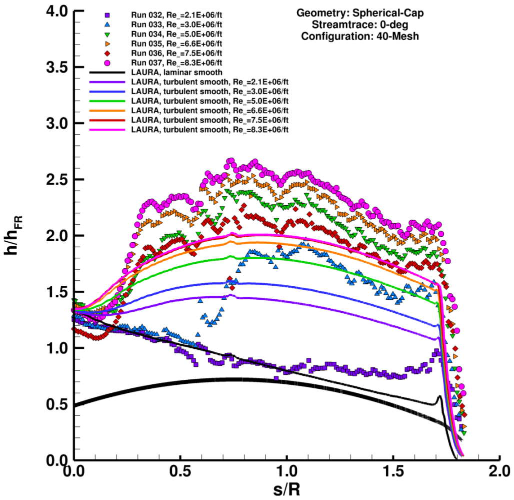

a) 0-deg streamline

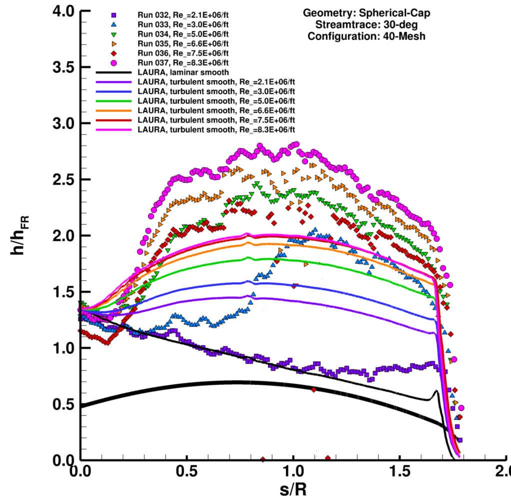

b) 30-deg streamline

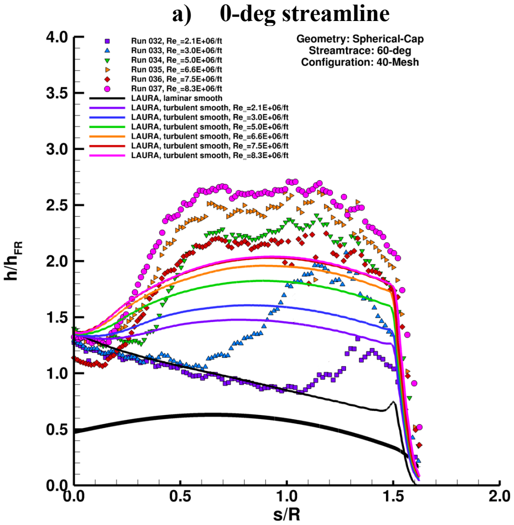

c) 60-deg streamline

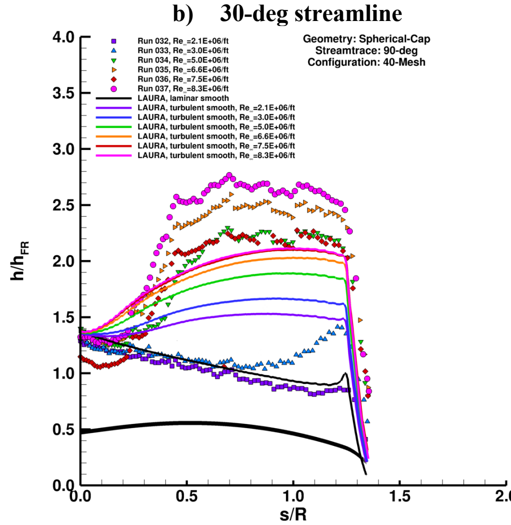

d) 90-deg streamline

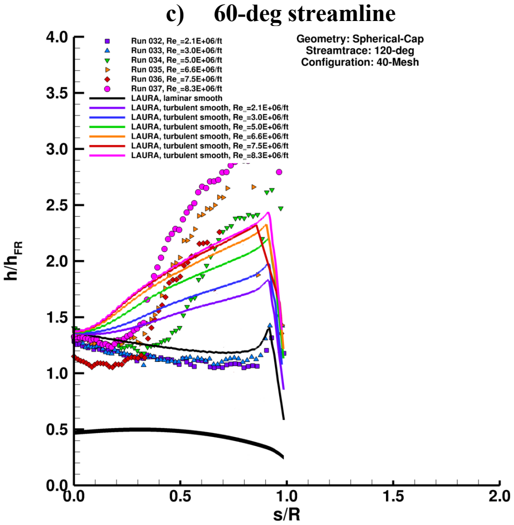

e) 120-deg streamline

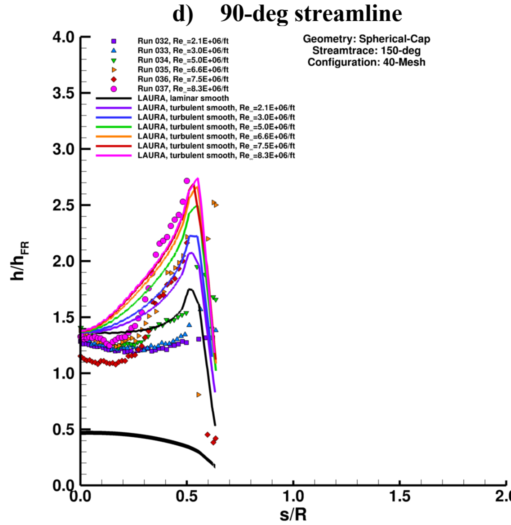

f) 150-deg streamline

Figure 58. Reynolds Number effects, spherical-cap geometry, 40-mesh model plots.

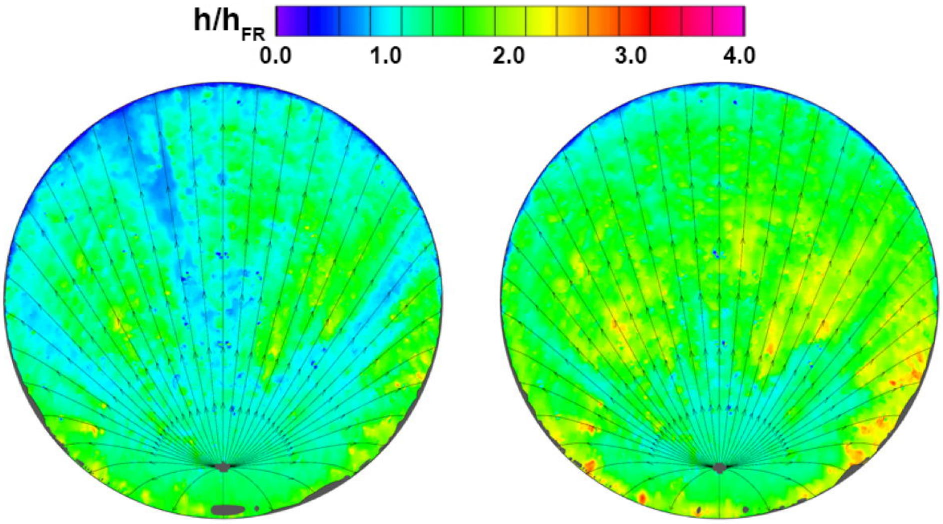

a) Test 7057, Run 55, $Re_\infty = 2.1\times10^6$/ft b) Test 7057, Run 56, $Re_\infty = 3.0\times10^6$/ft

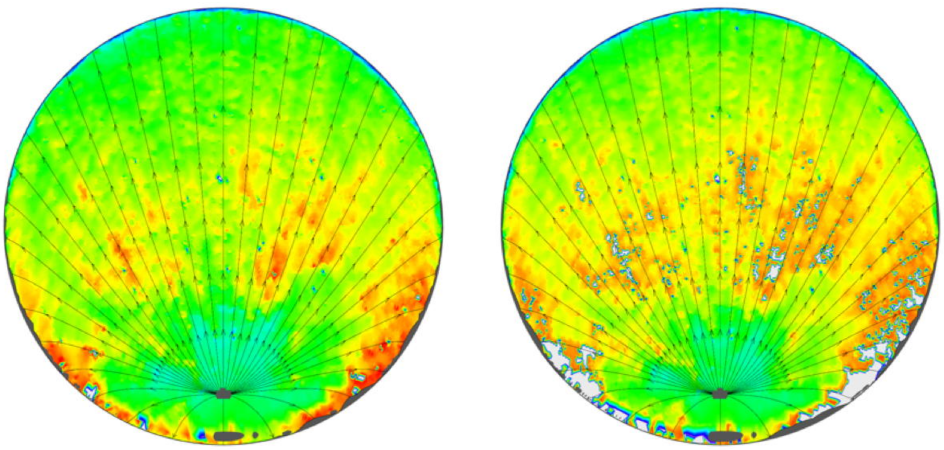

c) Test 7057, Run 57, $Re_\infty = 5.0\times10^6$/ft d) Test 7057, Run 58, $Re_\infty = 6.5\times10^6$/ft

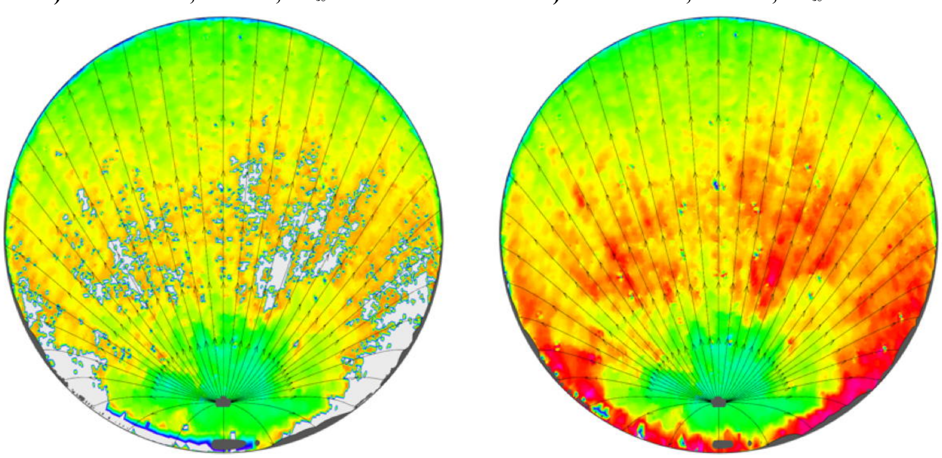

e) Test 7057, Run 59, $Re_\infty = 7.2\times10^6$/ft f) Test 7057, Run 60, $Re_\infty = 8.1\times10^6$/ft

Figure 59. Reynolds Number effects, spherical-cap geometry, 20-mesh model images.

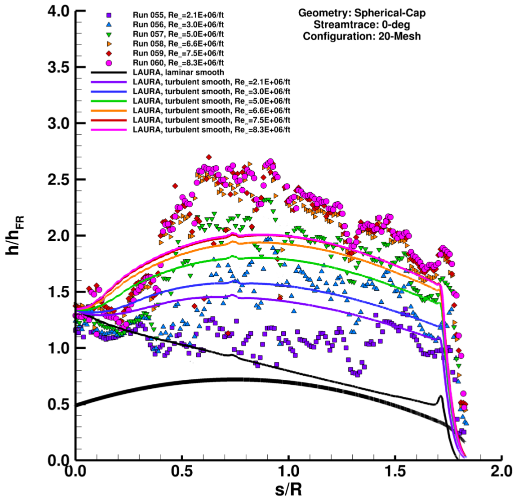

a) 0-deg streamline

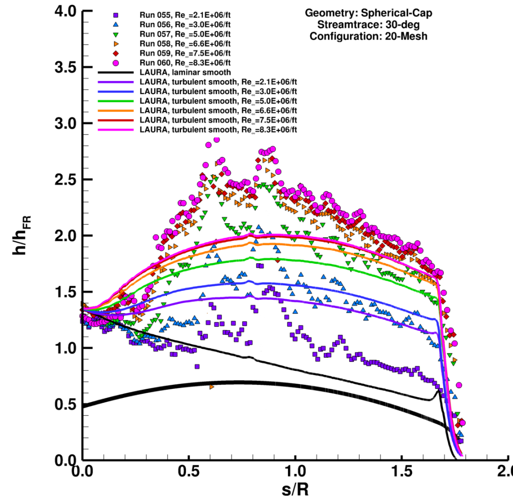

b) 30-deg streamline

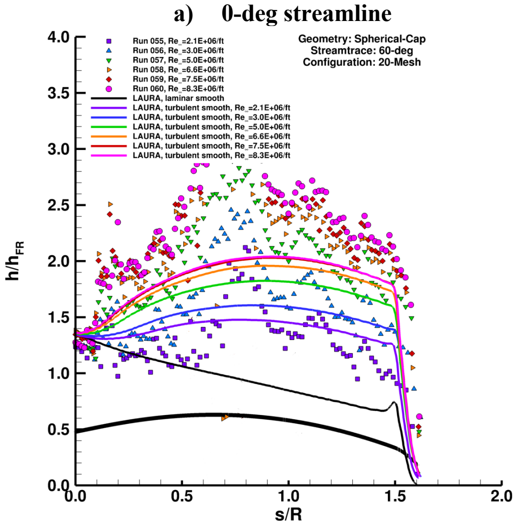

c) 60-deg streamline

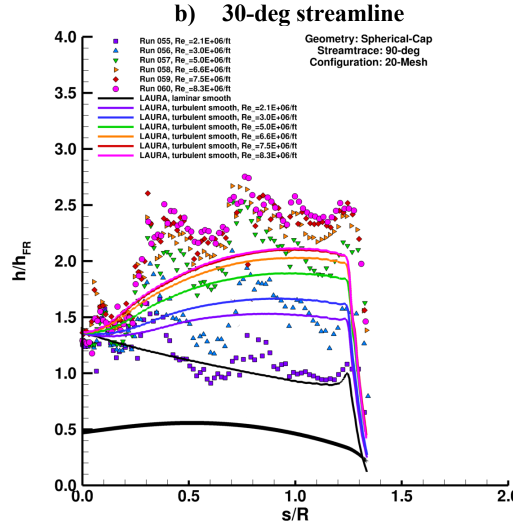

d) 90-deg streamline

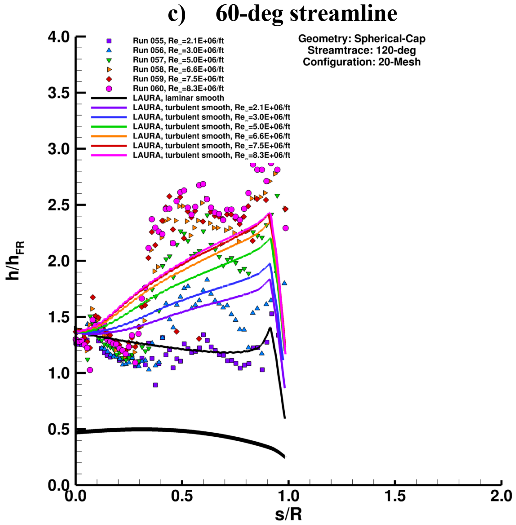

e) 120-deg streamline

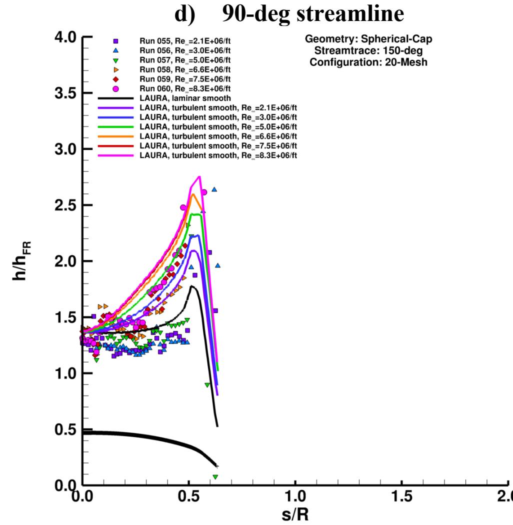

f) 150-deg streamline

Figure 60. Reynolds Number effects, spherical-cap geometry, 20-mesh model plots.

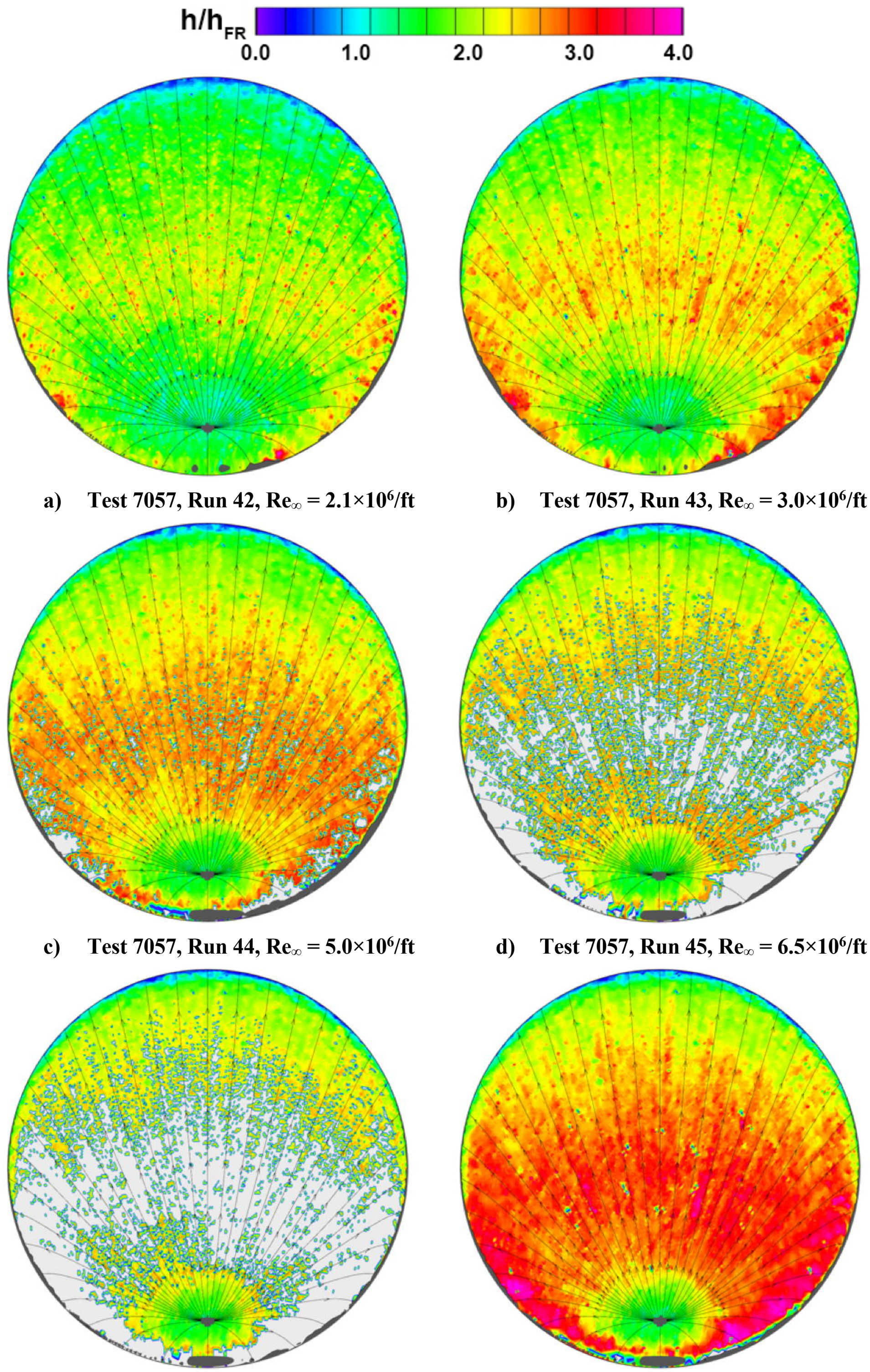

a) Test 7057, Run 42, $Re_\infty = 2.1\times10^6$/ft
b) Test 7057, Run 43, $Re_\infty = 3.0\times10^6$/ft

c) Test 7057, Run 44, $Re_\infty = 5.0\times10^6$/ft
d) Test 7057, Run 45, $Re_\infty = 6.5\times10^6$/ft

e) Test 7057, Run 46, $Re_\infty = 7.2\times10^6$/ft
f) Test 7057, Run 47, $Re_\infty = 8.1\times10^6$/ft

Figure 61. Reynolds Number effects, spherical-cap geometry, 10-mesh model images.

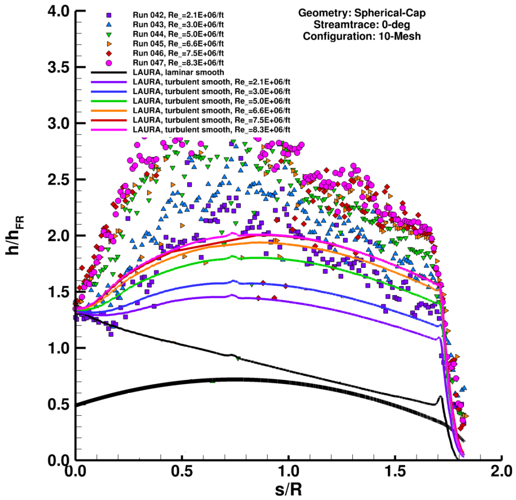

a) 0-deg streamline

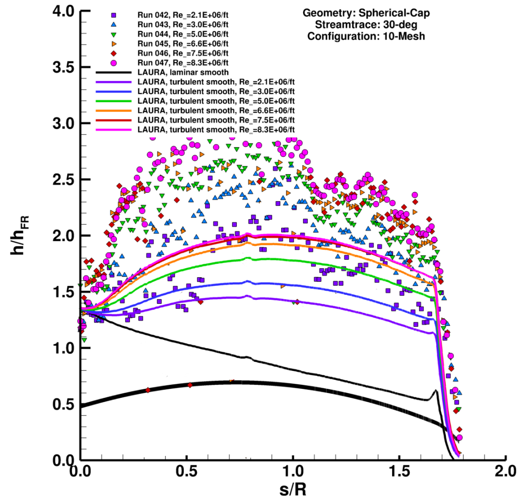

b) 30-deg streamline

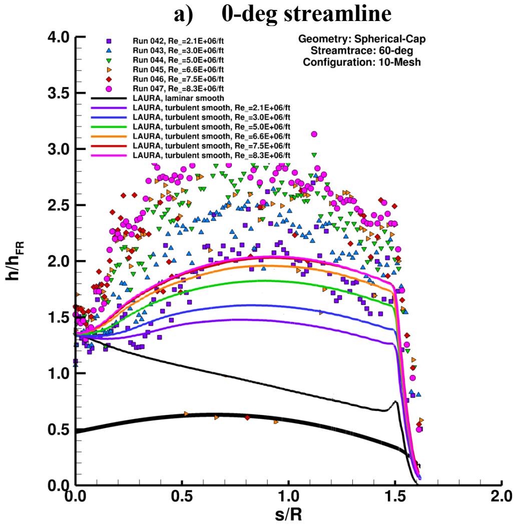

c) 60-deg streamline

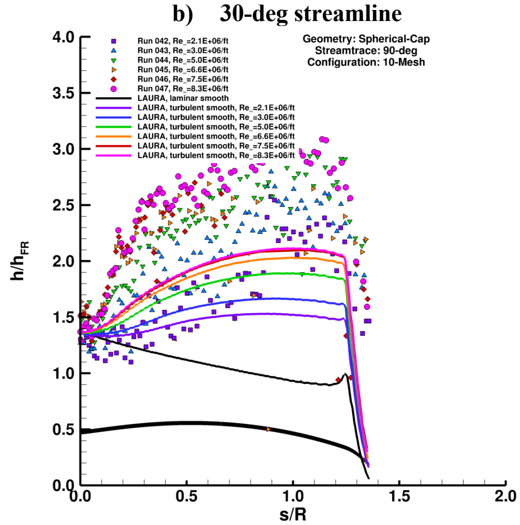

d) 90-deg streamline

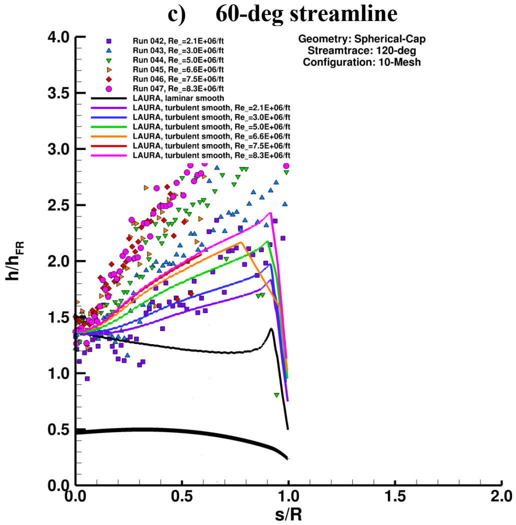

e) 120-deg streamline

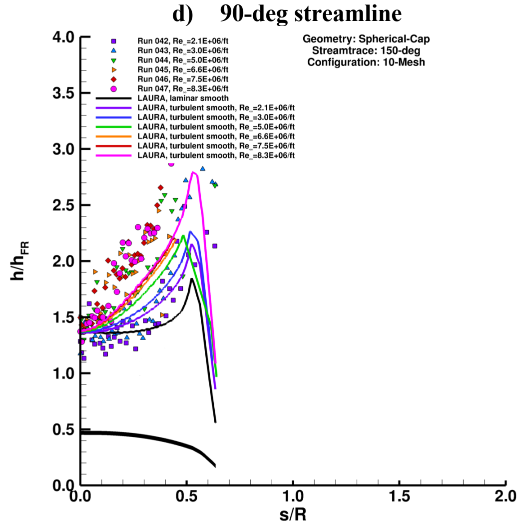

f) 150-deg streamline

Figure 62. Reynolds Number effects, spherical-cap geometry, 10-mesh model plots.

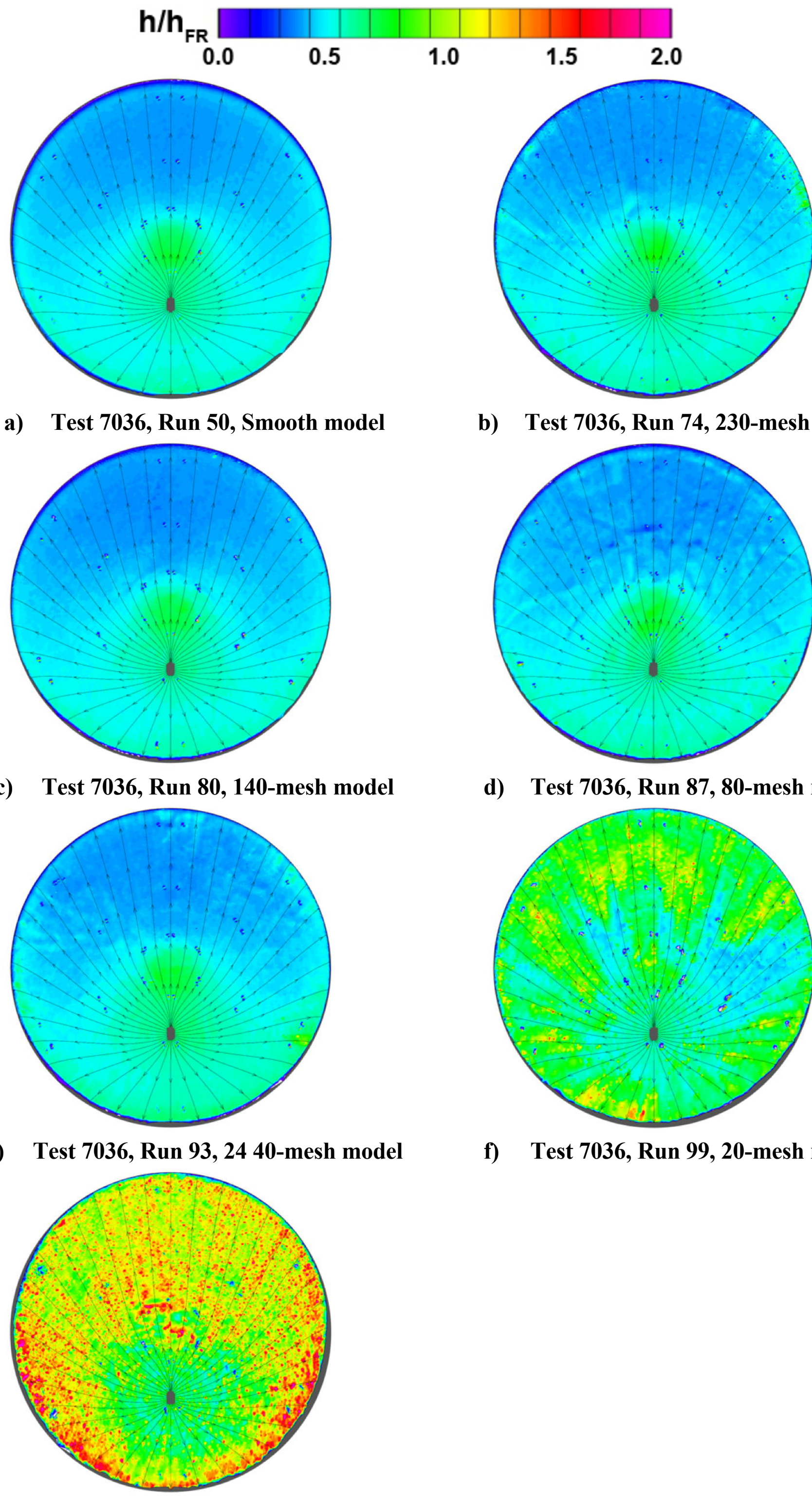

a) Test 7036, Run 50, Smooth model

b) Test 7036, Run 74, 230-mesh model

c) Test 7036, Run 80, 140-mesh model

d) Test 7036, Run 87, 80-mesh model

e) Test 7036, Run 93, 24 40-mesh model

f) Test 7036, Run 99, 20-mesh model

g) Test 7036, Run 107, 10-mesh model

Figure 63. Roughness height effects, sphere-cone geometry, $Re_\infty = 2.1\times10^6$/ft images.

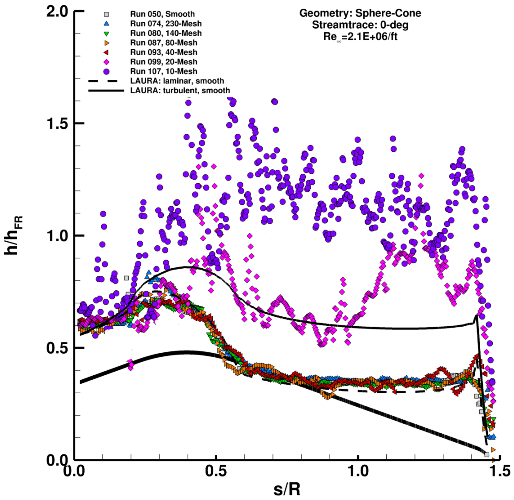

a) 0-deg streamline

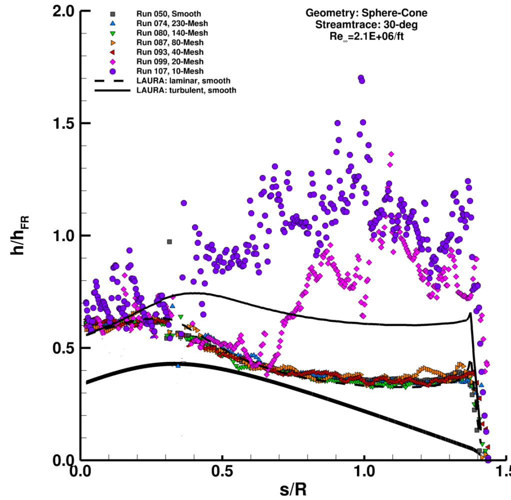

b) 30-deg streamline

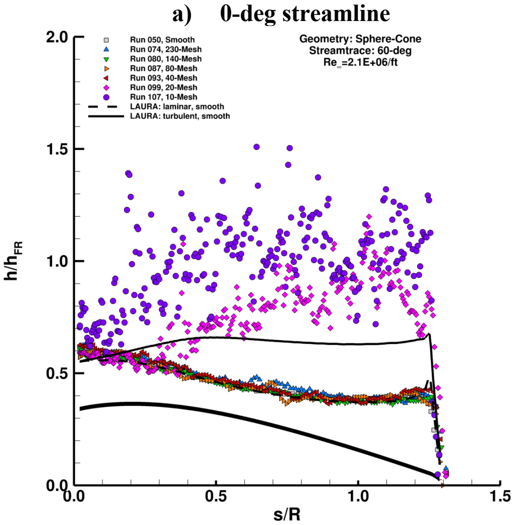

c) 60-deg streamline

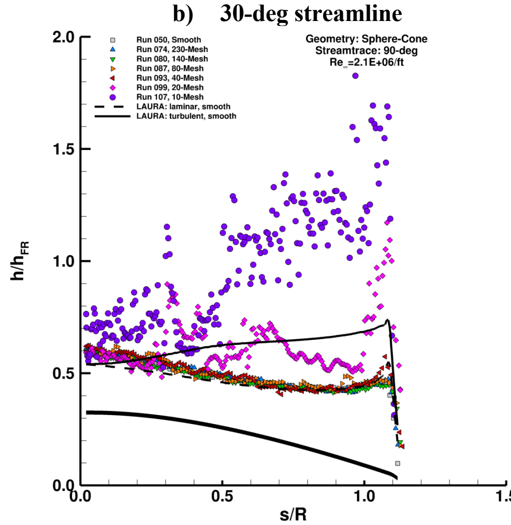

d) 90-deg streamline

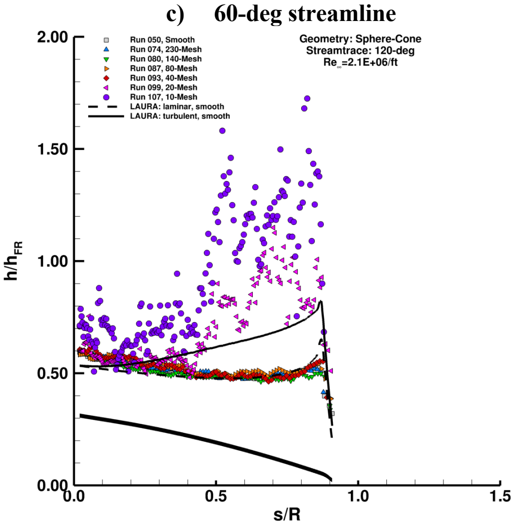

e) 120-deg streamline

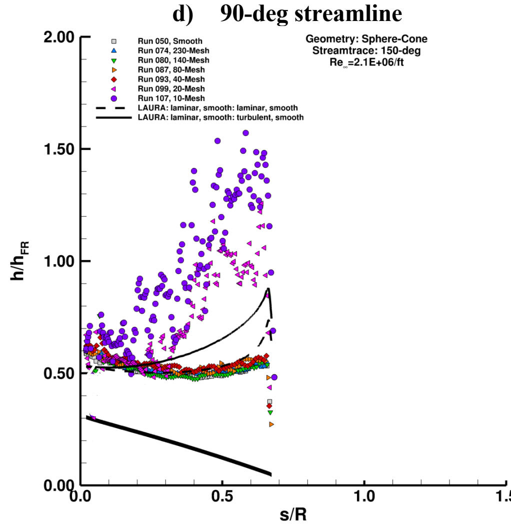

f) 150-deg streamline

Figure 64. Roughness height effects, sphere-cone geometry, $Re_\infty = 2.1\times10^6$/ft plots.

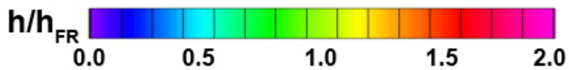

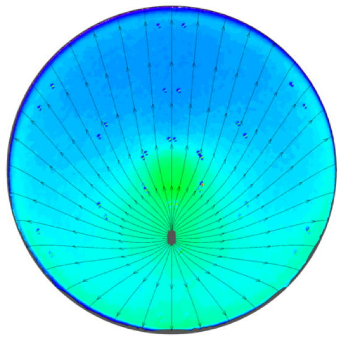

a) Test 7036, Run 51, Smooth model

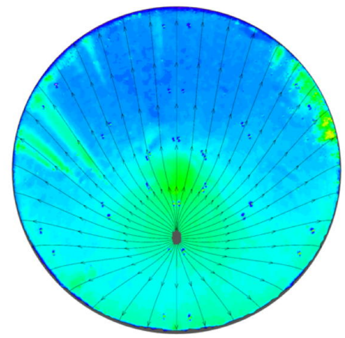

b) Test 7036, Run 75, 230-mesh model

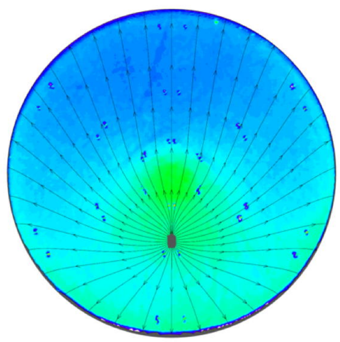

c) Test 7036, Run 81, 140-mesh model

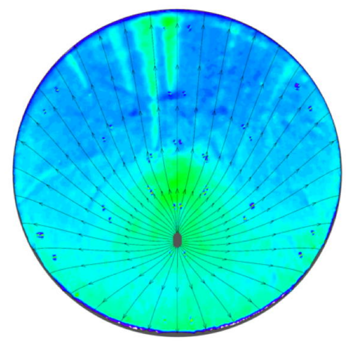

d) Test 7036, Run 88, 80-mesh model

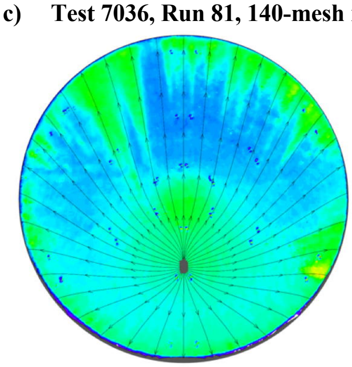

e) Test 7036, Run 94, 24 40-mesh model

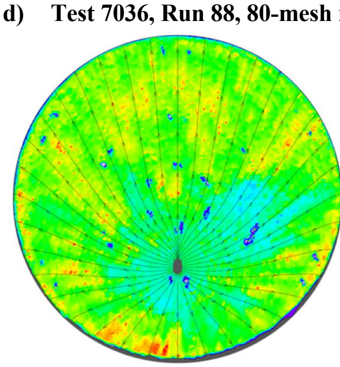

f) Test 7036, Run 100, 20-mesh model

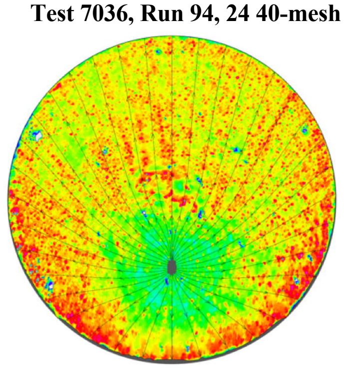

g) Test 7036, Run 106, 10-mesh model

Figure 65. Roughness height effects, sphere-cone geometry, Re∞ = 3.0×10^6/ft images.

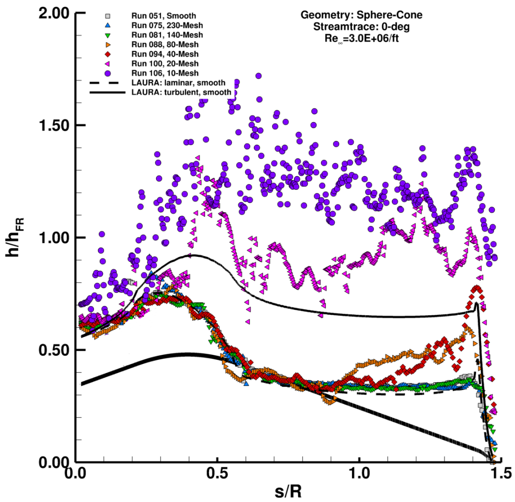

a) 0-deg streamline

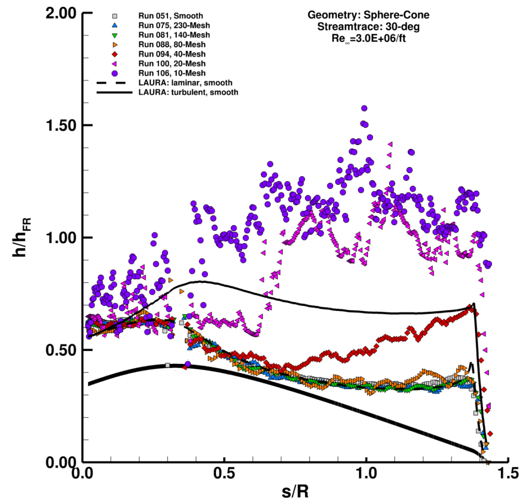

b) 30-deg streamline

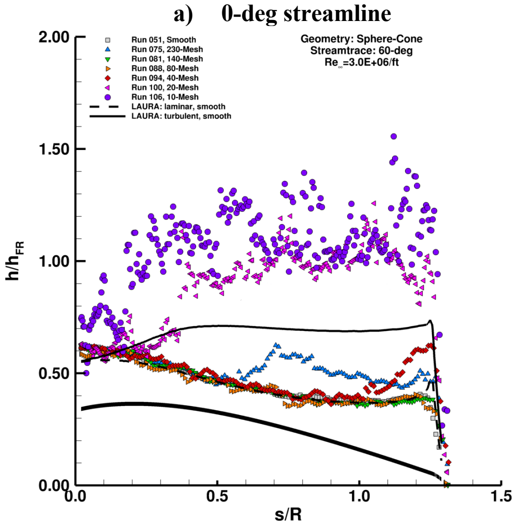

c) 60-deg streamline

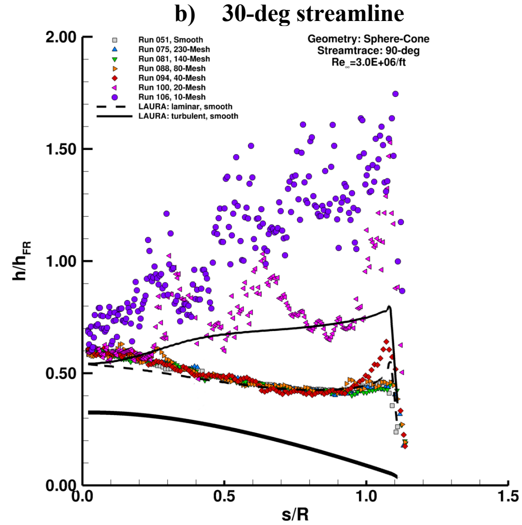

d) 90-deg streamline

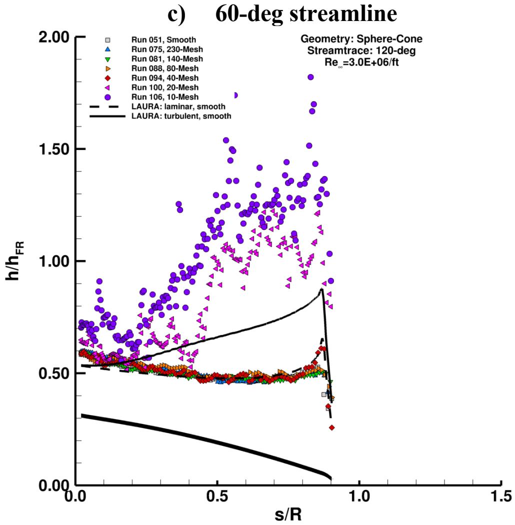

e) 120-deg streamline

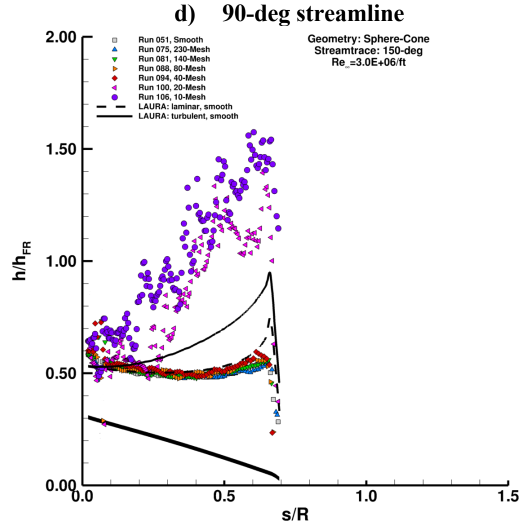

f) 150-deg streamline

Figure 66. Roughness height effects, sphere-cone geometry, $Re_\infty = 3.0\times10^6$/ft plots.

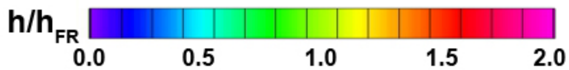

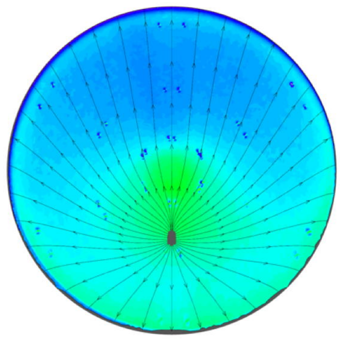

a) Test 7036, Run 52, Smooth model

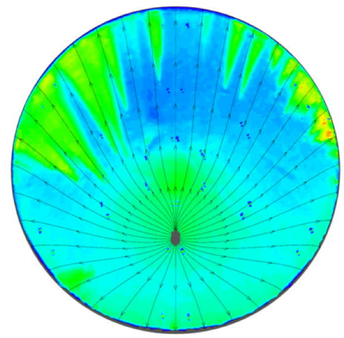

b) Test 7036, Run 76, 230-mesh model

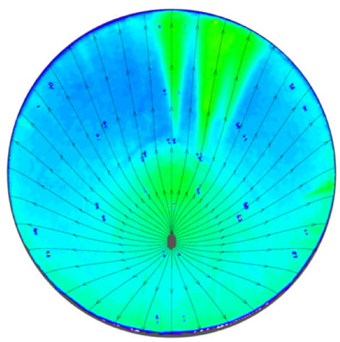

c) Test 7036, Run 82, 140-mesh model

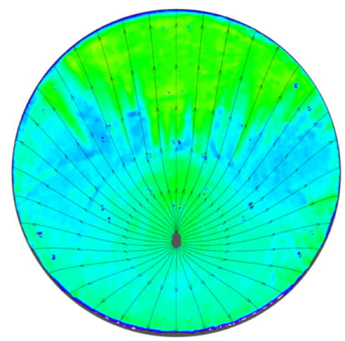

d) Test 7036, Run 89, 80-mesh model

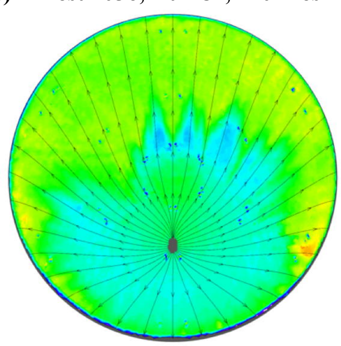

e) Test 7036, Run 95, 24 40-mesh model

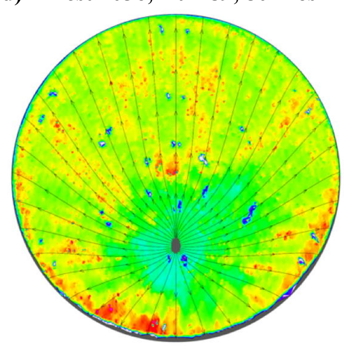

f) Test 7036, Run 101, 20-mesh model

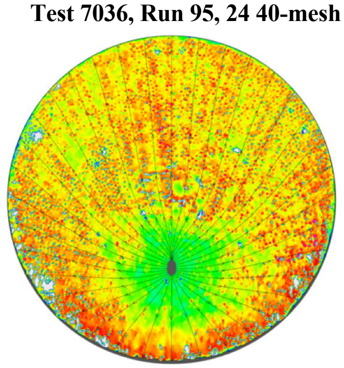

g) Test 7036, Run 105, 10-mesh model

Figure 67. Roughness height effects, sphere-cone geometry, $Re_\infty = 5.0\times10^6$/ft images.

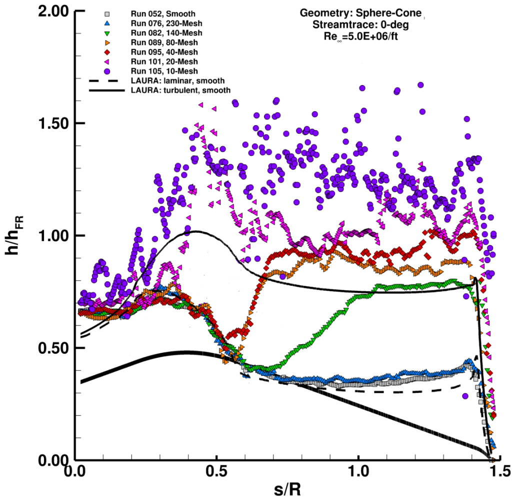

a) 0-deg streamline

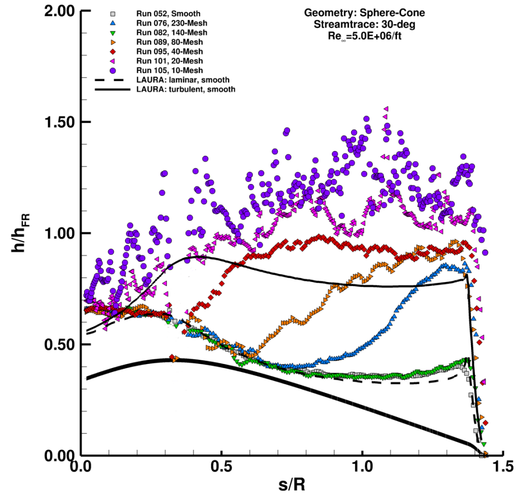

b) 30-deg streamline

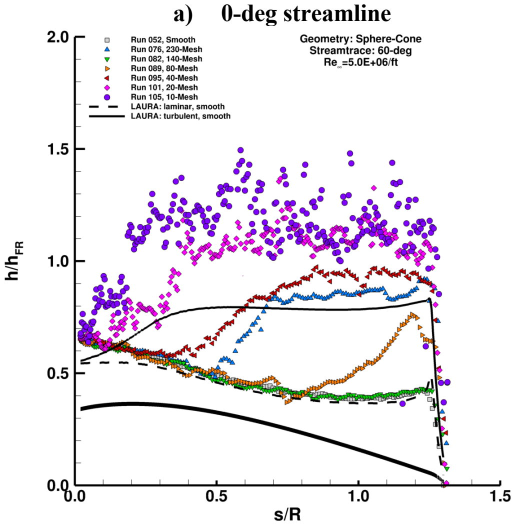

c) 60-deg streamline

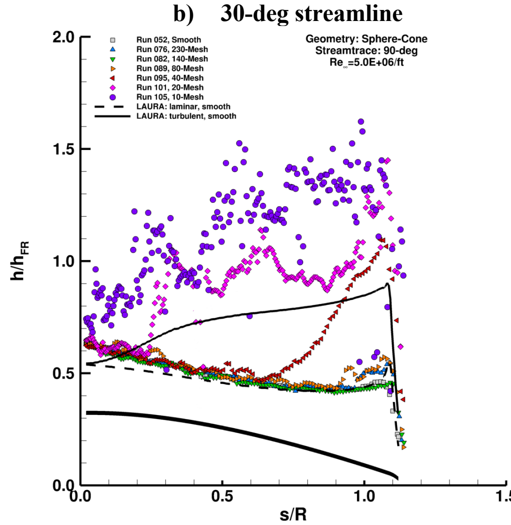

d) 90-deg streamline

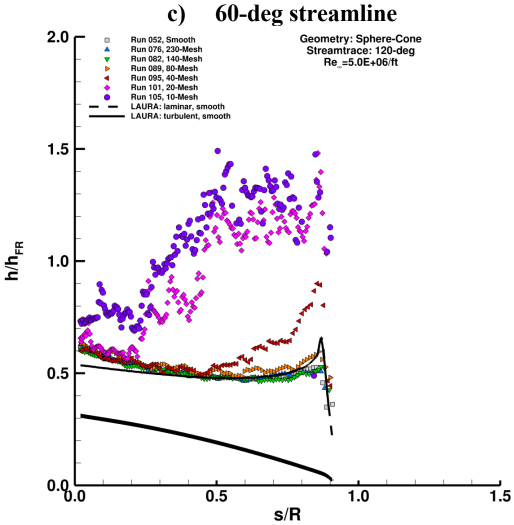

e) 120-deg streamline

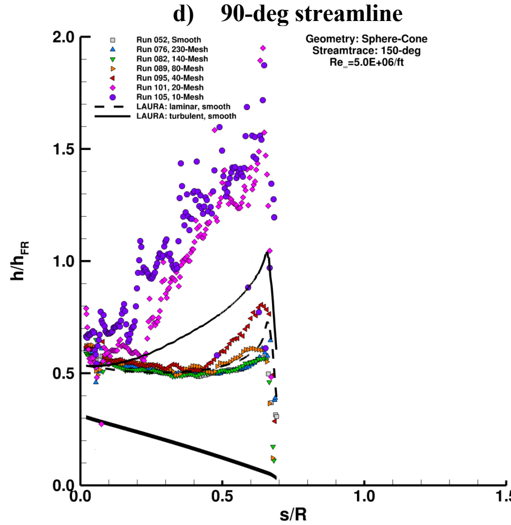

f) 150-deg streamline

Figure 68. Roughness height effects, sphere-cone geometry, $Re_\infty = 5.0\times10^6$/ft plots.

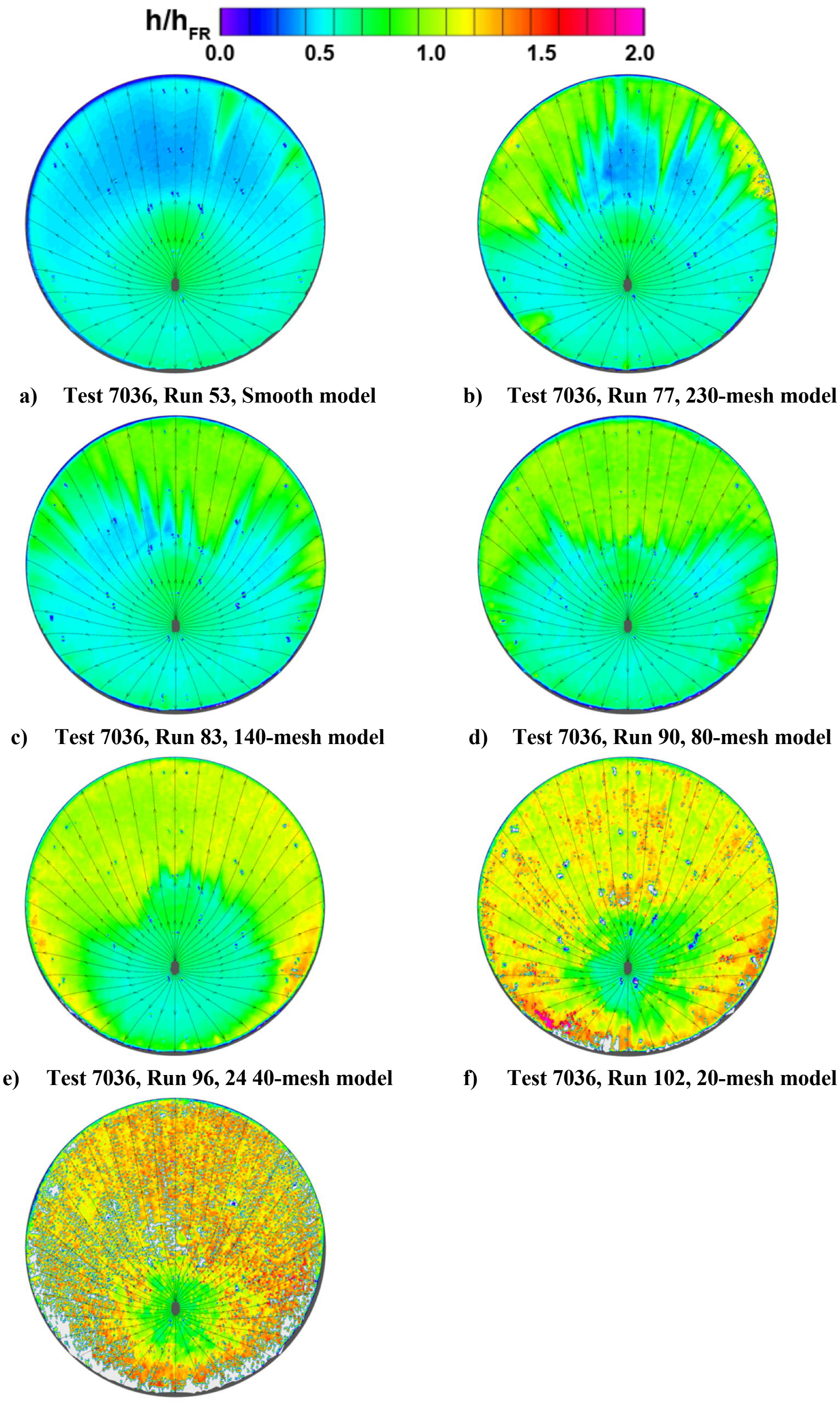

a) Test 7036, Run 53, Smooth model

b) Test 7036, Run 77, 230-mesh model

c) Test 7036, Run 83, 140-mesh model

d) Test 7036, Run 90, 80-mesh model

e) Test 7036, Run 96, 24 40-mesh model

f) Test 7036, Run 102, 20-mesh model

g) Test 7036, Run 108, 10-mesh model

Figure 69. Roughness height effects, sphere-cone geometry, $Re_\infty = 6.5\times10^6$/ft images.

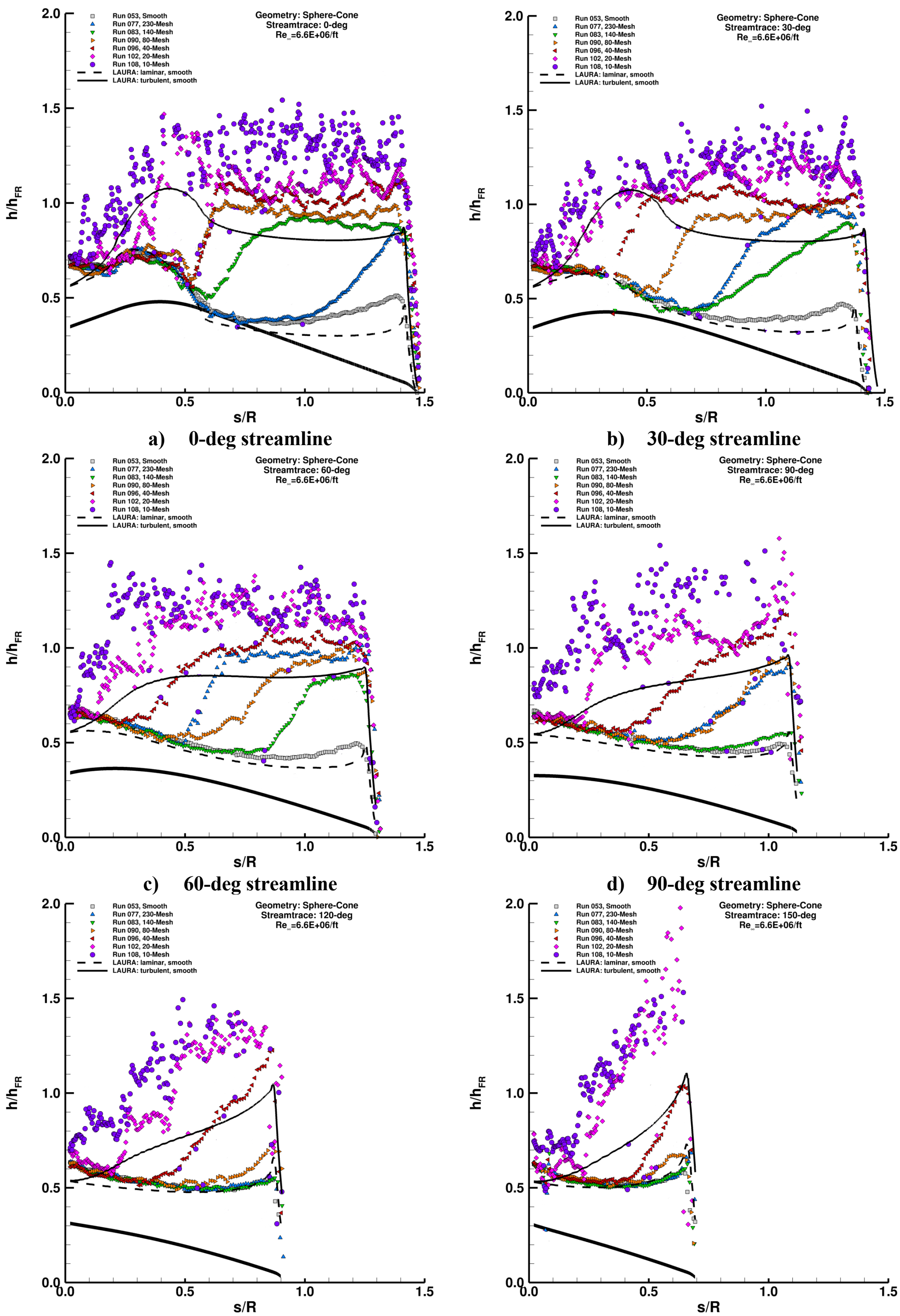

a) 0-deg streamline

b) 30-deg streamline

c) 60-deg streamline

d) 90-deg streamline

e) 120-deg streamline

f) 150-deg streamline

Figure 70. Roughness height effects, sphere-cone geometry, $Re_\infty = 6.5\times10^6$/ft plots.

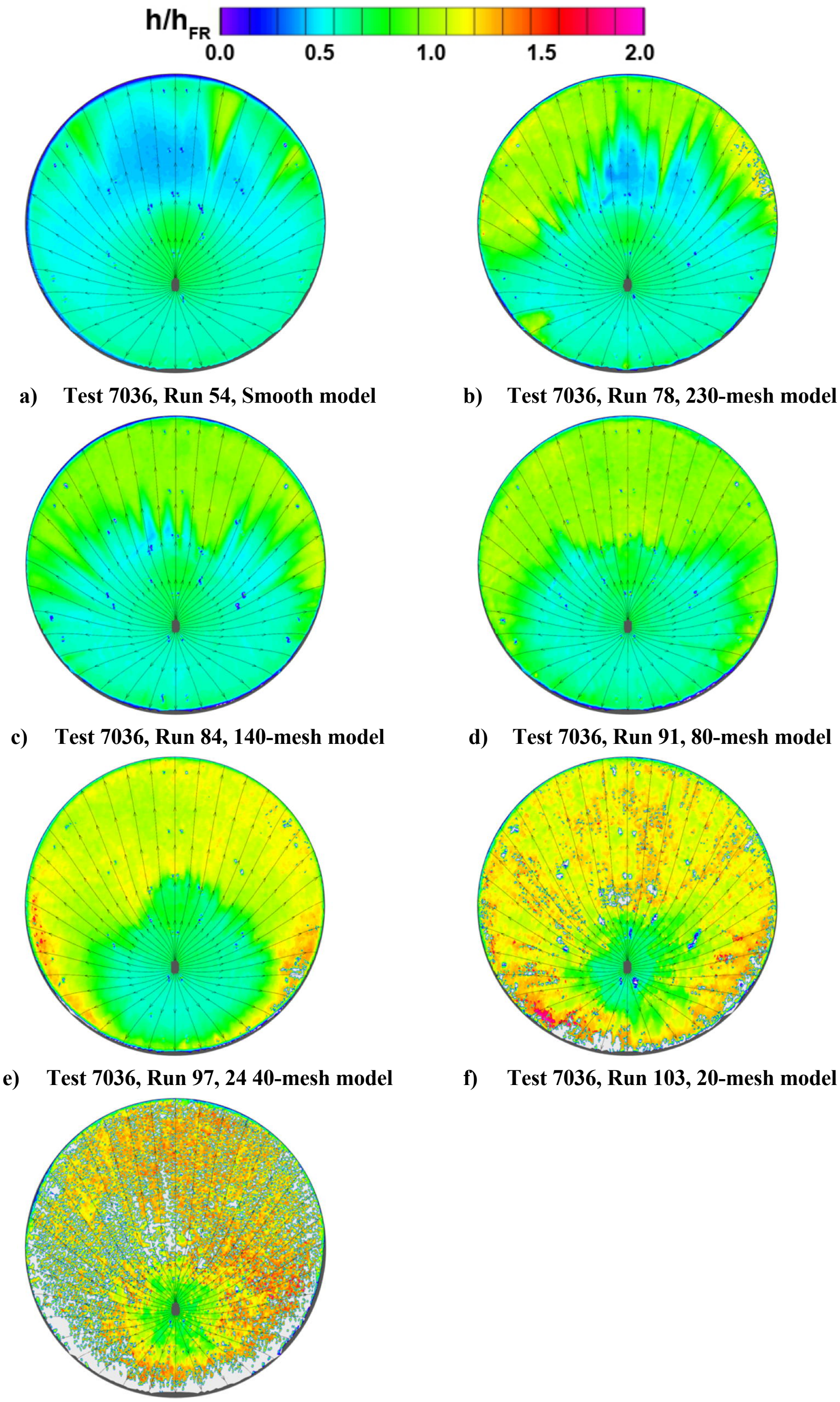

a) Test 7036, Run 54, Smooth model **b) Test 7036, Run 78, 230-mesh model**

c) Test 7036, Run 84, 140-mesh model **d) Test 7036, Run 91, 80-mesh model**

e) Test 7036, Run 97, 24 40-mesh model **f) Test 7036, Run 103, 20-mesh model**

g) Test 7036, Run 109, 10-mesh model

Figure 71. Roughness height effects, sphere-cone geometry, $Re_\infty = 7.2\times10^6$/ft images.

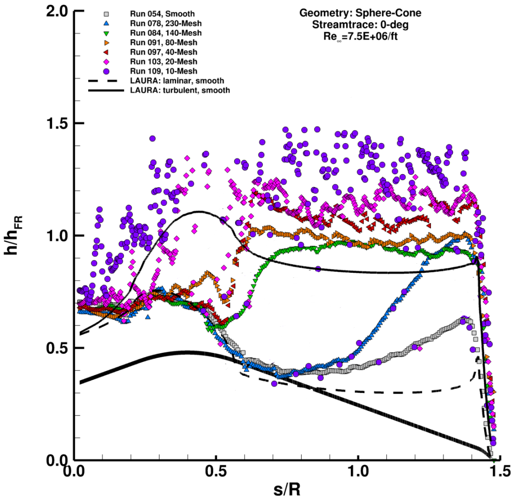

a) 0-deg streamline

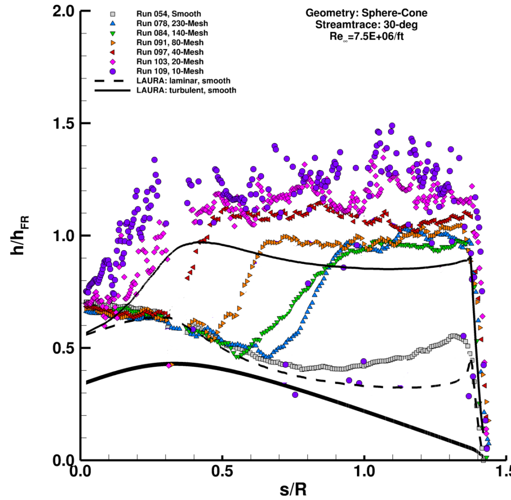

b) 30-deg streamline

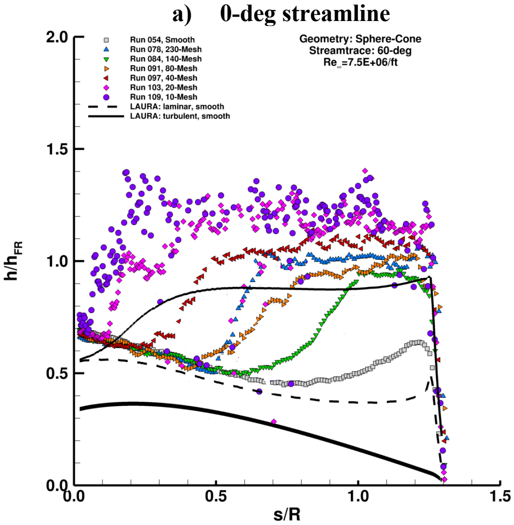

c) 60-deg streamline

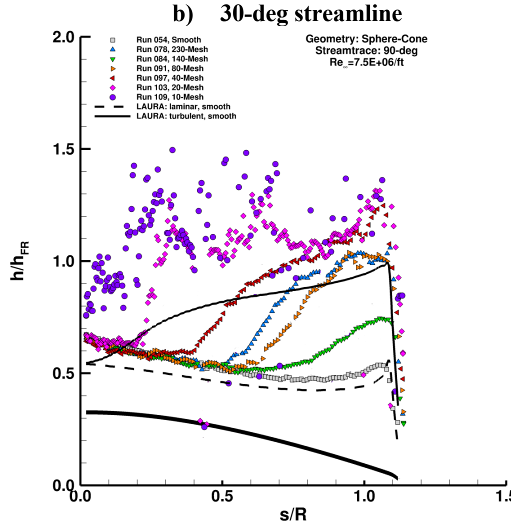

d) 90-deg streamline

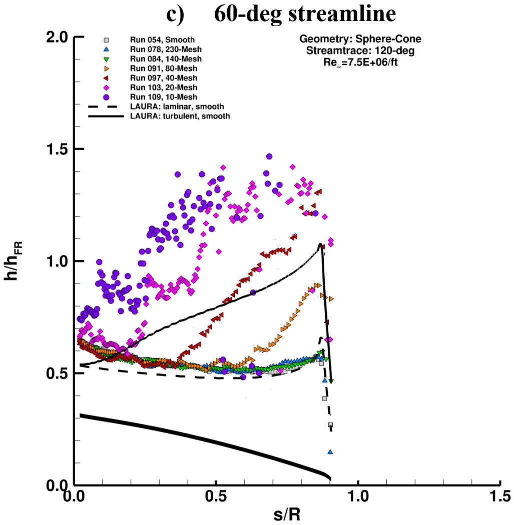

e) 120-deg streamline

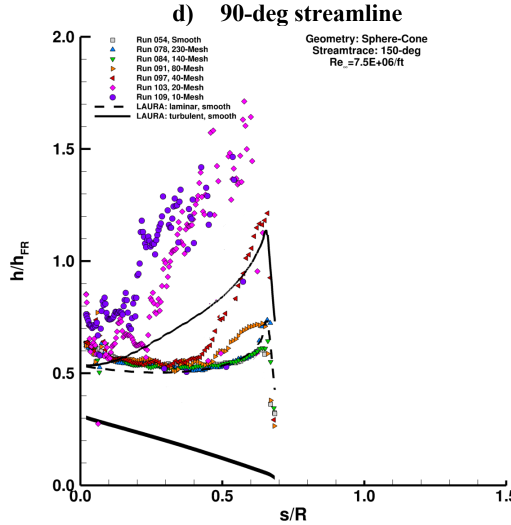

f) 150-deg streamline

Figure 72. Roughness height effects, sphere-cone geometry, $Re_\infty = 7.2\times10^6$/ft plots.

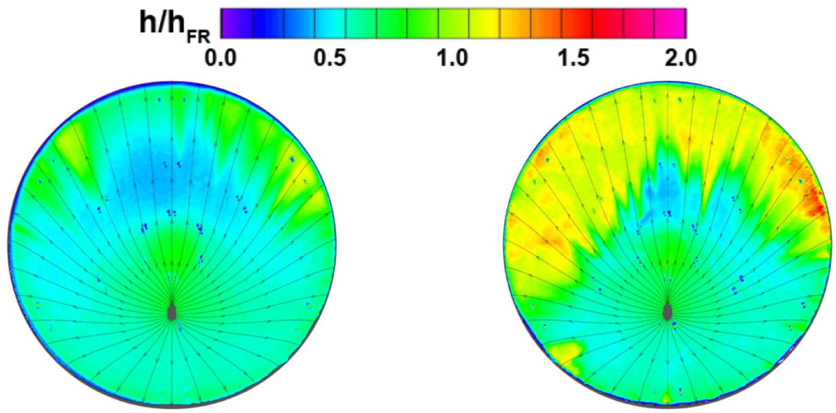

a) Test 7036, Run 55, Smooth model b) Test 7036, Run 79, 230-mesh model

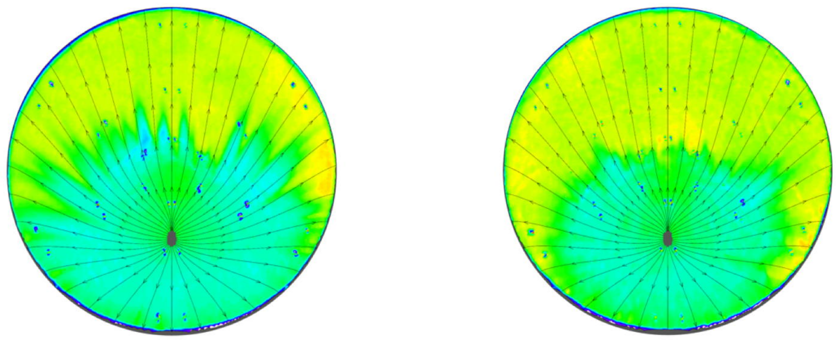

c) Test 7036, Run 85, 140-mesh model d) Test 7036, Run 92, 80-mesh model

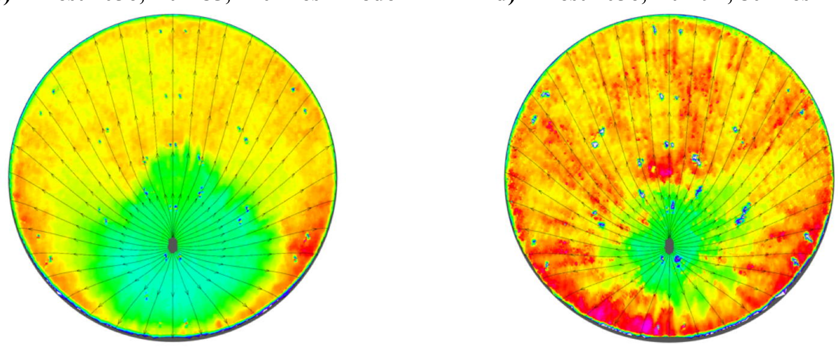

e) Test 7036, Run 98, 24 40-mesh model f) Test 7036, Run 104, 20-mesh model

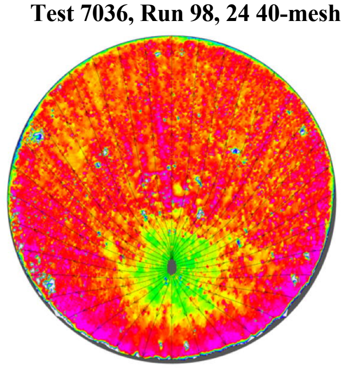

e) Test 7036, Run 110, 10-mesh model

Figure 73. Roughness height effects, sphere-cone geometry, Re∞ = 8.1×10^6/ft images.

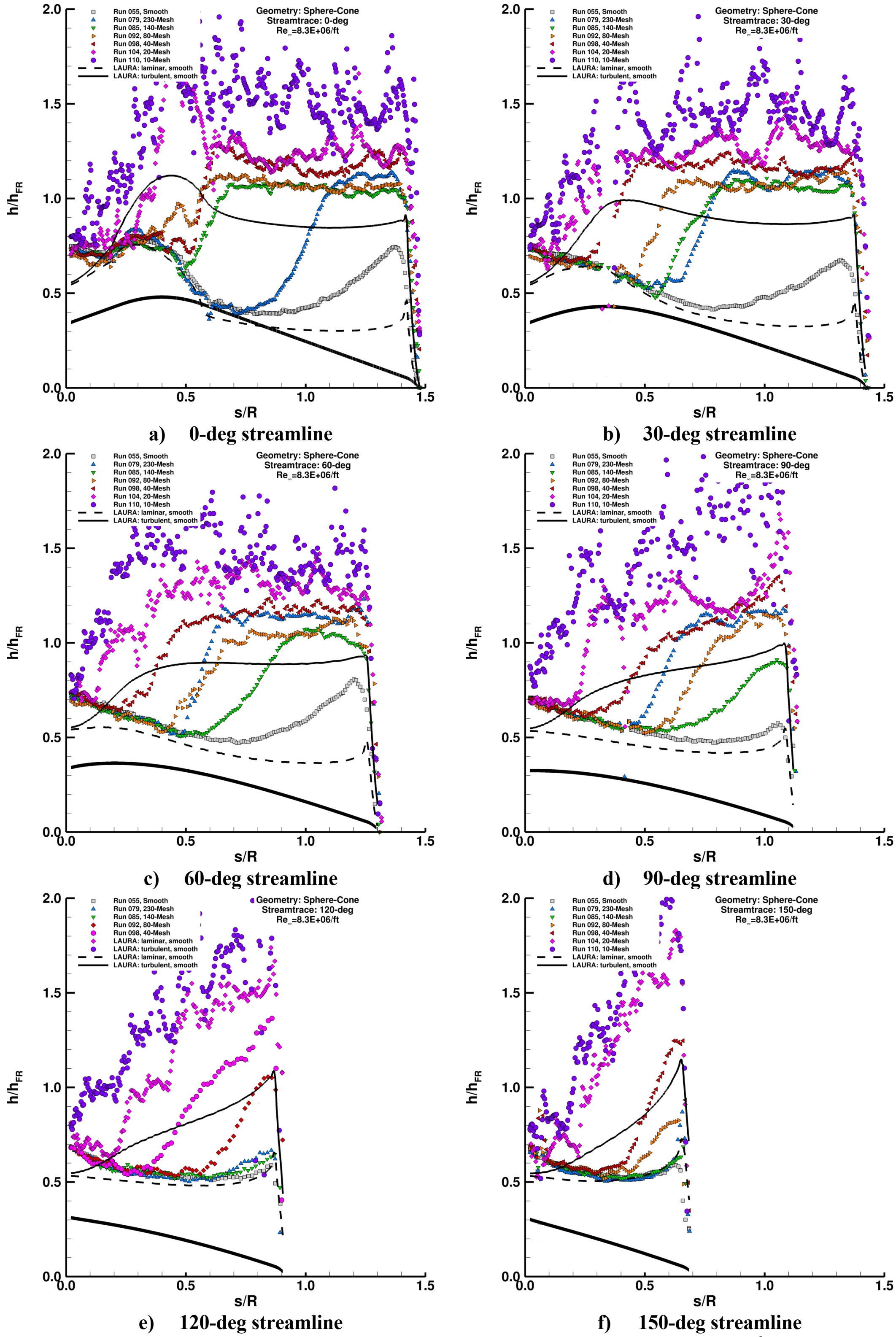

Figure 74. Roughness height effects, sphere-cone geometry, $Re_\infty = 8.1 \times 10^6$/ft plots.

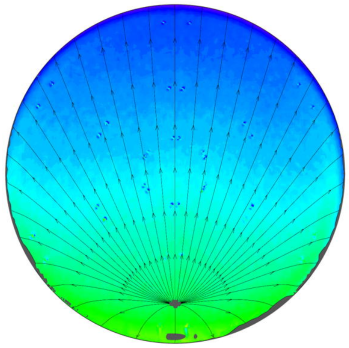

a) Test 7057, Run 7, Smooth model

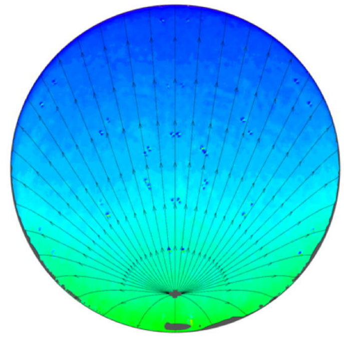

b) Test 7057, Run 13, 230-mesh model

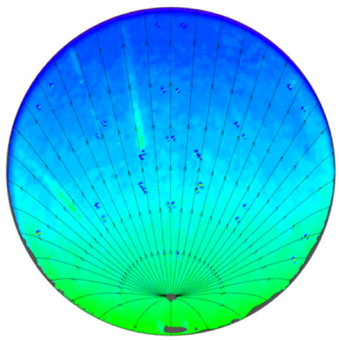

c) Test 7057, Run 19, 140-mesh model

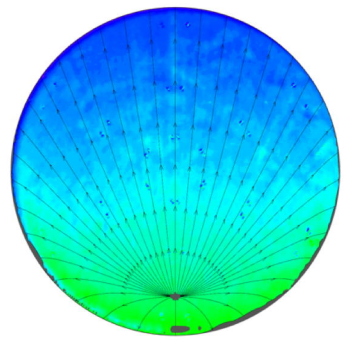

d) Test 7057, Run 25, 80-mesh model

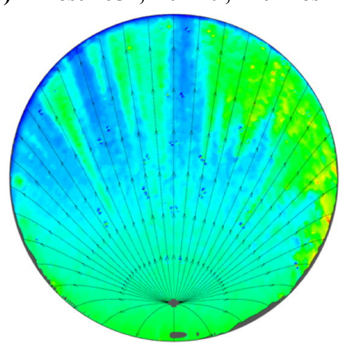

e) Test 7057, Run 32, 24 40-mesh model

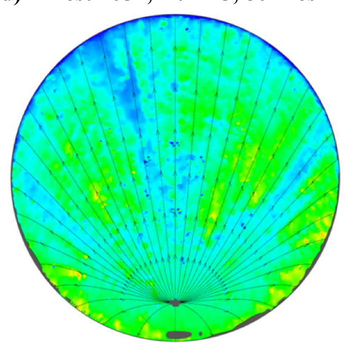

f) Test 7057, Run 55, 20-mesh model

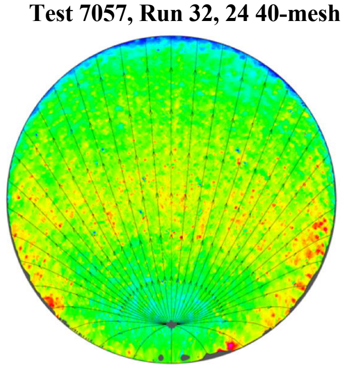

g) Test 7057, Run 42, 10-mesh model

Figure 75. Roughness height effects, spherical-cap geometry, $Re_\infty = 2.1\times10^6$/ft images.

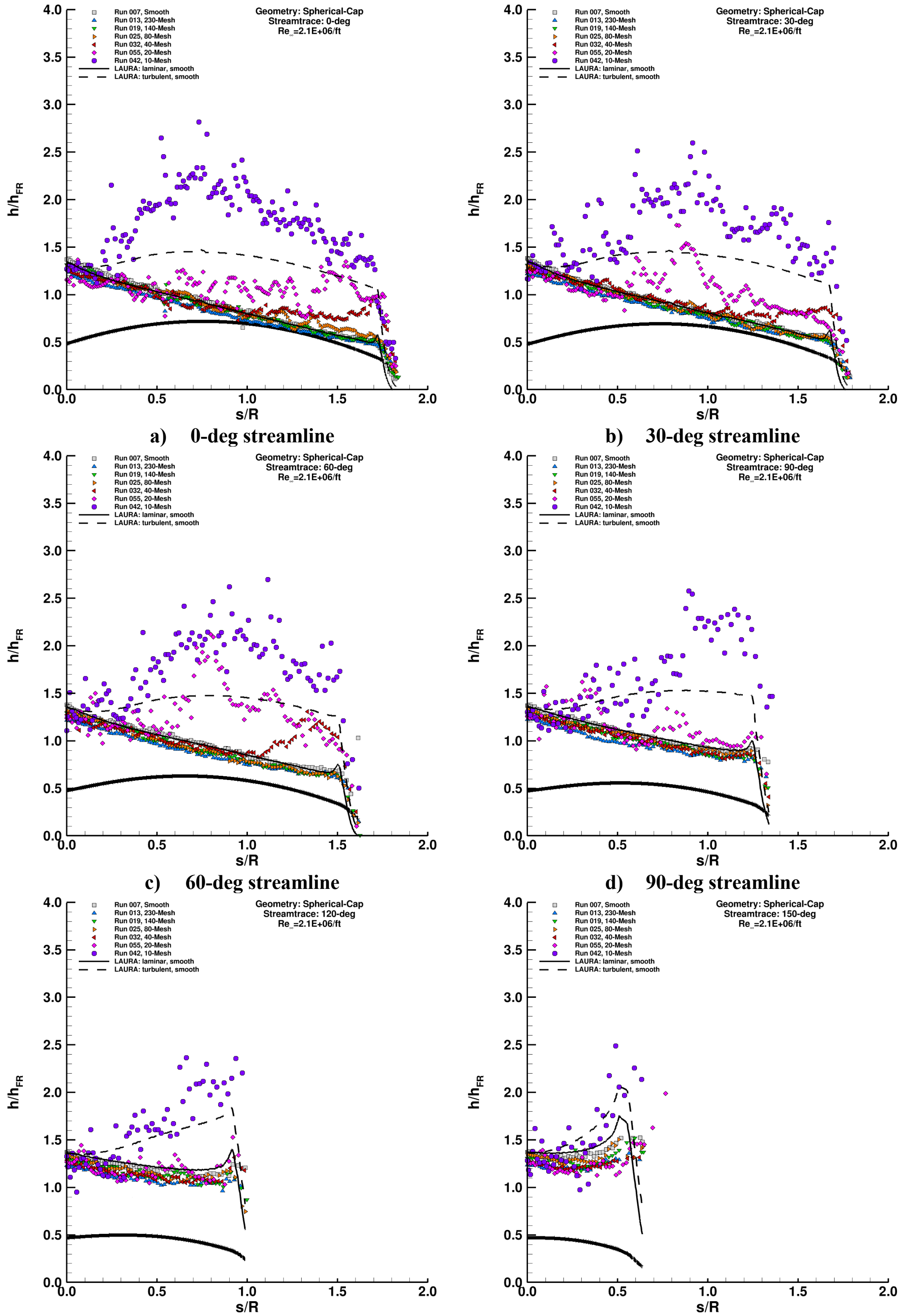

a) 0-deg streamline

b) 30-deg streamline

c) 60-deg streamline

d) 90-deg streamline

e) 120-deg streamline

f) 150-deg streamline

Figure 76. Roughness height effects, spherical-cap geometry, $Re_\infty = 2.1\times10^6$/ft plots.

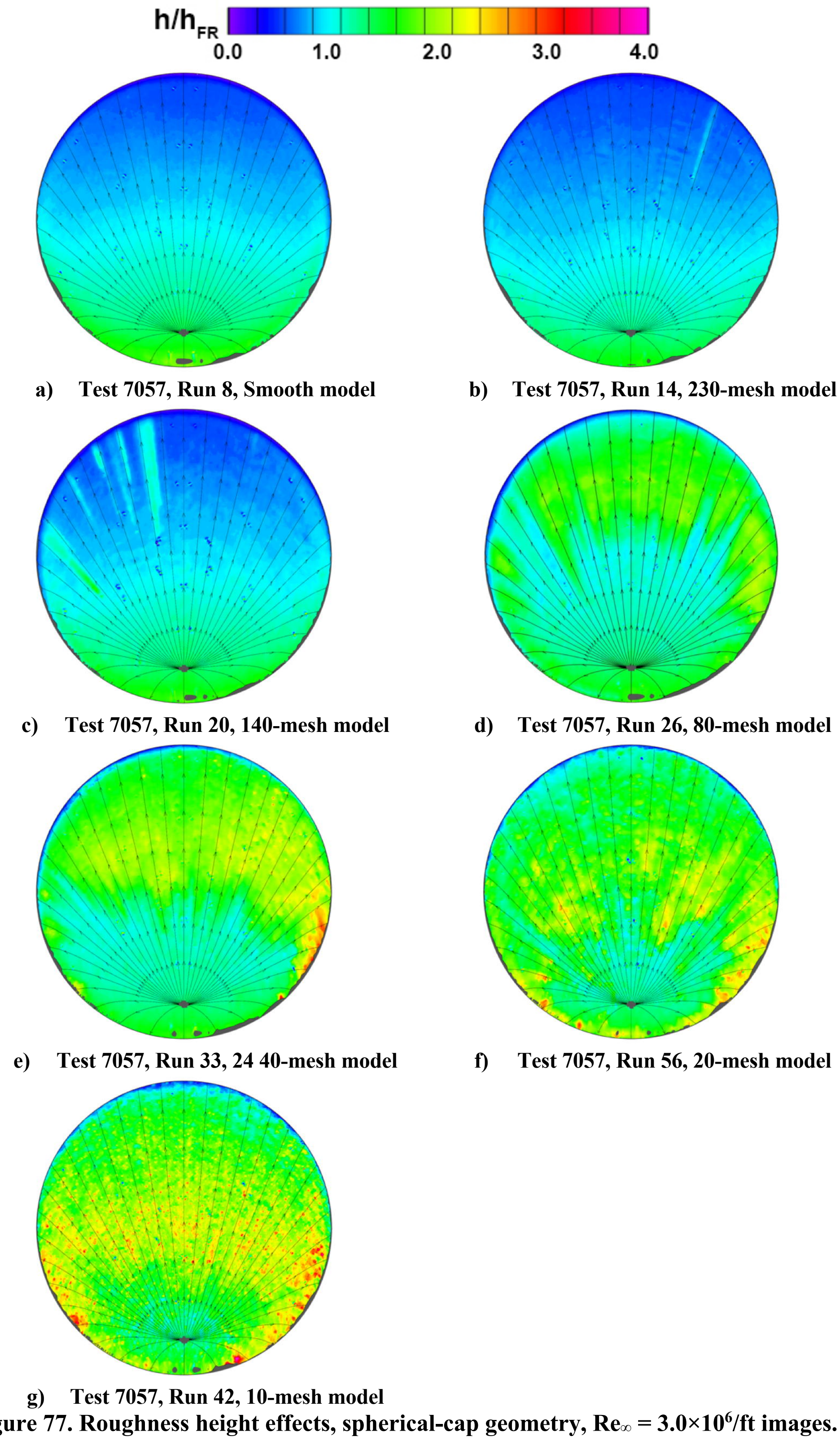

a) Test 7057, Run 8, Smooth model

b) Test 7057, Run 14, 230-mesh model

c) Test 7057, Run 20, 140-mesh model

d) Test 7057, Run 26, 80-mesh model

e) Test 7057, Run 33, 24 40-mesh model

f) Test 7057, Run 56, 20-mesh model

g) Test 7057, Run 42, 10-mesh model

Figure 77. Roughness height effects, spherical-cap geometry, $Re_\infty = 3.0\times10^6$/ft images.

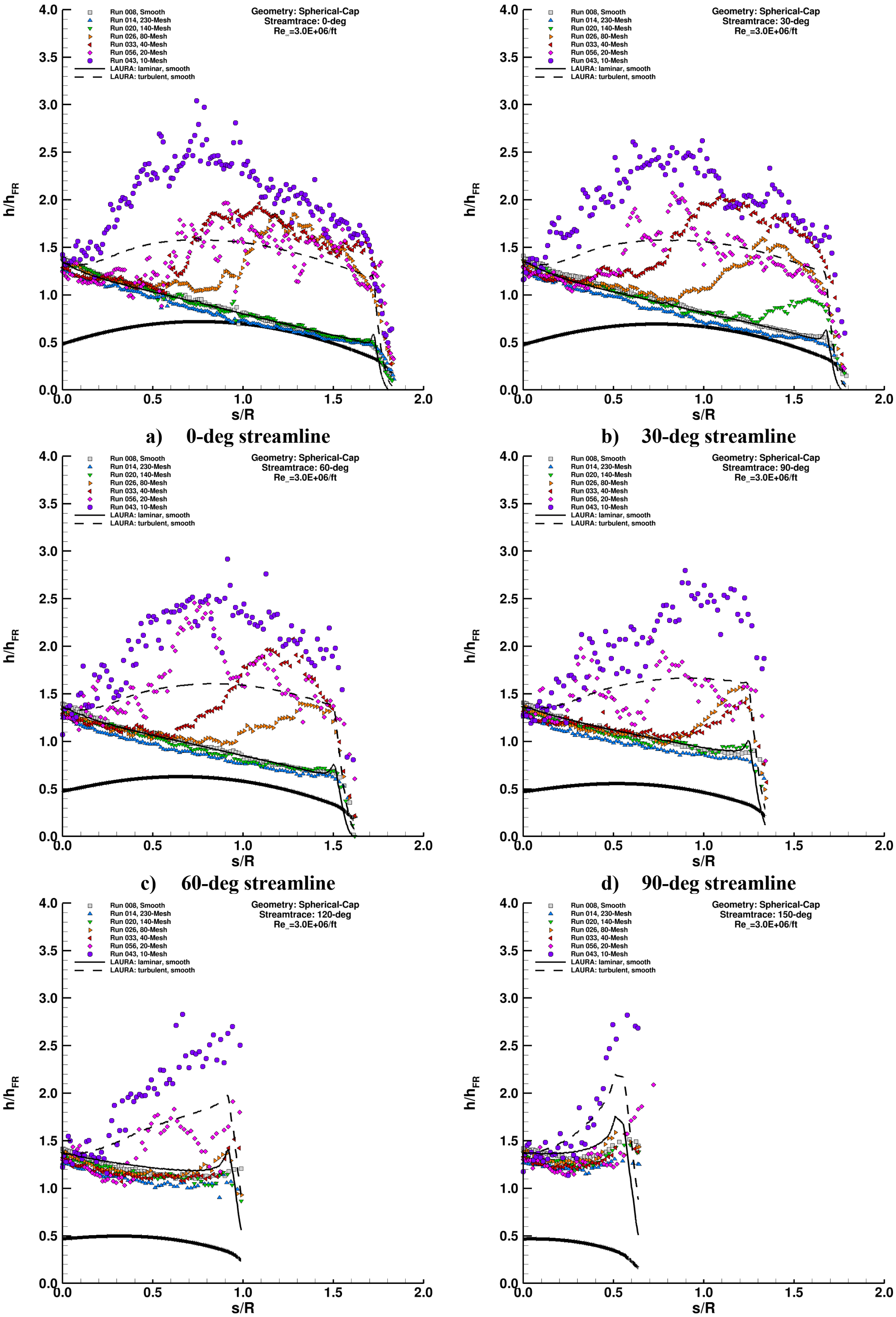

a) 0-deg streamline

b) 30-deg streamline

c) 60-deg streamline

d) 90-deg streamline

e) 120-deg streamline

f) 150-deg streamline

Figure 78. Roughness height effects, spherical-cap geometry, $Re_\infty = 3.0\times10^6$/ft plots.

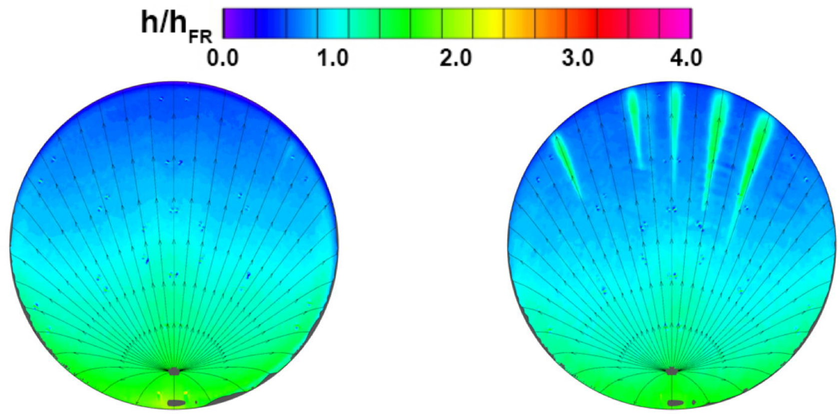

a) Test 7057, Run 9, Smooth model **b) Test 7057, Run 15, 230-mesh model**

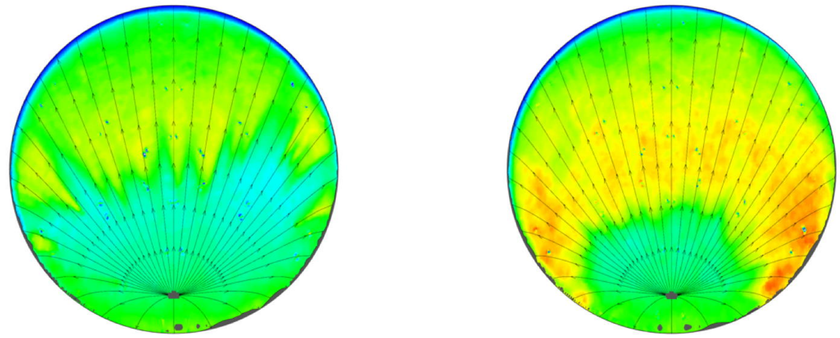

c) Test 7057, Run 21, 140-mesh model **d) Test 7057, Run 28, 80-mesh model**

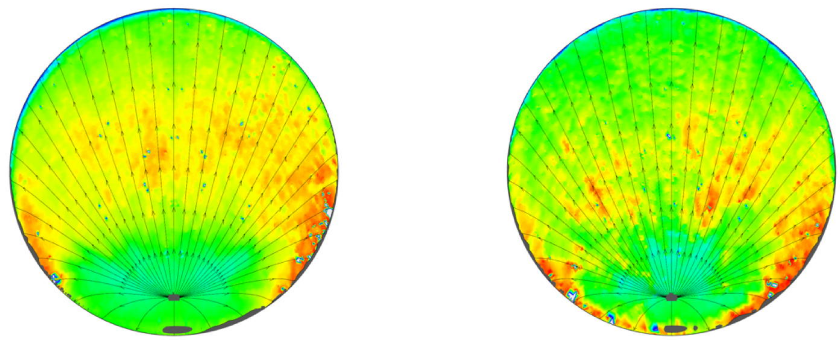

e) Test 7057, Run 34, 24 40-mesh model **f) Test 7057, Run 57, 20-mesh model**

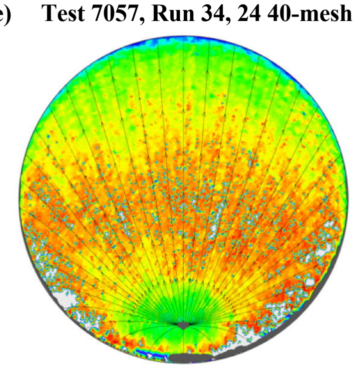

g) Test 7057, Run 44, 10-mesh model

Figure 79. Roughness height effects, spherical-cap geometry, $Re_\infty = 5.0\times10^6$/ft images.

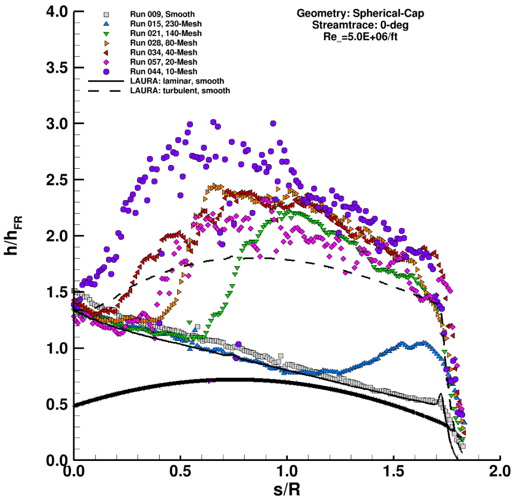

a) 0-deg streamline

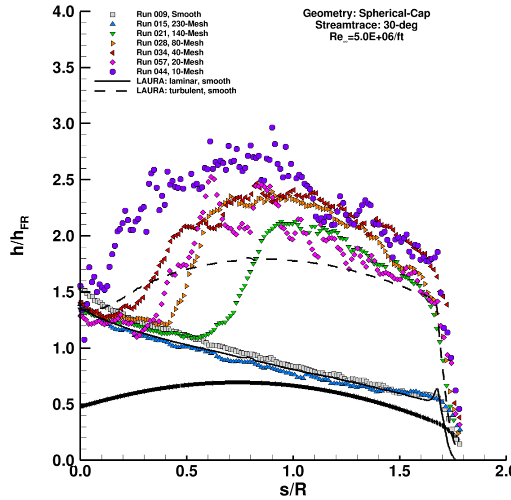

b) 30-deg streamline

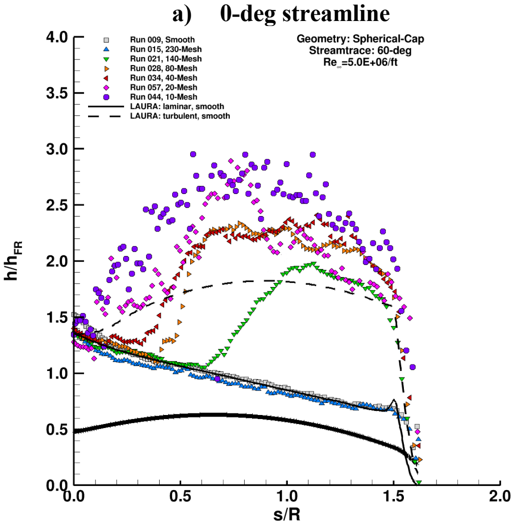

c) 60-deg streamline

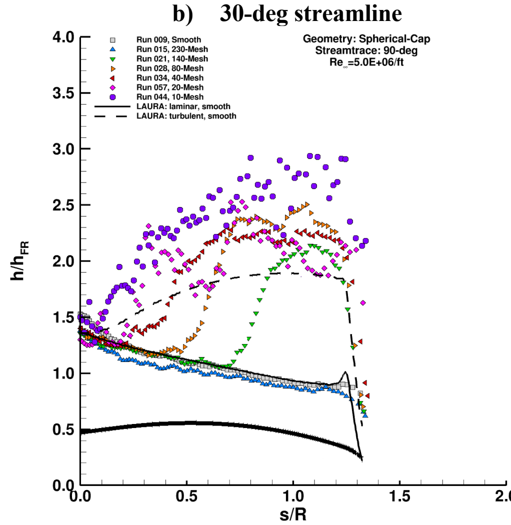

d) 90-deg streamline

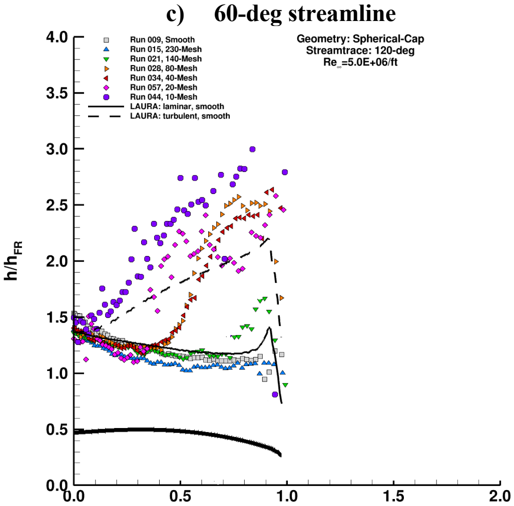

e) 120-deg streamline

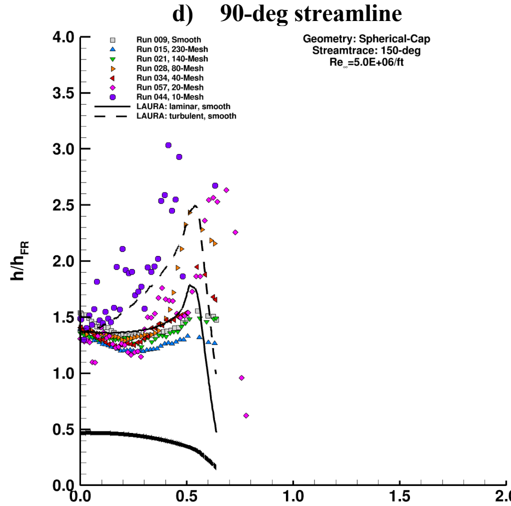

f) 150-deg streamline

Figure 80. Roughness height effects, spherical-cap geometry, $Re_\infty = 5.0\times10^6$/ft plots.

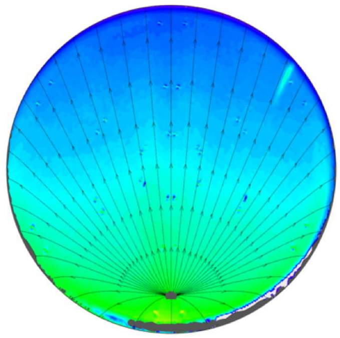

a) Test 7057, Run 10, Smooth model

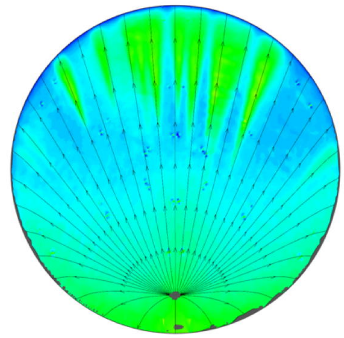

b) Test 7057, Run 16, 230-mesh model

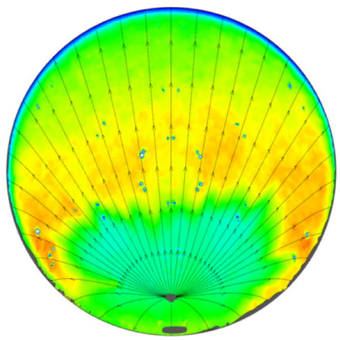

c) Test 7057, Run 22, 140-mesh model

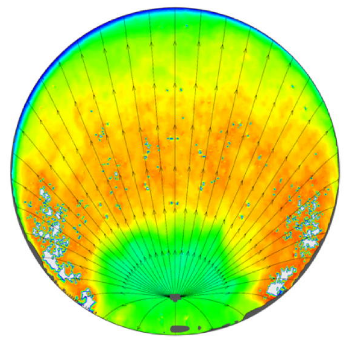

d) Test 7057, Run 29, 80-mesh model

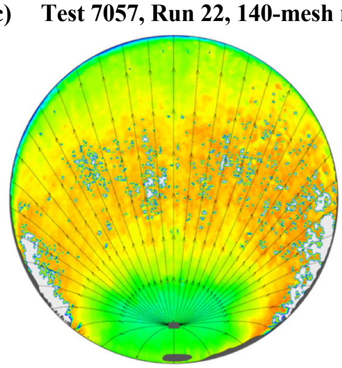

e) Test 7057, Run 35, 24 40-mesh model

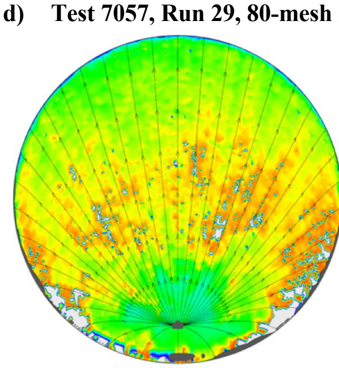

f) Test 7057, Run 58, 20-mesh model

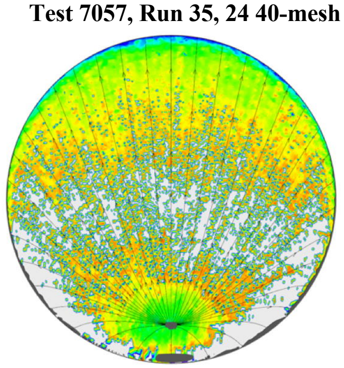

g) Test 7057, Run 45, 10-mesh model

Figure 81. Roughness height effects, spherical-cap geometry, $Re_\infty = 6.5\times10^6$/ft images.

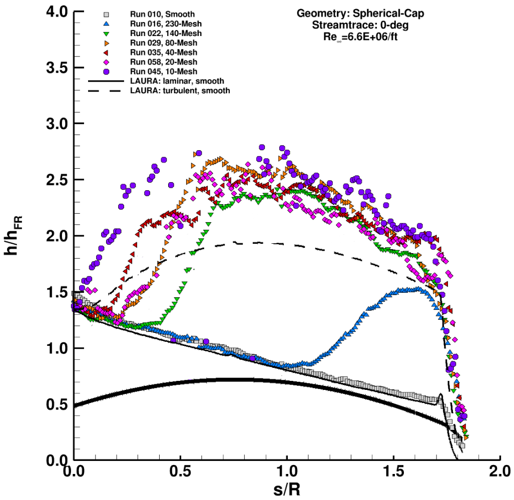

a) 0-deg streamline

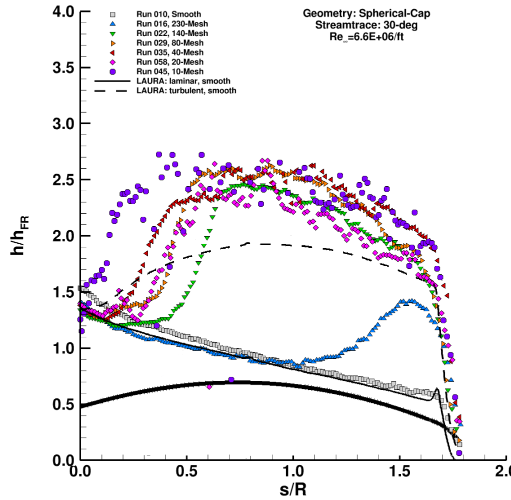

b) 30-deg streamline

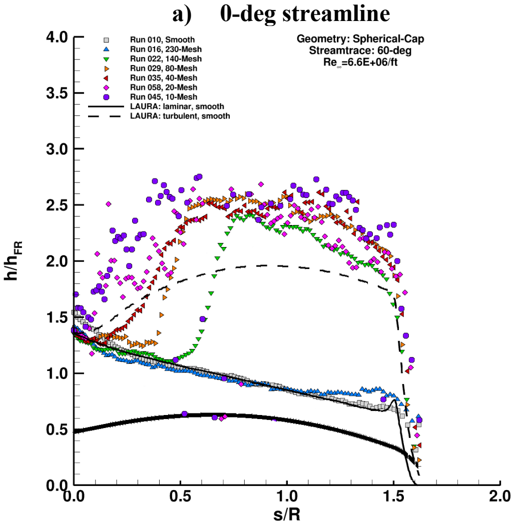

c) 60-deg streamline

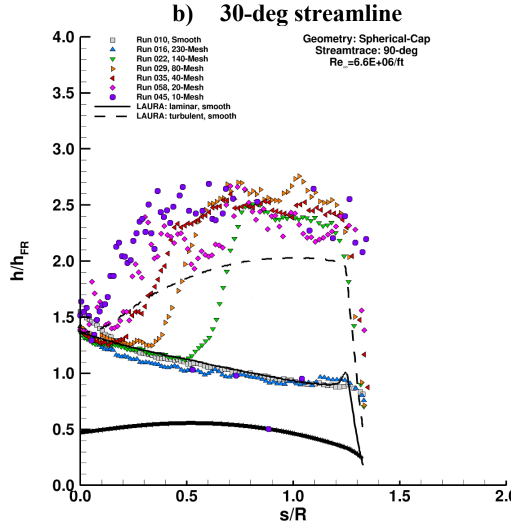

d) 90-deg streamline

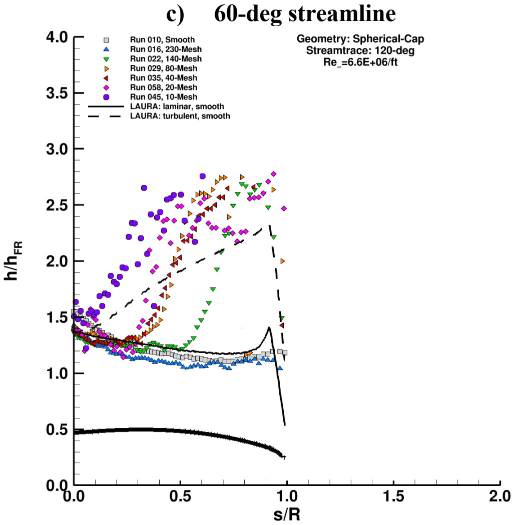

e) 120-deg streamline

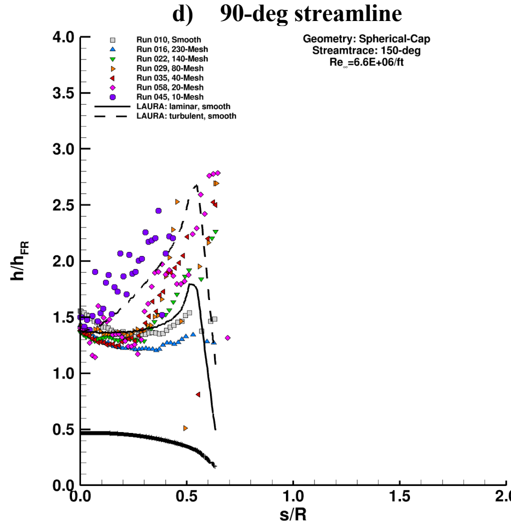

f) 150-deg streamline

Figure 82. Roughness height effects, spherical-cap geometry, $Re_\infty = 6.5\times10^6$/ft plots.

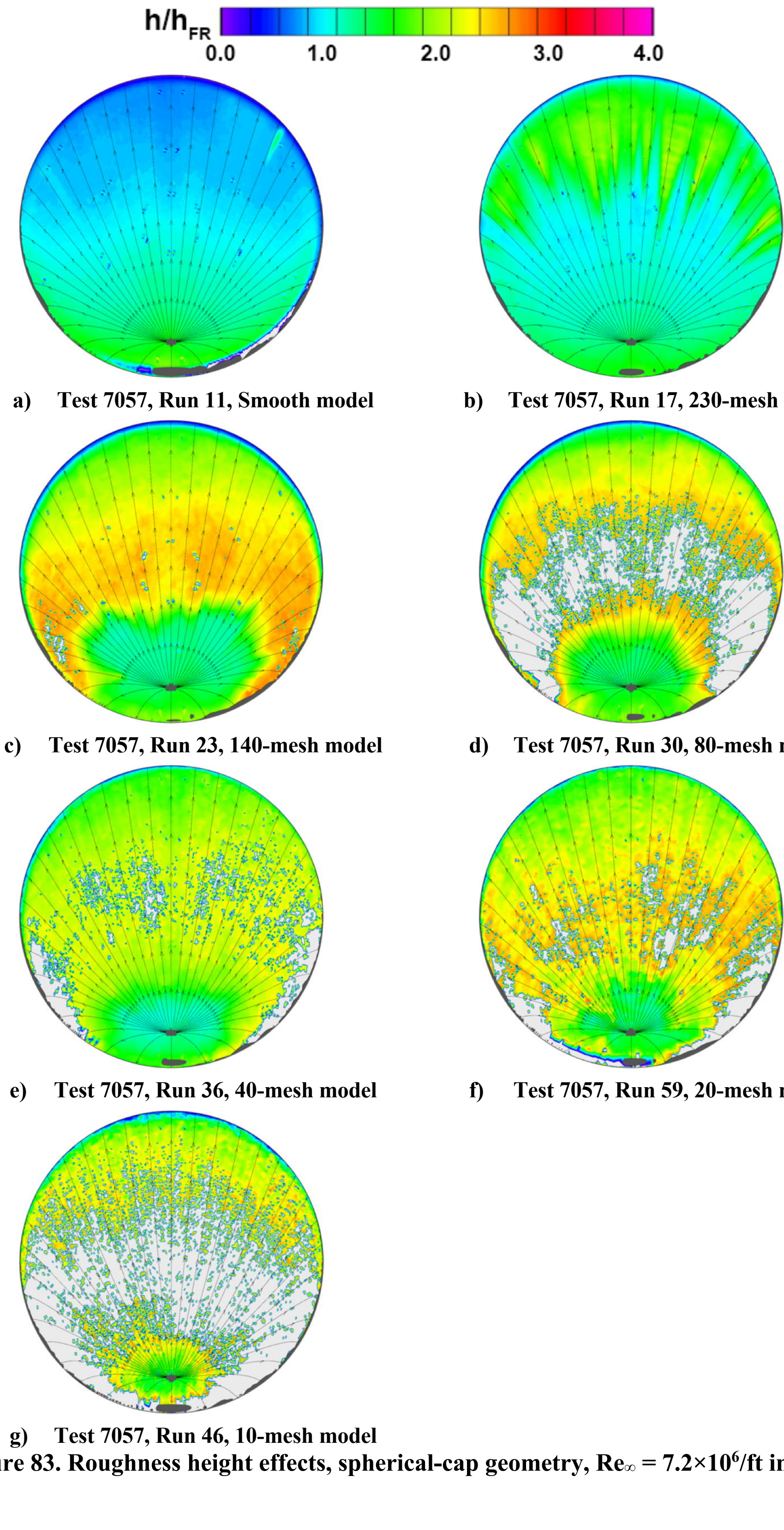

a) Test 7057, Run 11, Smooth model

b) Test 7057, Run 17, 230-mesh model

c) Test 7057, Run 23, 140-mesh model

d) Test 7057, Run 30, 80-mesh model

e) Test 7057, Run 36, 40-mesh model

f) Test 7057, Run 59, 20-mesh model

g) Test 7057, Run 46, 10-mesh model

Figure 83. Roughness height effects, spherical-cap geometry, $Re_\infty = 7.2\times10^6$/ft images.

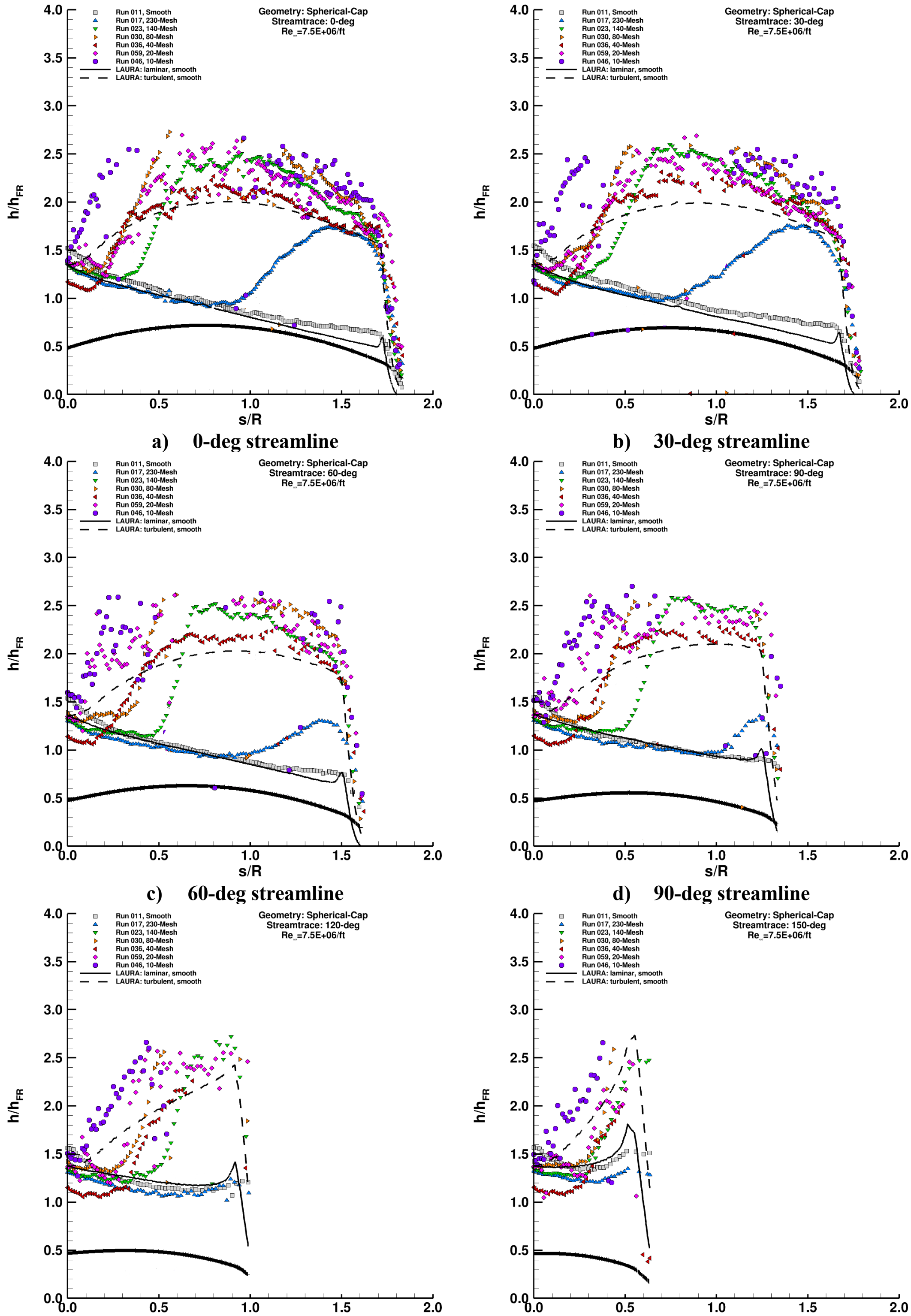

a) 0-deg streamline

b) 30-deg streamline

c) 60-deg streamline

d) 90-deg streamline

e) 120-deg streamline

f) 150-deg streamline

Figure 84. Roughness height effects, spherical-cap geometry, $Re_\infty = 7.2\times10^6$/ft plots.

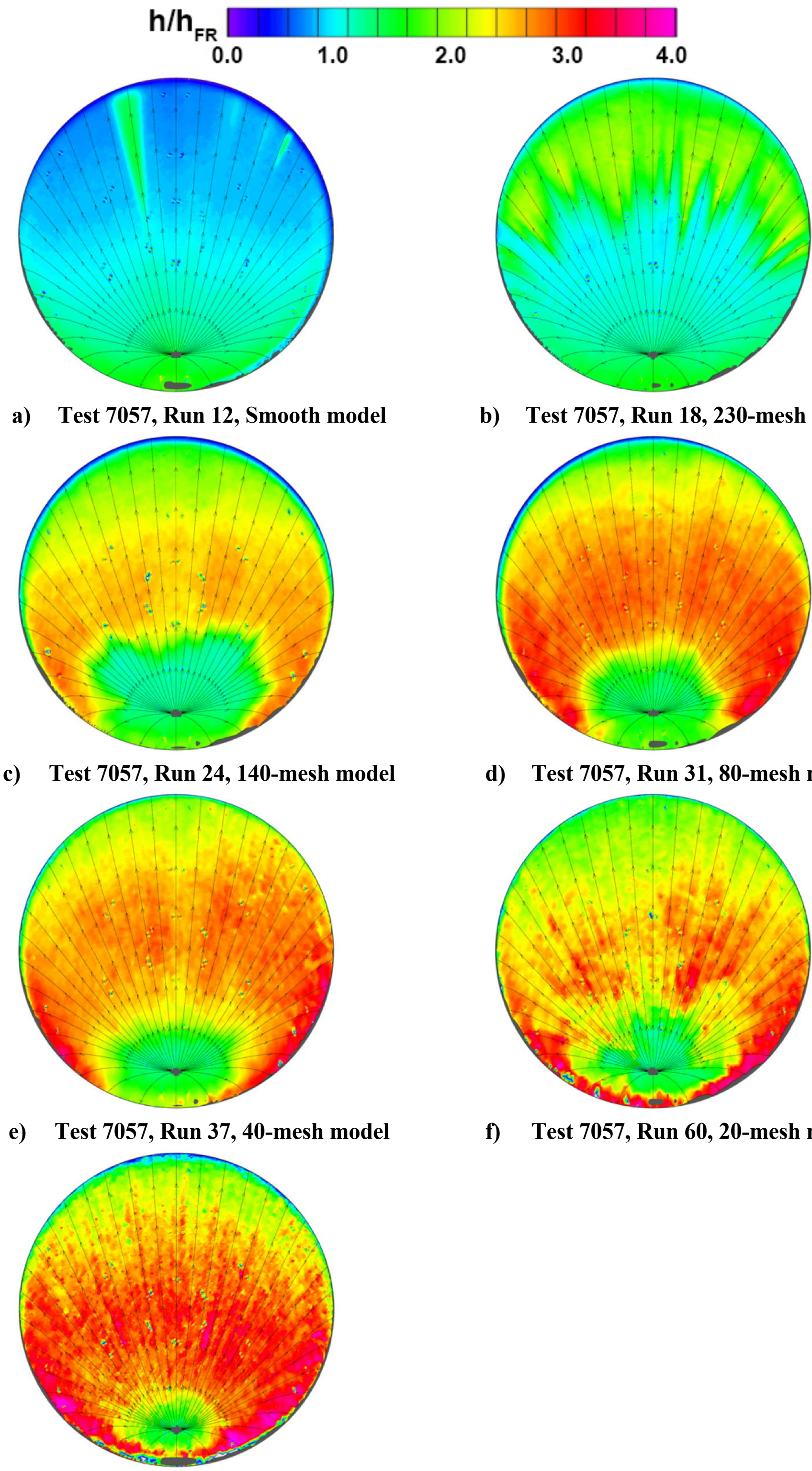

a) Test 7057, Run 12, Smooth model

b) Test 7057, Run 18, 230-mesh model

c) Test 7057, Run 24, 140-mesh model

d) Test 7057, Run 31, 80-mesh model

e) Test 7057, Run 37, 40-mesh model

f) Test 7057, Run 60, 20-mesh model

g) Test 7057, Run 47, 10-mesh model

Figure 85. Roughness height effects, spherical-cap geometry, $Re_\infty = 8.1\times10^6$/ft images.

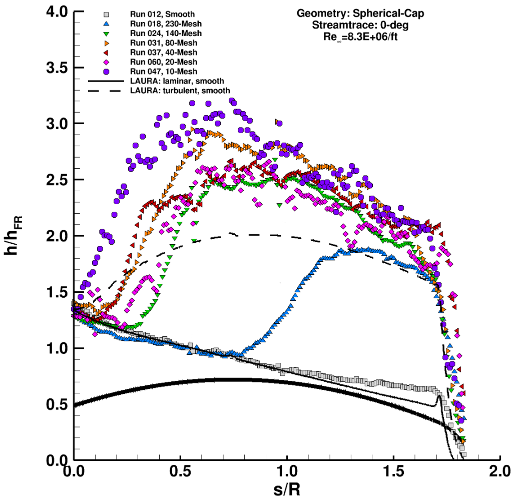

a) 0-deg streamline

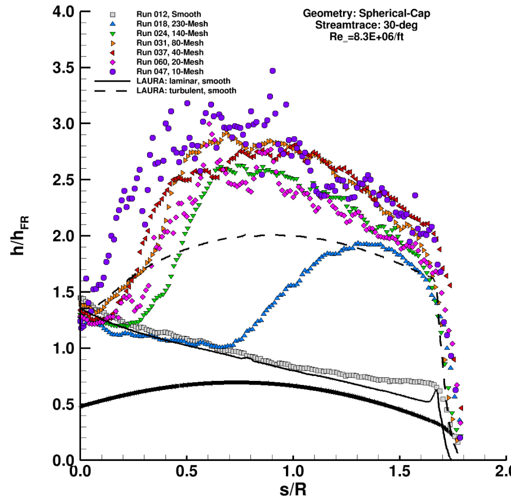

b) 30-deg streamline

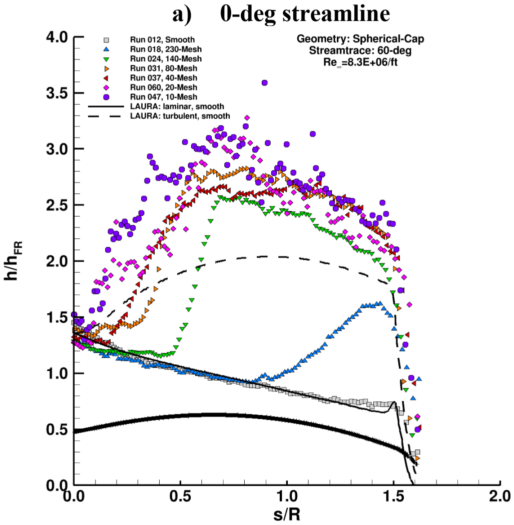

c) 60-deg streamline

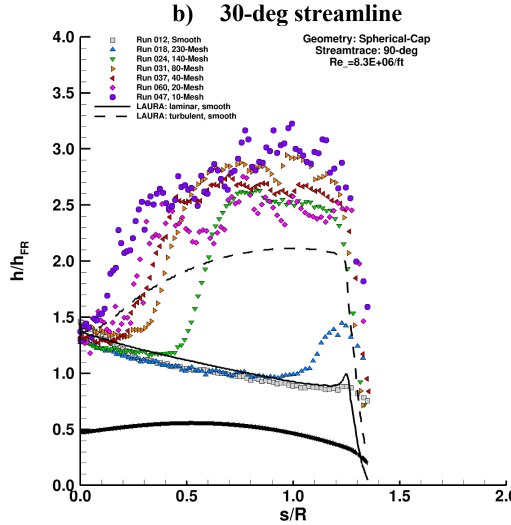

d) 90-deg streamline

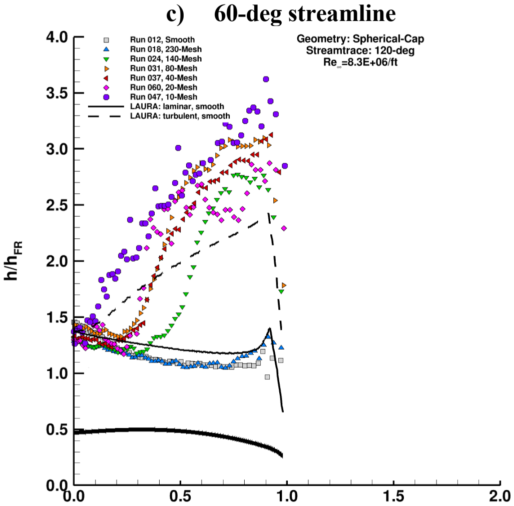

e) 120-deg streamline

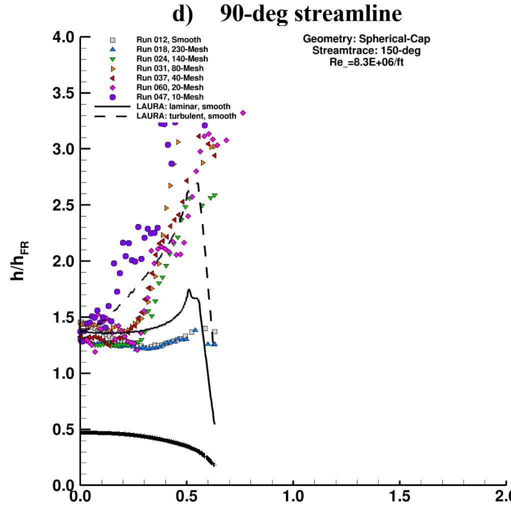

f) 150-deg streamline

Figure 86. Roughness height effects, spherical-cap geometry, $Re_\infty = 8.1\times10^6$/ft plots.

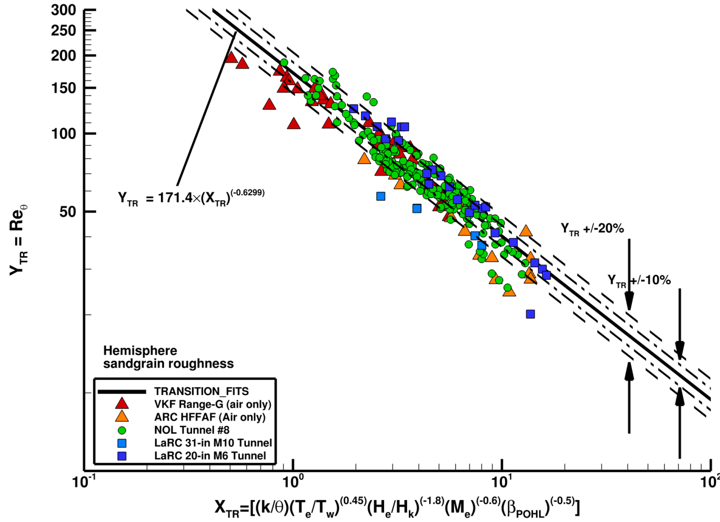

a) Applied to hemisphere geometry with sand-grain roughness

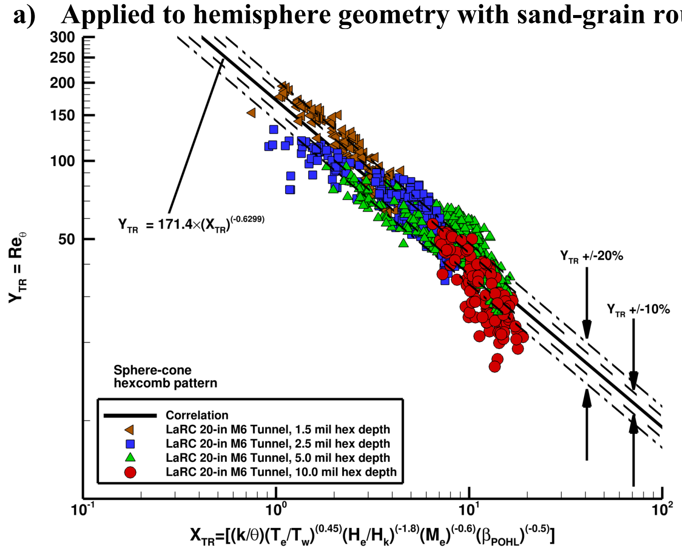

b) Applied to sphere-cone geometry with pattern-hexcomb roughness

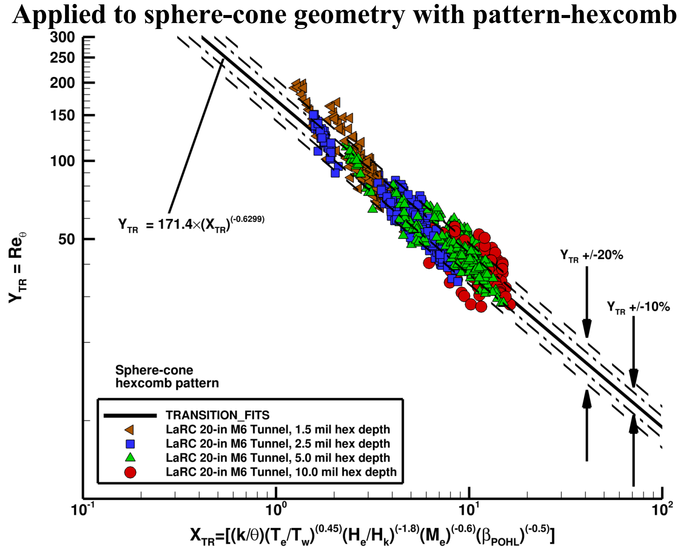

c) Applied to spherical-cap geometry with pattern-hexcomb roughness

Figure 87. Roughness transition correlation applied to prior datasets.

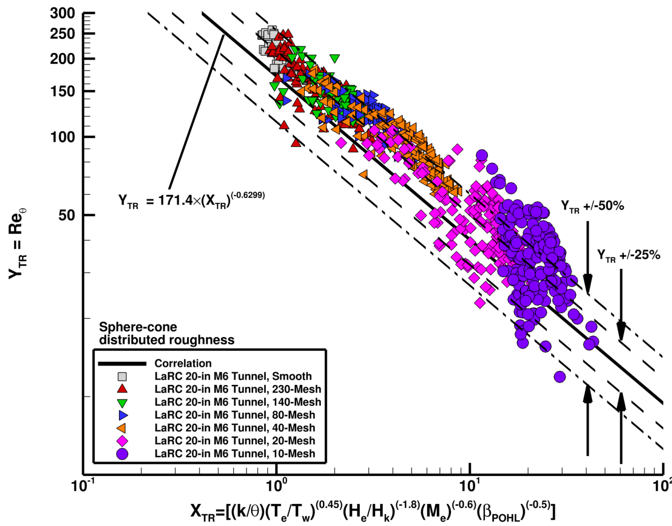

a) Applied to sphere-cone geometry with sand-grain roughness

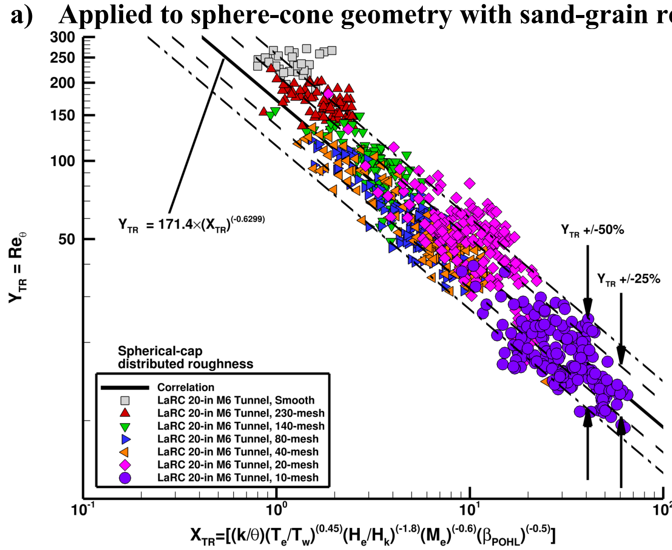

b) Applied to spherical-cap geometry with sand-grain roughness

Figure 88. Roughness transition correlation applied to current datasets.

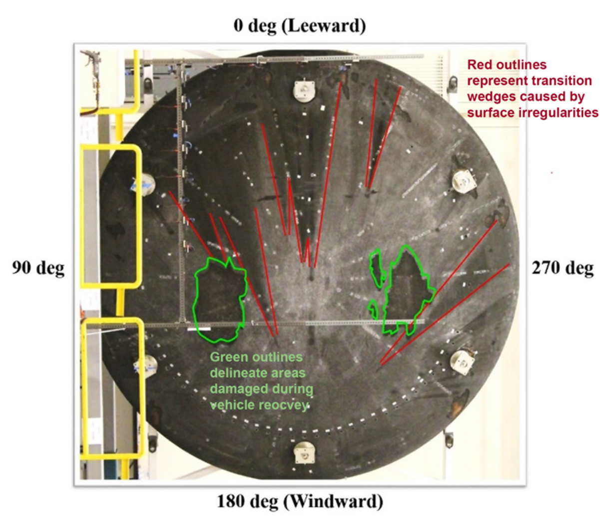

Figure 89. Post-flight recovery picture of Orion EFT-1 heatshield

Appendix A. Sphere-Cone Geometry Global Heating Images

Global heating images for the sphere-cone geometry from Test 7036 in the LAL 20-Inch Mach 6 Air Tunnel are presented in this Appendix in Figure 90 through Figure 131.

At higher Reynolds numbers and/or larger roughness heights, white patches on the images indicate areas where the measured surface temperatures exceed the calibrated range of the phosphor thermography and thus no valid data were obtained.

Boundary-layer edge streamlines determined from laminar, smooth-surface LAURA simulations have been superimposed on the images to illustrate the nature of the flow field.

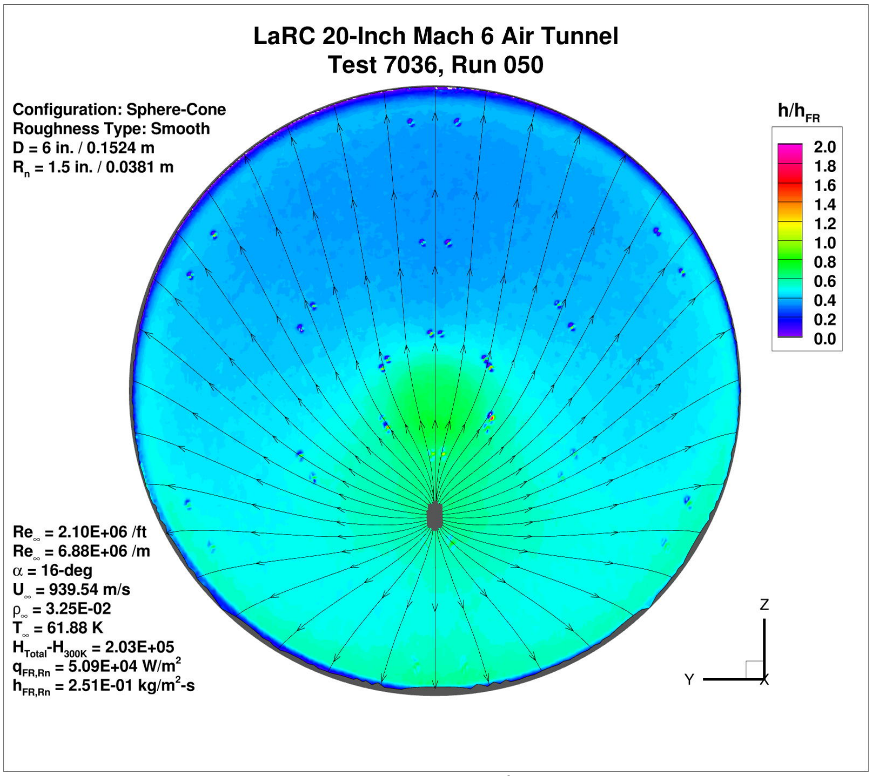

Figure 90. Test 7036, Run 50, Re∞ = 2.1×10^6/ft, sphere-cone, smooth OML.

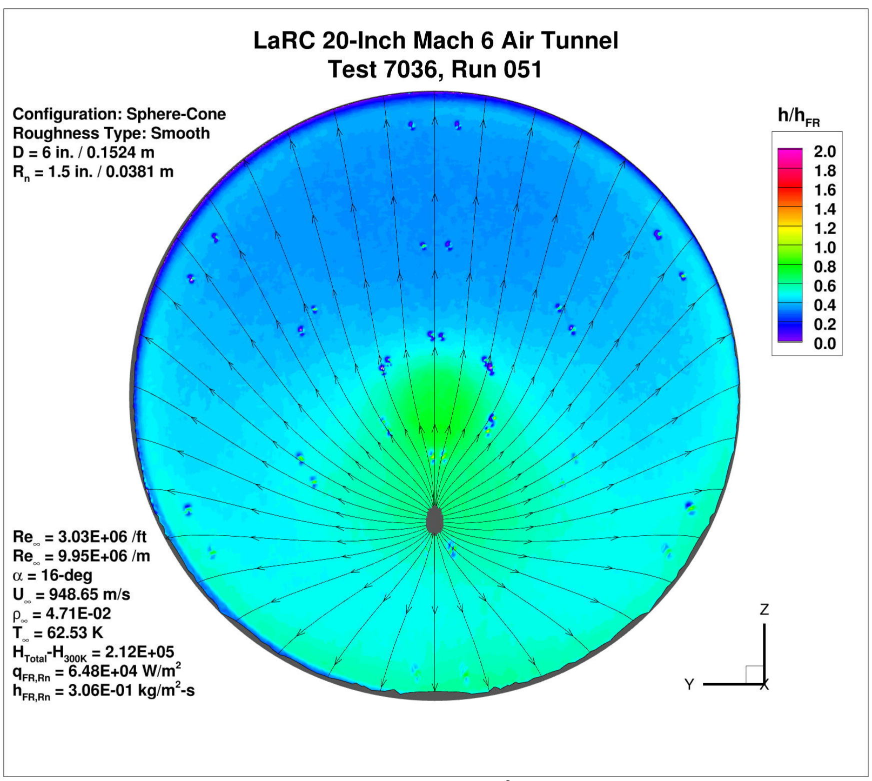

Figure 91. Test 7036, Run 51, Re∞ = 3.0×10^6/ft, sphere-cone, smooth OML.

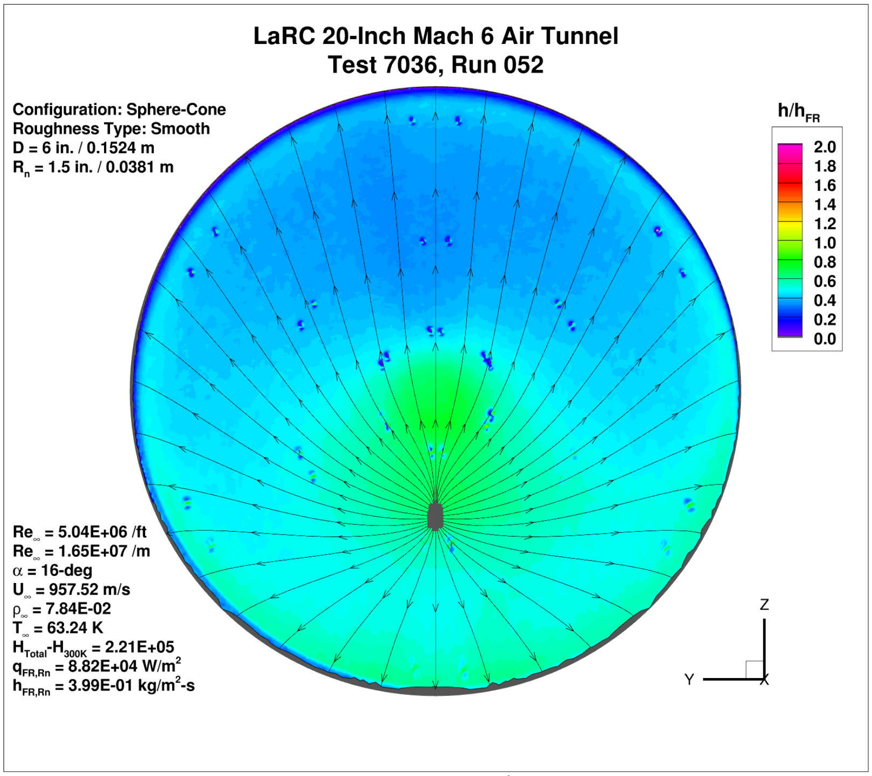

Figure 92. Test 7036, Run 52, Re∞ = 5.0×10^6/ft, sphere-cone, smooth OML.

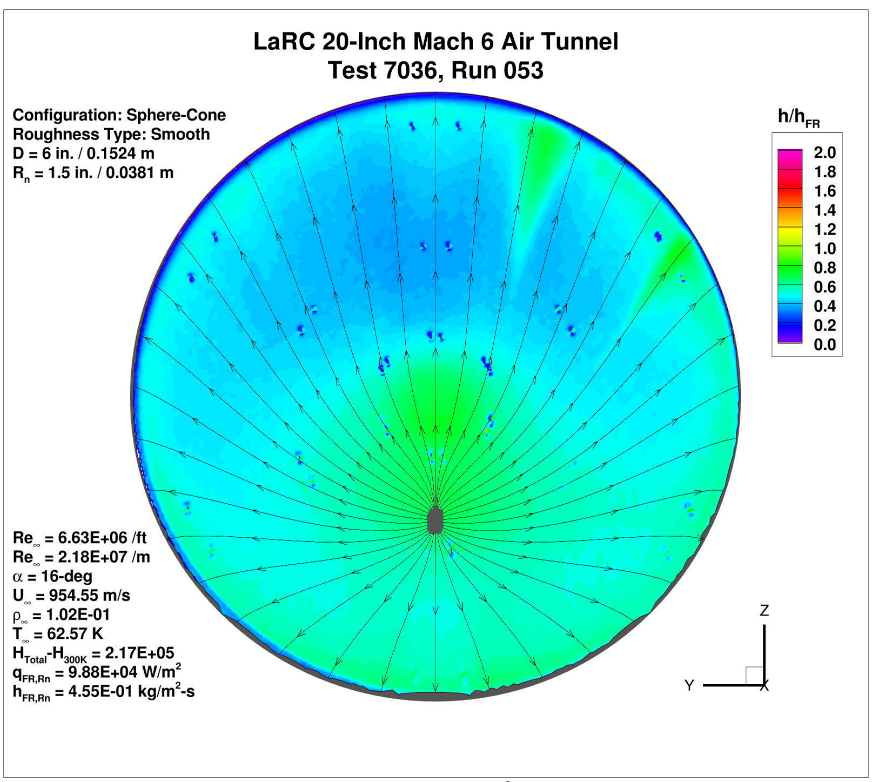

Figure 93. Test 7036, Run 53, Re∞ = 6.5×10^6/ft, sphere-cone, smooth OML.

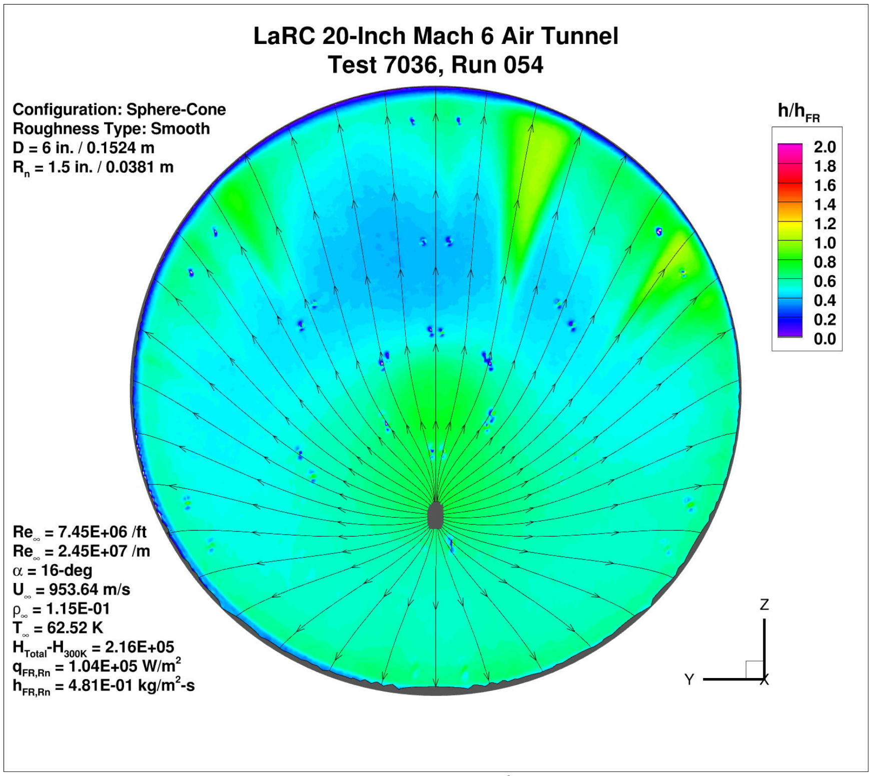

Figure 94. Test 7036, Run 54, Re∞ = 7.2×10^6/ft, sphere-cone, smooth OML.

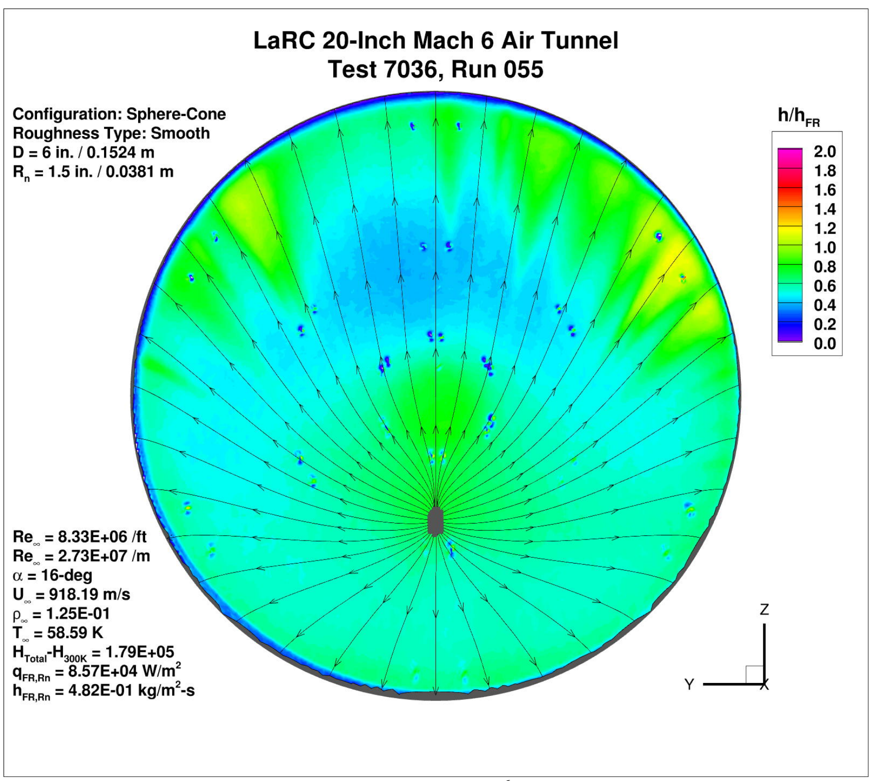

Figure 95. Test 7036, Run 55, Re∞ = 8.1×10^6/ft, sphere-cone, smooth OML.

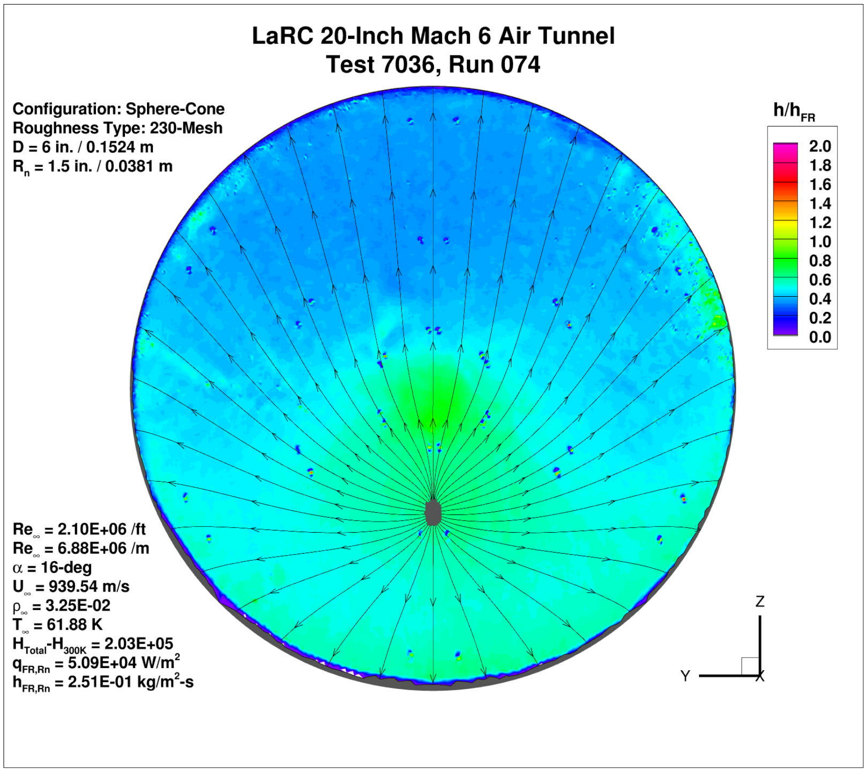

Figure 96. Test 7036, Run 74, Re∞ = 2.1×10^6/ft, sphere-cone, 230-mesh.

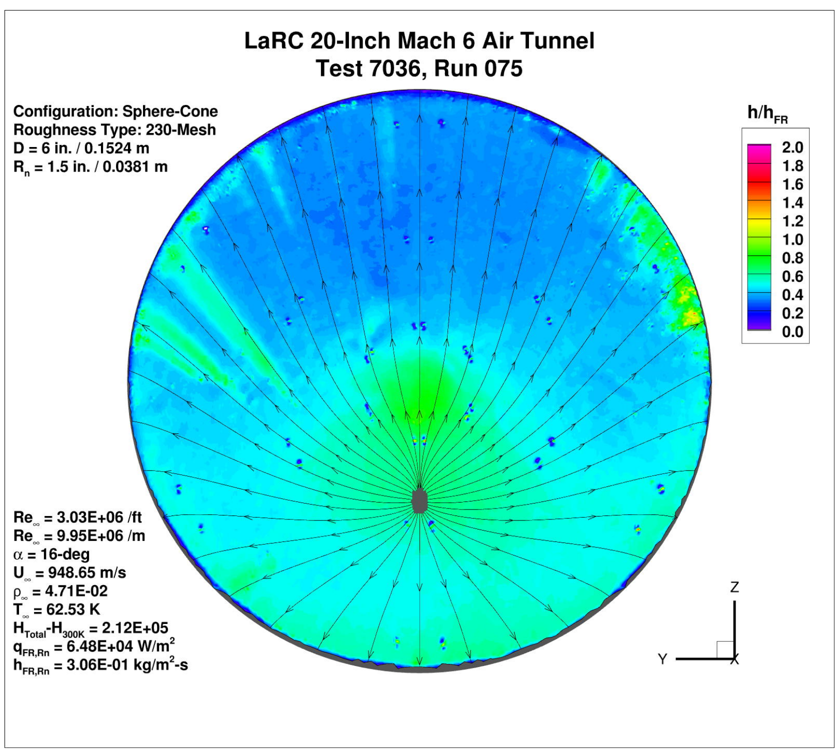

Figure 97. Test 7036, Run 75, Re∞ = 3.0×10^6/ft, sphere-cone, 230-mesh.

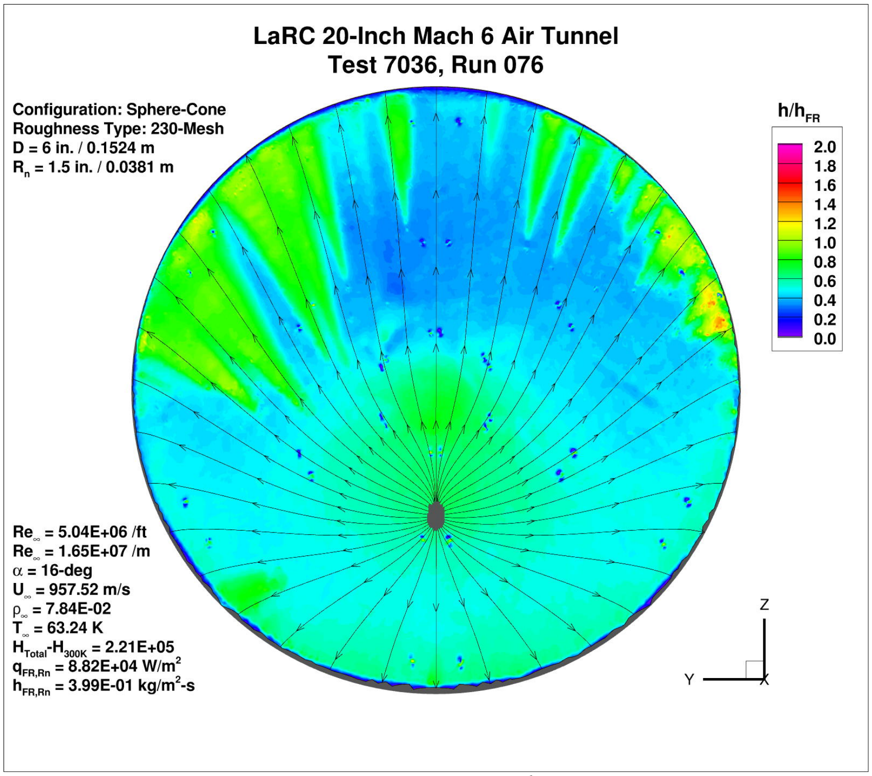

Figure 98. Test 7036, Run 76, $Re_\infty = 5.0\times10^6$/ft, sphere-cone, 230-mesh.

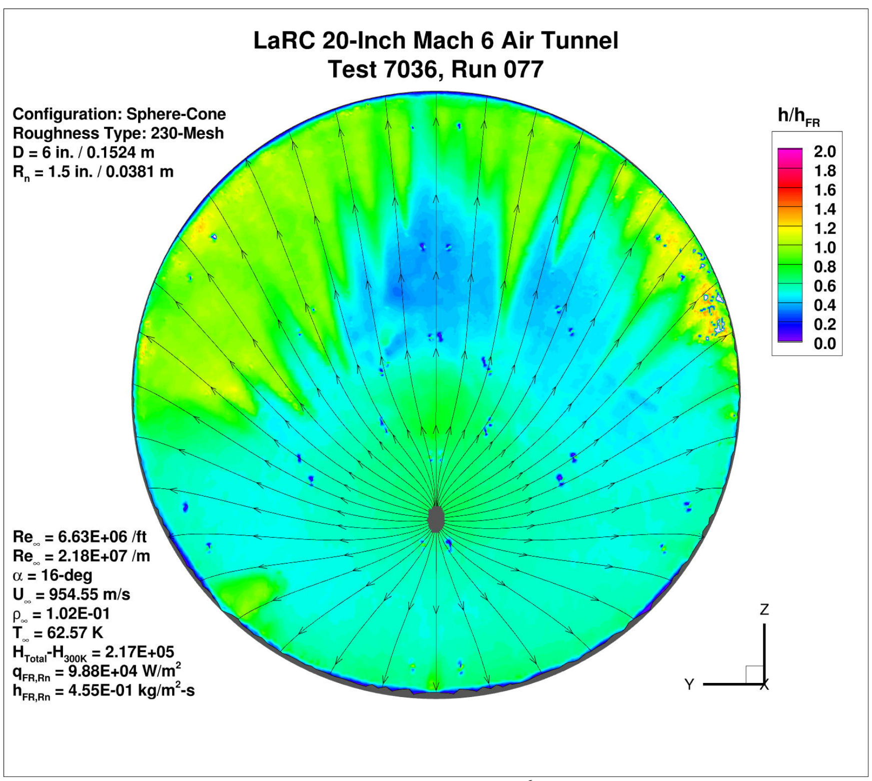

Figure 99. Test 7036, Run 77, $Re_\infty = 6.5\times10^6$/ft, sphere-cone, 230-mesh.

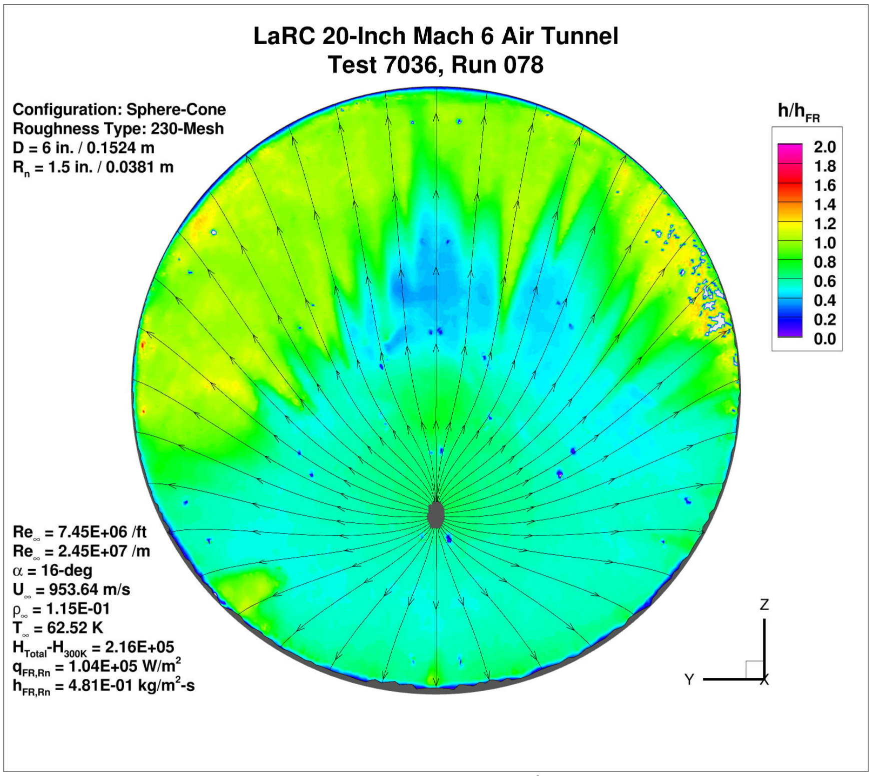

Figure 100. Test 7036, Run 78, Re∞ = 7.2×10^6/ft, sphere-cone, 230-mesh.

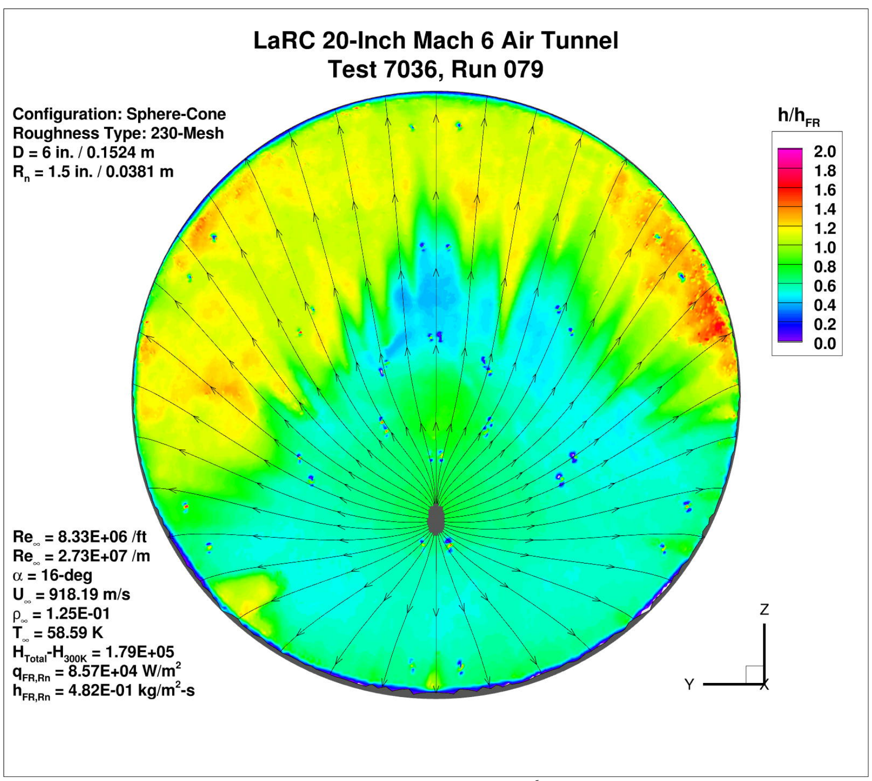

Figure 101. Test 7036, Run 79, Re∞ = 8.1×10^6/ft, sphere-cone, 230-mesh.

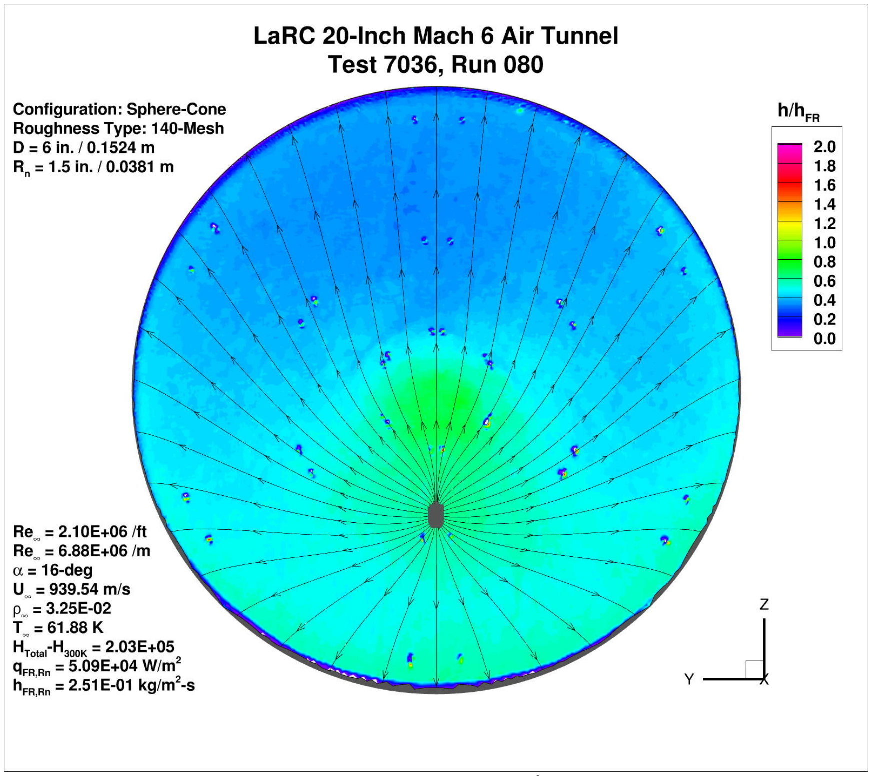

Figure 102. Test 7036, Run 80, $Re_\infty = 2.1\times10^6$/ft, sphere-cone, 140-mesh.

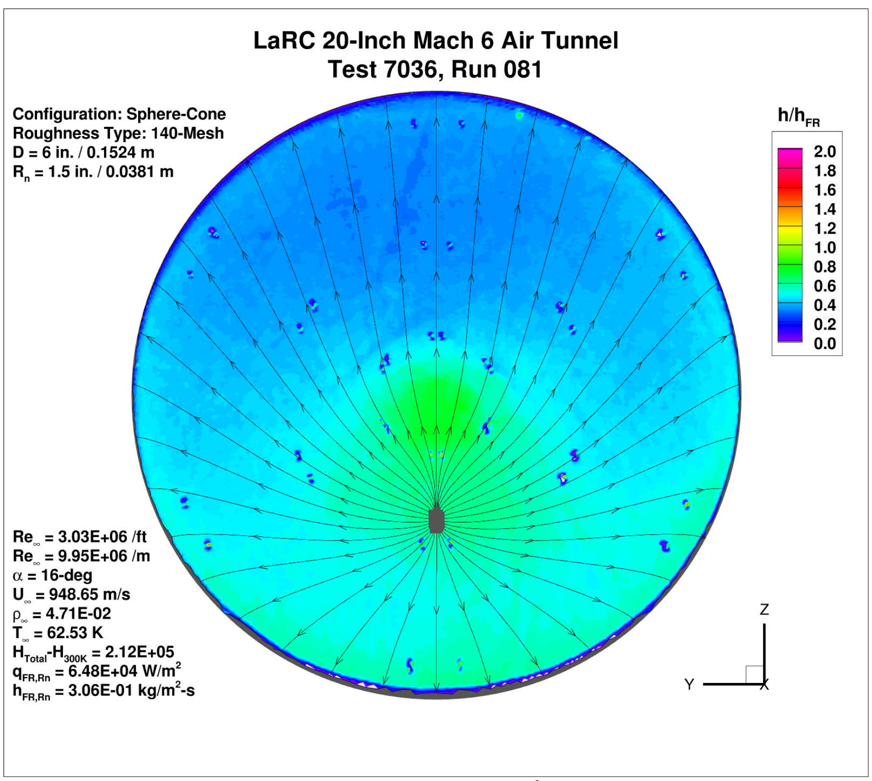

Figure 103. Test 7036, Run 81, $Re_\infty = 3.0\times10^6$/ft, sphere-cone, 140-mesh.

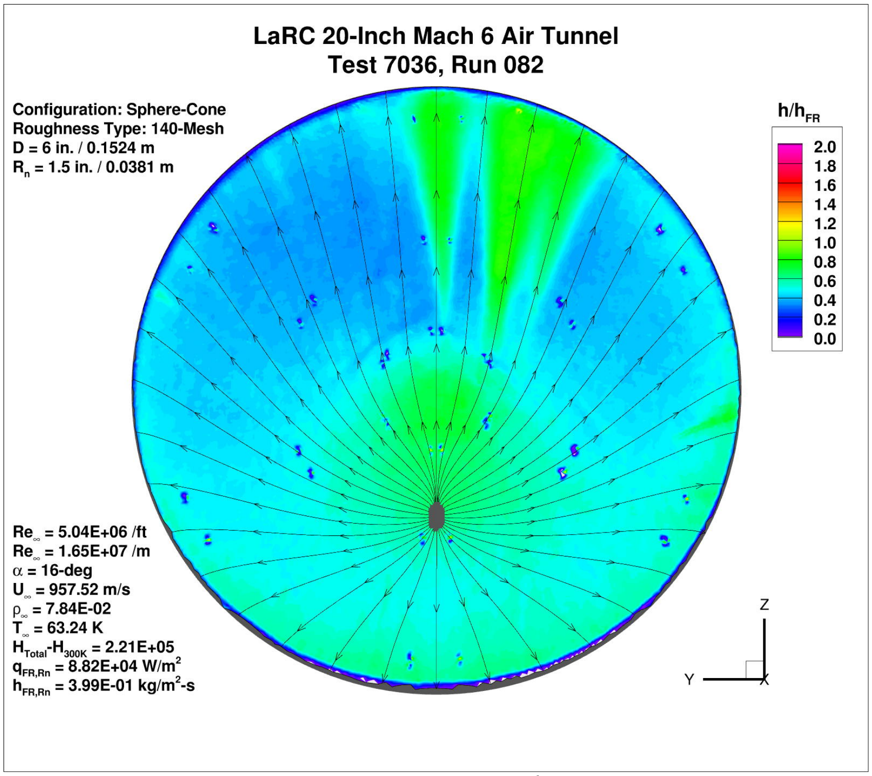

Figure 104. Test 7036, Run 82, Re∞ = 5.0×10⁶/ft, sphere-cone, 140-mesh.

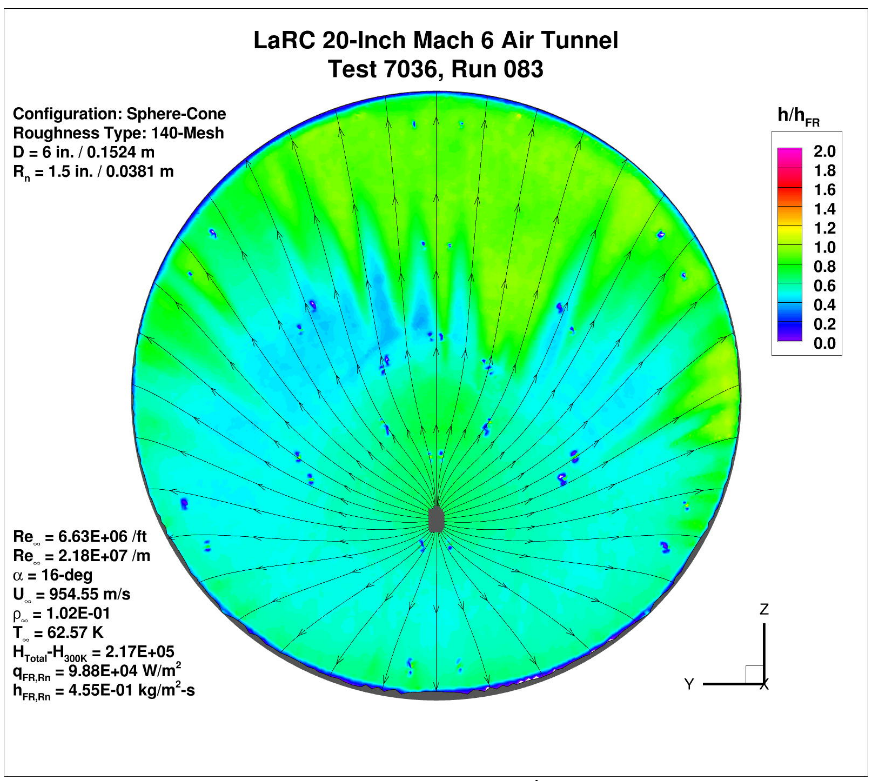

Figure 105. Test 7036, Run 83, Re∞ = 6.5×10⁶/ft, sphere-cone, 140-mesh.

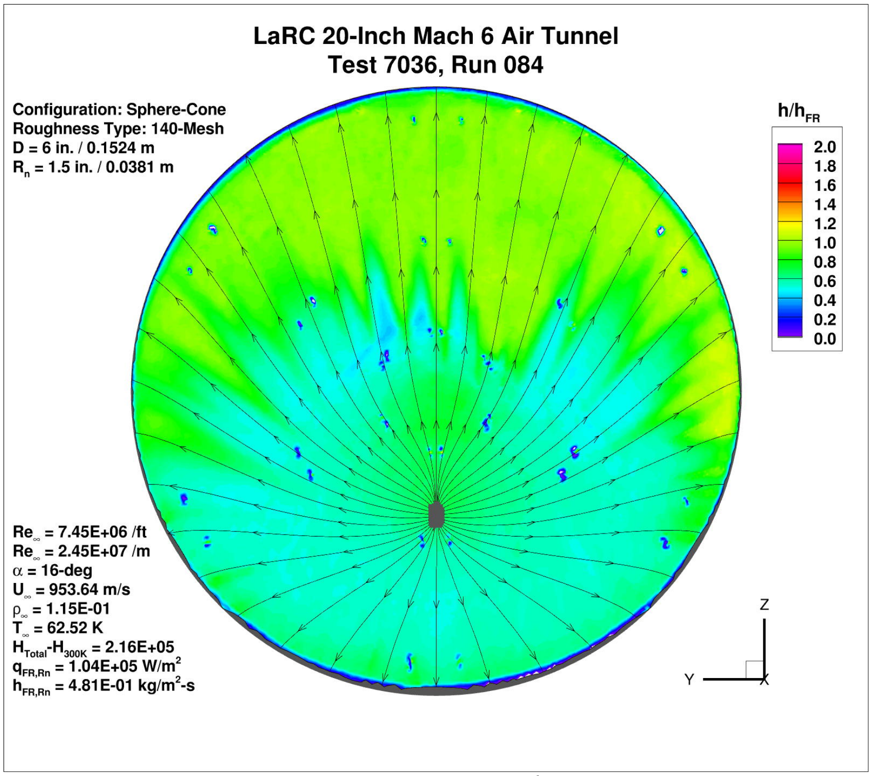

Figure 106. Test 7036, Run 84, $Re_\infty = 7.2 \times 10^6$/ft, sphere-cone, 140-mesh.

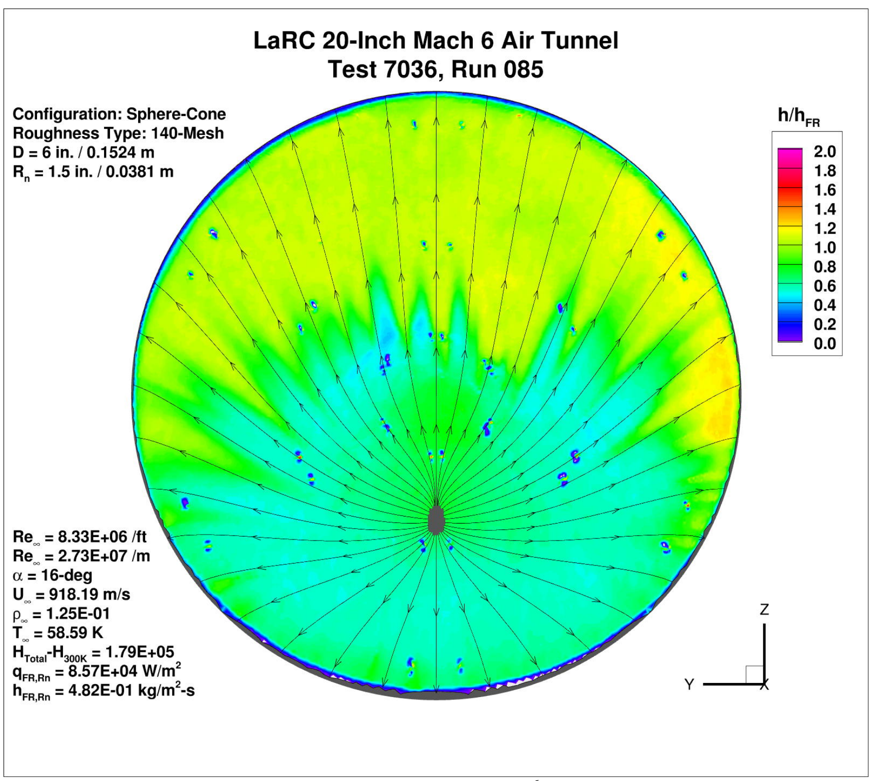

Figure 107. Test 7036, Run 85, $Re_\infty = 8.1 \times 10^6$/ft, sphere-cone, 140-mesh.

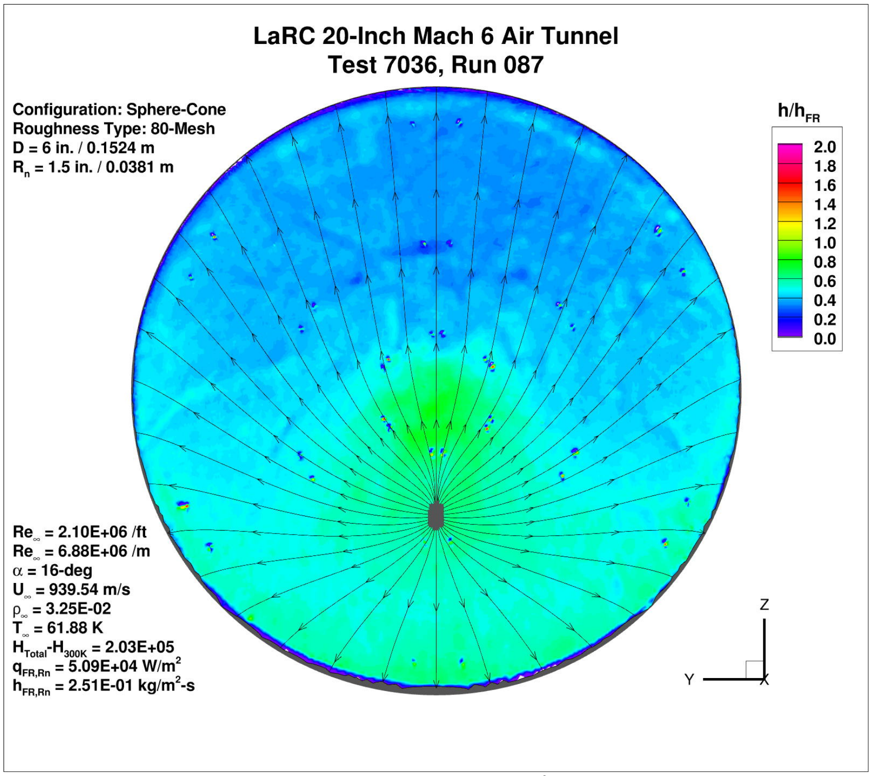

Figure 108. Test 7036, Run 87, $Re_\infty = 2.1\times10^6$/ft, sphere-cone, 80-mesh.

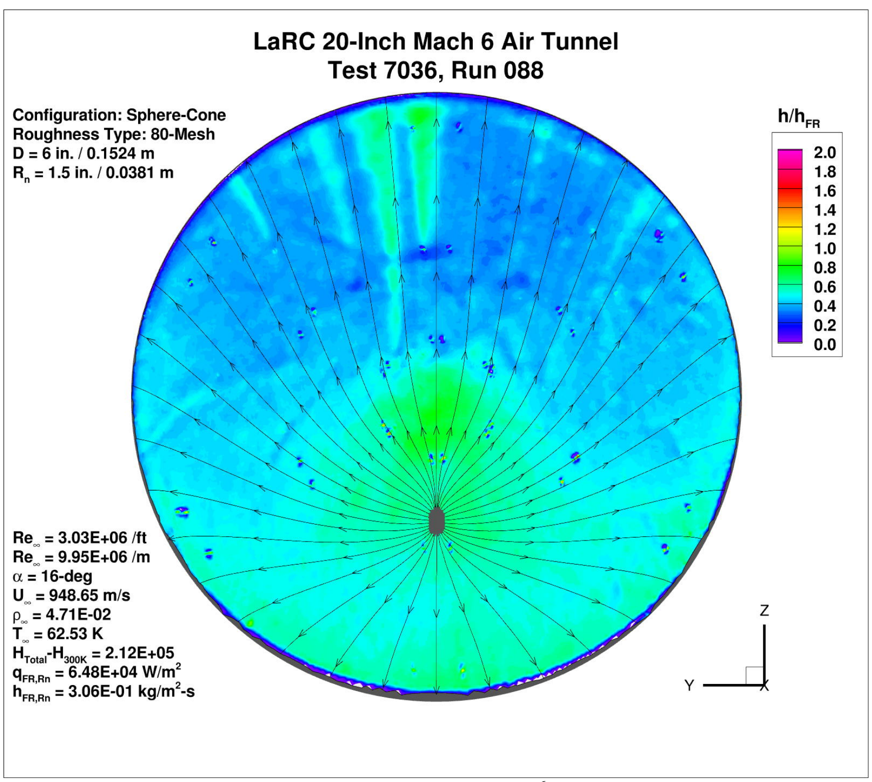

Figure 109. Test 7036, Run 88, $Re_\infty = 3.0\times10^6$/ft, sphere-cone, 80-mesh.

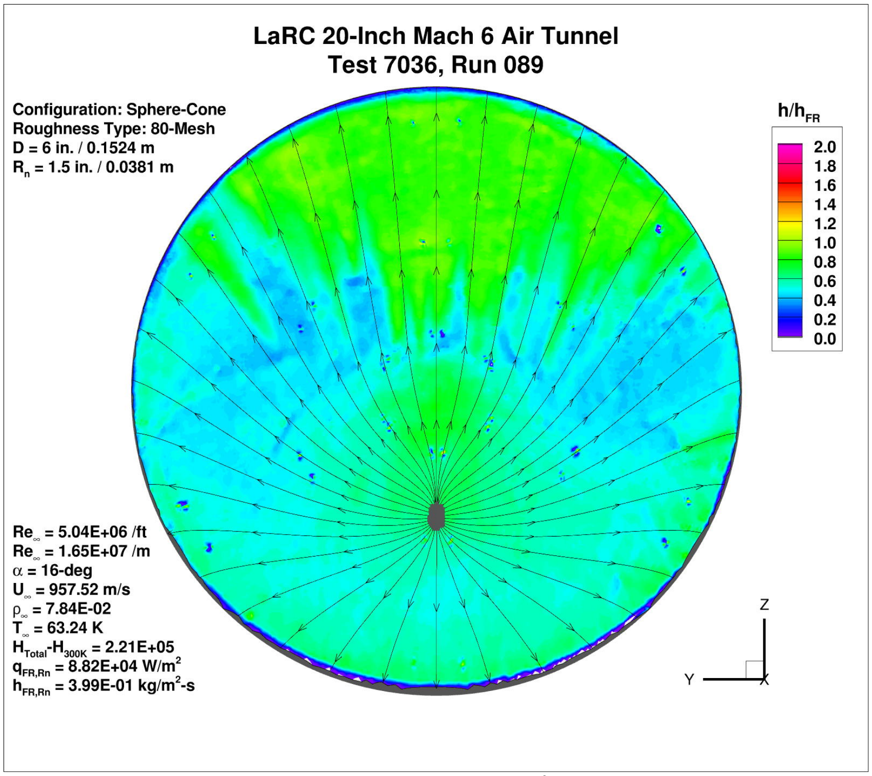

Figure 110. Test 7036, Run 89, Re∞ = 5.0×10^6/ft, sphere-cone, 80-mesh.

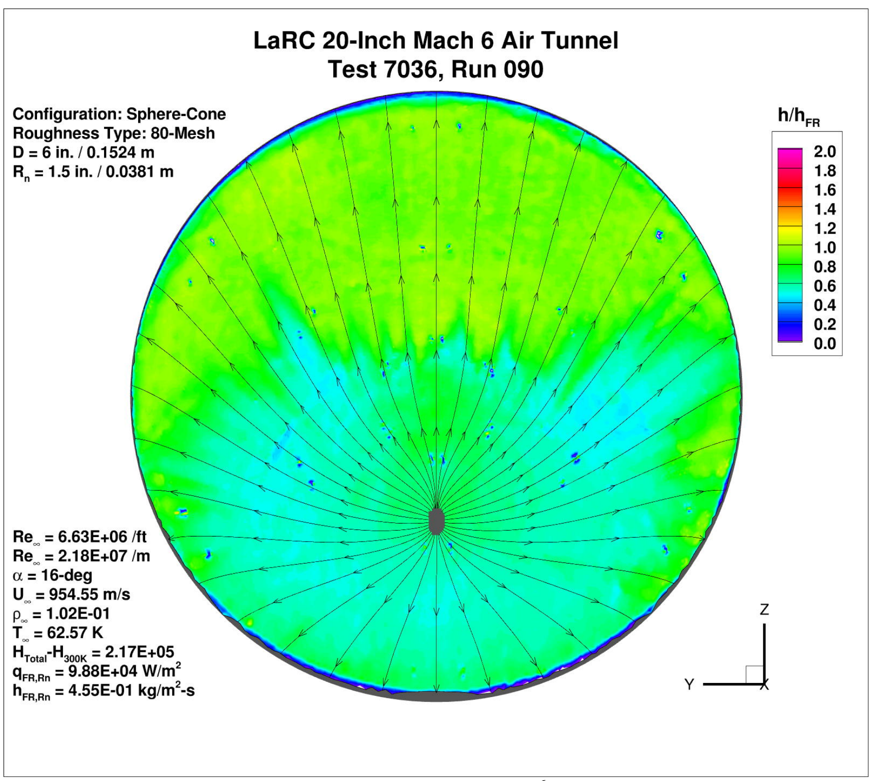

Figure 111. Test 7036, Run 90, Re∞ = 6.5×10^6/ft, sphere-cone, 80-mesh.

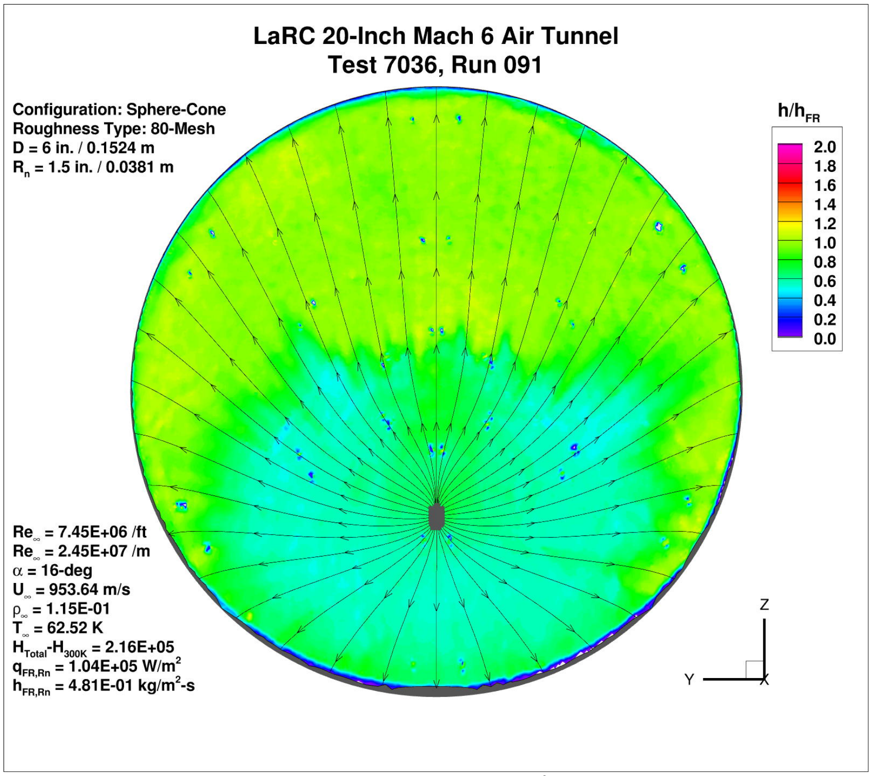

Figure 112. Test 7036, Run 91, Re∞ = 7.2×10^6/ft, sphere-cone, 80-mesh.

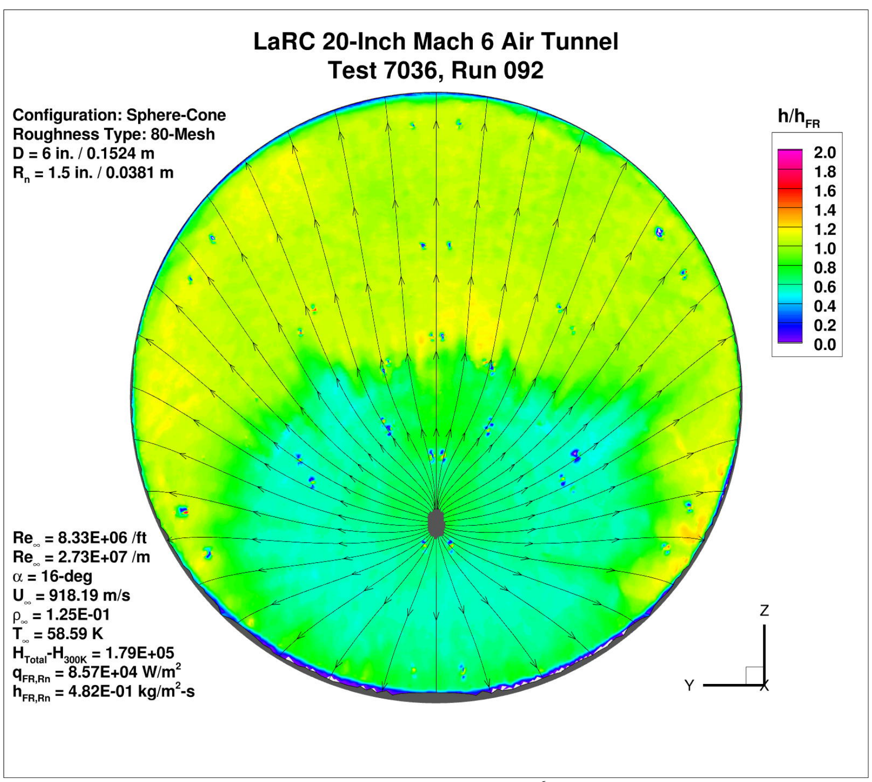

Figure 113. Test 7036, Run 92, Re∞ = 8.1×10^6/ft, sphere-cone, 80-mesh.

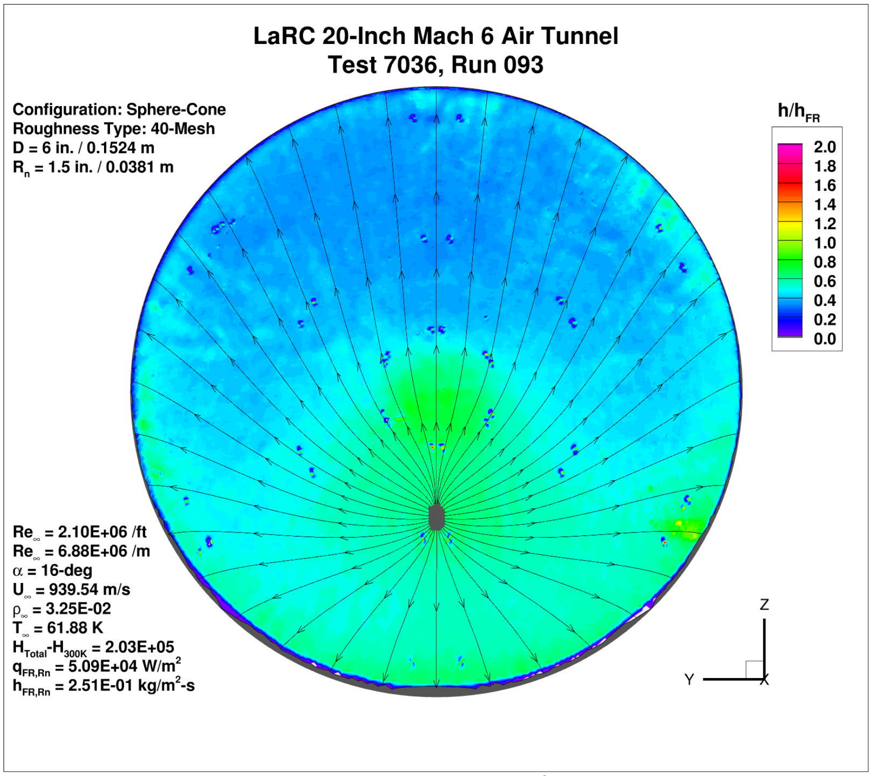

Figure 114. Test 7036, Run 93, Re∞ = 2.1×10^6/ft, sphere-cone, 40-mesh.

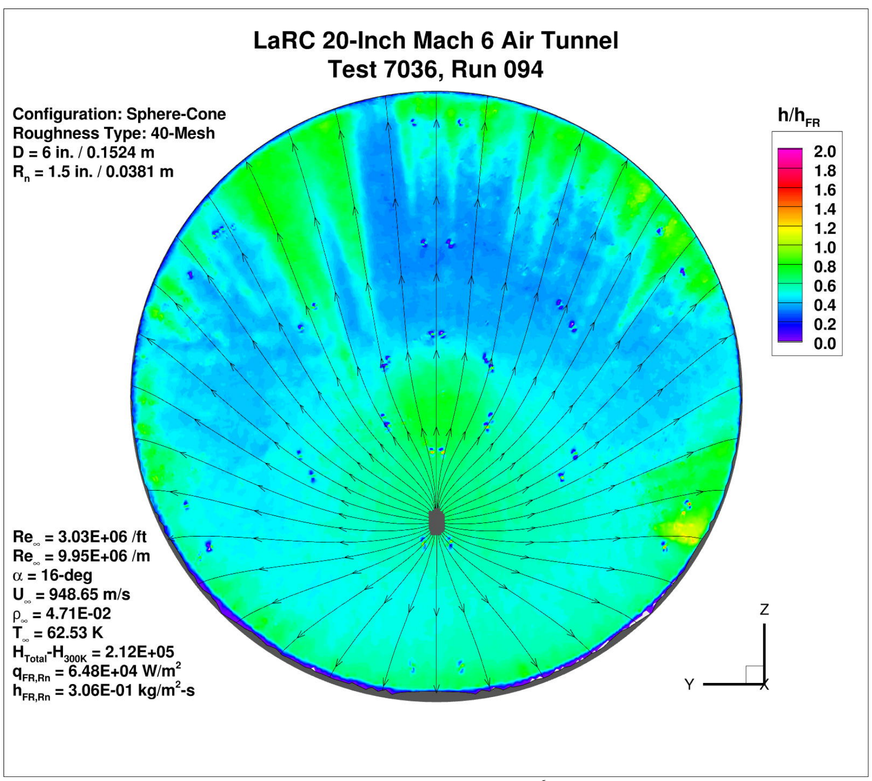

Figure 115. Test 7036, Run 94, Re∞ = 3.0×10^6/ft, sphere-cone, 40-mesh.

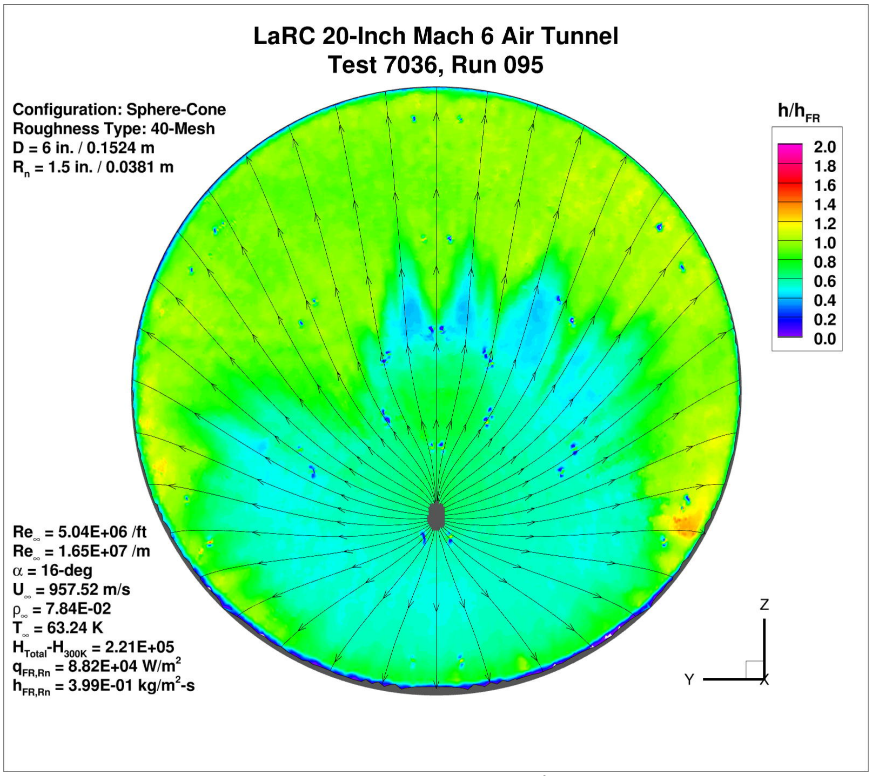

Figure 116. Test 7036, Run 95, $Re_\infty = 5.0\times10^6$/ft, sphere-cone, 40-mesh.

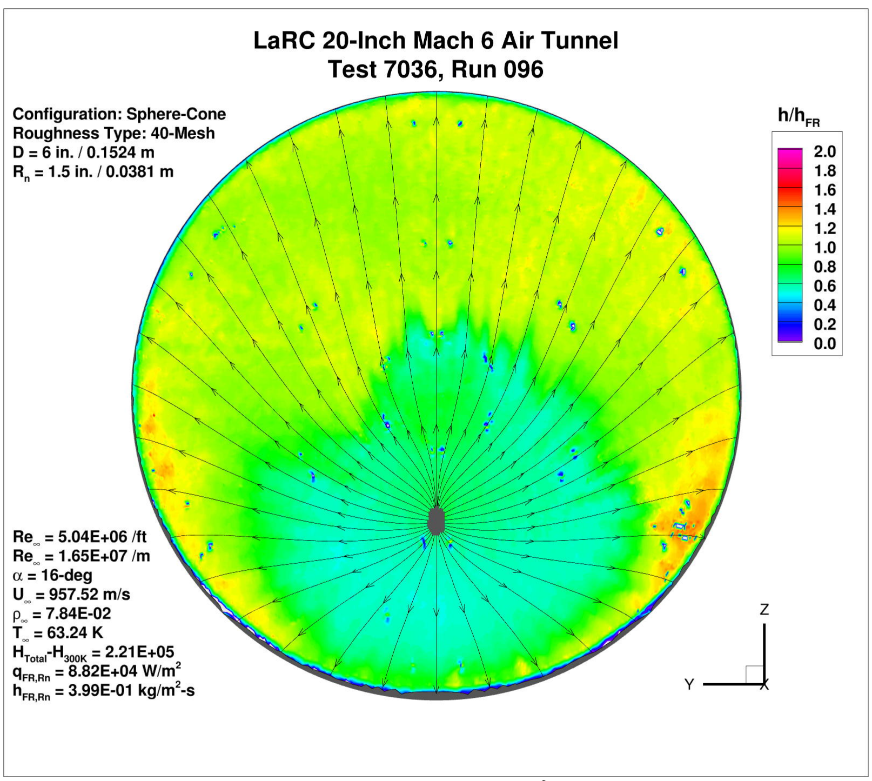

Figure 117. Test 7036, Run 96, $Re_\infty = 6.5\times10^6$/ft, sphere-cone, 40-mesh.

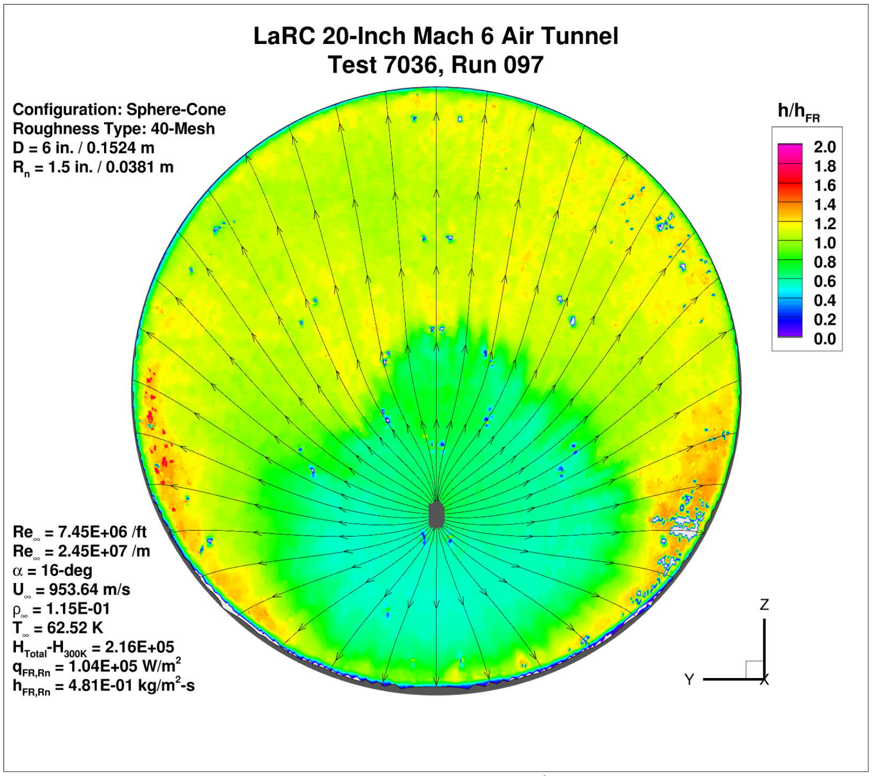

Figure 118. Test 7036, Run 97, Re∞ = 7.2×10^6/ft, sphere-cone, 40-mesh.

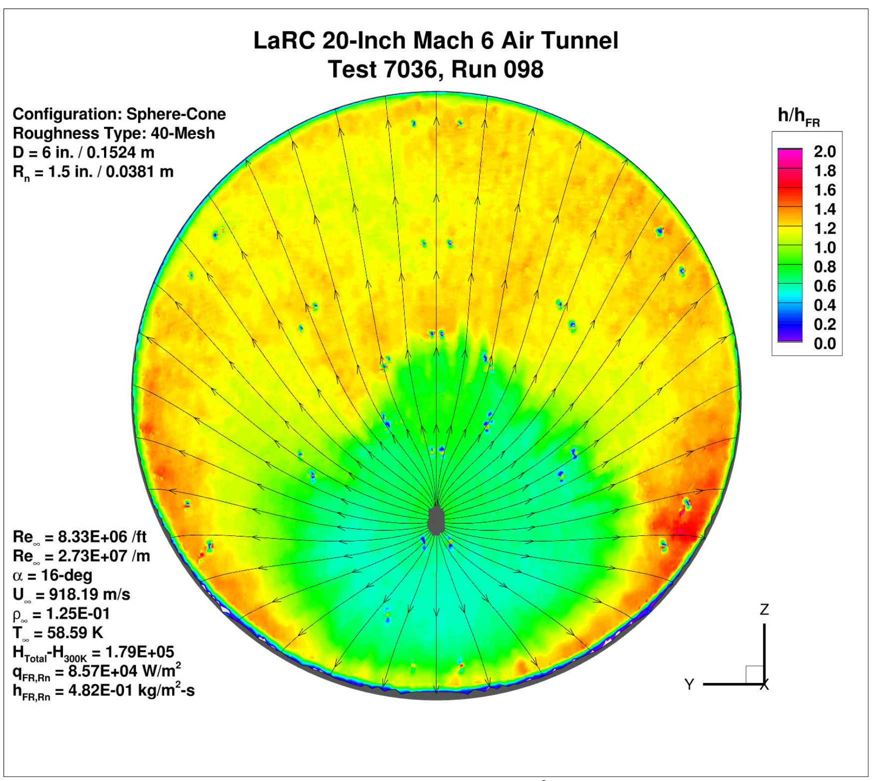

Figure 119. Test 7036, Run 98, Re∞ = 8.1×10^6/ft, sphere-cone, 40-mesh.

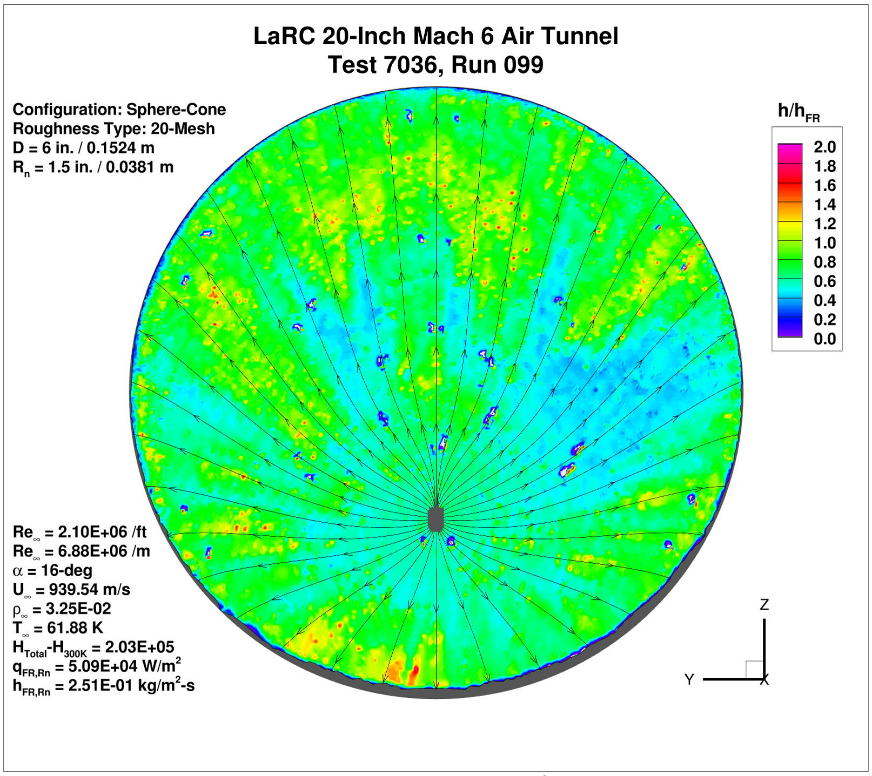

Figure 120. Test 7036, Run 99, Re∞ = 2.1×10^6/ft, sphere-cone, 20-mesh.

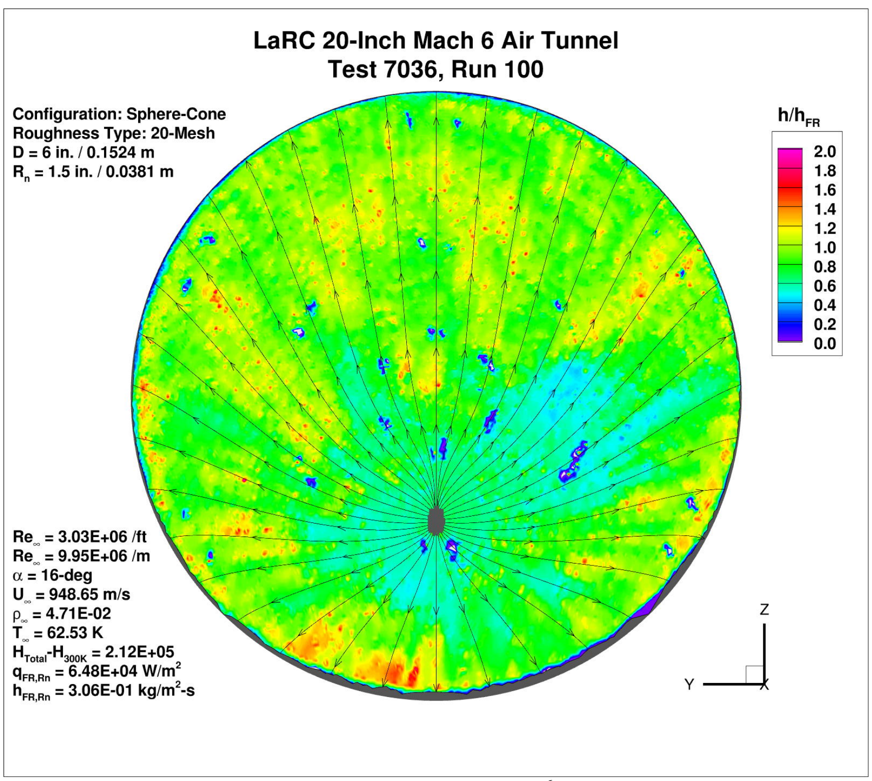

Figure 121. Test 7036, Run 100, Re∞ = 3.0×10^6/ft, sphere-cone, 20-mesh.

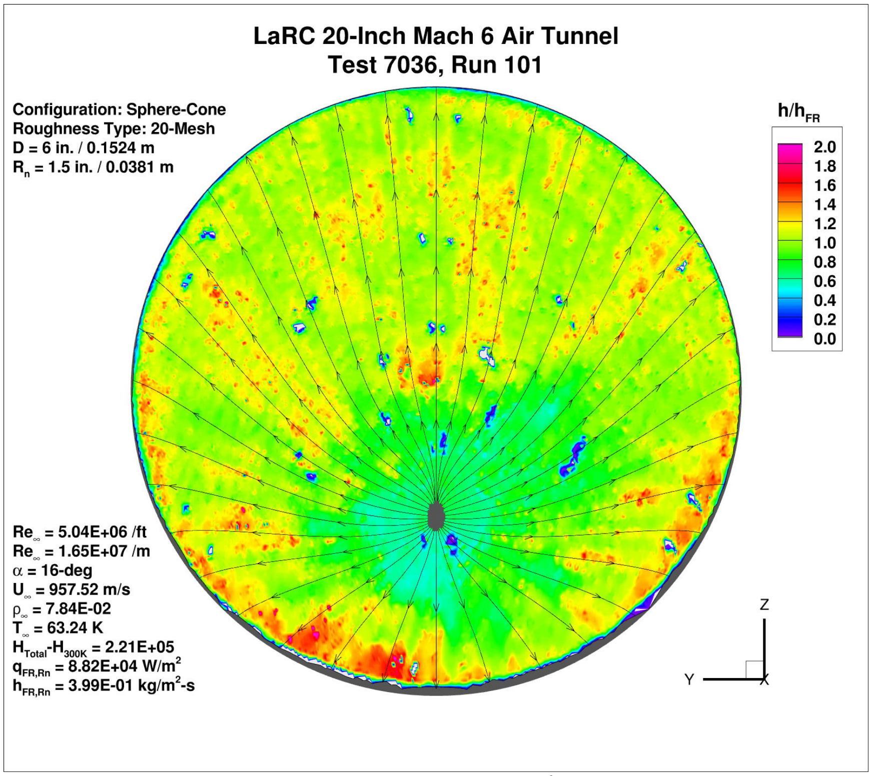

Figure 122. Test 7036, Run 101, Re∞ = 5.0×10^6/ft, sphere-cone, 20-mesh.

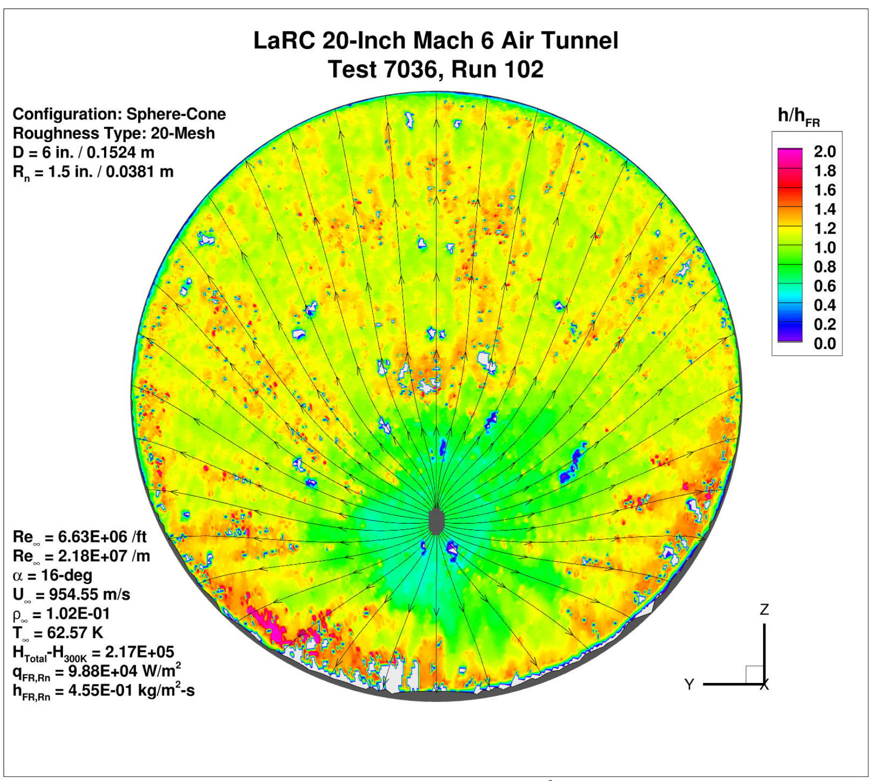

Figure 123. Test 7036, Run 102, Re∞ = 6.5×10^6/ft, sphere-cone, 20-mesh.

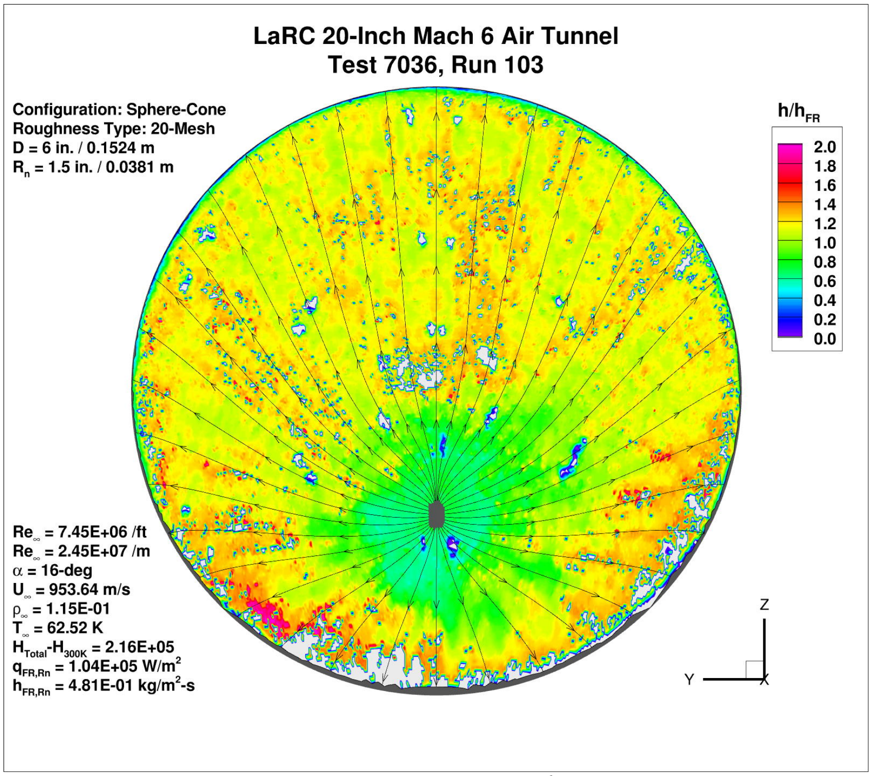

Figure 124. Test 7036, Run 103, $Re_\infty = 7.2\times10^6$/ft, sphere-cone, 20-mesh.

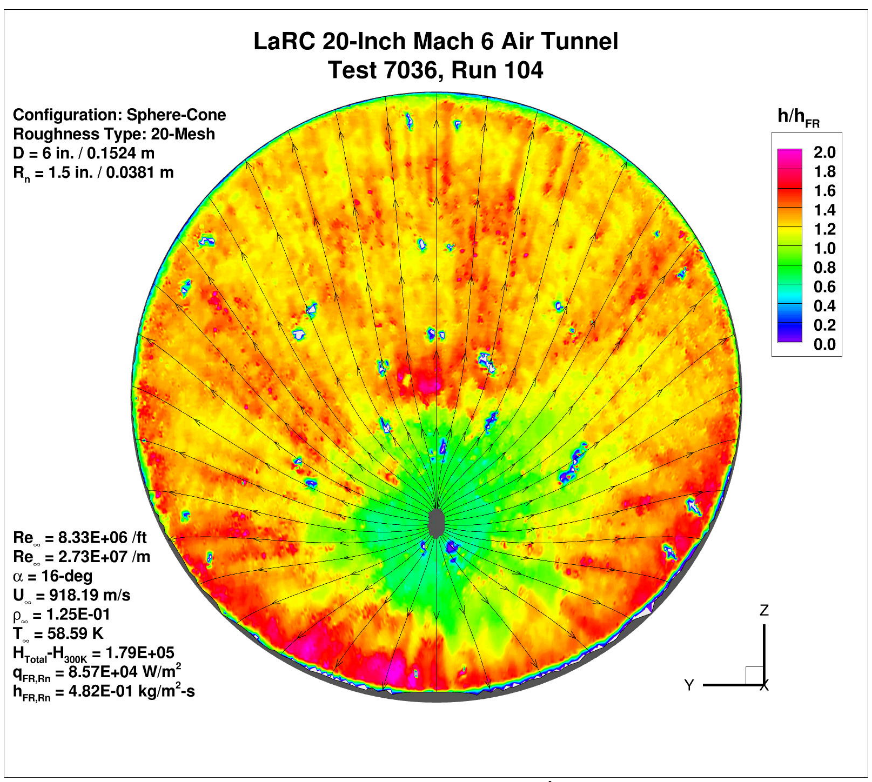

Figure 125. Test 7036, Run 104, $Re_\infty = 8.1\times10^6$/ft, sphere-cone, 20-mesh.

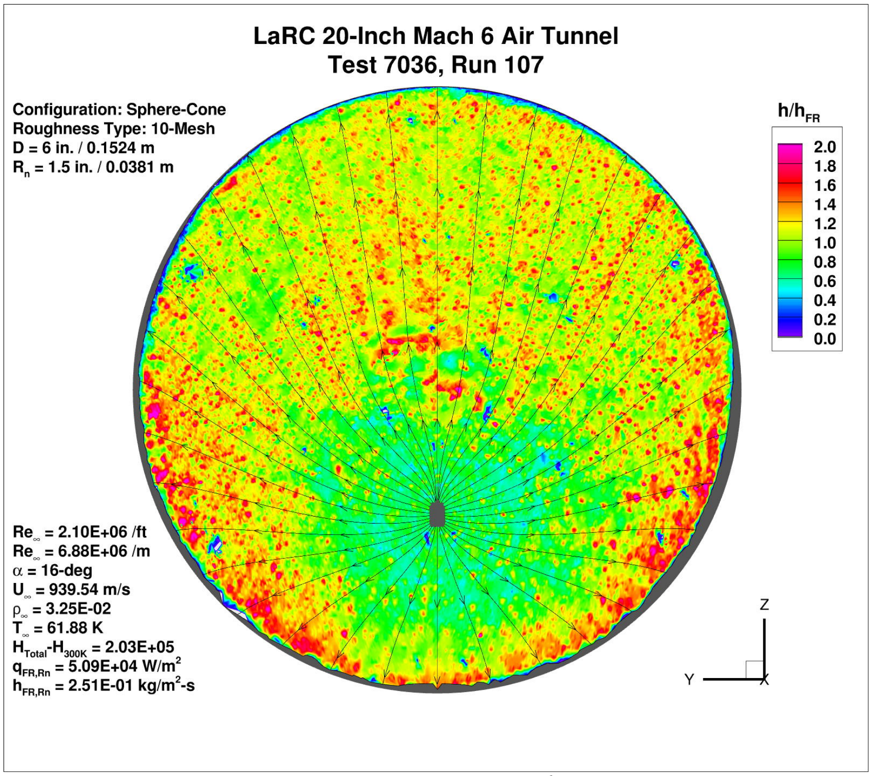

Figure 126. Test 7036, Run 107, $Re_\infty = 2.1\times10^6$/ft, sphere-cone, 10-mesh.

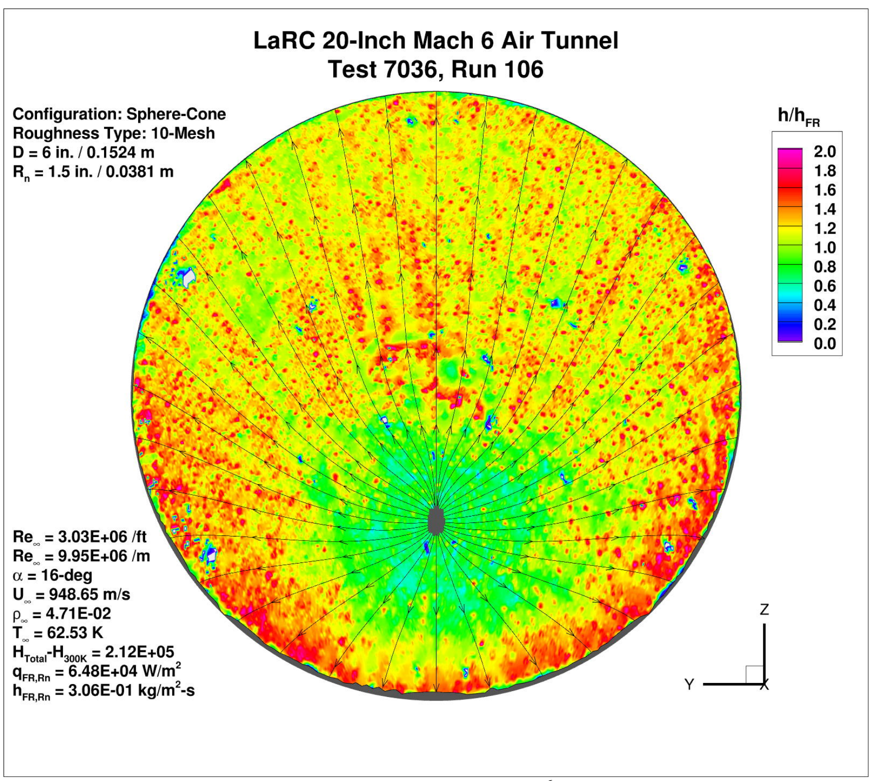

Figure 127. Test 7036, Run 106, $Re_\infty = 3.0\times10^6$/ft, sphere-cone, 10-mesh.

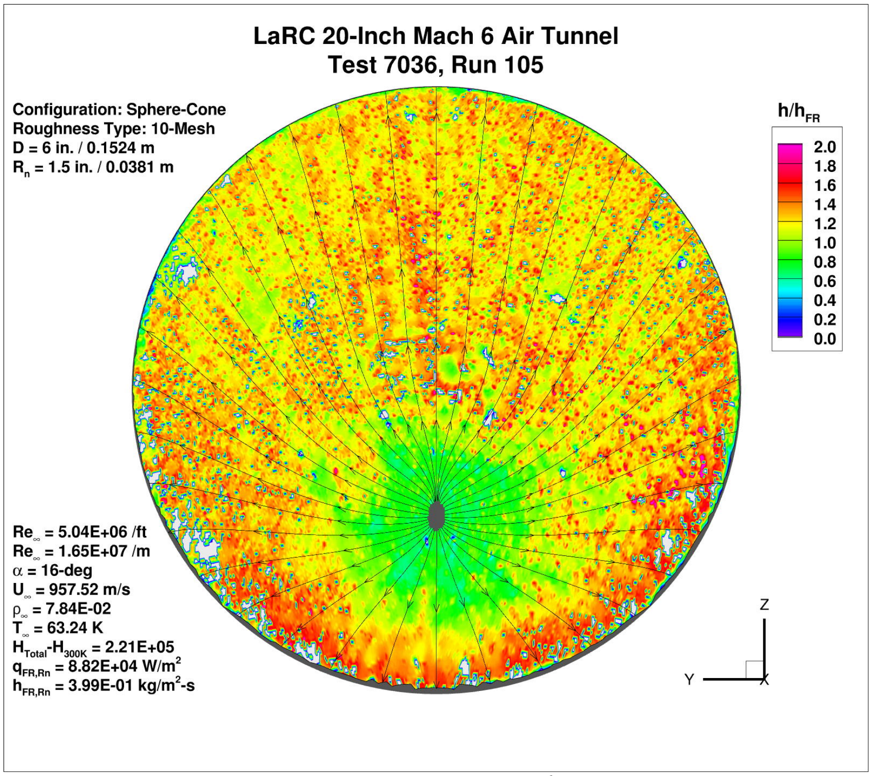

Figure 128. Test 7036, Run 105, Re∞ = 5.0×10^6/ft, sphere-cone, 10-mesh.

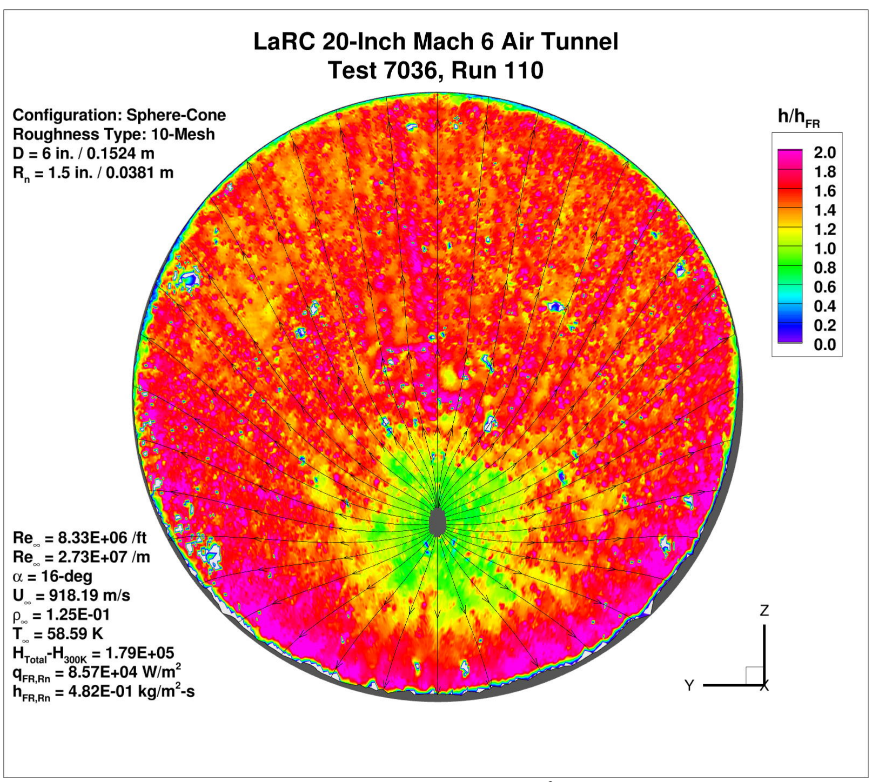

Figure 129. Test 7036, Run 108, Re∞ = 6.5×10^6/ft, sphere-cone, 10-mesh.

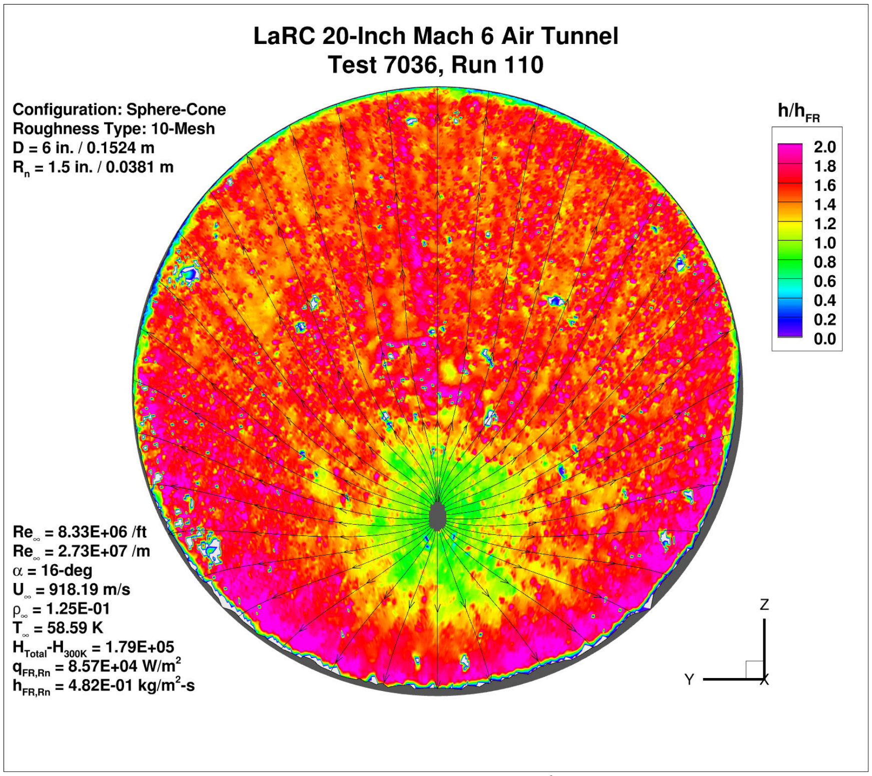

Figure 130. Test 7036, Run 109, $Re_\infty = 7.2\times10^6$/ft, sphere-cone, 10-mesh.

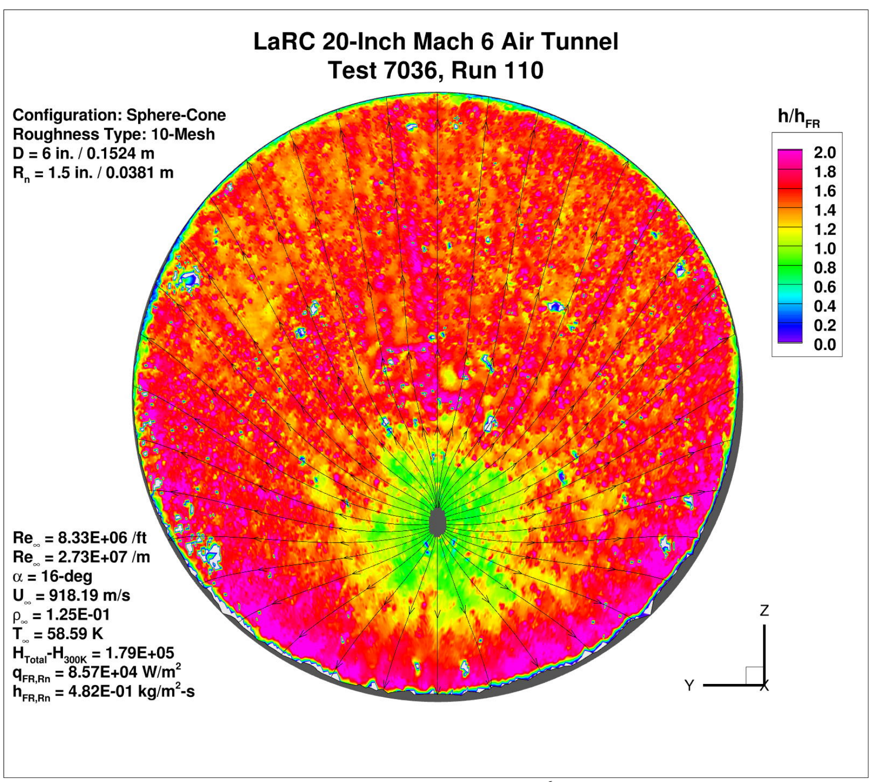

Figure 131. Test 7036, Run 110, $Re_\infty = 8.1\times10^6$/ft, sphere-cone, 10-mesh.

Appendix B. Spherical-Cap Geometry Global Heating Images

Global heating images for the sphere-cone geometry from Test 7057 in the LAL 20-Inch Mach 6 Air Tunnel are presented in this Appendix in Figure 132 through Figure 173.

At higher Reynolds numbers and/or larger roughness heights, white patches on the images indicate areas where the measured surface temperatures exceed the calibrated range of the phosphor thermography and thus no valid data were obtained.

Boundary-layer edge streamlines determined from laminar, smooth-surface LAURA simulations have been superimposed on the images to illustrate the nature of the flow field.

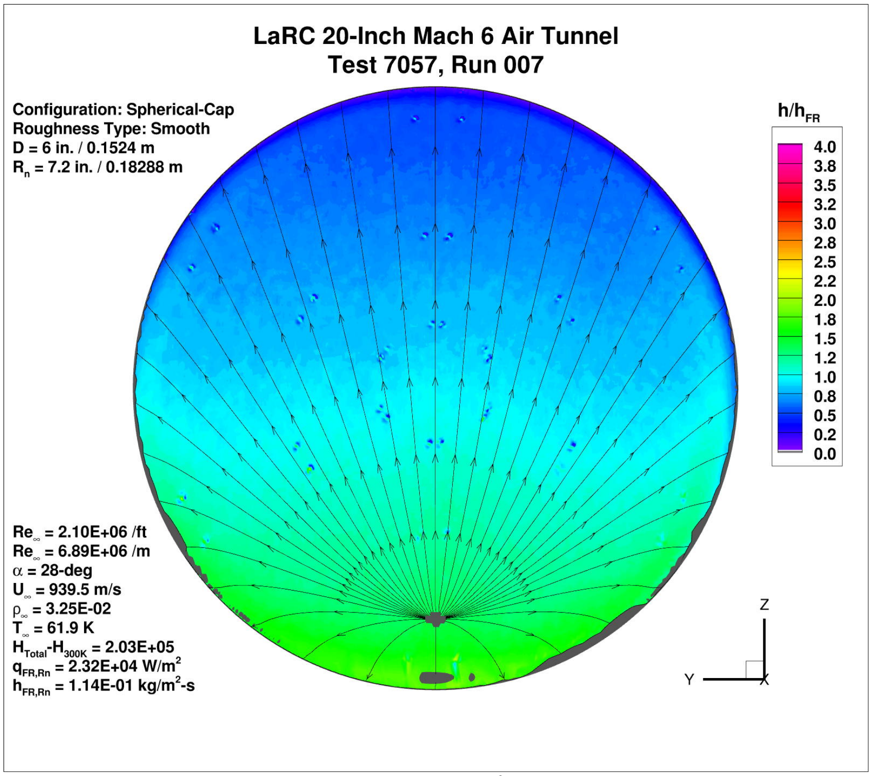

Figure 132. Test 7057, Run 7, Re∞ = 2.1×10^6/ft, spherical-cap, smooth OML.

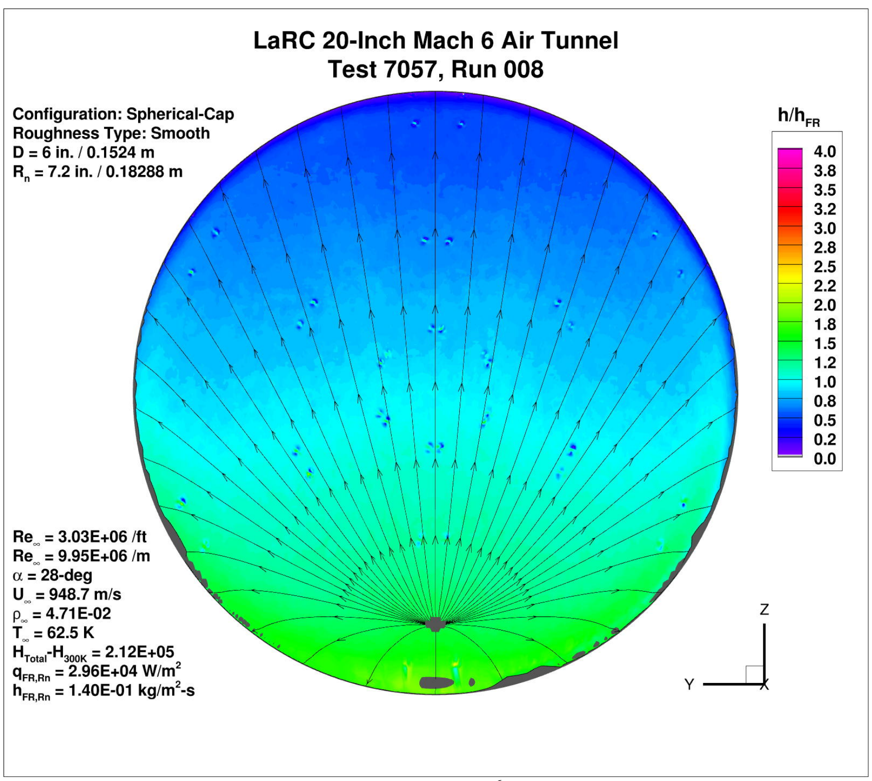

Figure 133. Test 7057, Run 8, Re∞ = 3.0×10^6/ft, spherical-cap, smooth OML.

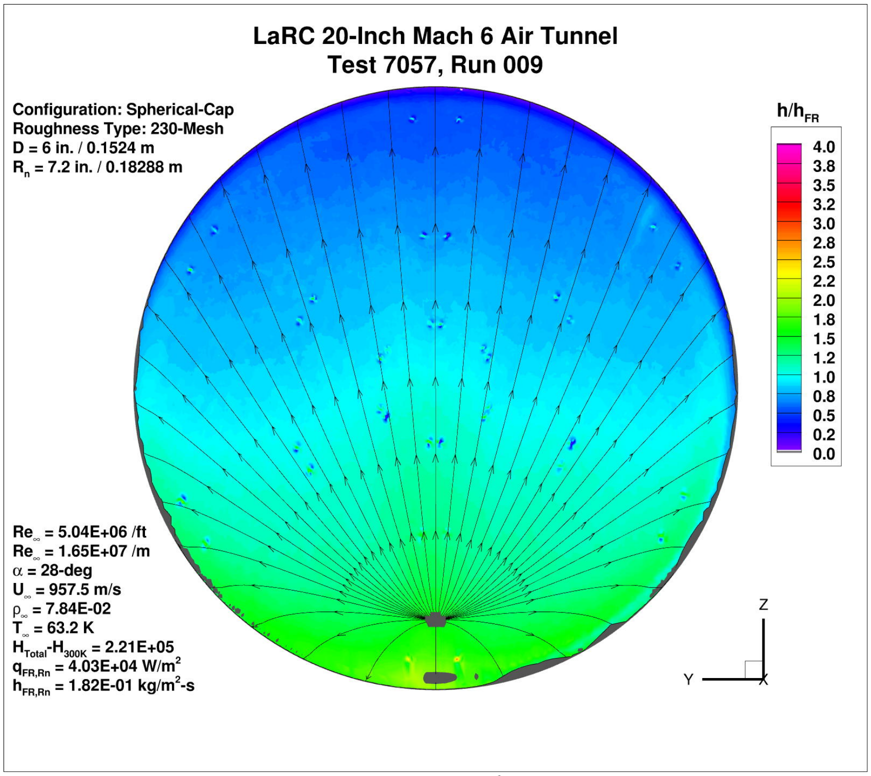

Figure 134. Test 7057, Run 9, Re∞ = 5.0×10^6/ft, spherical-cap, smooth OML.

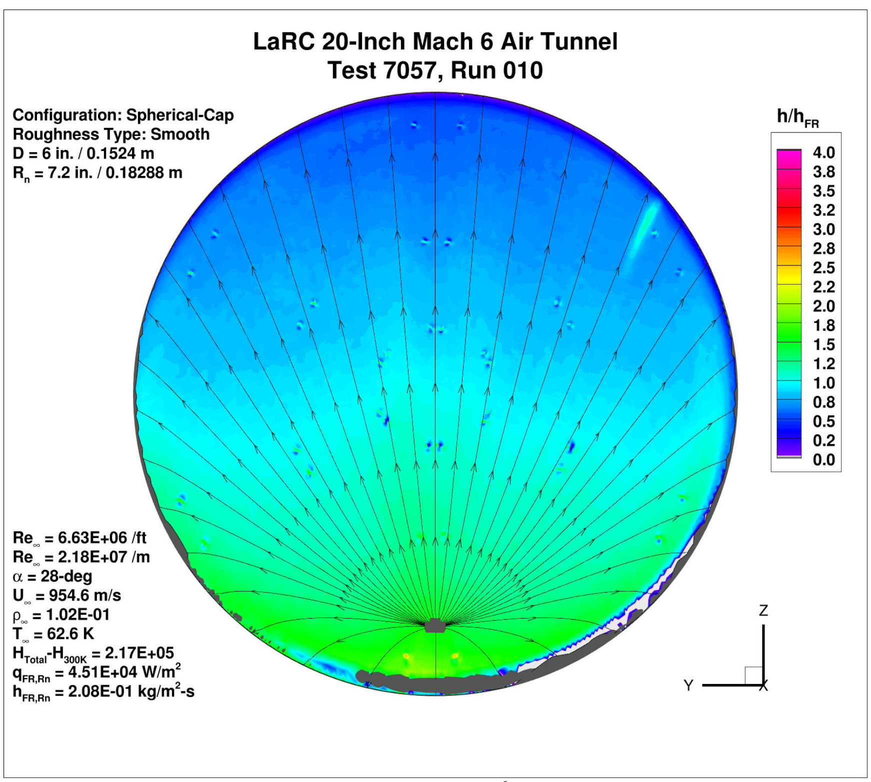

Figure 135. Test 7057, Run 10, Re∞ = 6.5×10^6/ft, spherical-cap, smooth OML.

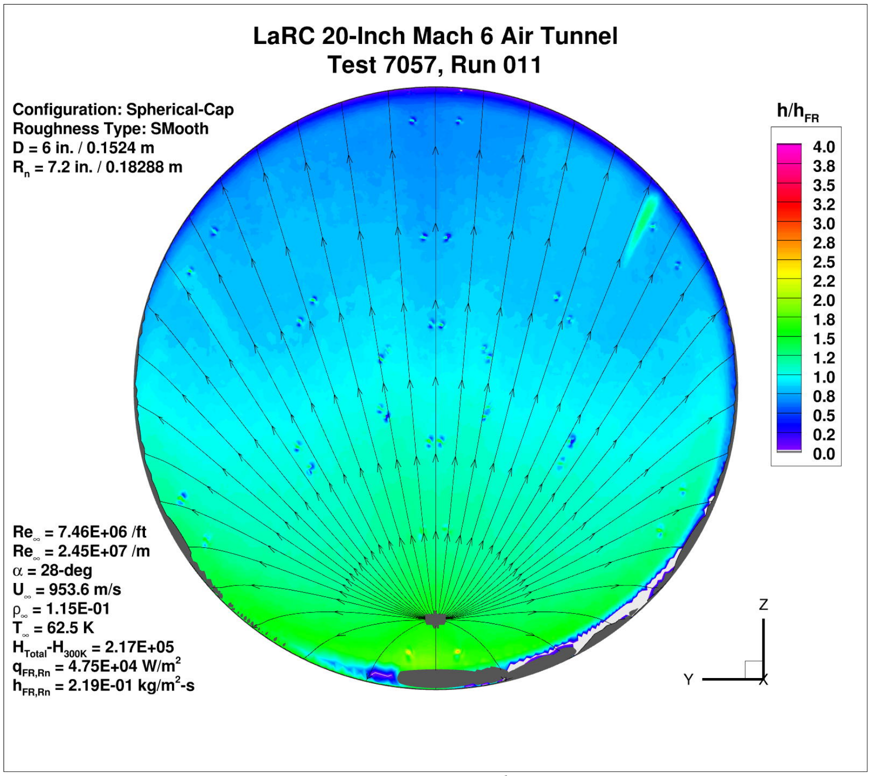

Figure 136. Test 7057, Run 11, Re∞ = 7.2×10^6/ft, spherical-cap, smooth OML.

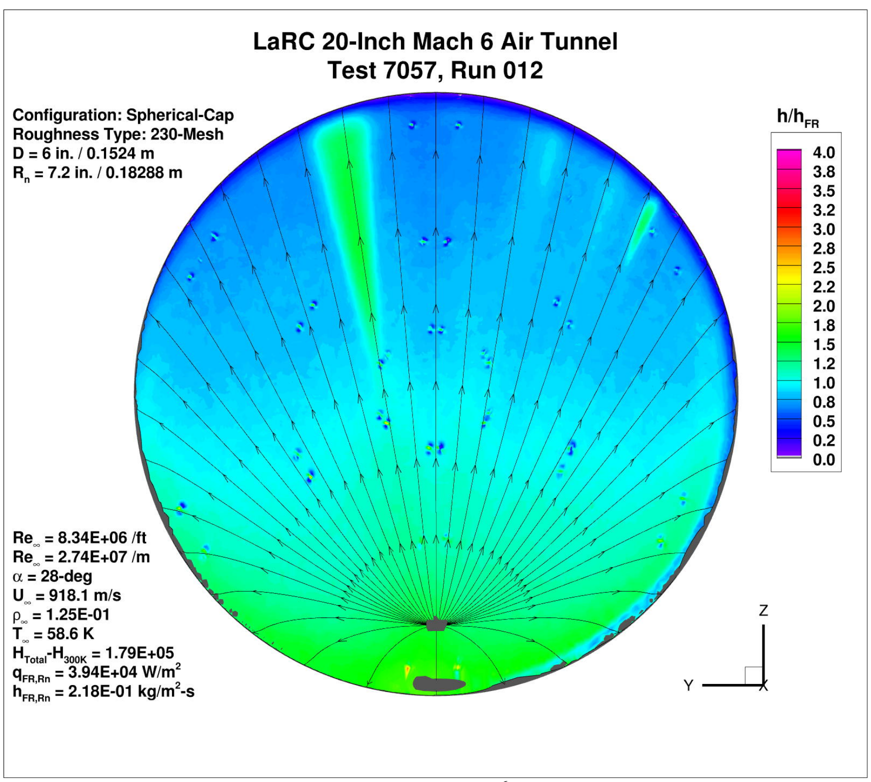

Figure 137. Test 7057, Run 12, Re∞ = 8.1×10^6/ft, spherical-cap, smooth OML.

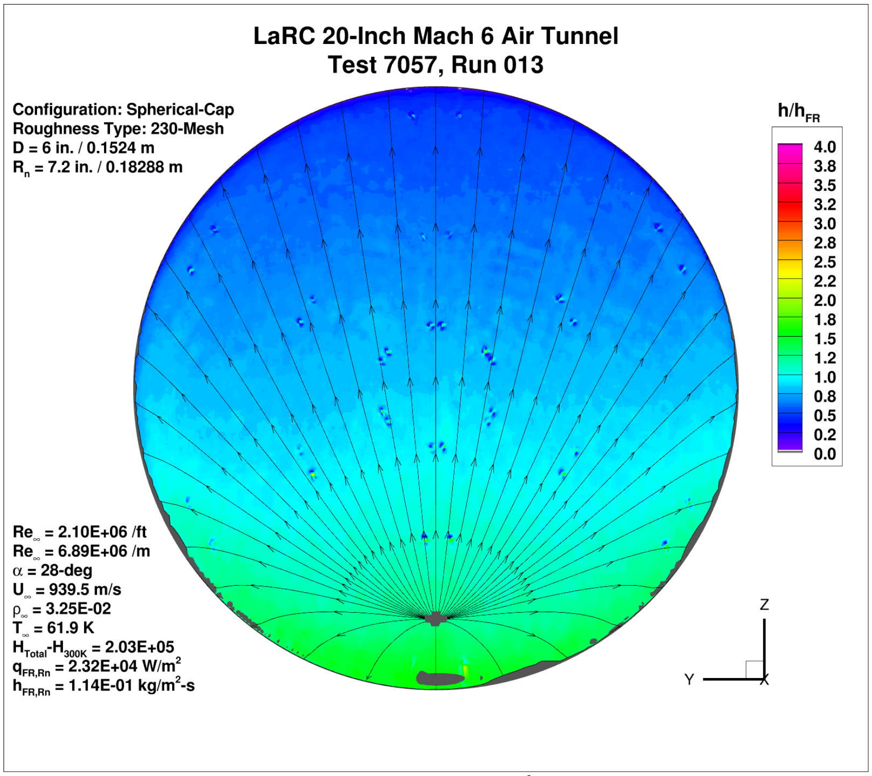

Figure 138. Test 7057, Run 13, Re$_\infty$ = 2.1×10^6/ft, spherical-cap, 230-mesh.

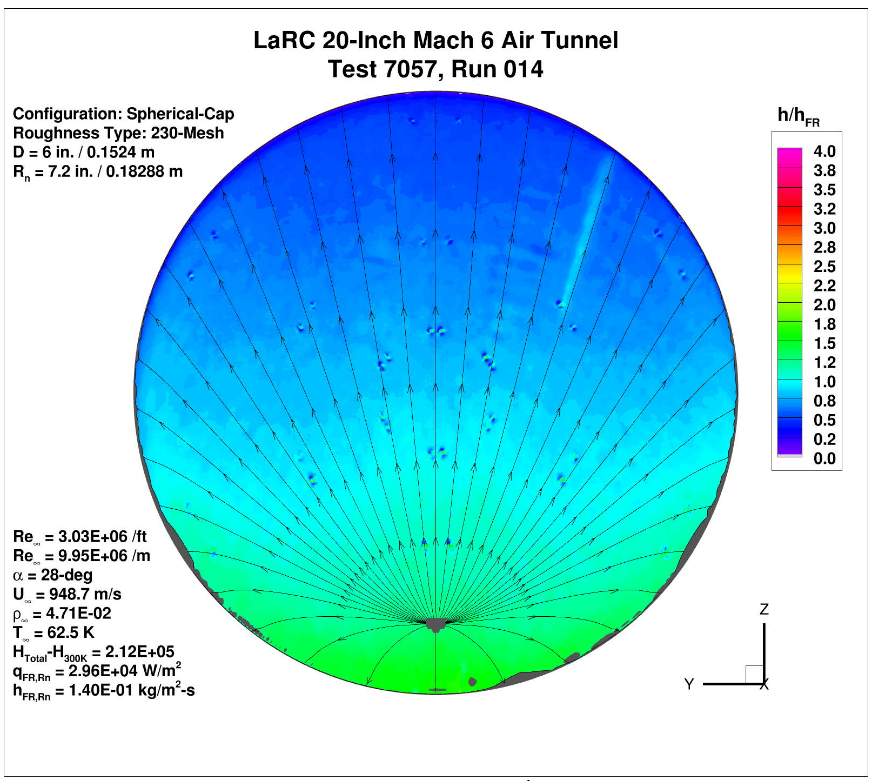

Figure 139. Test 7057, Run 14, Re$_\infty$ = 3.0×10^6/ft, spherical-cap, 230-mesh.

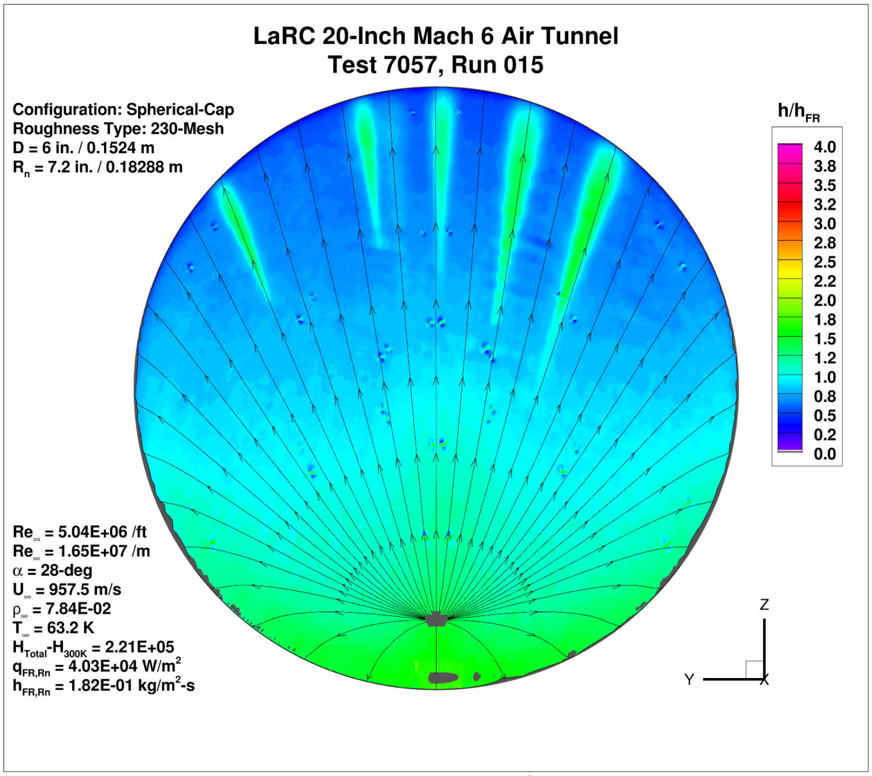

Figure 140. Test 7057, Run 15, Re∞ = 5.0×10^6/ft, spherical-cap, 230-mesh.

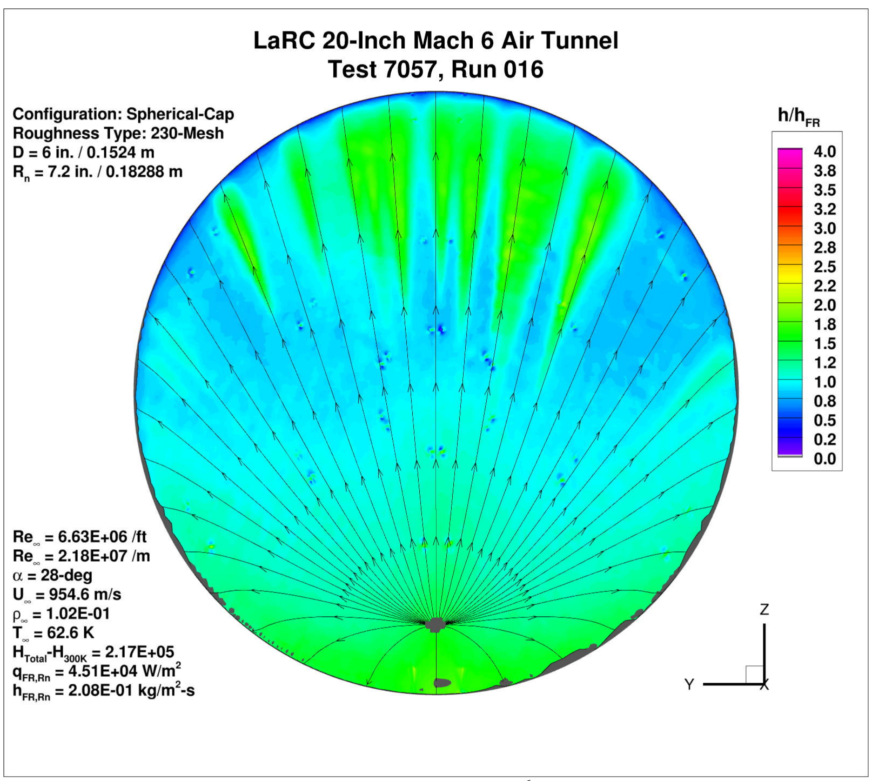

Figure 141. Test 7057, Run 16, Re∞ = 6.5×10^6/ft, spherical-cap, 230-mesh.

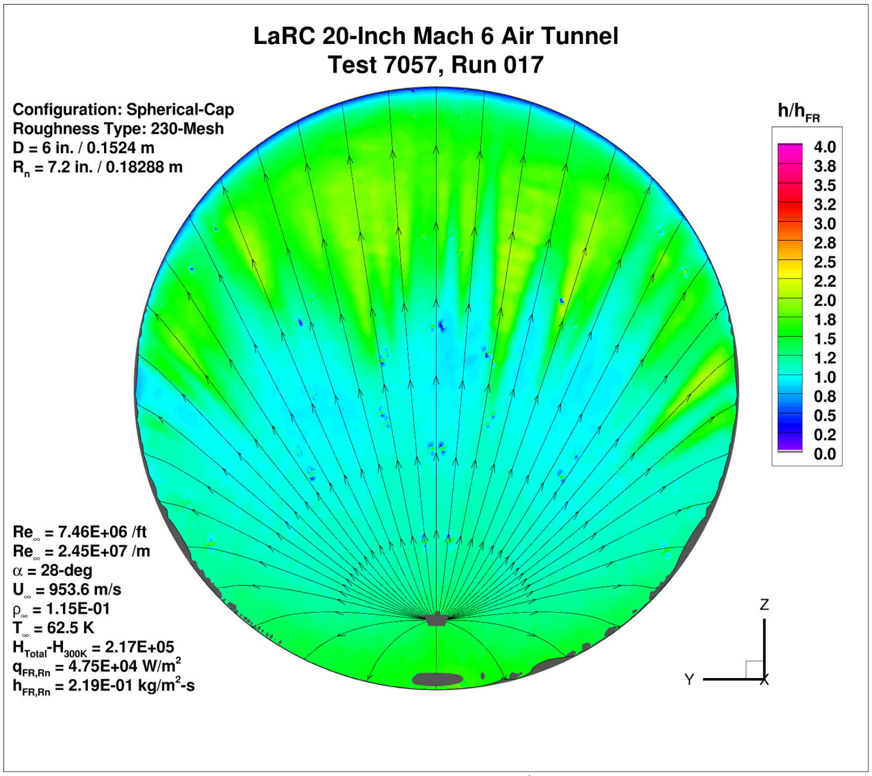

Figure 142. Test 7057, Run 17, Re∞ = 7.2×10^6/ft, spherical-cap, 230-mesh.

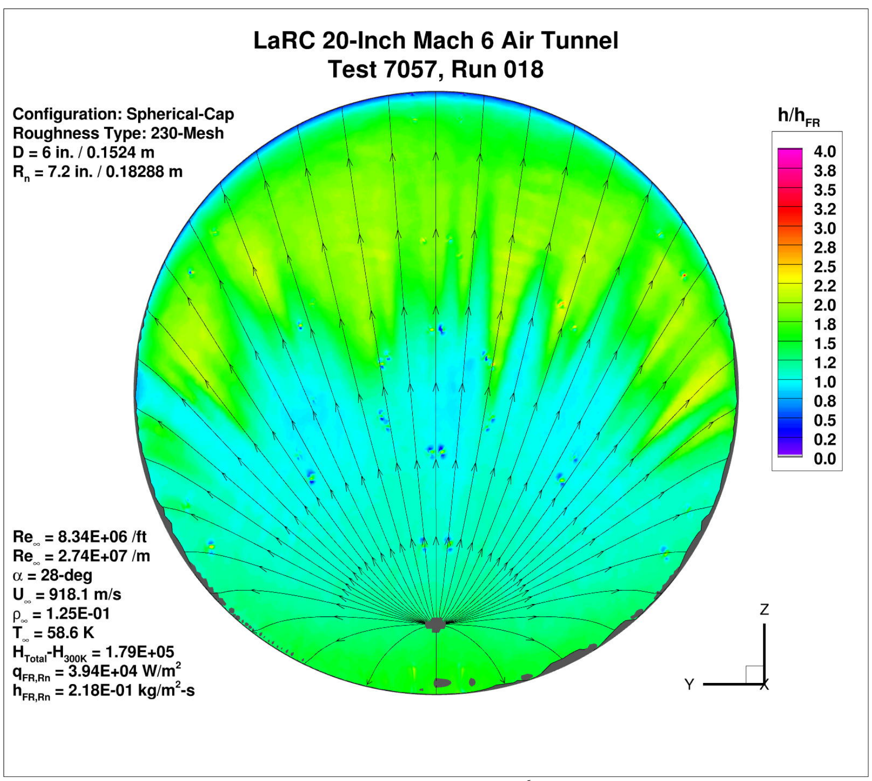

Figure 143. Test 7057, Run 18, Re∞ = 8.1×10^6/ft, spherical-cap, 230-mesh.

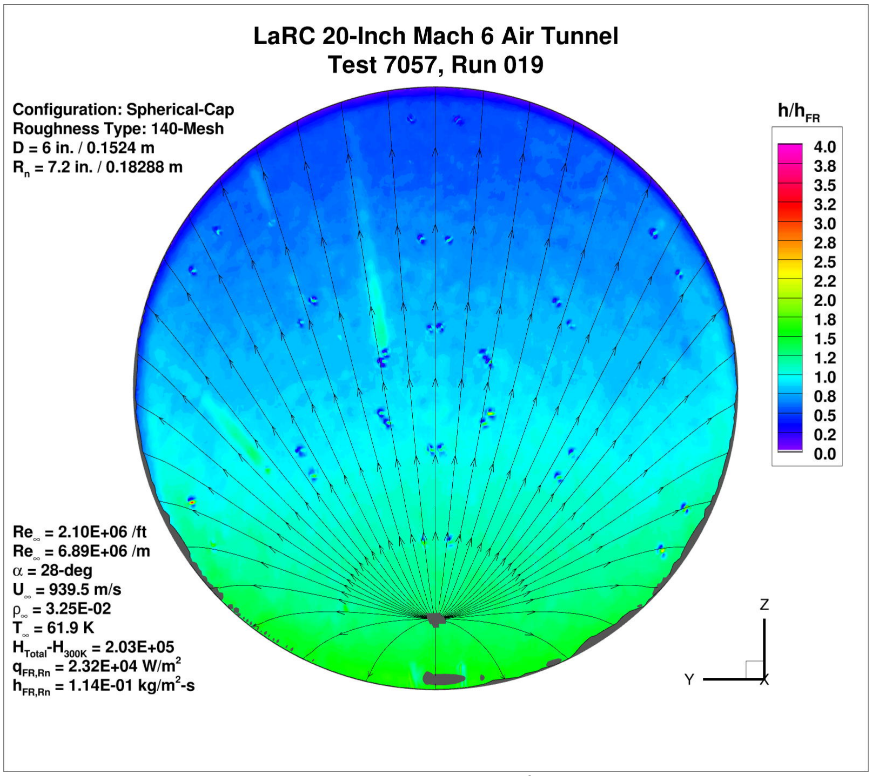

Figure 144. Test 7057, Run 19, Re∞ = 2.1×10⁶/ft, spherical-cap, 140-mesh.

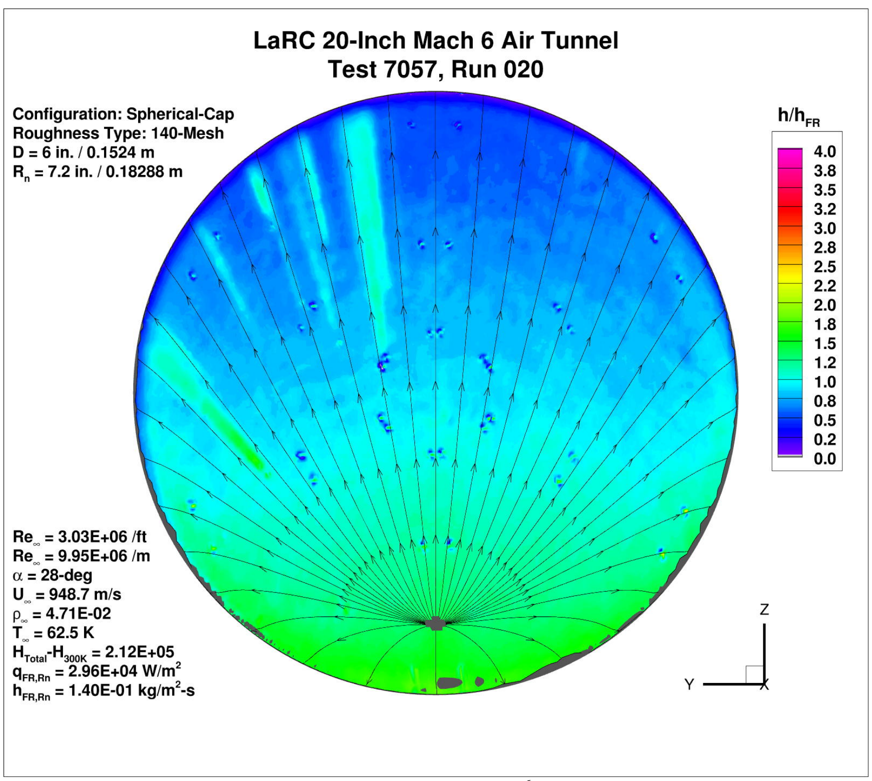

Figure 145. Test 7057, Run 20, $Re_\infty = 3.0\times10^6$/ft, spherical-cap, 140-mesh.

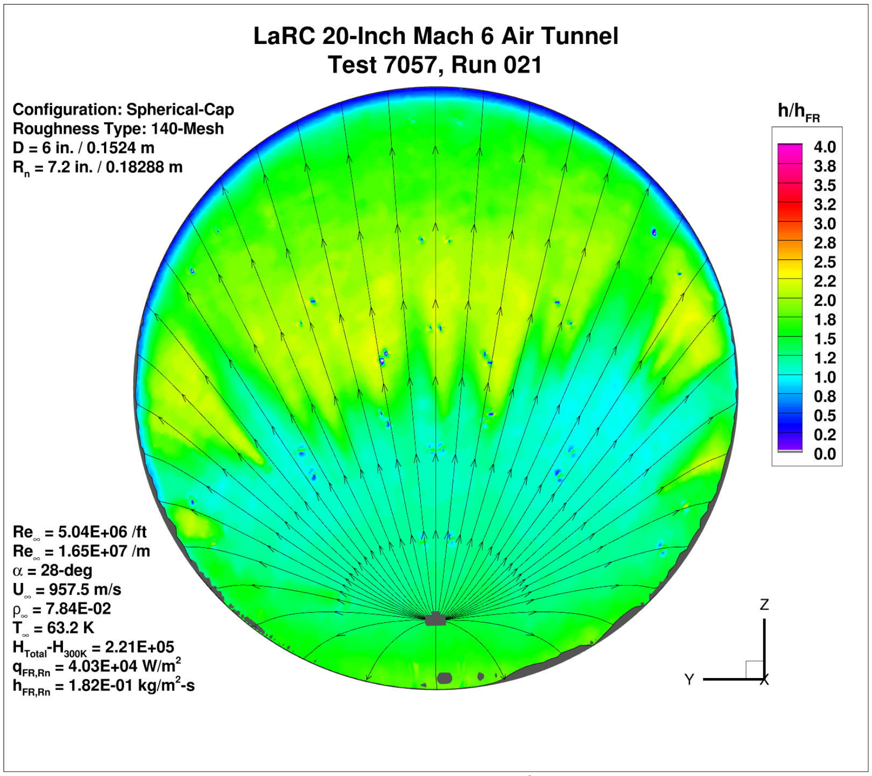

Figure 146. Test 7057, Run 21, Re∞ = 5.0×10^6/ft, spherical-cap, 140-mesh.

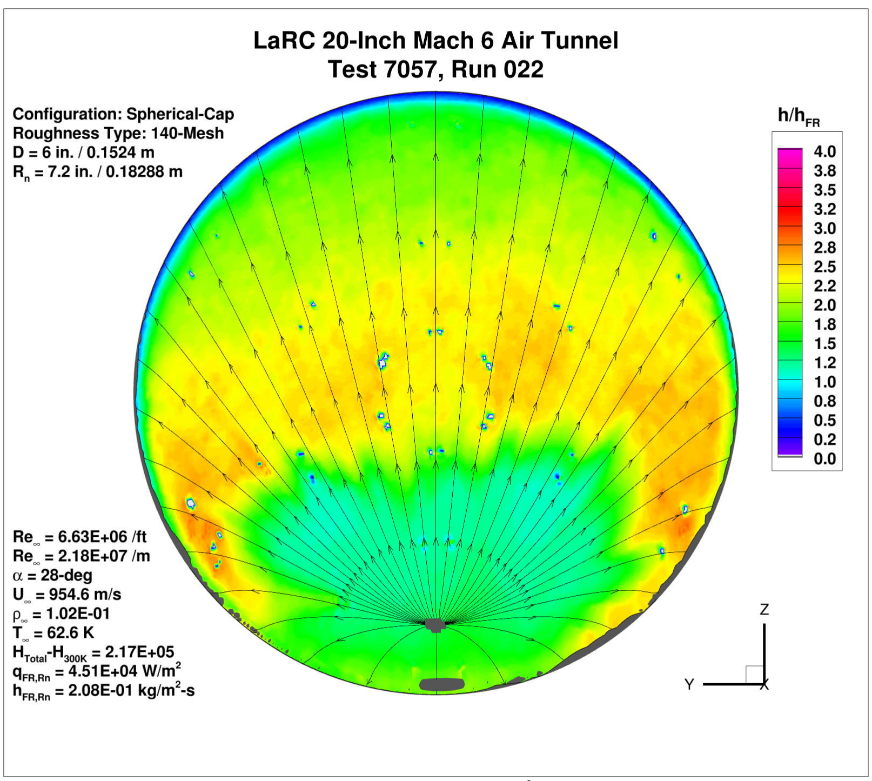

Figure 147. Test 7057, Run 22, Re∞ = 6.5×10^6/ft, spherical-cap, 140-mesh.

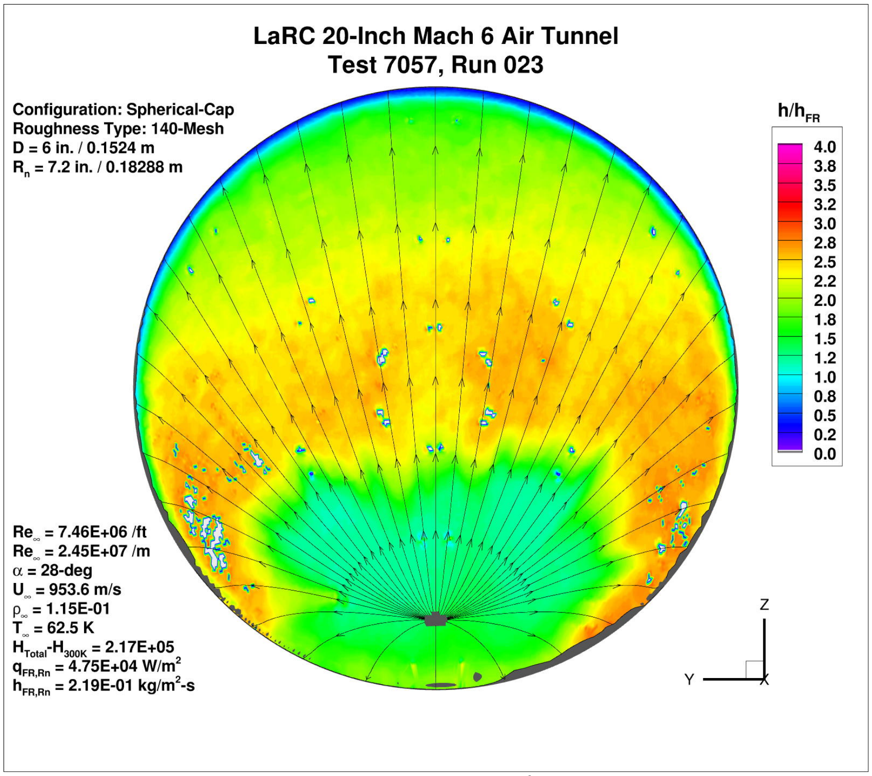

Figure 148. Test 7057, Run 23, Re∞ = 7.2×10^6/ft, spherical-cap, 140-mesh.

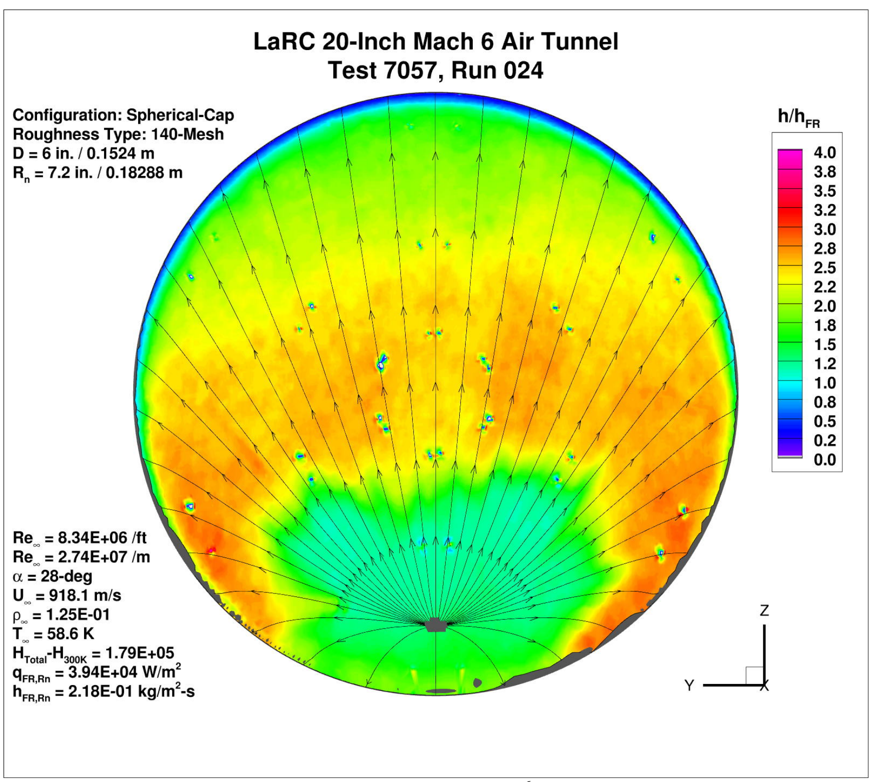

Figure 149. Test 7057, Run 24, Re∞ = 8.1×10^6/ft, spherical-cap, 140-mesh.

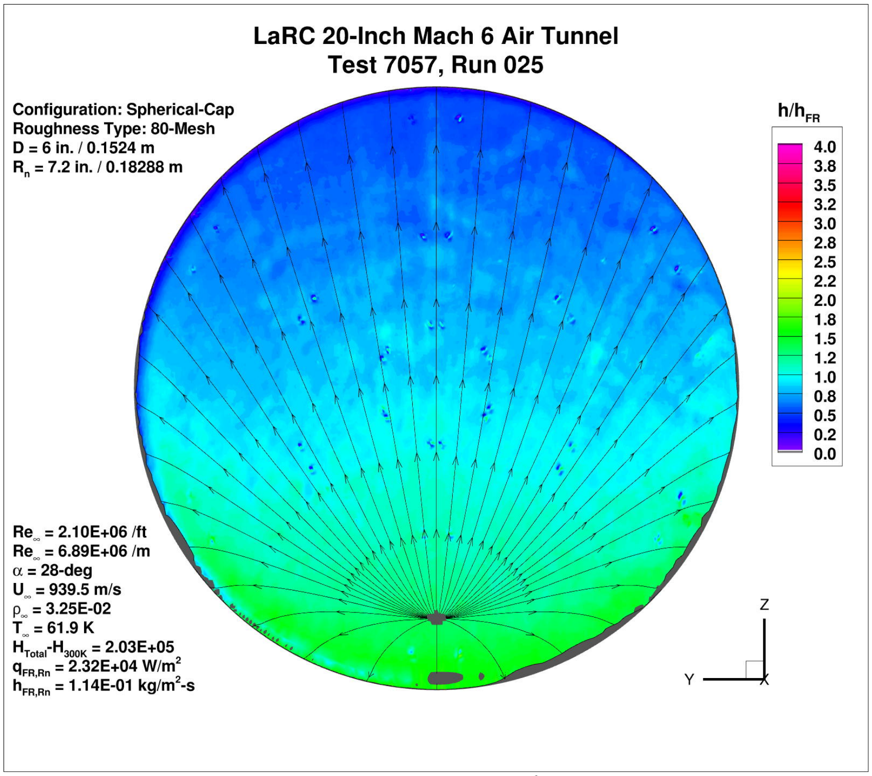

Figure 150. Test 7057, Run 25, Re∞ = 2.1×10⁶/ft, spherical-cap, 80-mesh.

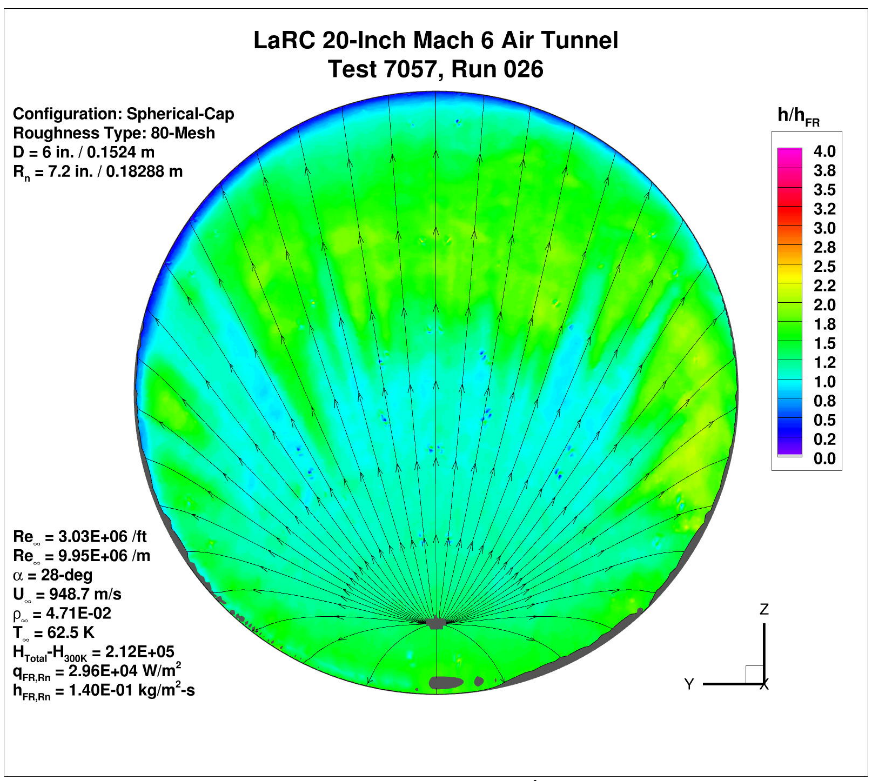

Figure 151. Test 7057, Run 26, Re∞ = 3.0×10⁶/ft, spherical-cap, 80-mesh.

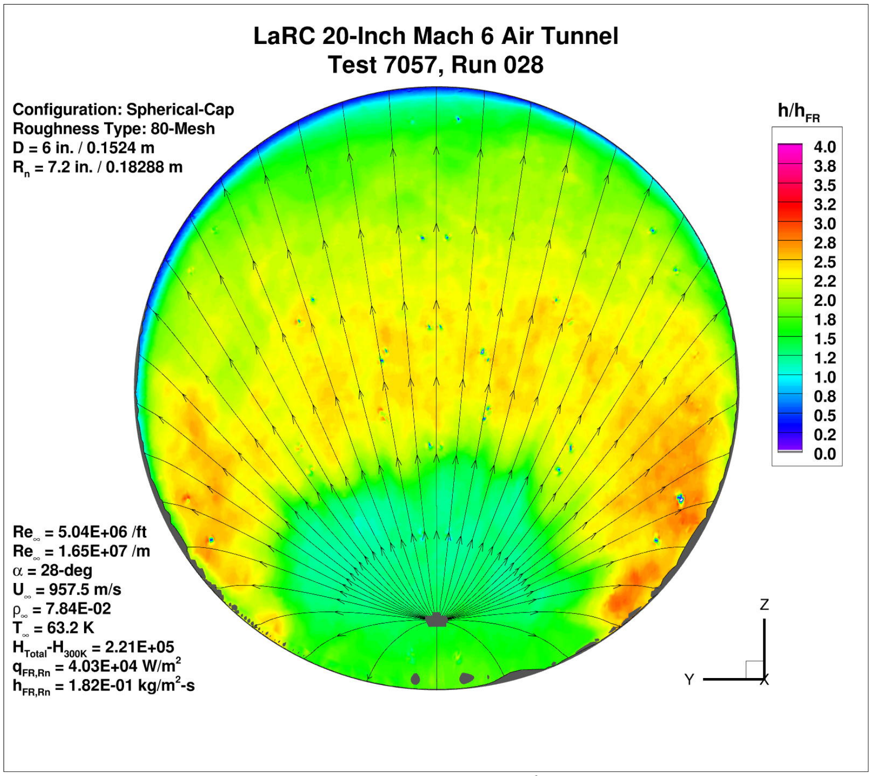

Figure 152. Test 7057, Run 28, Re∞ = 5.0×10^6/ft, spherical-cap, 80-mesh.

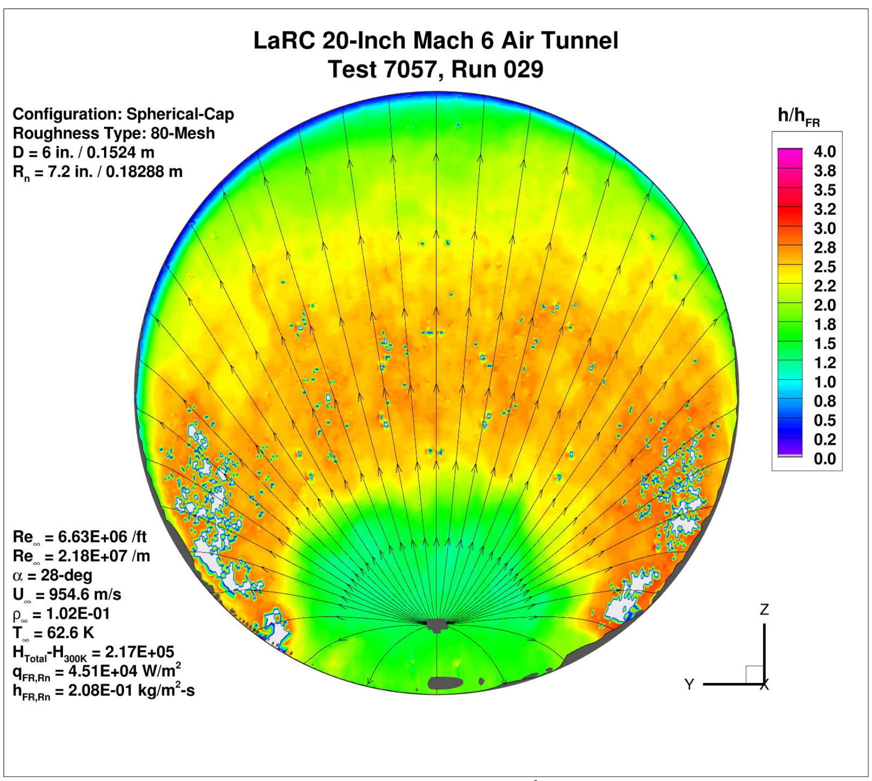

Figure 153. Test 7057, Run 29, Re∞ = 6.5×10^6/ft, spherical-cap, 80-mesh.

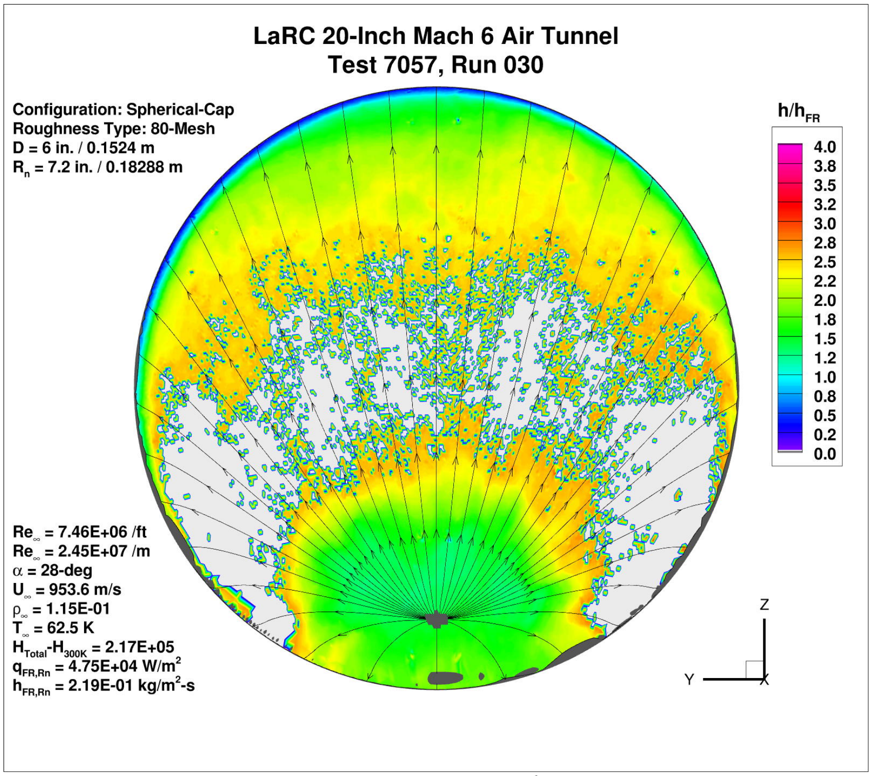

Figure 154. Test 7057, Run 30, Re∞ = 7.2×10^6/ft, spherical-cap, 80-mesh.

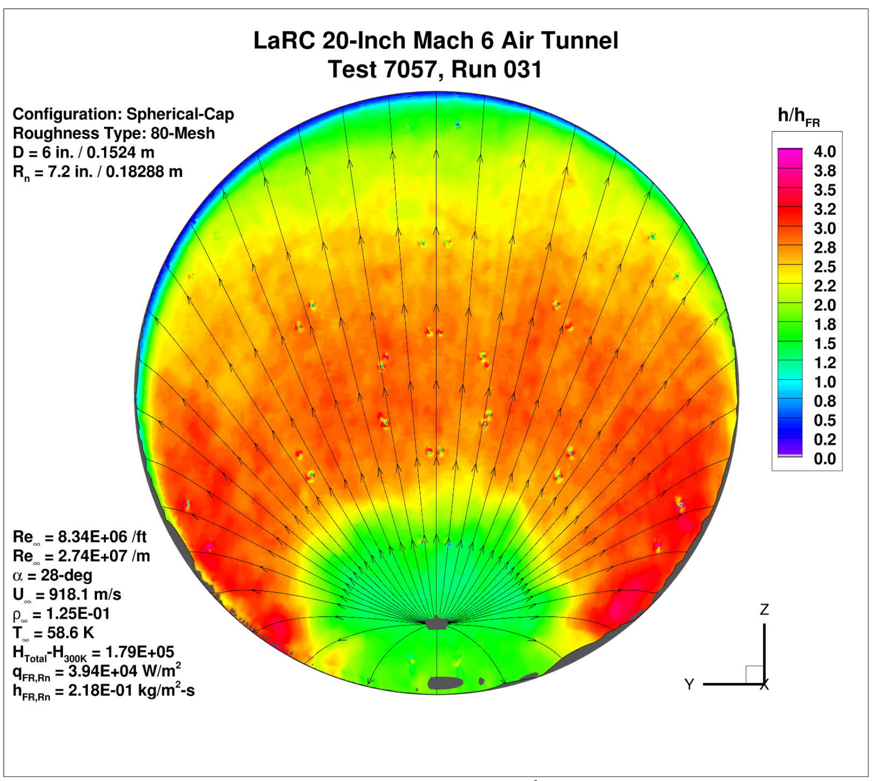

Figure 155. Test 7057, Run 31, Re∞ = 8.1×10^6/ft, spherical-cap, 80-mesh.

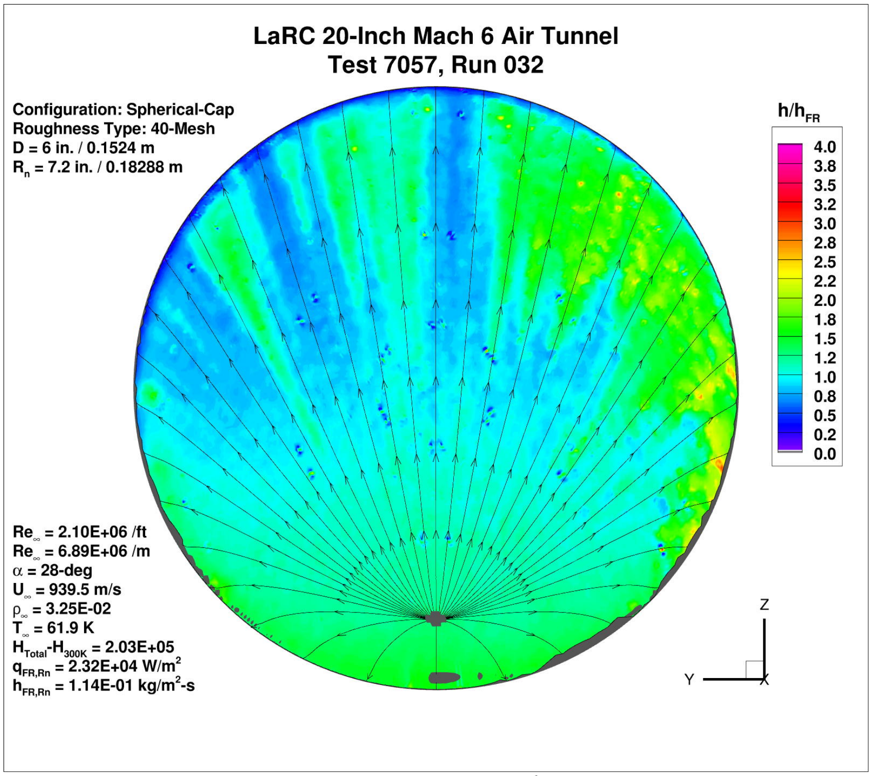

Figure 156. Test 7057, Run 32, Re∞ = 2.1×10^6/ft, spherical-cap, 40-mesh.

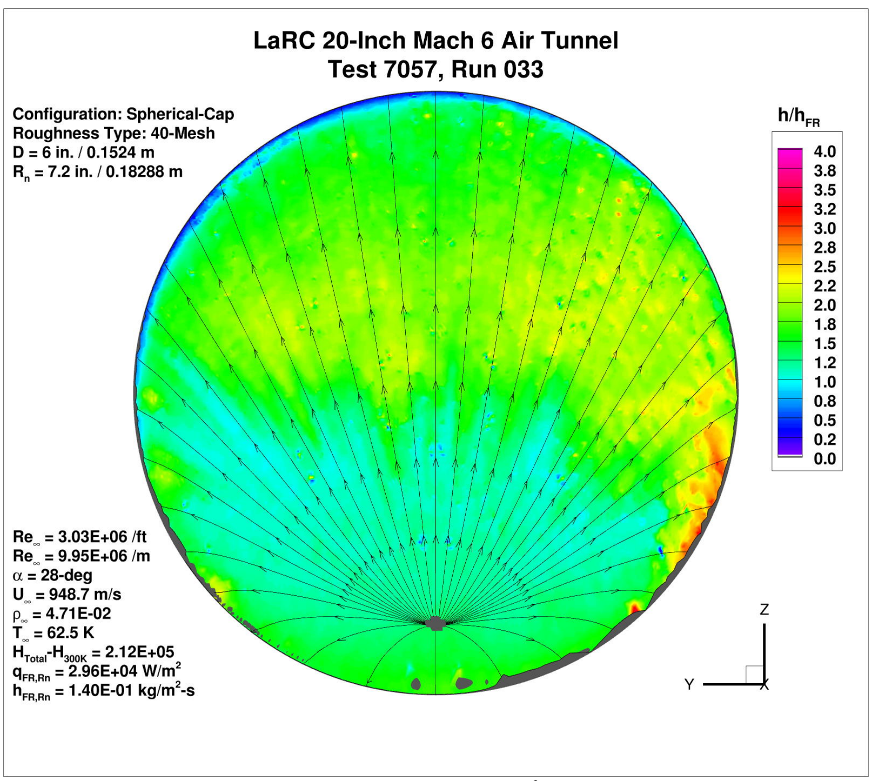

Figure 157. Test 7057, Run 33, Re∞ = 3.0×10^6/ft, spherical-cap, 40-mesh.

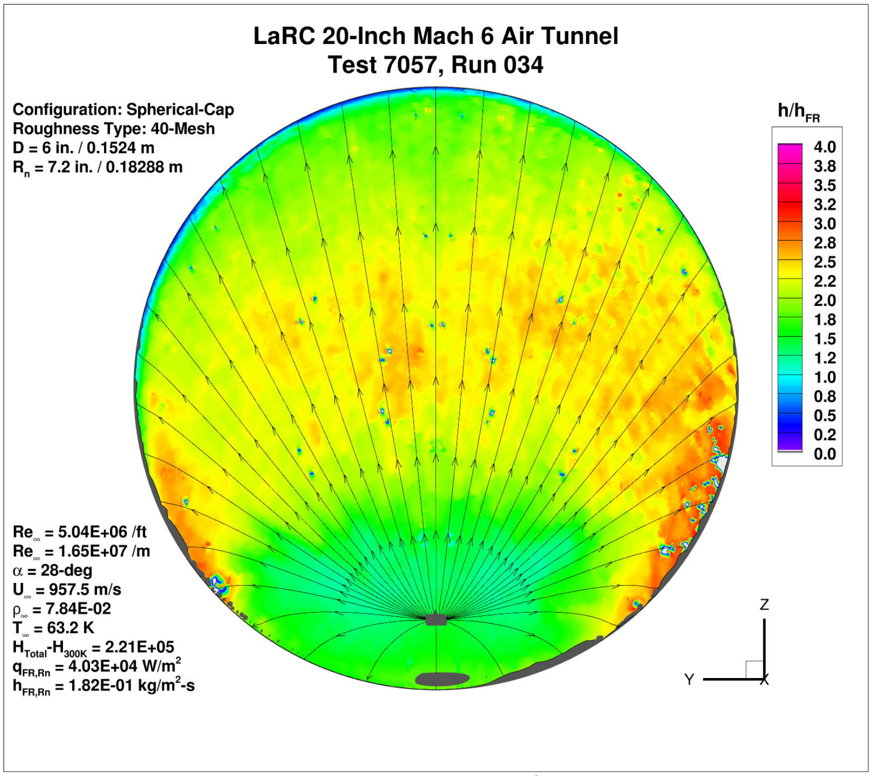

Figure 158. Test 7057, Run 34, Re∞ = 5.0×10^6/ft, spherical-cap, 40-mesh.

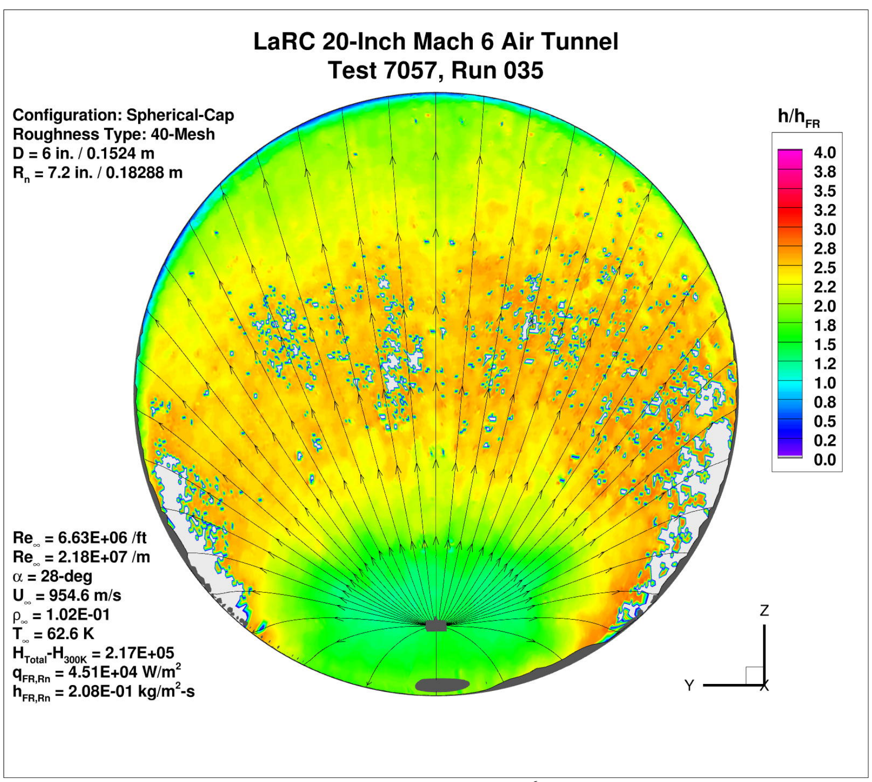

Figure 159. Test 7057, Run 35, Re∞ = 6.5×10^6/ft, spherical-cap, 40-mesh.

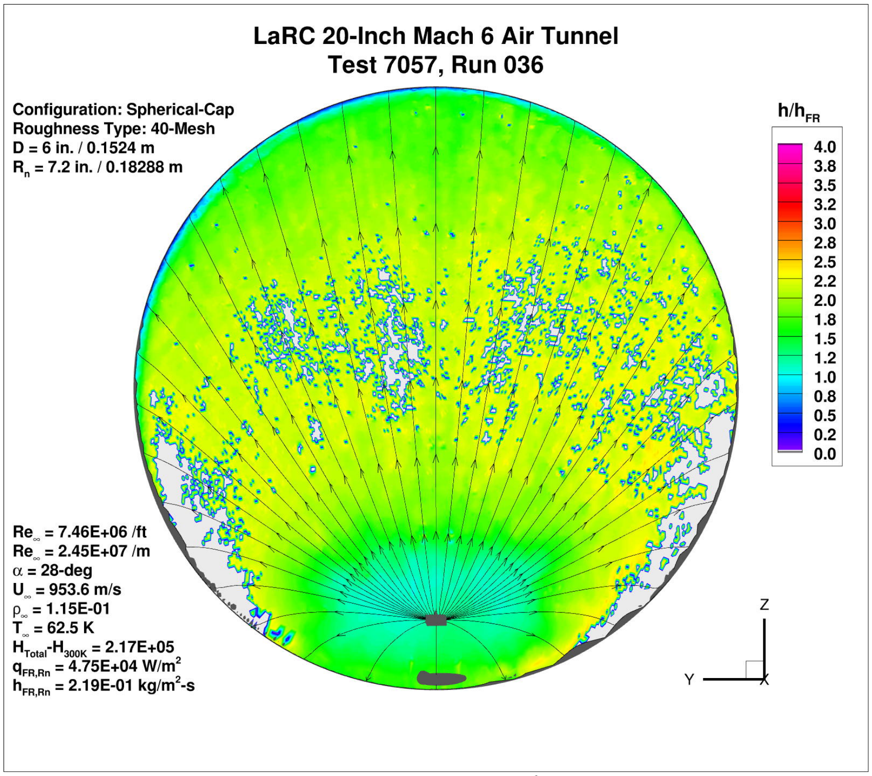

Figure 160. Test 7057, Run 36, Re$_\infty$ = 7.2×10^6/ft, spherical-cap, 40-mesh.

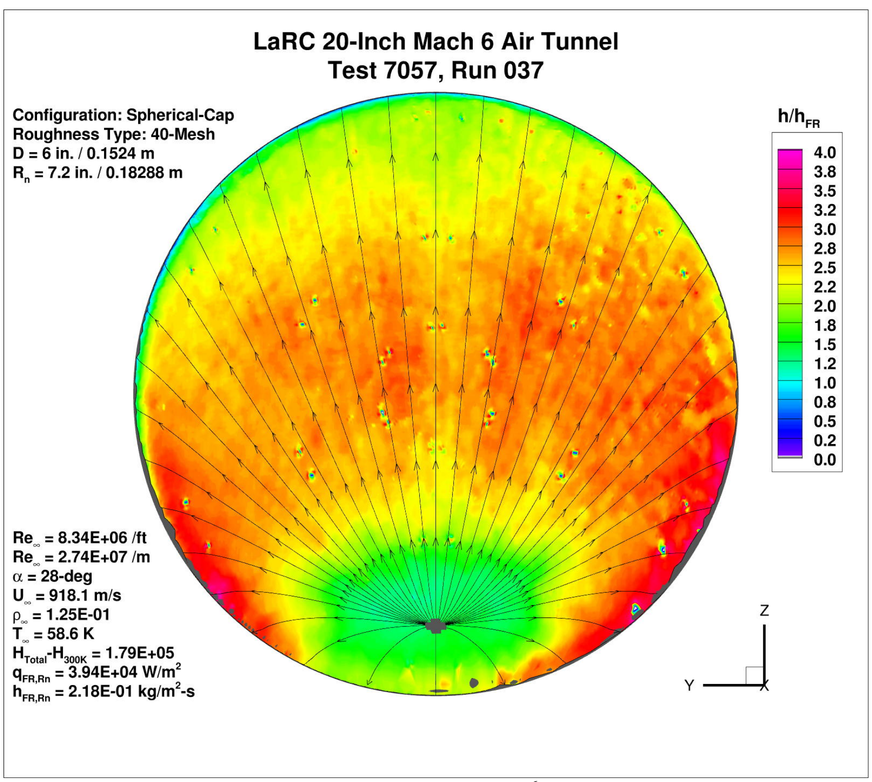

Figure 161. Test 7057, Run 37, Re$_\infty$ = 8.1×10^6/ft, spherical-cap, 40-mesh.

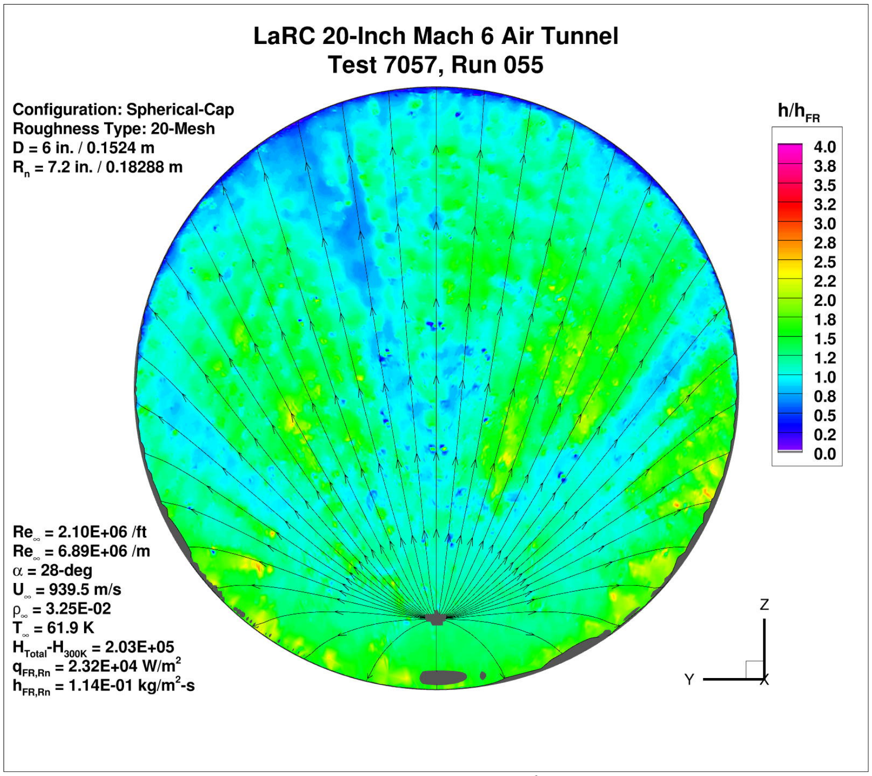

Figure 162. Test 7057, Run 55, Re∞ = 2.1×10⁶/ft, spherical-cap, 20-mesh.

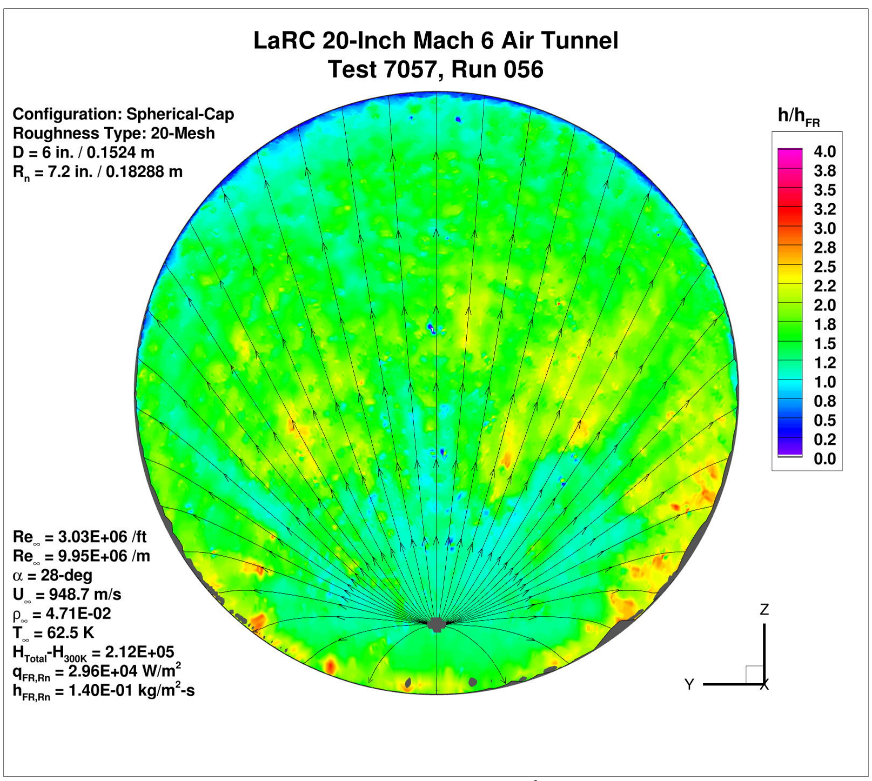

Figure 163. Test 7057, Run 56, Re∞ = 3.0×10⁶/ft, spherical-cap, 20-mesh.

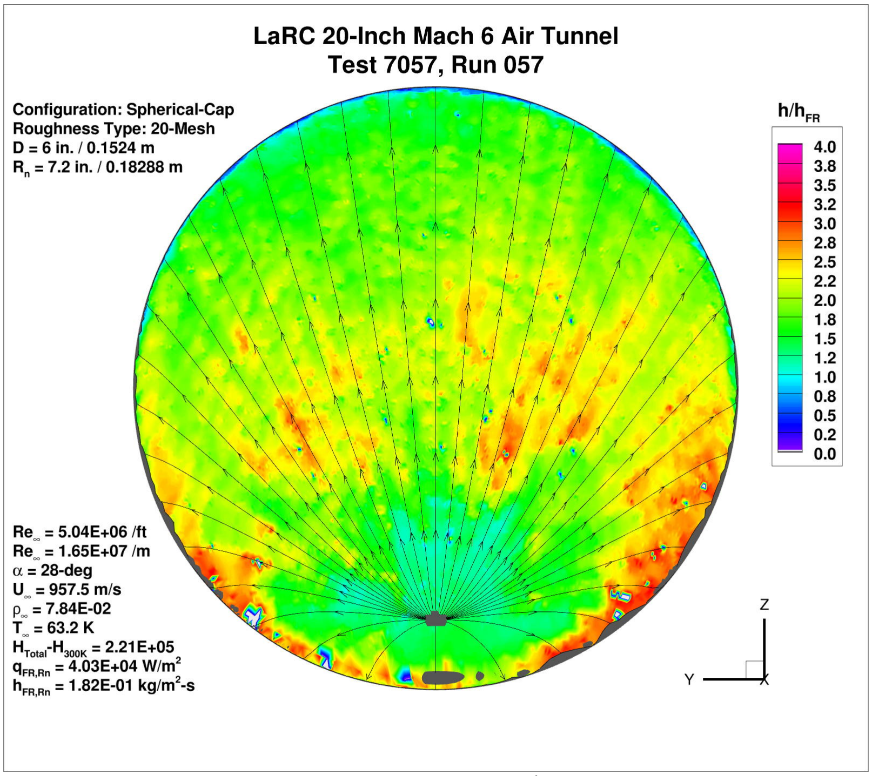

Figure 164. Test 7057, Run 57, Re∞ = 5.0×10^6/ft, spherical-cap, 20-mesh.

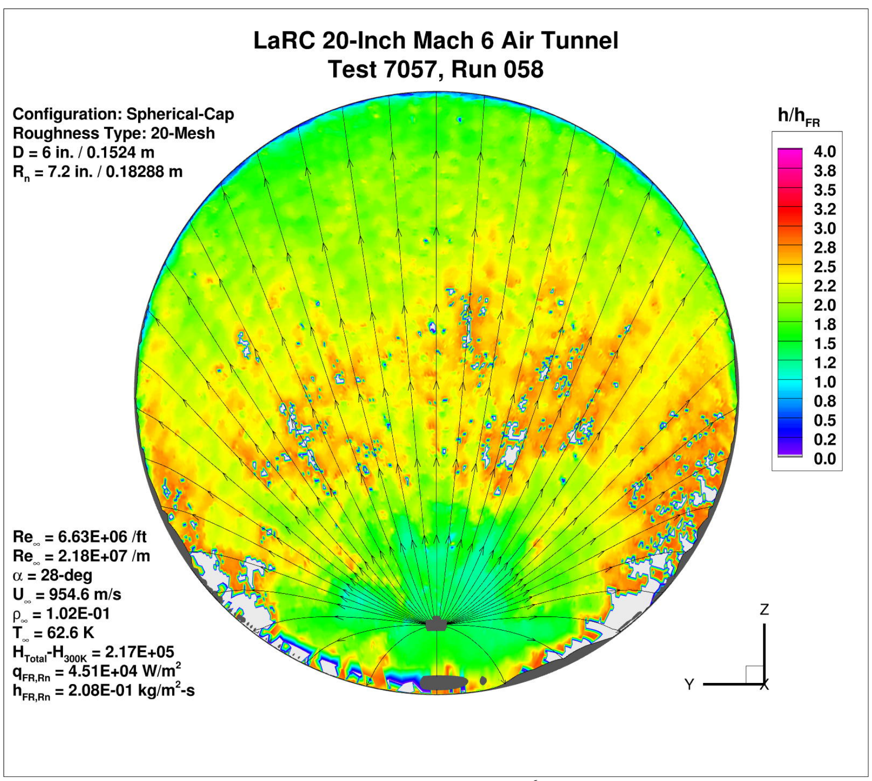

Figure 165. Test 7057, Run 58, Re∞ = 6.5×10^6/ft, spherical-cap, 20-mesh.

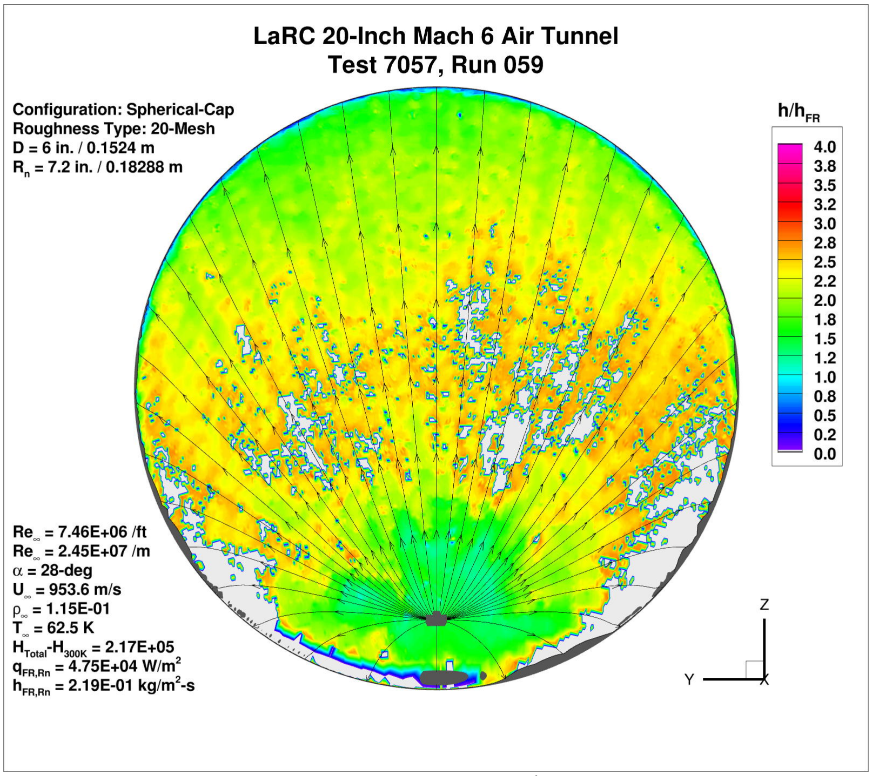

Figure 166. Test 7057, Run 59, Re∞ = 7.2×10^6/ft, spherical-cap, 20-mesh.

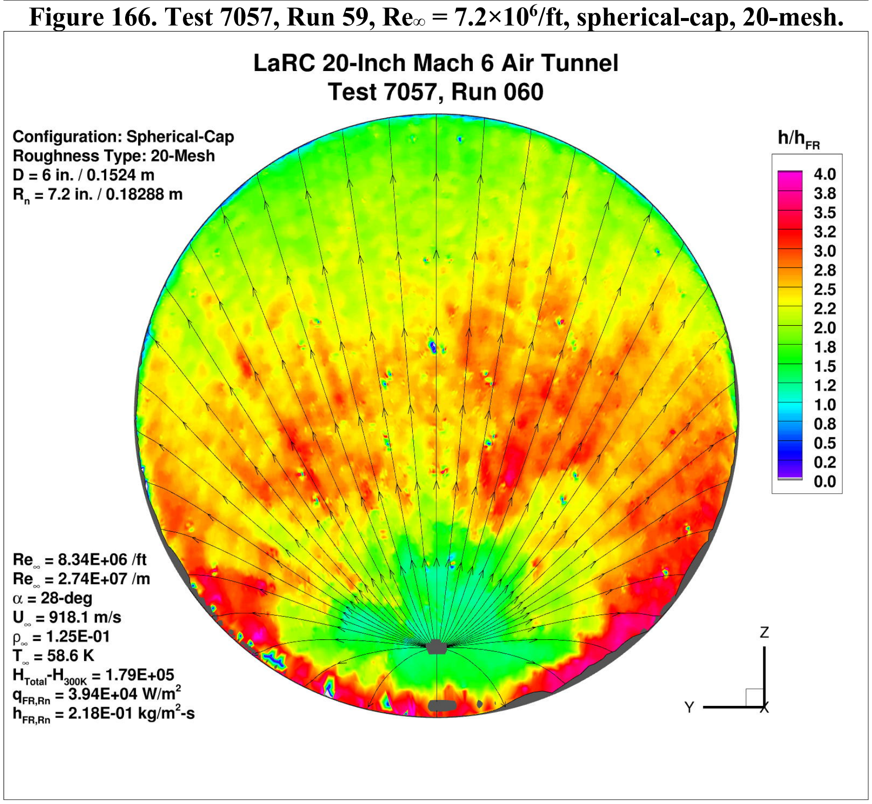

Figure 167. Test 7057, Run 60, Re∞ = 8.1×10^6/ft, spherical-cap, 20-mesh.

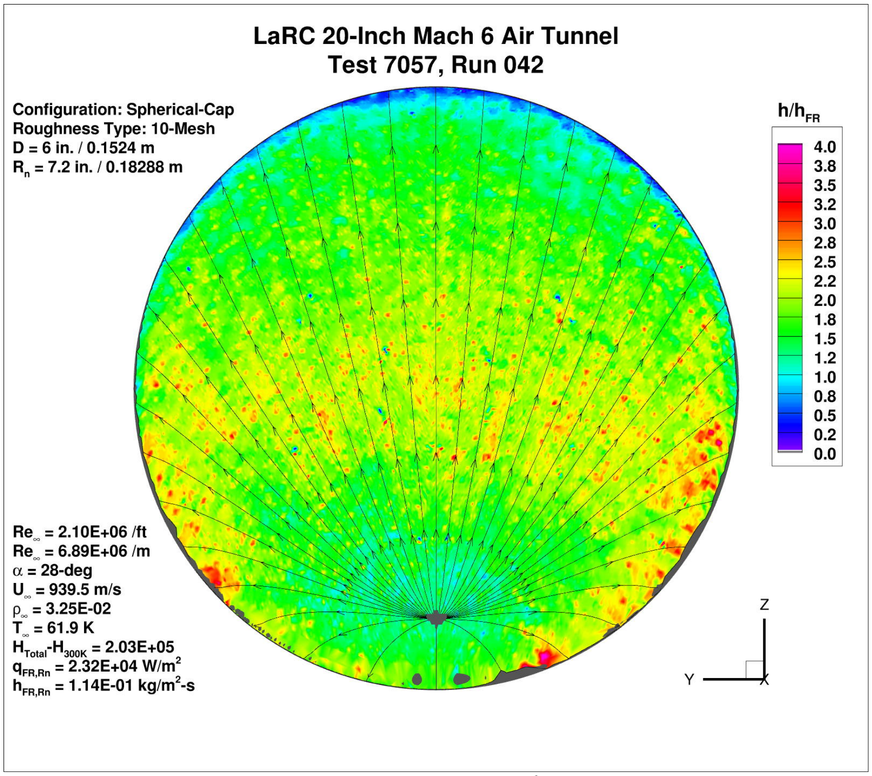

Figure 168. Test 7057, Run 42, Re∞ = 2.1×10^6/ft, spherical-cap, 10-mesh.

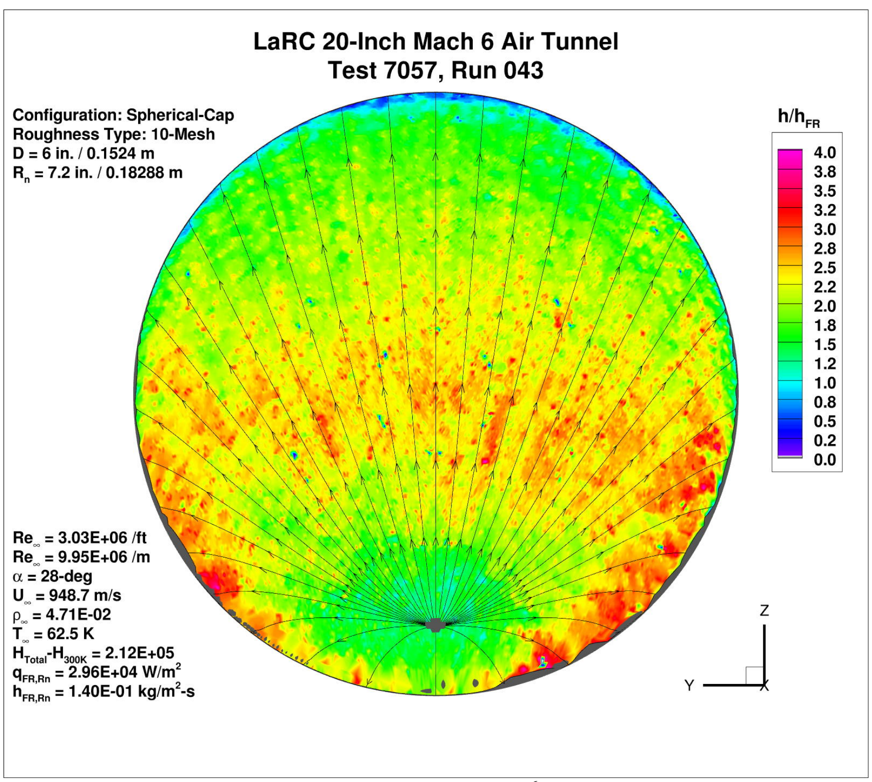

Figure 169. Test 7057, Run 43, Re∞ = 3.0×10^6/ft, spherical-cap, 10-mesh.

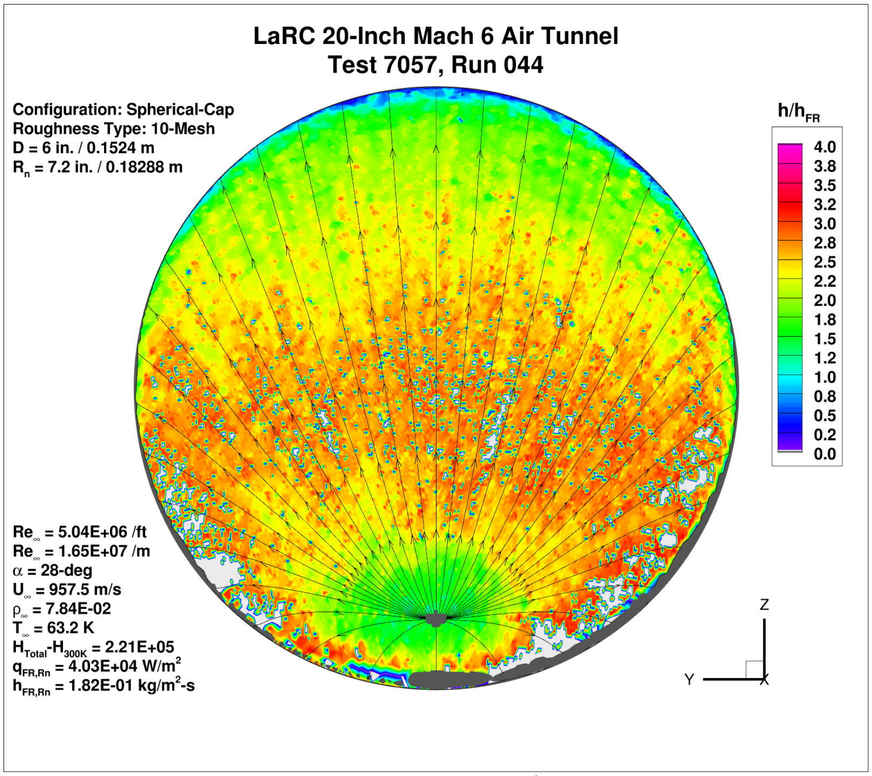

Figure 170. Test 7057, Run 44, Re∞ = 5.0×10^6/ft, spherical-cap, 10-mesh.

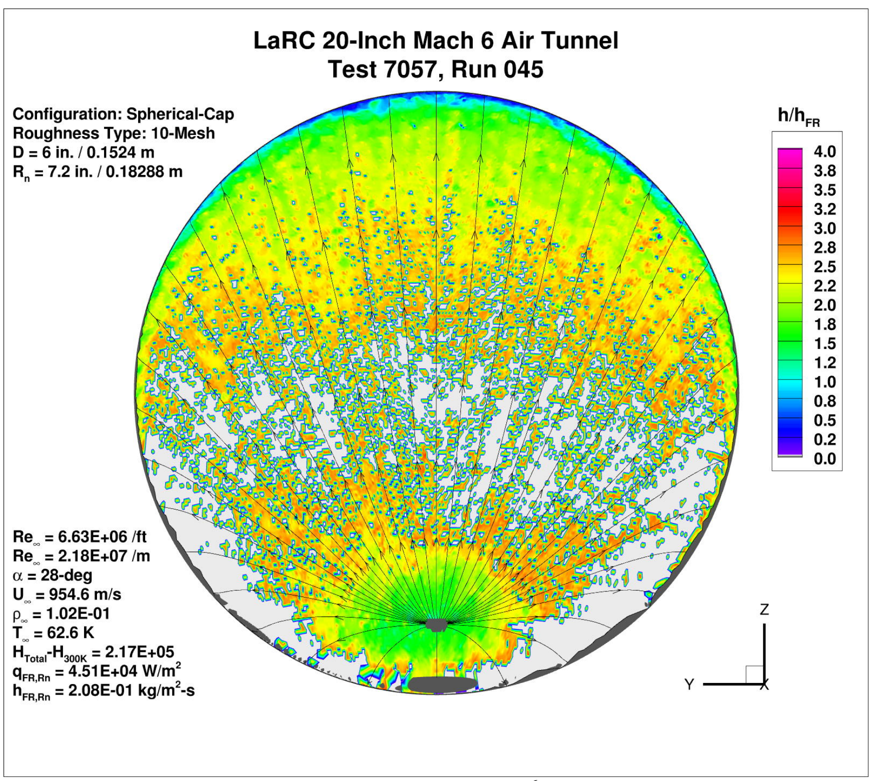

Figure 171. Test 7057, Run 45, Re∞ = 6.5×10^6/ft, spherical-cap, 10-mesh.

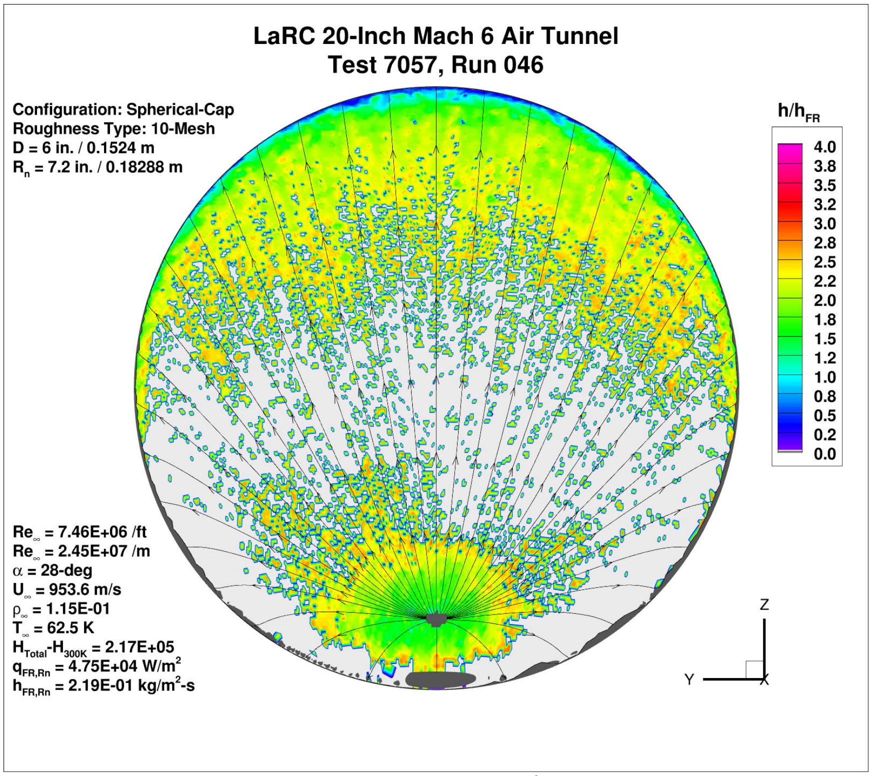

Figure 172. Test 7057, Run 46, Re∞ = 7.2×10^6/ft, spherical-cap, 10-mesh.

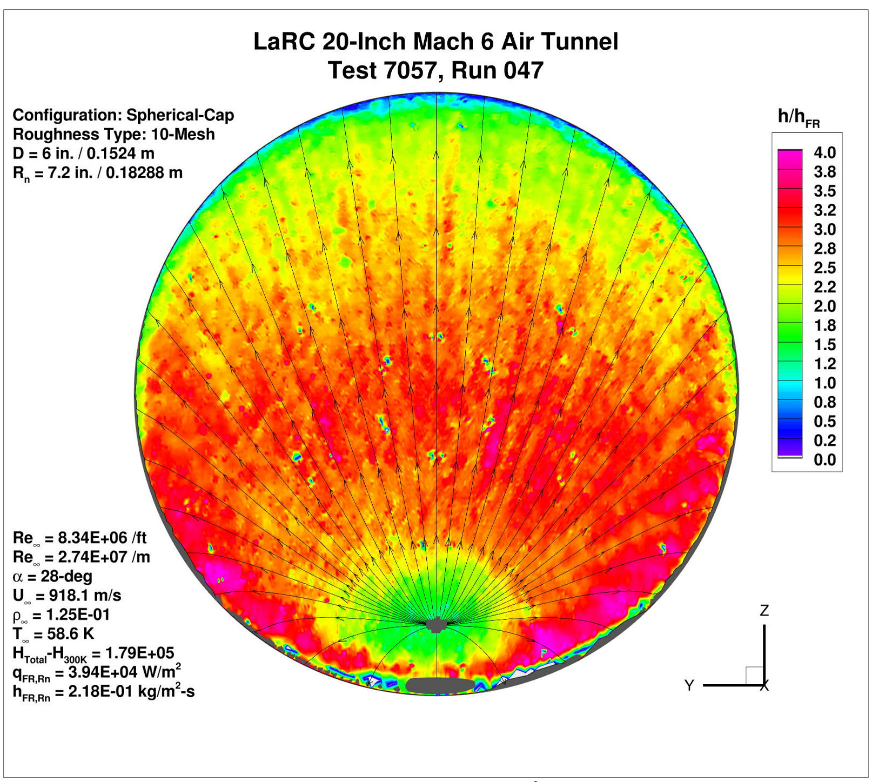

Figure 173. Test 7057, Run 47, Re∞ = 8.1×10^6/ft, spherical-cap, 10-mesh.